Doctorate Dissertation
博士論文

Study of the cosmic star formation history based on a multi-wavelength analysis of ALMA continuum sources and an unbiased search of millimeter line emitters

(ALMA 連続波天体の多波長解析と無バイアスミリ波輝線銀河探査に基づく宇宙星形成活動史の研究)

A Dissertation Submitted for Degree of Doctor of Philosophy
December 2018
平成 30 年 12 月 博士 (理学) 申請

Department of Astronomy, Graduate School of Science,
The University of Tokyo
東京大学大学院理学系研究科天文学専攻

Yuki Yamaguchi
山口 裕貴

Study of the cosmic star formation history based on a multi-wavelength analysis of ALMA continuum sources and an unbiased search of millimeter line emitters

a dissertation presented
by
Yuki Yamaguchi
to
The Department of Astronomy, Graduate School of Science,

in partial fulfillment of the requirements
for the degree of
Doctor of Philosophy
in the subject of
Science

The University of Tokyo
7-3-1, Hongo, Bunkyo-ku, Tokyo, Japan
December 2018

©2018 – Yuki Yamaguchi
all rights reserved.

Thesis advisor: Professor Kotaro Kohno Yuki Yamaguchi

Study of the cosmic star formation history based on a multi-wavelength analysis of ALMA continuum sources and an unbiased search of millimeter line emitters

Abstract

One of the main goals in astronomy is unveiling the cosmic star formation history. Thus, it is important to constrain the contributions of dusty star-forming galaxies to the cosmic star formation density (SFRD) in the high redshift universe and the evolution of the molecular gas mass content in the universe. In this theses, we report results of the multi-wavelengths analysis of 1.2 mm continuum sources and a blind millimeter line emitter search toward gravitational lensing clusters using the latest data of Atacama Large Millimeter/sub-millimeter Array (ALMA) in order to understand the cosmic star formation history comprehensively from the point of view of the dusty star-forming activity itself and material of star formation.

We make use of the ALMA deep 1.2 mm continuum observation of a 26 arcmin^2 region in the GOODS-S named ALMA twenty-Six Arcmin^2 survey of GOODS-S At One-millimeter (ASAGAO; Project ID: 2015.1.00098, PI: K. Kohno), to probe dust-enshrouded star formation in K-band selected (i.e., stellar-mass selected) galaxies, which are drawn from the FourStar galaxy evolution survey (ZFOURGE) catalog. Based on the ASAGAO final map, which was created by combining ASAGAO and ALMA archival data in the GOODS-S field, we find that 66 ZFOURGE sources have 1.2 mm counterparts with a signal-to-noise ratio (S/N) $>$ 3.5 ($1\sigma \simeq$ 30–70 μJy beam^{-1} at 1.2 mm). The flux densities of these ASAGAO sources tend to be fainter ($S_{1.2\mathrm{mm}} \lesssim 1.0$ mJy) than that of bright sub-millimeter galaxies (SMGs; $S_{1.2\mathrm{mm}} \gtrsim 1.0$ mJy). Their median redshift is estimated to be $z_{\mathrm{median}} = 1.77 \pm 0.23$, which is consistent with recent results of faint (sub-)millimeter sources detected in recent ALMA deep surveys. They generally ($\sim$ 90% of ASAGAO sources) follow the tight relationship of the stellar mass versus star formation rate (SFR;

i.e., the main sequence of star-forming galaxies). ALMA-detected ZFOURGE sources exhibit systematically larger ($\gtrsim$ 1–2 dex) infrared (IR) excess (IRX $\equiv L_{\rm IR}/L_{\rm UV}$) compared to ZFOURGE galaxies without ALMA detections even though they have similar redshift, stellar masses, and SFRs. This implies the consensus stellar-mass versus IRX relation, which is known to be tight among rest-frame-UV-selected galaxies, can not fully predict the ALMA detectability of stellar-mass-selected galaxies. The spatially resolved IRX-$\beta_{\rm UV}$ relation of ASAGAO sources suggests that the differences can partly be caused by the difference distribution between dust and stars. We estimate the evolution of the contributions of ASAGAO sources to the cosmic SFRD as a function of redshift and find that the shape of the evolution is similar to that of previous studies. The ALMA-detected ZFOURGE sources are the main contributors to the cosmic SFRD at z = 2–3 ($\sim$ 60% of the cosmic UV + IR SFRD and $\sim$ 80% of the cosmic IR SFRD).

We also detect five 1.2 mm continuum sources ($S_{1.2{\rm mm}}$ = 0.45–0.86 mJy) without any counterparts in the deep *H*- and/or *K*-band image. Their ratio between radio and millimeter flux densities as well as optical to radio spectral energy distributions indicate that they can lie at $z \gtrsim$ 3–5 and they can be in the early phase of massive galaxy formation. One of the *K*-band-dark ALMA sources has a red *Spitzer*/IRAC counterpart at 3.6 and 4.5 μm. Another one has been independently detected at 850 and 870 μm using SCUBA2 and ALMA Band 7, respectively. Their contribution to the cosmic SFRD is estimated to be $\sim$ 1–3 $\times$ 10^{-3} $M_{\odot}$ yr^{-1} Mpc^{-3} (corresponding to $\sim$ 10–30% of previous studies) if they lie somewhere in the redshift range of $z \sim$ 3–5. This value can be consistent with, or greater than that of bright submillimeter galaxies ($S_{870\mu{\rm m}} > 4.2$ mJy) at $z \sim$ 3–5. These results show that an unbiased ALMA survey can reveal the dust-obscured star formation activities, which were missed in previous deep optical/near-IR surveys.

In addition to the results on ALMA continuum sources, we also present the results of a blind millimeter line emitter search using ALMA Band 6 data with a single-frequency tuning toward four gravitational lensing clusters (RXJ1347.51145, Abell S0592, MACS J0416.12403, and Abell 2744). We construct 3-dimensional S/N cubes with 60 and 100 MHz binning, and search for millimeter line emitters. We do not detect any line emitters with a peak S/N $>$ 5, although we do find a line emitter candidate with a peak S/N $\simeq$ 4.5. These results provide upper limits to the CO(3–2), CO(4–3), CO(5–4), and [CII] luminosity

functions at $z \simeq 0.3$, 0.7, 1.2, and 6, respectively. Because of the magnification effect of gravitational lensing clusters, the new data provide the first constraints on the CO and [CII] luminosity functions at unprecedentedly low luminosity levels, down to $\lesssim 10^{-3}$–10^{-1} Mpc^{-3} dex^{-1} at $L'_{\rm CO} \sim 10^{8}$–10^{10} K km s^{-1} pc^{2} and $\lesssim 10^{-3}$–10^{-2} Mpc^{-3} dex^{-1} at $L_{\rm [CII]} \sim 10^{8}$–$10^{10}$ $L_{\odot}$, respectively. Although the constraints to date are not stringent yet, we find that the evolution of the CO and [CII] luminosity functions are broadly consistent with the predictions of semi-analytical models. This study demonstrates that the wide observations with a single frequency tuning toward gravitational lensing clusters are promising for constraining the CO and [CII] luminosity functions. [CII]

Acknowledgments

This work in this thesis is based on the research carried out at the Department of Astronomy, The University of Tokyo, Japan. No part of this thesis has been submitted elsewhere for any other degree or qualification.

First of all, I would like to dedicate my deepest appreciation to Professor Kotaro Kohno, my supervisor, for his kind education on me. He introduced me this interesting millimeter/sub-millimeter astronomy and I received generous support by him during my life as a graduate student. I also would like to appreciate to Bunyo Hatsukade (The University of Tokyo) and Yoichi Tamura (Nagoya University) for sharing a large amount of time to discuss various matters related to this thesis. They are pioneer in observational astronomy at millimeter/sub-millimeter wavelengths. I am really thankful to the present/former members of the Kohno group: Fumi Egusa, Tastuya Takekoshi, Hideki Umehata, Tao Wang, Yuri Nishimura, Tsuyoshi Ishida, Mamiko Sato, Yui Yamashita, Lee Kianhong, Yuki Yoshimura, Shinsuke Uno, Soh Ikarashi, Takuma Izumi, Akio Taniguchi, and Ryo Ando (see also the figure bellow).

The large parts of this thesis are coming from the works with my great collaborators all over the world: Yiping Ao, Karina I. Caputi, James S. Dunlop, Eiichi Egami, Daniel Espada, Seiji Fujimoto, Natsuki H. Hayatsu, Rob J. Ivison, Tadayuki Kodama, Haruka Kusakabe, Tohru Nagao, Masami Ouchi, Wiphu Rujopakarn, Ken-ichi Tadaki, Yoshihiro Ueda, Wei-Hao Wang, Min S. Yun, Masamune Oguri, Hajime Ezawa, Tetsu Kitayama, Yuichi Matsuda, Hiroshi Matsuo, Tai Oshima, and Naomi Ota. I would really appreciate for their enormous cooperation. The intensive discussion with them greatly improved my knowledge and skills on the millimeter/sub-millimeter astronomy.

This thesis makes use of the following ALMA data: ADS/JAO.ALMA#2013.1.00724.S, 2013.1.00999.S, 2013.1.00718.S, 2015.1.01222.S, 2015.1.00098.S, 2015.1.00543.S, and 2012.1.00173.S. ALMA is a partnership of ESO (representing its member states), NSF (USA), and NINS (Japan) together with NRC

(Canada), NSC and ASIAA (Taiwan), and KASI (Republic of Korea) in cooperation with the Republic of Chile. The Joint ALMA Observatory is operated by ESO, AUI/NRAO, and NAOJ. Data analysis was partly carried out on the common-use data analysis computer system at the Astronomy Data Center (ADC) of the National Astronomical Observatory of Japan. This research made use of the NASA/IPAC Extragalactic Database (NED), which is operated by the Jet Propulsion Laboratory, California Institute of Technology, under contract with the National Aeronautics and Space Administration.

I really appreciate the referees of this thesis: Kazuhiro Shimasaku, Seiichi Sakamoto, Masato Tsuboi, Kouji Ohta, and Kentaro Nagamine. Their comments and suggestions helped me to improve this thesis.

I would like to thank my classmates, especially those who at the Institute of Astronomy, The University of Tokyo, for intensive discussion on each of our project: Masahito Uchiyama and Jiang Jian.

I really appreciate for financial supports from the Japan Society for the Promotions of Science.

Finally, my deepest appreciation goes to my family who have supported me all the time.

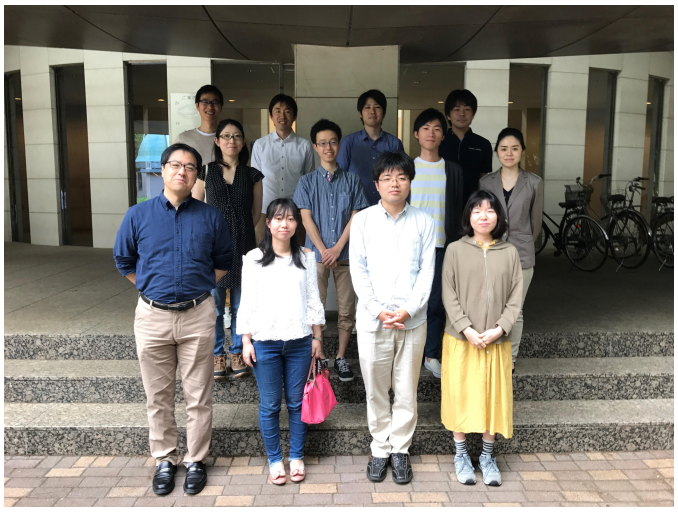

Picture of the Kohno Laboratory members (2018).

Contents

1

Introduction

1.1 The cosmic star formation history

One of the main goals in astronomy is unveiling the cosmic star formation history, in other words, the evolution of the cosmic star formation rate density (SFRD). In the past few decades, multi-wavelengths surveys using ground-based and satellite telescopes have resolved the evolution of the cosmic SFRD (e.g., Madau et al., 1996; Steidel et al., 1999; Kashikawa et al., 2003; Chapman et al., 2005; Bouwens et al., 2007, 2012, 2015, 2016; Wardlow et al., 2011; Burgarella et al., 2013; Madau & Dickinson, 2014, and references therein). In Figure 1.1 show the evolution of the cosmic SFRD as a function of redshift compiled by Madau & Dickinson (2014). As shown in Figure 1.1, the cosmic SFRD has a peak level at $z \simeq 2$–3 and then declines rapidly toward $z = 0$.

Young massive stellar populations in galaxies mainly emit their energy in the form of rest-frame ultraviolet (UV) radiation. Thus, we can use UV luminosity as an indicator of "un-obscured" star formation

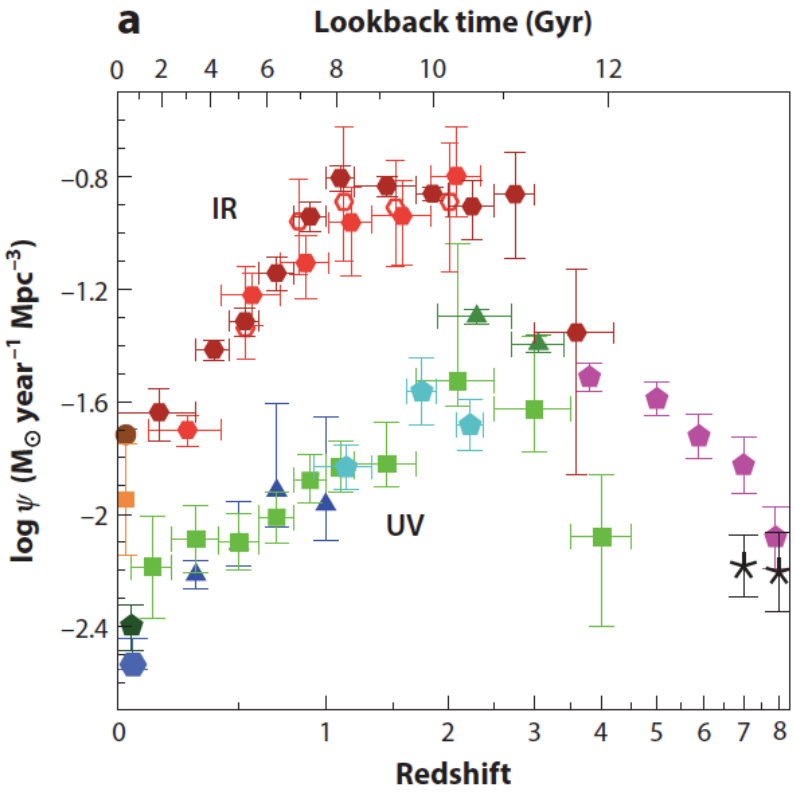

Figure 1.1 The evolution of the cosmic SFRD compiled by Madau & Dickinson (2014). Red symbols indicate the SFRD obtained by IR wavelengths. Green symbols are the SFRD obtained by UV observations. This figure is refereed from Figure 8 of Madau & Dickinson (2014).

rate (SFR) of a galaxy. However, some UV radiation from young massive stars can be absorbed by interstellar dust. The energy that interstellar dust absorbs from the UV is re-radiated at longer wavelengths. We can measure this "dust-obscured" SFR by using infrared (IR) luminosity of a galaxy. Therefore, un-obscured and dust-obscured star-forming activities are in a complementary relationship and we have to observe not only rest-frame UV radiation but also rest-frame IR radiation to constrain the evolution of the cosmic SFRD.

Many optical/near-IR (i.e., rest-frame UV) large surveys unveil the contribution of un-obscured star-fromation activities to the cosmic SFRD using rest-flame UV-selected galaxies such as Lyman-Alpha Emitters (LAEs) or Lyman Break Galaxies (LBGs; e.g., Madau et al., 1996; Kashikawa et al., 2003;

Bouwens et al., 2007, 2012, 2015, 2016). The contributions of dust-obscured star-formation activities to the cosmic SFRD have been studied by deep surveys at far-IR or (sub-)millimeter wavelengths using *Infrared Space Observatory* (*ISO*), *Infrared Astronomical Satellite* (*IRAS*), *AKARI*, *Herschel Space Telescope* (*Herschel*), or (sub-)millimeter cameras mounted on ground-based telescopes. These large far-IR/(sub-)millimeter surveys suggest that dust-obscured star-formation activities play a dominant role in the cosmic star-formation activities at $z \simeq 1$–3 (e.g., Takeuchi et al., 2005; Goto et al., 2011; Burgarella et al., 2013, see also Figure 1.1). However, their contribution at $z \gtrsim 3$–4 is still under debate because of the sensitivity limit attributed to the poor angular resolution at far-IR to (sub-)millimeter wavelengths, even though the contribution of rest-frame UV selected sources is well determined until $z \gtrsim 6$–7 using high-redshift LBGs (e.g., Ouchi et al., 2009; Bouwens et al., 2015, 2016). Therefore, determining the contribution of dust-obscured SFRs to the cosmic SFRD in the high-redshift universe is one of the main issues to constrain the cosmic star formation history.

Another big issue on the cosmic star formation history is the reason why the cosmic SFRD declines rapidly toward $z = 0$. To settle this issue, we have to focus on not only star formation activities in itself, but also material of stars, that is, cold molecular clouds in galaxies. The most abundant molecule in cold molecular clouds is molecular hydrogen, but the lowest rovibrational transitions of molecular hydrogen are forbidden because of the lack of a permanent dipole moment. Thus, rotational transition lines of carbon monoxide (CO), which is the second abundant molecule in cold molecular clouds, are often used to measure molecular gas mass in a galaxy. CO rotational transition lines are emitted at (sub-)millimeter wavelengths and have been observed by many (sub-)millimeter spectroscopic observations (Carilli & Walter, 2013, for review). However, the cause of the evolution of the cosmic SFRD is still under discussion. One possibility is that the star formation efficiency defined by SFR divided by molecular gas mass in a galaxy declines toward present (e.g., Sargent et al., 2014; Tacconi et al., 2018). The other possibility is that the molecular gas mass content in the universe decreases toward $z = 0$ (e.g., Decarli et al., 2016). Which is important to explain the evolution of the cosmic SFRD?

The primary objective of this study is to answer these two issues. In the following sections, we introduce the position of this thesis in the context of studying the cosmic star formation history from the

two viewpoints of continuum and spectroscopic observations at (sub-)millimeter wavelengths.

1.2 Continuum observations at (sub-)millimeter wavelengths

1.2.1 Discovery of bright SMGs

At the rest-frame far-IR to millimeter wavelengths, spectroscopic energy distributions (SEDs) of galaxies are dominated by the steep Rayleigh-Jeans slope of the thermal dust emission. This characteristic profile of galactic SEDs generates the effect called as "the negative k-correction". This effect makes observed flux densities at (sub-)millimeter wavelengths almost constant (or even *brighter*) for galaxies with a given IR luminosity[1] at $z \sim 1$–10. In the top panel of Figure 1.2 shows the SED of Arp 220 (a local dusty galaxy; Silva et al., 1998) at $z = 1$–8 and the bottom panel of Figure 1.2 indicates how the observed flux densities of Arp 220 is predicted to vary with redshift. As shown in Figure 1.2, at most observed wavelengths the galaxy is fainter at high redshifts, except at (sub-)millimeter wavelengths. Therefore, the negative k-correction makes it efficient to observed high redshift dusty galaxies at (sub-)millimeter wavelengths. In spite of the benefit of the negative k-correction, it was at the end of 1990s that the first sub-millimeter extragalactic surveys were taken with the Sub-millimeter Common-User Bolometer Array (SCUBA; Holland et al., 1999) on the James Clerk Maxwell Telescope (JCMT), whose observed wavelengths were 850 μm and 450 μm. These surveys uncovered a new population of galaxies, which is extremely bright at (sub-)millimeter wavelengths (e.g., Smail et al., 1997; Hughes et al., 1998; Barger et al., 1998). The observed flux density ($S_{\rm obs}$) at (sub-)millimeter wavelengths (i.e., $\simeq$ 850 μm–1 mm) of the population is larger than a few mJy. Hereafter, we call the population as bright sub-millimeter galaxies (SMGs).

The bright SMGs show huge rest-frame IR luminosities, $\log(L_{\rm IR}/L_{\odot}) \gtrsim 12$–13, which should be powered by dust-obscured star-forming activities (e.g., Alexander et al., 2005; Laird et al., 2010) and their median redshifts are estimated to be $z \simeq 2.1$–3.1 (e.g., Chapman et al., 2005; Simpson et al., 2014). The

[1] In this thesis, we define IR luminosities as luminosities at rest-frame 8–1000 μm.

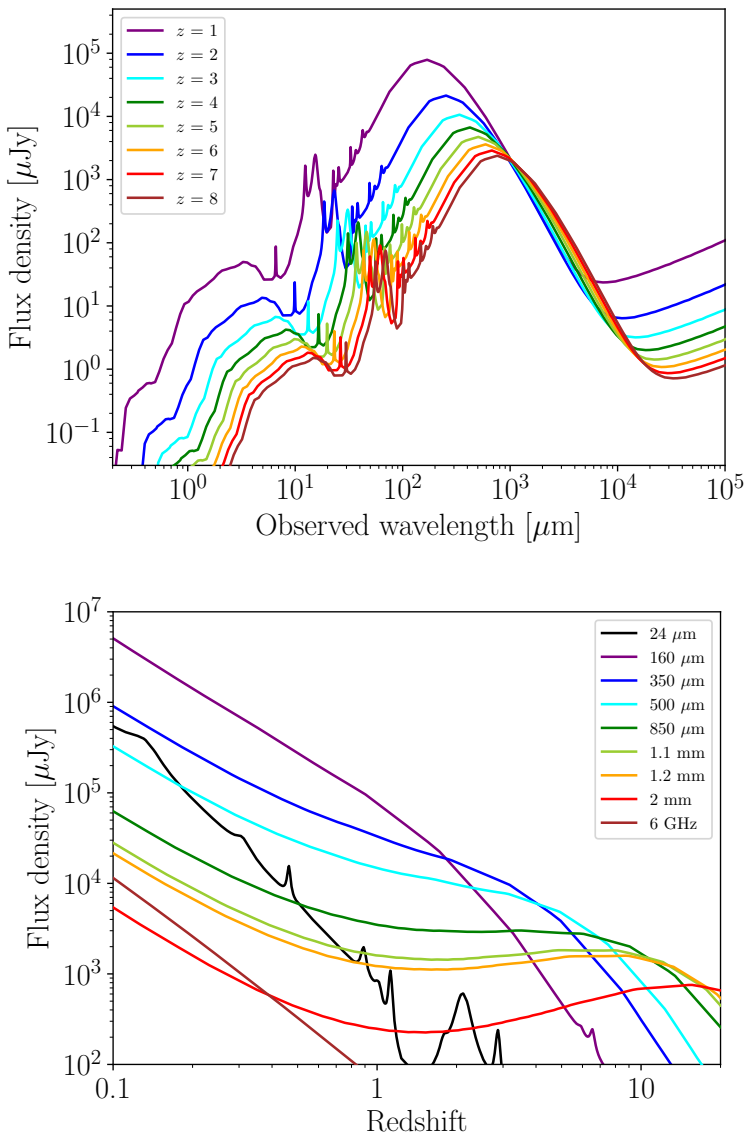

Figure 1.2 *Top)* The redshifted SED of Arp 220 (Silva et al., 1998). From purple to brown, the SED of Arp 220 at z = 1–8. *Bottom)* The flux variation with the redshift of the SED of Arp 220. From black to brown line indicate the case that the observed wavelengths is 24 μm to 5 cm (6 GHz).

extreme SFRs of bright SMGs (SFR $\gtrsim$ a few 100–1000 $M_\odot$ yr^{-1}) make them non-negligible contributors to the cosmic SFRD (e.g., Hughes et al., 1998; Casey et al., 2013; Wardlow et al., 2011; Swinbank et al., 2014).

1.2.2 Millimeter/sub-millimeter surveys using single-dish telescopes

From the discovery of bright SMGs, a number of large (sub-)millimeter surveys have been performed using ground-based and air-bone single-dish telescopes. Examples of large (sub-)millimeter surveys include: the 1.2 mm surveys using the Max-Planck Millimeter Bolometer (Kreysa et al., 1998) on the IRAM 30-m telescope (e.g., Greve et al., 2004), the 1.1 mm surveys using the Bolometer Camera (Glenn et al., 1998) on the Caltech Sub-millimeter Observatory (e.g., Laurent et al., 2005), the 1.1 mm surveys using the Astronomical thermal emission camera (AzTEC; Wilson et al., 2008) on the Atacama Sub-millimeter Telescope Experiment (ASTE; e.g., Scott et al., 2008, 2010; Tamura et al., 2009; Aretxaga et al., 2011; Hatsukade et al., 2011; Umehata et al., 2014), the 870 μm surveys using the Large APEX Bolometer Camera (LABOCA; Siringo et al., 2010) on the Atacama Pathfinder Experiment (e.g., Weiß et al., 2009), the 450 and 850 μm surveys using the SCUBA and SCUBA2 (Holland et al., 2013) on the JCMT (e.g., Ivison et al., 2000, 2007; Casey et al., 2013; Cowie et al., 2017), and the 250, 350, and 500 μm surveys by Spectral and Photometric Imaging Receiver (SPIRE; Griffin et al., 2010) on *Herschel* (e.g., Elbaz et al., 2011; Oliver et al., 2012).

These large surveys have played essential roles in revealing the contributions of dust-obscured star-forming activities, but their limited angular resolution (e.g., $\simeq 30''$ at 1.1 mm with AzTEC/ASTE) does not allow us to measure far-IR fluxes of individual sources if we go down to the luminous IR galaxy (LIRG) class sources [i.e., $\log(L_{\rm IR}/L_\odot) \simeq 11$–$12$] due to the confusion limit of single-dish telescopes. Indeed, the contributions of bright SMGs [i.e., ultra luminous IR galaxy (ULIRG) class galaxies with $\log(L_{\rm IR}/L_\odot) \simeq 12$–$13$] to the IR extragalactic background light is not so large ($\sim$ 20–40% at 850 μm and $\sim$ 10–20% at 1.1 mm; e.g., Eales et al., 1999; Coppin et al., 2006; Weiß et al., 2009; Hatsukade et al., 2011; Scott et al., 2012). This means that the bulk of dust-obscured star formation activities in the universe remained unresolved.

With single-dish telescopes, we can access the fainter (sub-)millimeter population (i.e., $S_{\rm obs} \lesssim 1$ mJy) using gravitational magnification by lensing clusters or stacking analysis (e.g., Knudsen et al., 2008; Geach et al., 2013; Coppin et al., 2015). However, in lensed object surveys, the effective sensitivity comes at the cost of a reduced survey volume. Knudsen et al. (2008) suggest that the effective (source-plane) area within sufficient magnification to detect fainter (sub-)millimeter populations is only ~ 0.1 arcmin^2 for a typical rich cluster. This effect increases the cosmic variance uncertainty (e.g., Robertson et al., 2014). In addition, the uncertainty of lensing models itself increase flux errors of (sub-)millimeter sources. The stacking technique is a useful way to obtain the average properties of less-luminous populations, but individual source properties have remained unexplored. Therefore, more sensitive observations with higher angular resolution are needed.

1.2.3 Millimeter/sub-millimeter continuum observations using ALMA

The advent of the Atacama Large Millimeter/sub-millimeter Array (ALMA), which offers high sensitivity and angular resolution capabilities, has allowed the fainter (sub-)millimeter population to be revealed below the confusion limit of single-dish telescopes. Several recent studies have presented follow-up observations of bright SMGs such as the ALMA follow-up observation of the LABOCA Extended Chandra Deep Field South surveys (ALESS; e.g., Hodge et al., 2013; Swinbank et al., 2014; Simpson et al., 2014; da Cunha et al., 2015). Some studies have used rich ALMA science archival data (e.g., Fujimoto et al., 2016; Oteo et al., 2016) and find many faint (sub-)millimeter sources. Some studies have investigated proto-clusters or blank fields contiguously. Figure 1.3 shows one of the example of such ALMA contiguous surveys performed in Subaru/*XMM–Newton* Deep Survey Field (SXDF-ALMA survey; Tadaki et al., 2015; Kohno et al., 2016; Hatsukade et al., 2016; Yamaguchi et al., 2016; Wang W.-H. et al., 2016). They observed the $\sim$ 2-arcmin^2 area around a bright SMGs with sub-millimeter bright filamentary structure discovered by AzTEC/ASTE (the left panel of Figure 1.3) and extracted 5 sources with signal-to-noise ratio (S/N) > 5 and 25 sources with S/N > 4.0 along the line with sub-millimeter filamentary structure (Yamaguchi et al., 2016; Hatsukade et al., 2016). In addition to the SXDF-ALMA survey, there are another examples of ALMA contiguous surveys such as the ALMA Deep Field in SSA22 (Ume-

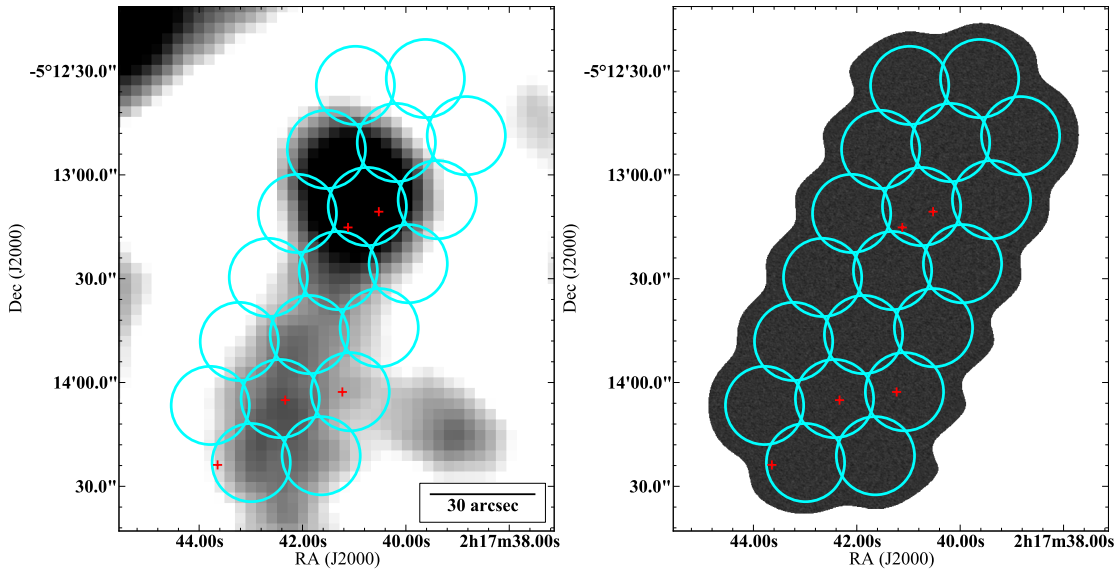

Figure 1.3 *Left)* The 1.1 mm image of AzTEC/ASTE in the SXDF field (Ikarashi, 2014). *right)* The 1.1 mm image of ALMA Band 6 (Kohno et al., 2016). Cyan circles indicate ALMA field-of-views at Band 6. Red crosses are SXDF-ALMA sources presented in Yamaguchi et al. (2016).

hata et al., 2017, 2018), the ALMA SPECtroscopic Survey in the *Hubble* Ultra-Deep Field (ASPECS; e.g., Aravena et al., 2016b; Walter et al., 2016), the ALMA deep observation in the *Hubble* Ultra Deep Field (HUDF; Rujopakarn et al., 2016; Dunlop et al., 2017), and the ALMA survey in the Great Observatories Origins Deep Survey-South (GOODS-ALMA survey; Franco et al., 2018).

These ALMA survey have begun to reveal the role of faint (sub-)millimeter sources in the cosmic SFRD. The contribution of faint (sub-)millimeter sources with $S_{\rm obs} \sim 0.1$–1 mJy at 1.1–1.3 mm to the IR extragalactic background light have been estimated to be $\simeq$ 40–80% (e.g., Ono et al., 2014; Carniani et al., 2015; Oteo et al., 2016; Aravena et al., 2016b; Hatsukade et al., 2013, 2016, 2018). Deeper number counts down to $\sim$ 0.02 mJy have obtained by Fujimoto et al. (2016), who craimed that $\sim$ 100% of the IR extragalactic background light at 1.2 mm. These studies suggest that faint (sub-)millimeter source play an important role in the cosmic SFRD in the high redshift universe, but in these studies their real contribution to the cosmic SFRD is still uncertain because of the lack of redshift information.

Multi-wavelength analysis of ALMA-detected (sub-)millimeter faint sources, which based on the

cross-matching of the ALMA-detected sources and optical/near-IR selected sources with reliable photometric redshifts and stellar-mass estimates, enable us to resolve as well as their contribution to the cosmic SFRD and their star-forming properties (e.g., da Cunha et al., 2015; Tadaki et al., 2015; Yamaguchi et al., 2016; Aravena et al., 2016b; Bouwens et al., 2016; Dunlop et al., 2017; Franco et al., 2018). These studies suggest that the ALMA-detected faint (sub-)millimeter sources mainly lie on the high-mass end of the main-sequence of star formation galaxies at $z \sim 1$–4 (the specific SFRs, the stellar masses divided by SFRs, $\sim 10^{-9}$–10^{-8} yr^{-1}), and they are dominant contributors to the cosmic SFRD at $z \sim 2$–4. Despite these progress, current studies are still affected by the cosmic variance uncertainty because these ALMA studies are based on targeted or small-area (i.e., $\lesssim$ a few arcmin^2) observations, except for the GOODS-ALMA survey by Franco et al. (2018). The GOODS-ALMA survey observed a $\simeq 69$ arcmin^2 area in the GOODS-S field; however, their source detection rate is small due to their sensitivity ($\sigma \simeq 0.18$ mJy beam^{-1} at 1.1 mm). Therefore, wide, deep, and contiguous observations using ALMA are essential for studying the evolution of the dust-obscured star formation activities in the universe.

In addition to the direct observations of (sub-)millimeter populations, the estimating of IR luminosity of a galaxy from its UV luminosity using the IR excess or IRX, defined as a ratio of IR luminosity to UV luminosity ($L_{\rm IR}/L_{\rm UV}$) is one of the other ways to constrain the cosmic IR SFRD at high redshift. The relation between the IRXs and physical parameters of galaxies have been studied. For example, a tight correlation between the stellar masses and the IRXs has been proposed (IRXs of galaxies increase significantly with their stellar masses; e.g., Bouwens et al. 2016; Fudamoto et al. 2017; Koprowski et al. 2018), mainly based on the rest-frame-UV-selected galaxies such as LBGs. Indeed, recent ALMA studies of stellar mass-selected galaxies report that ALMA detected sources, which show large IRX values, tend to preferentially have large stellar masses ($M_* \gtrsim 10^{10}\ M_\odot$; Tadaki et al. 2015; Hatsukade et al. 2015; Aravena et al. 2016b; Bouwens et al. 2016; Dunlop et al. 2017). However, it is not entirely clear if the stellar mass is the unique parameter to predict IRXs in galaxies, and whether such a trend can be applicable to other types of galaxies such as rest-frame-optical-selected galaxies. It is also intriguing to see if there are low-mass galaxies with an elevated IRX or high-mass galaxies with a low IRX. Indeed, Faisst et al. (2017) suggest that different dust properties make the relation between IRXs and UV-slope ($\beta_{\rm UV}$) of

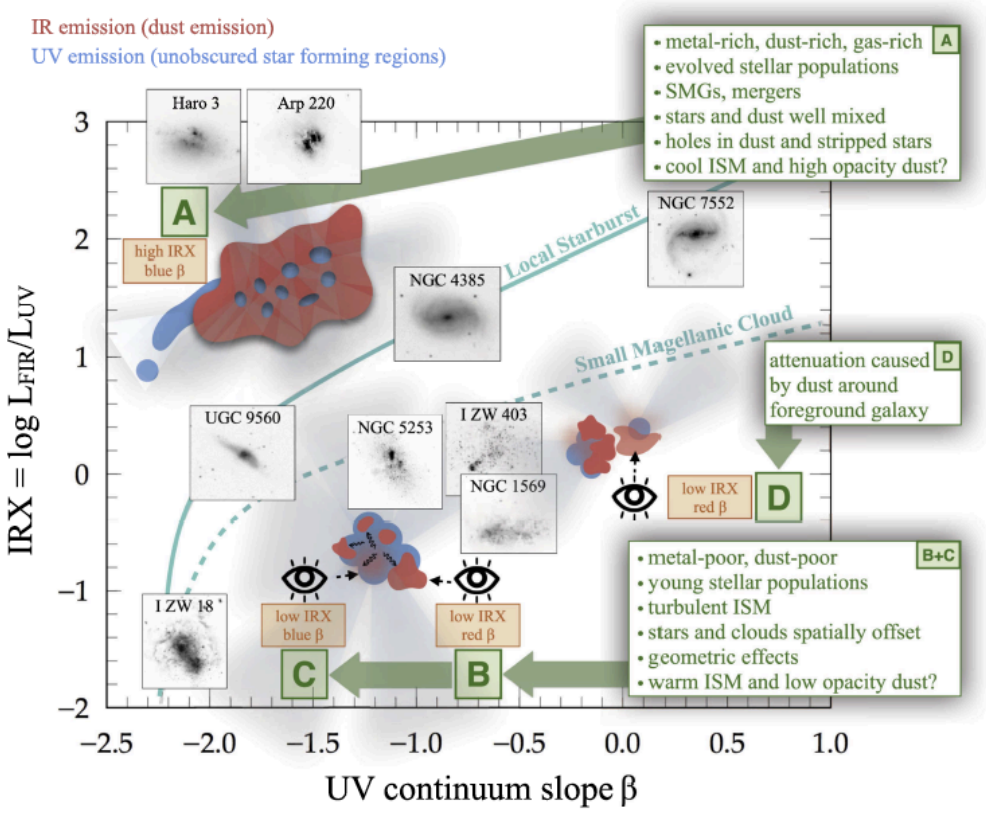

Figure 1.4 Schematic of different population of galaxies on the IRX-$\beta_{\rm UV}$ plane (refereed from Figure 14 of Faisst et al., 2017).

galaxies more complex (see Figure 1.4), which can affect the IRX-M_* relation of galaxies. Currently, the number of galaxies with both stellar-mass and IRX measurements using ALMA is still insufficient to address these questions.

Some of these ALMA observations also report that there are ALMA-detected faint (sub-)millimeter sources which are not well characterized by such a cross-matching technique, i.e., faint (sub-)millimeter sources without significant counterparts at optical/near-IR wavelengths (e.g., Fujimoto et al., 2016; Yamaguchi et al., 2016; Franco et al., 2018). The existence of optical/near-IR-dark faint (sub-)millimeter sources have already reported by using pre-ALMA interferometers (e.g., Yun et al., 2008; Wang et al., 2009; Tamura et al., 2010). In the ALMA era, Simpson et al. (2014) found that a significant fraction (17

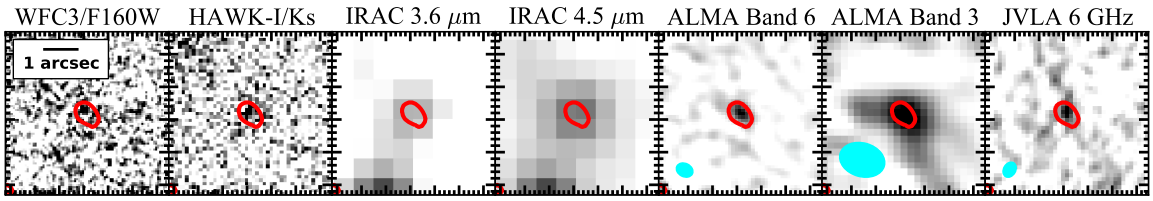

Figure 1.5 Multi-wavelength view of a near-IR-faint SMG, SXDF-ALMA3, reported in Yamaguchi et al. (2016). From left to right, the *HST* WFC3/*F160W*, the VLT HAWK-I/K_s, the *Spitzer* IRAC/3.6 μm, the *Spitzer* IRAC/4.5 μm, the ALMA 1.1 mm, the ALMA 3.0 mm, and the JVLA 6 GHz image ($5'' \times 5''$). The red solid line is the 5σ contour at the ALMA 1.1mm. The cyan marks indicate the synthesized beam size of ALMA Band 6, ALMA Band 3, and JVLA 6 GHz data.

out of 96) of the bright ALMA sources detected by ALESS are too faint in the optical/near-IR bands to obtain reliable constraints on their photometric redshift, arguing that such "near-IR-faint" SMGs tend to lie at higher redshift than the typical SMGs based on the *Herschel* stacking. Similarly, ALMA follow-up observations of SCUBA2-selected SMGs in UDS revealed that 4 bright ALMA sources out of 23 does not have significant near-IR counterparts (Simpson et al., 2015). And in fact, such trend extends to the faint (sub-)millimeter galaxies purely selected by ALMA. For instance, Fujimoto et al. (2016) suggest that $\simeq$ 40% of faint ALMA sources ($S_{1.2\mathrm{mm}}$ = 0.02–1 mJy) uncovered in the ALMA archival images of various fields (the total coverage is $\sim$9 arcmin^2) have no counterparts at optical/near-IR wavelengths (the 5σ limiting magnitude of $\sim$ 27–28 mag at optical wavelengths and $\sim$ 25–26 mag at near-IR wavelengths in the AB system). Yamaguchi et al. (2016) find that one out of five ALMA sources detected by the SXDF-ALMA survey are faint at *H*-band ($\simeq$ 25.3 mag in the AB system) and not detected at wavelengths shorter than $\sim$ 1.3 μm (Figure 1.5). All these studies strongly motivate us to conduct a systematic search for near-IR-dark faint (sub-)millimeter galaxies in the fields where the deepest near-IR images to date are available. If these populations of galaxies lie at high redshift, they can be make a big impact on the cosmic SFRD at high redshift.

1.3 Scope of this thesis on ALMA continuum sources

As we introduce in Section 1.2.3, the ALMA-detected faint (sub-)millimeter sources seem to play a significant role in the cosmic SFRD. However, their quantitative contribution to the cosmic SFRD as a function of redshift and the differences between ALMA detected and non-detected sources are still uncertain because of the cosmic variance and a limited number of samples. Therefore, in this thesis, we present the results of multi-wavelength analysis of 1.2 mm continuum sources detected by the deep and wide-field ($\simeq$ 26 arcmin^2) ALMA survey. We separate the ALMA detected continuum sources into two populations; one is the ALMA detected sources with near-IR counterparts and the other is the near-IR-dark ALMA sources. In following chapters, we discuss the physical properties of each populations and their contributions to the cosmic SFRD.

1.4 Emission lines at millimeter/sub-millimeter wavelengths

In addition to the deep, wide, and contiguous observations using ALMA, one of the promising ways to study the cosmic star formation history is to observe (sub-)millimeter emission lines. As we introduce in section 1.1, the molecular gas content of galaxies can be observed via CO rotational transition lines (e.g., Solomon et al., 1987; Tacconi et al., 2013; Carilli & Walter, 2013, and references therein). The molecular gas mass of galaxies is one of the fundamental properties to understand the galaxy evolution and the cause of the cosmic star formation history. This is because the galaxy evolution is governed by the cycle of molecular gases exchanging between a galaxy and surrounding gases (e.g., Bouché et al., 2010; Davé et al., 2012) and the molecular phase of the interstellar medium is considered to be the fuel for star formation activities (Carilli & Walter, 2013). Furthermore, the [CII] $^2P_{3/2} \rightarrow {}^2P_{1/2}$ fine-structure transition line at 1900.5 GHz (157.74 μm), which is redshfted to (sub-)millimeter wavelengths at $z \simeq$ 4–6 is expected to be a tracer of dust-obscured star formation in local to distant galaxies and one of the brightest fine-structure transition lines at far-IR wavelengths (e.g., De Looze et al., 2011, 2014; Smail et al., 2011; Sargsyan et al., 2012, 2014).

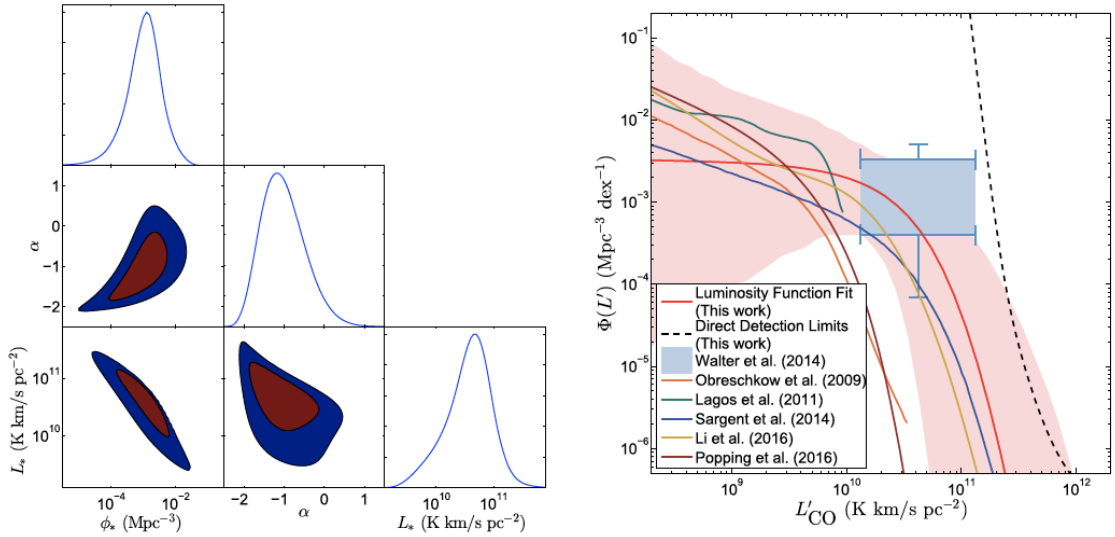

Figure 1.6 *Left)* The constraints on the individual Schechter parameters of the luminosity function. *Right)* The constrained CO(1–0) luminosity function at $z \sim 3$ (Reffered from Figure 8 of Keating et al. 2016).

1.4.1 Observations of millimeter/sub-millimeter emission lines

Because of their importance for the galaxy evolution and the cosmic star formation history, observations of (sub-)millimeter emission lines have been performed toward local and high-redshift galaxies. For example, Tacconi et al. (2013) observed the CO(3–2) transition line from main-sequence star-forming galaxies at $z \sim 1.2$ and 2.2 using the IRAM Plateau de Bure millimeter Interferometer (PdBI; Guilloteau et al., 1992). They found that molecular gas mass fractions[2] of galaxies dropped with their stellar masses and correlated strongly with specific SFRs. Tacconi et al. (2018) compiled CO observations for main sequence star forming galaxies at $z \sim$ 1–4 and suggested that the ratio of molecular gas mass to stellar mass depended on redshift and it tracked the evolution of the specific SFRs. As for [CII] observations, Walter et al. (2012) detected the [CII] line from the bright SMGs (HDF 850.1) at $z \simeq 5.2$. Capak et al. (2015) observed the [CII] emission from LAEs and LBGs at $z \sim$ 5–6 and suggested that the [CII] emission is enhanced relative to the far-IR continuum emission at high redshift. In these cases, however, the

[2]Molecular gas mass fractions, $f_{\rm gas}$ is defined as $f_{\rm gas} = M_{\rm gas}/(M_{\rm gas} + M_*)$.

selection is based on the star formation properties or stellar mass of a given galaxy. In other words, they are pre-selected by optical, near-IR, or (sub-)millimeter wavelengths.

Based on the above reasons, constraining the luminosity functions of (sub-)millimeter line emitters via unbiased (sub-)millimeter line emitter surveys is necessary in order to unveil the cosmic star formation history. The "line intensity mapping" technique is one of the useful ways to constrain (sub-)millimeter line luminosity functions blindly. Keating et al. (2016) applied the technique to galaxies at $z \sim 3$ with the Sunyaev–Zel'dovich Array (Muchovej et al., 2007) and constrained the CO(1–0) luminosity function (Figure 1.6). Serra et al. (2016) simulated three-dimensional power spectra of [CII] emission line fluctuations at $z > 4$ for upcoming spectroscopic surveys. On the other hand individual properties of line emitters have remained unexpected so far, because the emission from a multitude of galaxies over a wide range of line luminosities are integrated in this line intensity mapping technique.

1.4.2 Unbiased line emitter searches at millimeter/sub-millimeter wavelengths

The development of observational instruments such as the IRAM PdBI, or Northern Extended Millimeter Array, and ALMA make unbiased (sub-)millimeter line emitter searches feasible. Walter et al. (2014) and Decarli et al. (2014) tried to detect CO line emitters blindly using the PdBI, but there was no significant detections because of the lack of the sensitivity and/or bandwidth. In the ALMA era, Walter et al. (2016) performed the large unbiased millimeter line emitter survey named ASPECS. Using the ASPECS data, Decarli et al. (2016) putted constraint on CO luminosity functions at $z \simeq 0.5$–3.8 (Figure 1.7) and Aravena et al. (2016b) constrained the [CII] luminosity function at $z \simeq 6$. However, such line emitter searches based on spectroscopic scan observations (i.e., the observed frequency range $>$ several tens of gigahertz) can often be expensive in terms of total observation time. For example, the total observation time of the ASPECS was $\sim$ 40 hours to cover only $\sim$ 1 arcmin^2.

The advent of the ALMA sensitivity and bandwidth, some serendipitous detections of (sub-)millimeter line emitters have been reported. Swinbank et al. (2012) detected the [CII] emission from 2 ALESS SMGs at z = 4.42 and 4.44 serendipitously. Tamura et al. (2014) reported the serendipitous detection of a millimeter line emitter behind the nearby merging galaxies VV114. Hayatsu et al. (2017) found serendipitous

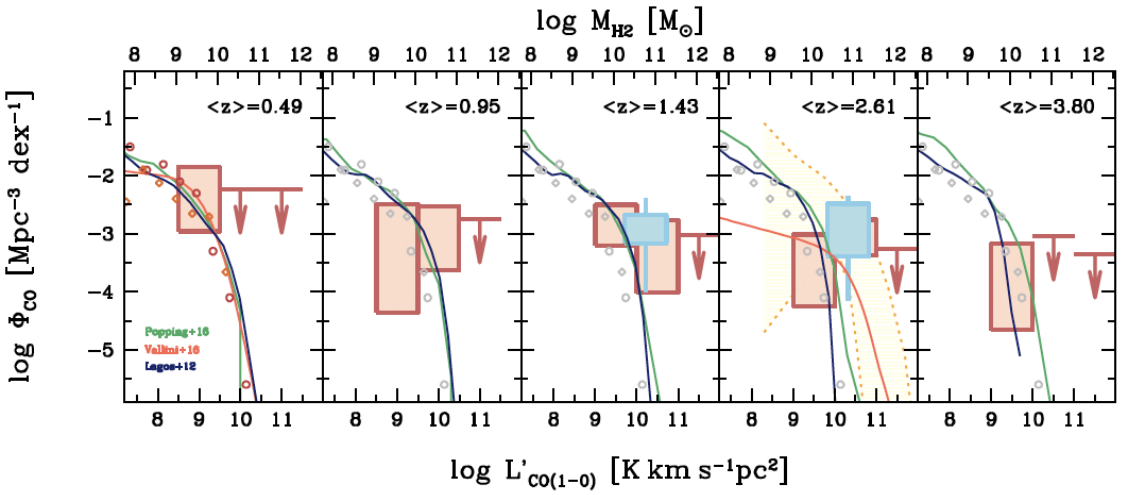

Figure 1.7 CO(1–0) luminosity functions at $z \simeq 0.5$–3.8. Orange boxes indicate constraints from the ASPECS. The observed CO(1–0) luminosity functions of local galaxies by Keres et al. (2003) and Boselli et al. (2014) are shown as red circles and orange diamonds in the first panel, respectively, and as gray points for comparison in all the other panels. The yellow shaded region indicate constraints from the intensity mapping by Keating et al. (2016). The cyan boxes are constraints from the 3 mm scan with PdBI by Walter et al. (2014). Green, and blue solid lines indicate predictions from semi-analytical models obtained by Popping et al. (2016) and Lagos et al. (2012), respectively, The orange solid line is a constraint from empirical predictions by Vallini et al. (2016). This figure is refereed from Figure 5 of Decarli et al. 2016.

4 millimeter line emitter using their continuum observation data in SSA22 Field. In addition, some studies have tried to constrain (sub-)millimeter line luminosity functions using rich ALMA archival data (e.g., Matsuda et al., 2015; Miller et al., 2016). Therefore, using ALMA archival data seems to be one of the useful way to constrain (sub-)millimeter line luminosity functions.

1.5 Scope of this thesis on millimeter line emitter searches

In this thesis, we constrain CO and [CII] luminosity functions by a blind millimeter line emitter search using ALMA Band 6 data toward four gravitational lensing clusters. The data is obtained by not only our observations but also ALMA archive data. Although, previous studies using the ASPECS data

constrained CO and [CII] luminosity functions at various redshifts (e.g., Decarli et al., 2016; Aravena et al., 2016a, see also Figure 1.7), our study can put constraints on CO and [CII] luminosity functions at unprecedentedly low luminosity level because of the magnification effect of gravitational lensing clusters. This study can demonstrate that the wide observations with a single frequency tuning toward gravitational lensing clusters are promising for constraining the CO and [CII] luminosity functions.

1.6 Structure of this thesis

This thesis is structured as follows. In Chapter 1, we have introduced backgrounds of this study and scope of the thesis. In Chapter 2 we explain about our deep and wide ALMA continuum observations and multi-wavelength images which are used in the ALMA continuum study. Next, we present our results of multi-wavelength analysis of ALMA continuum sources with *K*-band counterparts in Chapter 3 and ALMA continuum sources without *K*-band counterparts in Chapter 4. Then, we show our results of a blind millimeter line emitter search in Chapter 5. Chapter 6 is the summary of this thesis.

Throughout this thesis, we assume a Λ cold dark matter cosmology with $\Omega_{\rm M} = 0.3$, $\Omega_{\Lambda} = 0.7$, and $H_0 = 70$ km s^{-1} Mpc^{-1}. All magnitude are given according to the AB system. We adopt the Chabrier Initial Mass Function (IMF; Chabrier, 2003) when necessary to compute the stellar masses and SFRs in galaxies in this thesis.

2

ALMA & multi-wavelength images

In this chapter, we summarize multi-wavelength images which we use in this thesis. In addition to ALMA band 6 data, we use UV to radio data to estimate multi-wavelength properties of ALMA continuum sources.

2.1 ALMA observations & data analysis

In this section, we explain about the ALMA data obtained by our survey named ALMA twenty-Six Arcmin^2 survey of GOODS-S At One-millimeter (ASAGAO; Project ID: 2015.1.00098.S, PI: K. Kohno).

2.1.1 Observation area & ALMA observations

ASAGAO observations were performed toward the Great Observation Origins Deep Survey-*South* field (GOODS-S field; Dickinson et al., 2003). The GOODS-S field is one of the legacy fields where deep multi-wavelengths survey have been performed. Deep multi-wavelength images in the GOODS-S field are useful to obtain physical properties of ALMA detected sources. ASAGAO observation area centered at (R.A., Dec.) = (53.1608 deg, -27.7833 deg). The area was covered by a $\sim 5' \times 5'$ square (the red square in Figure 2.1). As shown in Figure 2.1, the GOODS-S field has been also observed by some ALMA surveys (e.g., Walter et al., 2016; Aravena et al., 2016b; Dunlop et al., 2017; Franco et al., 2018).

The details of ASAGAO observations are explained in ASAGAO related papers (e.g., Hatsukade et al., 2018; Ueda et al., 2018; Fujimoto et al., 2018). Here, we give the brief summary of the ASAGAO observations. The ALMA observations were carried out in September 02–29, 2016 as part of an ALMA Cycle 3 program. The 26 arcmin^2 map of ASAGAO field was covered by $\sim 90 \times 9$ pointings of ALMA with Nyquist sampling. We put 2 frequency tunings to cover a wider frequency range. The center frequency (wavelength) of each frequency tuning was 262.56 GHz (1.14 mm) and 253.56 GHz (1.18 mm), respectively. We utilized the Time Division Mode (TDM), which is mostly used for continuum observations. Four basebands were used for each tuning, and a spectral window was placed of each baseband with a bandwidth of 2 GHz (15.625 MHz $\times$ 128 channels), providing a total nominal bandwidth of 16 GHz or an effective bandwidth of 15 GHz, centered at 258.6 GHz (1.16 mm). For observations, 38–45 antennas were employed, and the array was the C40-6 array configuration, which had minimum and maximum baseline of 1770 m and 3247 m, respectively. This configuration yielded a synthesized beam of $0''.21 \times 0''.17$ with a position angle of $-77°$ in a naturally weighted map (see Section 2.1.2 for details about imaging). The total observation time was 45 hours and the on-source integration time was 29 hours. Quasars, J0522$-$3627, J0238$+$1636, and J0334$-$4008 were used as bandpass calibrators, and the phase calibrator was J0348$-$2749. The flux was calibrated using J0334$-$4008 and J2357$-$5311.

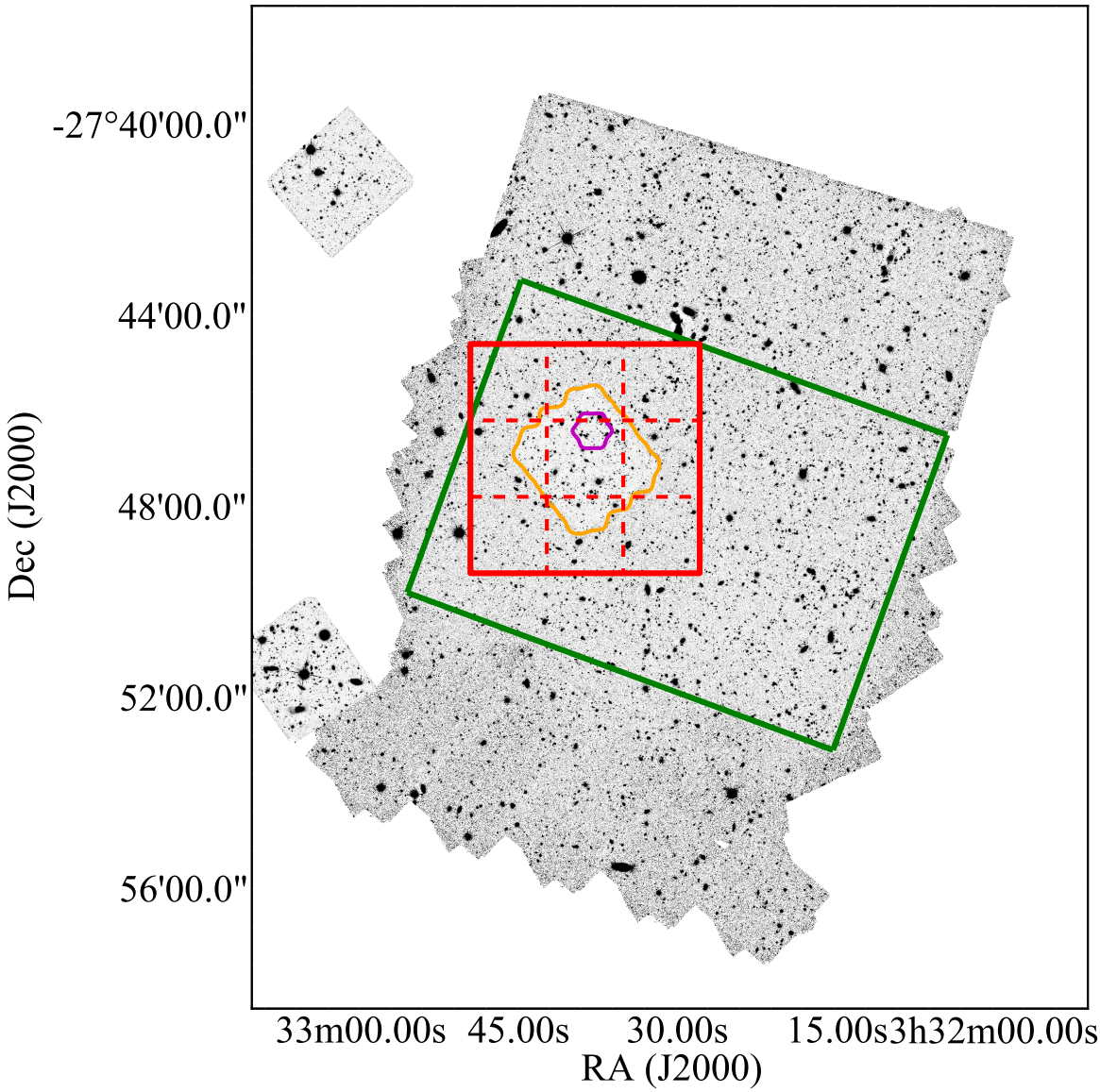

Figure 2.1 ASAGAO observation area. The ASAGAO observed area is sown as the red square. The green, orange, and magenta enclosed region indicates the ALMA observed region obtained by ASPECS (Walter et al., 2016; Aravena et al., 2016b), HUDF (Dunlop et al., 2017), and GOODS-ALMA (Franco et al., 2018), respectively. The background image is the *HST*/WFC3 F160W image.

2.1.2 ALMA data analysis

Here, we summarize our data analysis (see also Hatsukade et al., 2018, for details). The ALMA data were reduced with the Common Astronomy Software Applications package (CASA; McMullin et al., 2007) version 5.1.1, but calibration was done with the ALMA Science Pipeline Software of CASA version 4.7.2. The map were processed with the CLEAN algorithm (Högbom, 1974) with the task tclean of CASA version 5.1.1. We adopted natural weighting[1]. Clean boxes were placed when a component with a peak S/N $>$ 5 is identified, and cleaned down to a 2σ level. The obtained map reached a synthesized beam of $0''.21 \times 0''.17$ with a position angle of $-77°$ and the typical noise level of $\sigma \simeq 50$ μJy beam^{-1}. We also adopted a *uv*-taper of 250 kλ to improve the surface brightness sensitivity, which gives a synthesized beam of $0''.51 \times 0''.45$ with a position angle of $81°$.

In addition to our ASAGAO data, we also included ALMA archival data of the same field obtained by HUDF survey (Project ID: 2012.1.00173.S, PI: J. S. Dunlop; Dunlop et al., 2017) and GOODS-ALMA survey (Project ID: 2015.1.00543, PI: D. Elbaz; Franco et al., 2018) to improve the sensitivity. Although ASPECS (Walter et al., 2016; Aravena et al., 2016b) also observed the same region (see Figure 2.1), we did not include their data set. This is because its synthesized beam size ($1''.68 \times 0''.92$) is largely different from those of the others ($\lesssim 0''.5$). Finally, our ASAGAO final map reached a level of $\sigma \sim 30$ μJy beam^{-1} at the central ~ 4 arcmin^2 and ~ 70 μm beam^{-1} at the remaining area with the synthesized beam of $0''.59 \times 0''.53$ (position angle = $-83°$). The ALMA final map and its primary beam coverage are shown in Figure 2.2.

2.1.3 ALMA source identifications

We used the source-finding algorithm of AEGEAN (Hancock et al., 2012, 2018) for ASAGAO source identifications. AEGEAN uses a curvature image derived by a Laplacian transformation of the input im-

[1]The visibility surface density of (u, v)-plane for low-spatial-frequency components is higher than that of high-spatial-frequency components. In natural weighting, density weighting factors for all spatial-frequency components are unity. Therefore, side-lobe level becomes low (i.e., the sensitivity is high) at the expense of spatial resolution (e.g., Thompson et al., 2017).

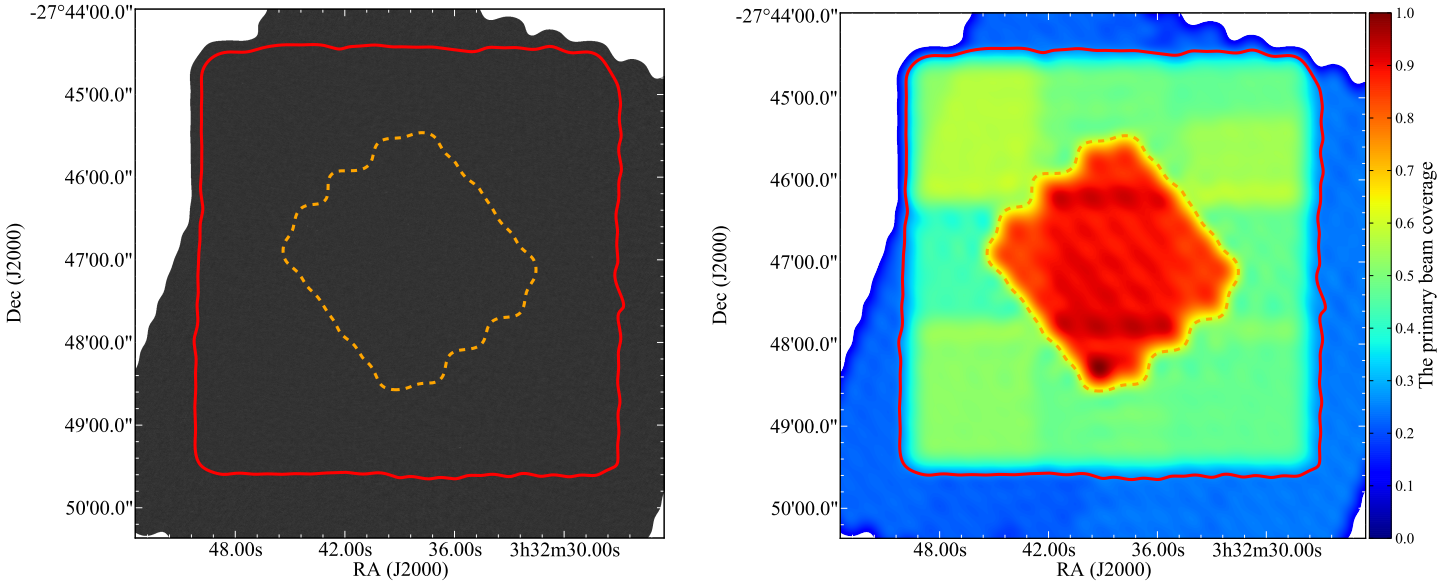

Figure 2.2 *Left)* The ASAGAO final map. The red enclosed region indicates the observed area by ASAGAO. The orange enclosed region indicate HUDF obtained by Dunlop et al. (2017). *Right)* The primary beam coverage of ASAGAO final map. The color codes are same as those of the left panel.

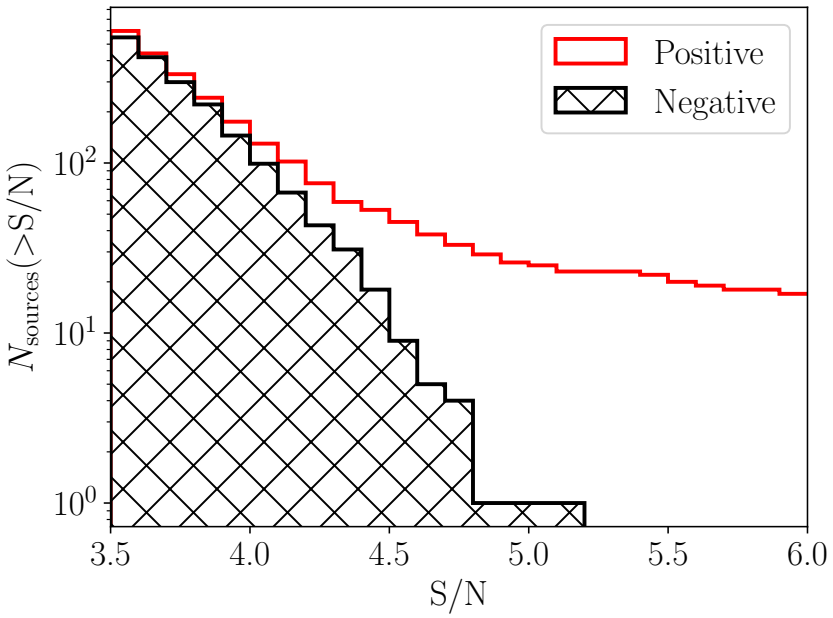

Figure 2.3 The cumulative number of positive and negative sources as a function of S/N. The red histogram indicate the positive source and the black hatched histogram denotes negative sources.

age. Thanks to the curvature image, AEGEAN can determine the number of compact components (see Hancock et al., 2012, for details). AEGEAN can achieve high reliability and completeness performance for radio maps. We adopt the S/N threshold of 3.5 learned from previous studies on faint (sub-)millimeter sources by ALMA (e.g., Aravena et al., 2016b; Dunlop et al., 2017). Note that we only extracted ALMA continuum source candidates within the area covered by ASAGAO (i.e., the red enclosed region in Figure 2.2). Finally, we extracted 598 ALMA continuum source candidates with S/N $>$ 3.5.

In Figure 2.3, we show the cumulative number of positive and negative sources detected by ASAGAO as a function of their peak S/N. As shown in Figure 2.3, the initial 598 ALMA continuum sources candidates may contain a significant number of spurious sources, especially for S/N $\lesssim$ 4.5. To avoid contamination of spurious sources, these sources candidates were cross-matched against the *K*-band selected sources. The details of our cross-matching strategy is explained in Section 3.1.1.

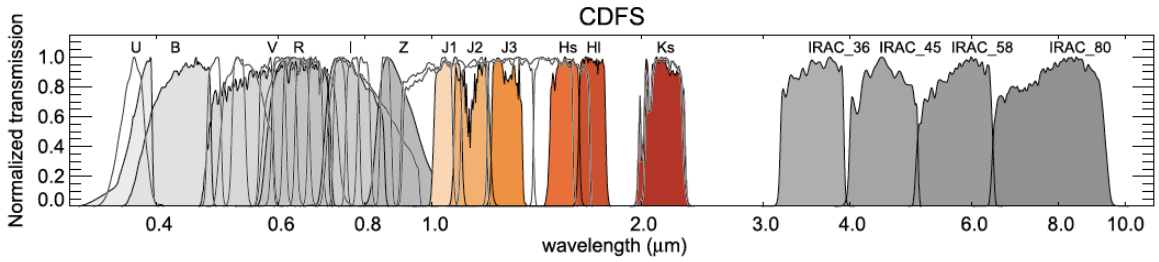

Figure 2.4 Normalized transmission corresponding to the ForStar medium-band filters and ancillary filters (refered from Figure 1 of Straatman et al., 2016).

2.2 Multi-wavelength images

In this section, we introduce multi-wavelength images which are used to investigate physical properties (e.g., stellar masses or SFRs) of ASAGAO sources in Chapter 3 and Chapter 4.

2.2.1 ZFOURGE data

We used the *K*-band selected source catalog obtained by the FourStar galaxy evolution survey (ZFOURGE; Straatman et al., 2016)[2]. The ZFOURGE is a large program with the FourStar near-IR camera (Persson et al., 2013) on the Magellan Baade Telescope. The FourStar has 6 medium-band filters; J_1, J_2, J_3, H_s, H_l, and K_s. The 5σ limiting magnitude of each band in the *Chandra* Deep Field South (CDFS) is 25.6, 25.5, 25.5, 24.9, 25.0, and 24.8 mag for J_1, J_2, J_3, H_s, H_l, and K_s-band, respectively (Straatman et al., 2016). The ZFOURGE catalog contains 30,911 *K*-band selected galaxies over 128 arcmin^2 in the CDFS, which fully includes the ASAGAO field, with 5σ limiting magnitude of K_s = 26.0 and 26.3 mag at the 80% and 50% completeness levels (with masking), respectively.

In addition to the FourStar data, the ZFOURGE compile 34 filters from UV to near-IR wavelengths into their catalog (i.e., 40 filters in total; Straatman et al., 2016). In ECDF, they include the Very Large Telescope (VLT)/Visible Multi-Object Spectrograph (VIMOS; Le Fèvre et al., 2003)/*U*, *R*-imaging (Nonino et al., 2009), *Hubble Space Telescope* (*HST*)/Advanced Camera for Survey (ACS; Ford et al., 1998)/*B*,

[2]The ZFOURGE catalog is available at http://zfourge.tamu.edu/.

V, *I*, *Z*-imaging (Giavalisco et al., 2004; Wuyts et al., 2008), ESO/MPG/Wide Field Image (WFI; Baade et al., 1999)/U_{38}, *V*, R_c-imaging (Erben et al., 2005; Hildebrandt et al., 2006), *HST*/Wide Field Camera 3 (WFC3; Kimble et al., 2008)/*F098M*, *F105W*, *F125W*, *F140W*, *F160W* and *HST*/ACS/*F606W*, *F814W*-imaging (Grogin et al., 2011; Koekemoer et al., 2011; Windhorst et al., 2011; Brammer et al., 2011), 11 Subaru/Suprime-Cam (Miyazaki et al., 2002) optical medium bands (Cardamone et al., 2010), Canada France Hawaii Telescope (CFHT)/Wide-field InfraRed Camera (WIRCam; Puget et al., 2004)/*K*-imaging (Hsieh et al., 2012), VLT/Infrared Spectrometer And Array Camera (ISAAC; Moorwood et al., 1999)/*K*-image (Retzlaff et al., 2010), VLT/High Acuity Wide field *K*-band Imager (HAWK-I; Kissler-Patig et al., 2008)/K_s-imaging (Fontana et al., 2014), and *Spitzer*/InfraRed Array Camera (IRAC; Fazio et al., 2004)/3.6, 4.5, 5.8, 8.0 μm-image (Dickinson et al., 2003; Labbé et al., 2015). In Figure 2.4, we show normalized transmission of filters which are explaned in this section.

2.2.2 Mid-IR to radio data

Spitzer/MIPS

The *Spitzer*/Multiband Imaging Photometer for the *Spizter* (MIPS; Rieke et al., 2004)/24 μm image is obtained by Dickinson & FIDEL Team (2007). The image reahes a 1σ noise level of 3.9 μJy.

Herschel/PACS

The *Herschel*/Photodetector Array Camera and Spectrometer (PACS; Poglitsch et al., 2010)/100 and 160 μm images are obtained by the PACS Evolutionary Probe (PEP) survey (Magnelli et al., 2013) and reach a 1σ sensitivity of 205 and 354 μJy at 100 and 160 μm, respectively.

Herschel/SPIRE

The *Herschel*/SPIRE/250, 350, and 500 μm images are taken as a part of the *Herschel* Multi-tiered Extragalactic Survey (HerMES; Oliver et al., 2012). In CDFS, the final combined map reaches a 1σ sensitivity of 1.6, 1.3, and 1.9 mJy at 250, 350, and 500 μm, respectively.

JVLA

The Karl G. Jansky Very Large Array (JVLA)/6 GHz image is obtained by Rujopakarn et al., (in preparation). The image reaches a 1σ noise level of 3.5 μJy beam^{-1} with a synthesized beam of $0''.61 \times 0''.30$ (position angle of $-3.4°$).

2.2.3 X-ray data

The *Chandra X-ray Observatory* (*Cahndra;* Weisskopf et al., 2000) X-ray images are taken by the CDFS survey by Luo et al. (2017) at 0.5–7.0, 0.5–2.0, and 2–7 keV band. The sensitivity limit of the *Chandra* data reaches $\sim$ (2–8) $\times$ 10^{-17} erg cm^{-2} s^{-1} at 0.5–7 keV.

3

Millimeter properties of *K*-selected galaxies

In this chapter, we make use of the ASAGAO to probe dust-ensured star formation in *K*-band selected (i.e., stellar mass selected) galaxies, which are drawn from the ZFOURGE catalog. As shown in Figure 2.3, the initial ASAGAO continuum sources candidates with S/N $>$ 3.5 contain a number of spurious detections. Therefore, we use *K*-band selected sources as a prior to exclude false detections. Although Bouwens et al. (2016) consider a S/N threshold of 2.0 to search for ALMA counterparts of LBGs, we adopt a more conservative threshold of S/N = 3.5 learned from previous studies on ALMA-detected faint (sub-)millimeter sources with optical/near-IR counterparts (e.g., Aravena et al., 2016b; Dunlop et al., 2017), as explained in Section 2.1.3.

3.1 ALMA counterparts of ZFOURGE sources

3.1.1 Cross-matching ZFOURGE sources with ASAGAO sources

We measure ALMA flux densities of ZFOURGE sources, after correcting for a systematic offset between ZFOURGE coordinates and ALMA coordinates (-0”.086 in right ascension and $+0$”.282 in declination), which is calibrated by the positions of stars in the Gaia Data Release 1 catalog (Gaia Collaboration et al., 2016) within the ASAGAO field.

In this study, we allow the positional offsets between ZFOURGE position and ALMA positions of less than $0''.5$ for point-like ZFOURGE sources, which is comparable with the synthesized beam of the final ALMA map. Considering the number of ZFOURGE sources within the ASAGAO field ($\sim$ 3,000), the likelihood of random coincidence is estimated to be 0.03 (this likelihood is often called the p-value; Downes et al., 1986). The p-value is defined as the following equation;

$$p = 1 - \exp\left(-\pi|\Delta_{\rm offset}|^2 n_{\rm source}\right), \tag{3.1}$$

where $\Delta_{\rm offset}$ and $n_{\rm source}$ is the positional separation between ZFOURGE sources and ASAGAO sources and the source density of ZFOURGE sources, respectively. In the case that a counterpart is largely extended (e.g., ID1; see figures in Appendix A), we allow a larger positional offset, up to half-light radius of K_s-band emission. We exclude ZFOURGE sources with “use flag $= 0$” (e.g., sources with low S/N at K-band or catastrophic SED fits; see Straatman et al., 2016, for details) in order to prevent mismatching. When we apply the same procedure to the negative values of the ALMA map, we find that 10 negative sources with an S/N ~ -3.5–-4.0 show chance coincidence and no negative sources with S/N < -4.0 show chance coincidence with ZFOURGE sources. This coincidence rate is comparable with the estimated value by Casey et al. (2018).

Flux measurements in the ALMA map were performed at the position of ZFOURGE sources considering positional offset as explained above. We consider the flux-boosting effect by calculating the ratio between input and output integrated flux densities of inserted 30,000 artificial sources into the signal map

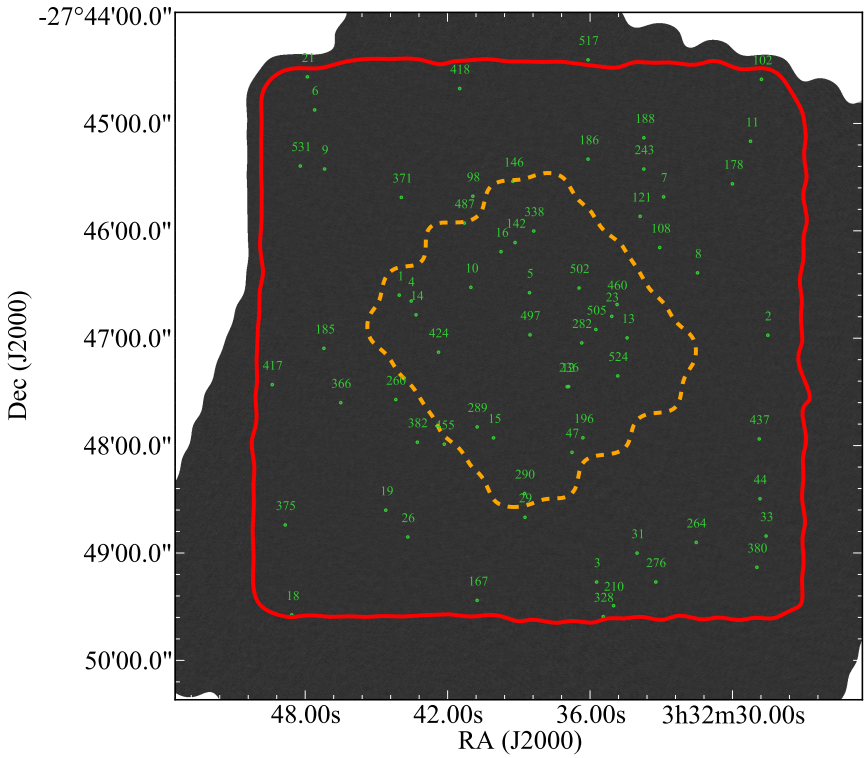

Figure 3.1 ASAGAO sources positions. The green symbols indicate an 66 ASAGAO continuum sources with *K*-band counterparts. The red enclosed region indicate the observed area by ASAGAO. The orange shaded region indicates observed area by HUDF Dunlop et al. (2017). See also Figure 2.3 in Section 2.1.2.

(see Hatsukade et al., 2018, for details). The effect of flux boosting for the sources with S/N $>$ 3.5 is $\sim$ 20%.

Finally, we identify 66 ZFOURGE sources that have ALMA counterparts (hereafter, we define them as ASAGAO sources). In Table 3.1, we summarize these ASAGAO sources in order of ALMA peak S/N. As shown in Table 3.1, some ASAGAO sources show larger p-value than the traditional threshold of $p < 0.05$ (e.g., Biggs et al., 2011; Casey et al., 2013). Although such ASAGAO sources can be chance coincidences and should be treated carefully in following discussions, this does not affect the conclusions of this study significantly. We show the positions of ASAGAO sources and their multi-wavelength postage stamps in Figure 3.1 and Appendix A, respectively. Note that all ALMA flux densities

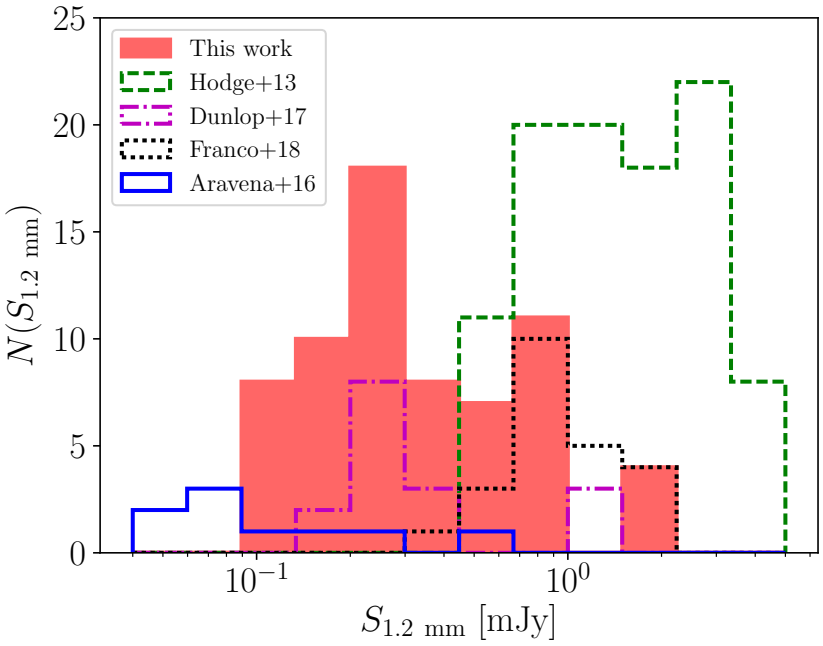

Figure 3.2 Flux-density distribution of ASAGAO sources (red-shaded region). The flux-density distributions of other ALMA continuum source with optical/near-IR counterparts in ALESS (Hodge et al., 2013), HUDF (Aravena et al., 2016b; Dunlop et al., 2017), and GOODS-S (Franco et al., 2018) are also shown.

presented in Table 3.1 are de-boosted.

Ueda et al. (2018) and Fujimoto et al. (2018) also use ASAGAO data. In the tables of Appendix B, we present the correspondence of their ID to ASAGAO ID, which is presented in this thesis. The GOODS-S field is also observed with AzTEC/ASTE at 1.1 mm (Scott et al., 2010; Yun et al., 2012). Two AzTEC sources are located within the ASAGAO region and detected as four ASAGAO sources (ASAGAO ID1, 4, 6, and 14; see Hatsukade et al., 2018). We also cross-matched the ASAGAO sources with 1.3 mm sources of HUDF (Dunlop et al., 2017), 1.1 mm sources of GOODS-ALMA (Franco et al., 2018), 1.2 mm sources of ASPECS (Aravena et al., 2016b), and 870 μm sources obtained by Cowie et al. (2018). The results of cross-matching are presented in Appendix B.

Table 3.1. ZFOURGE counterparts with ALMA counterparts

ID (ZFOURGE)	R.A.[a] (ZFOURGE) (deg.)	Dec.[a] (ZFOURGE) (deg.)	ID (ASAGAO)	S_{ALMA} (mJy)	S/N_{peak}	R.A. (ASAGAO) (deg.)	Dec. (ASAGAO) (deg.)	$\lvert\Delta_{offset}\rvert$ (arcsec)	p-value	z_{photo}	z_{spec}
(1)	(2)	(3)	(4)	(5)	(6)	(7)	(8)	(9)	(10)	(11)	(12)
18658	53.18341	−27.77646	1	0.985±0.036	25.995	53.18348	−27.777	0.735	0.0578	$2.83^{+0.07}_{-0.08}$	–
17856	53.11880	−27.78289	2	1.973±0.075	25.625	53.11881	−27.783	0.048	0.0003	$2.38^{+0.17}_{-0.10}$	–
13086	53.14885	−27.82119	3	1.748±0.070	24.008	53.14885	−27.821	0.021	0.0	$2.58^{+0.04}_{-0.04}$	2.582
18645	53.18137	−27.77756	4	0.906±0.041	21.045	53.18137	−27.778	0.044	0.0002	$2.92^{+0.06}_{-0.06}$	–
18701	53.16061	−27.77622	5	0.735±0.039	18.101	53.16063	−27.776	0.228	0.0057	$2.61^{+0.07}_{-0.05}$	2.543[b]
22177	53.19835	−27.74788	6	0.922±0.074	12.421	53.19830	−27.748	0.153	0.0026	$1.93^{+0.04}_{-0.03}$	–
20298	53.13735	−27.76163	7	0.778±0.086	8.785	53.13710	−27.761	1.124	0.13	$0.52^{+0.02}_{-0.01}$	0.523
19033	53.13112	−27.77319	8	0.610±0.072	8.654	53.13115	−27.773	0.084	0.0008	$2.22^{+0.03}_{-0.03}$	2.225
21234	53.19656	−27.75704	9	0.457±0.055	8.575	53.19656	−27.757	0.123	0.0017	$2.46^{+0.05}_{-0.05}$	–
18912	53.17092	−27.77547	10	0.261±0.031	8.550	53.17091	−27.775	0.099	0.0011	$2.36^{+0.10}_{-0.11}$	–
21730	53.12185	−27.75278	11	0.635±0.078	8.506	53.12186	−27.753	0.071	0.0006	$2.01^{+0.06}_{-0.04}$	–
16952	53.15405	−27.79093	12	0.376±0.049	7.378	53.15401	−27.791	0.251	0.0069	$1.88^{+0.04}_{-0.03}$	1.317[b]
17733	53.14349	−27.78328	13	0.400±0.053	7.227	53.14351	−27.783	0.05	0.0003	$1.62^{+0.04}_{-0.05}$	1.415[b]
18336	53.18053	−27.77972	14	0.238±0.035	7.178	53.18053	−27.780	0.038	0.0002	$2.67^{+0.11}_{-0.15}$	–
15702	53.16692	−27.79882	15	0.416±0.064	6.637	53.16694	−27.799	0.082	0.0007	$1.93^{+0.03}_{-0.03}$	1.998
19487	53.16558	−27.76987	16	0.488±0.065	6.491	53.16562	−27.770	0.194	0.0041	$1.61^{+0.08}_{-0.06}$	1.551[b]
12438	53.20235	−27.82627	18	0.975±0.172	5.803	53.20236	−27.826	0.063	0.0004	$1.07^{+0.03}_{-0.03}$	–
14580	53.18585	−27.81004	19	0.387±0.073	5.659	53.18585	−27.810	0.024	0.0001	$2.81^{+0.10}_{-0.10}$	2.593
22760	53.19958	−27.74277	21	0.895±0.178	5.472	53.19957	−27.743	0.271	0.0081	$2.16^{+0.06}_{-0.06}$	2.187[c]
18270	53.14617	−27.77995	23	0.182±0.037	5.360	53.14620	−27.780	0.096	0.001	$2.61^{+0.05}_{-0.06}$	–
14146	53.18201	−27.81420	26	0.222±0.052	4.923	53.18198	−27.814	0.107	0.0013	$2.41^{+0.18[d]}_{-0.14}$	–
14419	53.16144	−27.81116	29	0.197±0.046	4.835	53.16141	−27.811	0.115	0.0015	$2.77^{+0.11}_{-0.10}$	–
13714	53.14167	−27.81665	31	0.733±0.158	4.714	53.14175	−27.817	0.328	0.0118	$2.53^{+0.09}_{-0.10}$	–
14122	53.11914	−27.81402	33	0.318±0.079	4.701	53.11911	−27.814	0.136	0.002	$3.32^{+0.44}_{-0.45}$	–

Table 3.1 *(continued)*

ID (ZFOURGE) (1)	R.A.[a] (ZFOURGE) (deg.) (2)	Dec.[a] (ZFOURGE) (deg.) (3)	ID (ASAGAO) (4)	$S_{\rm ALMA}$ (mJy) (5)	$S/N_{\rm peak}$ (6)	R.A. (ASAGAO) (deg.) (7)	Dec. (ASAGAO) (deg.) (8)	$\lvert\Delta_{\rm offset}\rvert$ (arcsec) (9)	p-value (10)	$z_{\rm photo}$ (11)	$z_{\rm spec}$ (12)
14700	53.12011	−27.80834	44	1.768±0.447	4.546	53.12018	−27.808	0.401	0.0175	$1.83^{+0.05}_{-0.05}$	–
15752	53.15323	−27.80112	47	0.290±0.069	4.436	53.15317	−27.801	0.289	0.0092	$0.32^{+0.14}_{-0.31}$	–
20550	53.17047	−27.76144	98	0.217±0.062	4.117	53.17056	−27.761	0.551	0.0329	$0.16^{+0.01}_{-0.01}$	–
22905	53.11989	−27.74316	102	1.545±0.356	4.104	53.11995	−27.743	0.192	0.004	$3.85^{+0.46}_{-0.38}$	–
19490	53.13759	−27.76918	108	0.195±0.055	4.058	53.13779	−27.769	0.703	0.0529	$0.36^{+0.02}_{-0.02}$	0.368
20394	53.14115	−27.76441	121	0.543±0.155	4.024	53.14122	−27.764	0.207	0.0047	$4.53^{+0.21}_{-0.22}$	–
19903	53.16318	−27.76859	142	0.135±0.039	3.967	53.16316	−27.768	0.315	0.0108	$1.48^{+0.04}_{-0.03}$	–
20694	53.16361	−27.75902	146	0.295±0.083	3.958	53.16355	−27.759	0.209	0.0048	$1.06^{+0.04}_{-0.04}$	–
12763	53.16980	−27.82402	167	0.532±0.160	3.921	53.16982	−27.824	0.1	0.0011	$2.13^{+0.06}_{-0.04}$	2.13
20728	53.12530	−27.75958	178	0.256±0.077	3.897	53.12503	−27.759	1.121	0.1293	$0.64^{+0.01}_{-0.01}$	0.647
17785	53.19677	−27.78483	185	0.284±0.084	3.885	53.19670	−27.785	0.392	0.0168	$2.98^{+0.10}_{-0.11}$	–
21368	53.15033	−27.75557	186	0.196±0.060	3.885	53.15036	−27.756	0.117	0.0015	$2.31^{+0.05}_{-0.05}$	–
21702	53.14057	−27.75220	188	0.213±0.063	3.881	53.14057	−27.752	0.132	0.0019	$1.87^{+0.06}_{-0.06}$	–
15919	53.15122	−27.79877	196	0.162±0.049	3.864	53.15126	−27.799	0.176	0.0034	$0.61^{+0.01}_{-0.01}$	–
12904	53.14589	−27.82474	210	0.448±0.139	3.841	53.14587	−27.825	0.431	0.0202	$3.90^{+0.30}_{-0.23}$	–
16977	53.15376	−27.79069	236	0.093±0.027	3.803	53.15377	−27.791	0.592	0.0379	$1.32^{+0.02}_{-0.03}$	1.318
21193	53.14036	−27.75726	243	0.197±0.062	3.794	53.14057	−27.757	0.905	0.0864	$1.59^{+0.07}_{-0.07}$	–
16522	53.18417	−27.79272	260	0.316±0.096	3.774	53.18409	−27.793	0.633	0.0432	$0.73^{+0.02}_{-0.02}$	0.737
13876	53.13137	−27.81503	264	0.285±0.090	3.772	53.13137	−27.815	0.036	0.0001	$1.70^{+0.04}_{-0.04}$	–
13269	53.13852	−27.82121	276	0.359±0.111	3.760	53.13847	−27.821	0.215	0.0051	$3.65^{+0.09}_{-0.09}$	–
17959	53.15145	−27.78400	282	0.102±0.033	3.755	53.15146	−27.784	0.249	0.0068	$0.73^{+0.13}_{-0.06}$	–
16040	53.16974	−27.79714	289	0.248±0.069	3.740	53.16981	−27.797	0.243	0.0065	$2.03^{+0.05}_{-0.05}$	–
14901	53.16153	−27.80760	290	0.162±0.052	3.740	53.16148	−27.807	0.557	0.0336	$2.71^{+0.12}_{-0.12}$	–
12682	53.14777	−27.82650	328	0.886±0.249	3.705	53.14768	−27.827	0.347	0.0132	$4.89^{+0.11}_{-0.08}$	–

Table 3.1 *(continued)*

ID (ZFOURGE) (1)	R.A.[a] (ZFOURGE) (deg.) (2)	Dec.[a] (ZFOURGE) (deg.) (3)	ID (ASAGAO) (4)	S_{ALMA} (mJy) (5)	S/N_{peak} (6)	R.A. (ASAGAO) (deg.) (7)	Dec. (ASAGAO) (deg.) (8)	$\|\Delta_{offset}\|$ (arcsec) (9)	p-value (10)	z_{photo} (11)	z_{spec} (12)
20008	53.15988	−27.76691	338	0.129±0.040	3.693	53.15987	−27.767	0.755	0.0608	$1.06^{+0.03}_{-0.03}$	–
16562	53.19388	−27.79337	366	0.263±0.088	3.673	53.19374	−27.793	0.465	0.0235	$0.69^{+0.02}_{-0.01}$	0.707
19915	53.18372	−27.76159	371	0.211±0.069	3.670	53.18310	−27.761	1.961	0.3454	$0.50^{+0.01}_{-0.01}$	–
14407	53.20363	−27.81228	375	0.296±0.096	3.662	53.20349	−27.812	0.46	0.0231	$2.86^{+0.05}_{-0.05}$	–
12998	53.12080	−27.81905	380	0.229±0.068	3.656	53.12072	−27.819	0.605	0.0395	$1.09^{+0.02}_{-0.02}$	1.094
15617	53.18025	−27.79901	382	0.203±0.060	3.654	53.18031	−27.799	1.706	0.2744	$0.66^{+0.02}_{-0.02}$	0.666
16874	53.20547	−27.79070	417	0.338±0.114	3.625	53.20576	−27.791	1.079	0.1203	$0.14^{+0.01}_{-0.01}$	–
22495	53.17288	−27.74454	418	0.679±0.202	3.624	53.17287	−27.745	0.183	0.0037	$1.22^{+0.07}_{-0.06}$	1.296
17465	53.17659	−27.78552	424	0.101±0.033	3.621	53.17659	−27.786	0.036	0.0001	$1.32^{+0.04}_{-0.03}$	–
15768	53.11997	−27.79884	437	0.275±0.086	3.603	53.12031	−27.799	1.193	0.1452	$1.37^{+0.03}_{-0.03}$	1.383
18476	53.14526	−27.77798	460	0.114±0.039	3.589	53.14526	−27.778	0.444	0.0215	$1.03^{+0.02}_{-0.02}$	1.097
20073	53.17225	−27.76517	487	0.129±0.042	3.573	53.17206	−27.765	1.258	0.16	$0.56^{+0.02}_{-0.02}$	–
18096	53.16058	−27.78283	497	0.162±0.155	3.569	53.16053	−27.783	0.166	0.003	$0.92^{+0.18}_{-0.11}$	–
18813	53.15188	−27.77551	502	0.182±0.054	3.564	53.15194	−27.776	0.25	0.0069	$1.05^{+0.02}_{-0.02}$	1.047
18047	53.14904	−27.78204	505	0.132±0.042	3.560	53.14898	−27.782	0.255	0.0071	$1.87^{+0.05}_{-0.05}$	–
23130	53.15015	−27.74001	517	0.687±0.228	3.553	53.15035	−27.740	0.783	0.0653	$1.03^{+0.01}_{-0.01}$	1.038
17007	53.14510	−27.78950	524	0.108±0.036	3.551	53.14514	−27.789	1.101	0.125	$1.30^{+0.03}_{-0.02}$	–
21317	53.20073	−27.75655	531	0.226±0.074	3.546	53.20083	−27.757	0.345	0.013	$0.52^{+0.02}_{-0.02}$	–

Note. — ZFOURGE sources with ALMA counterpart in order of ALMA S/N. (1) ZFOURGE ID. (2) and (3) ZFOURGE position. (4) ASAGAO ID. (5) Spatially integrated ALMA flux density (de-boosted). (6) ALMA peak S/N. (7) and (8) ASAGAO position. (9) The positional offset between ALMA and ZFOURGE. (10) The p-Values for each ASAGAO source. (11) The photometric redshift. (12) The spectroscopic redshift.

[a]The systematic coordinate offsets have been corrected.

[b]The spectroscopic redshift presented by Inami et al. (2017) using MUSE.

[c]The spectroscopic redshift given by Wisnioski et al. (2015).

[d]The photometric redshift presented by Luo et al. (2017).

3.1.2 Observed flux density at 1.2 mm

In Figure 3.2, we plot the histogram of observed flux densities of ASAGAO sources at 1.2 mm. As a comparison, we also show the histograms of observed flux densities obtained by ALESS (Hodge et al., 2013; da Cunha et al., 2015), HUDF (Dunlop et al., 2017), GOODS-ALMA (Franco et al., 2018), and ASPECS (Aravena et al., 2016b). Note that ALESS sources, HUDF sources, and GOODS-ALMA sources were observed at 870 μm, 1.3 mm, and 1.1 mm, respectively. Therefore, we converted these flux densities to 1.2-mm flux densities with the assumption of a modified blackbody with a dust emissivity index of 1.5 and dust temperature of 35 K [for example, $S_{1.2\ \mathrm{mm}}/S_{870\ \mu\mathrm{m}} = 0.44$, $S_{1.2\ \mathrm{mm}}/S_{1.3\ \mathrm{mm}} = 1.26$, and $S_{1.2\ \mathrm{mm}}/S_{1.1\ \mathrm{mm}} = 0.79$ at $z = 2.83$, 2.04, and 2.54 (median redshifts of ALESS, HUDF, and GOODS-ALMA sources)].

Figure 3.2 shows that ASAGAO sources tend to have the fainter flux densities ($S_{1.2\ \mathrm{mm}} \lesssim 1$ mJy) than most of the ALESS sources ($S_{1.2\ \mathrm{mm}} \gtrsim 1$ mJy). Although recent ALMA contiguous surveys focusing on stellar mass selected sources (e.g., Aravena et al., 2016b; Dunlop et al., 2017; Franco et al., 2018) also suggest that their samples tend to have the flux densities of $S_{1.2\ \mathrm{mm}} \lesssim 1$ mJy, we provide the largest number of stellar mass selected sources with 1.2 mm flux densities.

3.1.3 The redshift distribution of ASAGAO sources

Straatman et al. (2016) estimate photometric redshifts of the ZFOURGE sources using the optical to near-IR SED fitting code EAZY constructed by Brammer et al. (2008). EAZY uses the least χ^2 method in conjunction with the Bayesian technique. In the least χ^2 method, the best fit photometric redshift is defined as the redshift which minimizes the $\chi^2(z)$ defined by the following equation;

$$\chi^2(z) = \sum_{i=1}^{n_{\mathrm{filter}}} \left[\frac{F_{\mathrm{obs},i} - \alpha F_{\mathrm{temp,i}}(z)}{\delta F_{\mathrm{obs},i}} \right]^2, \tag{3.2}$$

where n_{filter} is the number of filters and $F_{\mathrm{obs},i}$, $F_{\mathrm{temp},i}$, and $\delta F_{\mathrm{obs},i}$ is the observed flux density, the template flux density, and the observed flux error at the i-th filter, respectively. The normalization parameter is

defined as α. In addition to the least χ^2 method, EAZY makes use of the Bayesian technique considering a prior $p(z|m_0)$. The prior is the probability that an object with apparent magnitude m_0 locates at a redshift z, and defined as

$$p(z|m_{0.i}) \propto z^{\gamma_i} \exp[-(z/z_{0.i})^{\gamma_i}]. \tag{3.3}$$

Here, γ_i and $z_{0,i}$ are fitting parameters for the redshift distributions in each magnitude bin, $m_{0,i}$ (Brammer et al., 2008). Straatman et al. (2016) uses a K-band luminosity prior to estimate photometric redshifts of ZFOURGE sources. The prior is estimated by a semi-analytic model by Brammer et al. (2008) with $\sim 10^6$ galaxy samples. The posterior distribution $p(z|m_0, C)$ is expressed by following equation;

$$p(z|m_0, C) \propto p(z|C)p(z|m_0), \tag{3.4}$$

where $p(z|C) = \exp[-\chi^2(z)/2]$. In EAZY, a confidence interval, $[z_{\rm lo}, z_{\rm up}]$, for a confidence level a ($0 \leq a \leq 1$) is calculate by

$$\frac{1-a}{2} = \int_0^{z_{\rm lo}} p(z|C, m_0)dz, \tag{3.5}$$

$$\frac{1-a}{2} = \int_{z_{\rm up}}^{\infty} p(z|C, m_0)dz. \tag{3.6}$$

Here, 1, 2, and 3σ confidence limits are calculated by a = 0.683, 0.9954, and 0.9997, respectively. Hereafter, we adopt 1σ confidence limits.

As described in Section 2.2.1, Straatman et al. (2016) use 40 filters for SED fitting using EAZY. Some ZFOURGE sources have spectroscopic redshifts presented by Skelton et al. (2014). Although the ASAGAO ID 21 has "use flag = 0" in Straatman et al. (2016), we assume this sources as a real counterpart, because it has a spectroscopic redshift obtained by Wisnioski et al. (2015). Also one of the ASAGAO sources, ASAGAO ID26, has an extremely large photometric redshift (z = 9.354), which is apparently caused by a incorrect SED fitting. On the other hand, Luo et al. (2017) present its photometric redshift as z = 2.14[1] and this is the value we use. Some sources are also observed by Inami et al. (2017) with the

[1]This value is obtained by the SED fitting of Hsu et al. (2014)

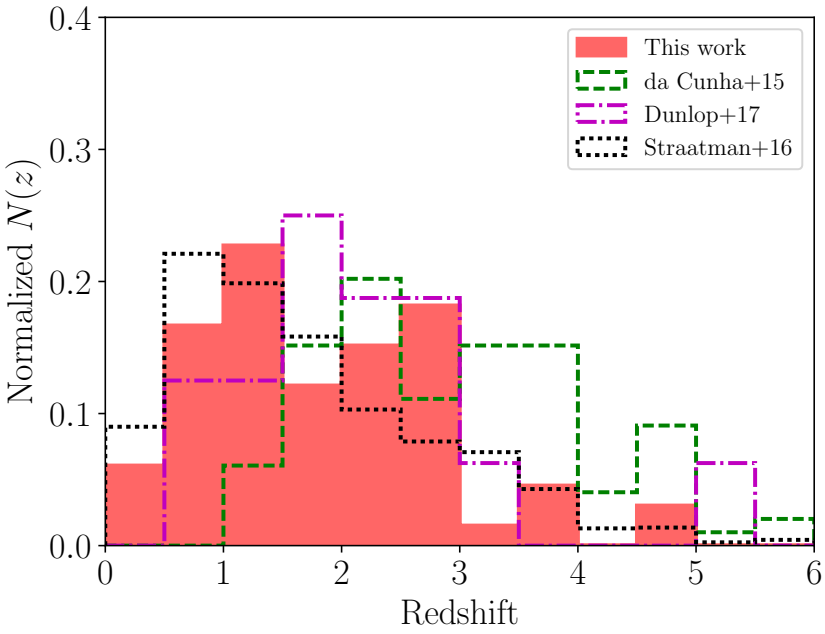

Figure 3.3 Normalized redshift distribution of the 66 ASAGAO sources with ZFOURGE counterparts (red-shaded region). The green dashed line, magenta dot-dashed line, and black dotted line indicate redshift distribution of ALESS sources (da Cunha et al., 2015), ALMA selected sources (Dunlop et al., 2017), and ZFOURGE sources within ASAGAO field (Straatman et al., 2016), respectively.

Multi Unit Spectroscopic Explorer (MUSE; Bacon et al., 2010). We use the spectroscopic redshifts of Inami et al. (2017) for ASAGAO sources that are detected by MUSE. In Table 3.1, we show photometric and spectroscopic redshifts of ZFOURGE sources.

As shown in Table 3.2, some ASAGAO sources have X-ray counterparts obtained by the CDFS survey (Luo et al., 2017). Therefore, some ASAGAO sources appear to have active galactic nuclei (AGNs). However, Cowley et al. (2016) suggest that photometric redshifts estimated by ZFOURGE are appropriate for AGNs because of the benefits of medium-band filters. We also have to note that the EAZY adopts *K*-luminosity priors, but it does not affect our results significantly. Indeed, Simpson et al. (2017) estimate the photometric redshifts of ALMA detected sources that there are no any bias in the photometric redshifts. They also show that the EAZY have demonstrated good agreement between the photometric

and spectroscopic redshifts of SMGs.

Figure 3.3 shows the redshift distribution of ASAGAO sources. As a comparison, we also plot the results of ALESS (da Cunha et al., 2015), ALMA detected sources with rest-frame optical/near-IR counterparts obtained by HUDF (Dunlop et al., 2017), and ALMA non-detected ZFOURGE sources within the ASAGAO field (Straatman et al., 2016). The median redshift of 66 ASAGAO sources is estimated to be $z_{\rm median} = 1.77 \pm 0.23$[2]. Although this median redshift is similar to that in Dunlop et al. (2017, $z_{\rm median} = 2.04 \pm 0.29$), it is lower than that of ALESS ($z_{\rm median} = 2.83 \pm 0.22$; da Cunha et al., 2015).

Many previous studies on "classical" SMGs ($S_{1.2\ {\rm mm}} \gtrsim$ a few mJy), including ALESS, report that median redshifts of "classical" SMGs are $z \simeq 2.1$–3.1, with a putative tail extending out to $z \sim 6$ (e.g., Chapman et al., 2005; Simpson et al., 2014; da Cunha et al., 2015; Strandet et al., 2016). On the other hand, Aravena et al. (2016b) suggest that their faint ALMA sources with optical/near-IR counterparts ($S_{1.2\ {\rm mm}} \sim 50$–$500\ \mu$Jy) reside in a lower redshift range than "classical" SMGs, although they only have small samples. The redshift distribution of ASAGAO sources ($S_{1.2\ {\rm mm}} \lesssim 1$ mJy) is consistent with their results. Although we have to note that the difference of redshift distributions between (sub-)millimeter bright and faint sources can be caused by our sample selection (completeness of optical/near-IR surveys drop significantly at high redshift), the difference is consistent with phenomenological models by Béthermin et al. (2015), which suggest that the median redshift of (sub-)millimeter sources declines with decreasing flux densities. According to Koprowski et al. (2017), the fact that lower redshift sources tend to have lower (sub-)millimeter flux densities can be a direct consequence of the redshift evolution of the IR luminosity function.

[2]The median redshift of ALMA non-detected ZFOURGE sources is $z_{\rm median} = 1.45 \pm 0.04$.

Table 3.2. ASAGAO sources with the *Chandra* counterparts

ID (ZFOURGE) (1)	ID (ASAGAO) (2)	X-ray counterpart? (3)	ID (ZFOURGE) (4)	ID (ASAGAO) (5)	X-ray counterpart? (6)
18658	1	Y	20728	178	–
17856	2	Y	17785	185	–
13086	3	Y	21368	186	–
18645	4	–	21702	188	–
18701	5	Y	15919	196	–
22177	6	Y	12904	210	–
20298	7	–	16977	236	–
19033	8	Y	21193	243	–
21234	9	–	16522	260	Y
18912	10	–	13876	264	Y
21730	11	Y	13269	276	Y
16952	12	–	17959	282	–
17733	13	–	16040	289	Y
18336	14	Y	14901	290	–
15702	15	Y	12682	328	–
19487	16	Y	20008	338	–
12438	18	Y	16562	366	–
14580	19	Y	19915	371	–
22760	21	–	14407	375	–
18270	23	Y	12998	380	–
14146	26	Y	15617	382	–
14419	29	Y	16874	417	–
13714	31	Y	22495	418	–
14122	33	–	17465	424	–
14700	44	–	15768	437	Y
15752	47	–	18476	460	–
20550	98	–	20073	487	–
22905	102	–	18096	497	–
19490	108	Y	18813	502	Y
20394	121	–	18047	505	–
19903	142	–	23130	517	–
20694	146	–	17007	524	Y
12763	167	Y	21317	531	–

Note. — (1) ZFOURGE ID. (2) ASAGAO ID. (3) Based on cross-matching with the *Chandra* catalog (Luo et al., 2017);"Y" is assigned if the angular separation between the ALMA and *Chandra* sources is less than three times their combined 1σ positional error (see also Ueda et al., 2018). (4) ZFOURGE ID. (5) ASAGAO ID. (6) Based on cross-matching with the *Chandra* catalog.

3.2 SED fitting from optical to millimeter wavelengths

3.2.1 ASAGAO photometry at mid-IR to far-IR wavelengths

In order to investigate the properties of dusty star-formation among ASAGAO sources, we have to estimate dust-obscured SFRs. Therefore, we compile photometries from mid-IR to far-IR wavelengths in addition to ZFOURGE photometries and millimeter photometries by ALMA to estimate IR luminosities accurately. Photometries at *Spitzer*/MIPS/24 μm, *Herschel*/PACS/100 μm, and 160 μm are performed by Straatman et al. (2016) and available at the ZFOURGE website[3].

The beam sizes of *Herschel*/SPIRE bands are large compared with other wavelengths (the mean FWHM values of $18''.1$, $25''.2$, and $36''.6$ at 250, 350, and 500 μm, respectively; Griffin et al., 2010). Therefore, we estimate de-blended flux densities obtained from de-blended SPIRE images based on the 24 μm sources position as a potential prior catalog. We use the de-blended technique in a similar manner as in Liu et al. (2018). In their methods, they run the SED fitting to predict the flux density of each prior sources for each band, moving from less to more confused bands. Then, they determine the critical flux value for choosing an actual prior source list at each band by considering both the number density and the expected flux density limit. The detail of the de-blending procedure in the ASAGAO field will be explained by T. Wang et al. (in preparation).

3.2.2 SED fitting by MAGPHYS

In this study, we perform the bayesian-based SED fitting from optical to millimeter wavelengths using the Multi-wavelength Analysis of Galaxy Physical Properties (MAGPHYS; da Cunha et al., 2008, 2015)[4] to estimate the physical properties of the ASAGAO sources. In this code, they compare luminosities of observed galaxies in all the observed bands with the each model model galaxy. The least χ^2 against the

[3] http://zfourge.tamu.edu/ (see also Section 2.2.1).
[4] MAGPHYS is available at http://www.iap.fr/magphys/

j-th model is calculated as folloews;

$$\chi_j^2 = \sum_{i=1}^{N_{\rm obs}} \left(\frac{L_i^{\rm obs} - w_j \times L_{i,j}^{\rm mod}}{\sigma_i^{\rm obs}} \right)^2 , \tag{3.7}$$

where $N_{\rm obs}$ is the number of observed bands, $L_i^{\rm obs}$ and $\sigma_i^{\rm obs}$ is the observed luminosity and the observed uncertainty at the i-th band, and $L_{i,j}^{\rm mod}$ is the estimated luminosity at the i-th band by the j-th model. According to da Cunha et al. (2008), w_j is the model scaling factor that minimizes χ_j^2 described by

$$w_j = \left(\sum_{i=1}^{N_{\rm obs}} \frac{L_i^{\rm obs} L_{i,j}^{\rm mod}}{\sigma_i^2} \right) \left[\sum_{i=1}^{N_{\rm obs}} \left(\frac{L_{i,j}^{\rm mod}}{\sigma_i} \right)^2 \right]^{-1} . \tag{3.8}$$

Then, the MAGPHYS calculates the probability density functions for physical parameters of galaxies by weighting the value of that parameter in the j-th model by the probability $\exp(-\chi_j^2/2)$. The MAGPHYS adopts the median values if the resulting probability density functions as the "best estimates" and the associated confidence interval to be the 16th–84th percentile range, which corresponds to $\pm 1\sigma$ range in a Gaussian distribution. The more details of SED fitting by MAGPHYS are explained in (da Cunha et al., 2008).

In this thesis, we adopt the SED templates of Bruzual & Charlot (2003) and the dust extinction model of Charlot & Fall (2000). In the SED fitting, we fixed the redshift of the ASAGAO sources to the best-fit photometric redshift or spectroscopic redshift if available (see Table 3.1). Even if we consider the redshift uncertainties, our conclusions do not change significantly. For example, the changes in the estimated physical parameters are within ~ 0.3 dex when we consider the relatively large photometric redshift uncertainties of ID102. Although we consider photometry errors in each band, we do not consider systematic uncertainties (e.g., absolute flux calibration errors)[5], which does not affect our SED fitting results significantly. For ASAGAO sources at $z > 1$, we use the MAGPHYS high-z extension version. This code uses priors which are optimized for IR luminous dusty star-forming galaxies at high redshift

[5]For example, according to ALMA Cycle 3 proposer's guide, the absolute flux calibration uncertainty of Band 6 data is expected to be $< 10\%$.

(da Cunha et al., 2015). On the other hand, we use the MAGPHYS original package, whose priors are calibrated for local galaxies of typically lower IR luminosities and SFRs (da Cunha et al., 2008), for ASAGAO sources at $z < 1$.

We have to note that MAGPHYS ignores any contribution by an AGN. Although Hainline et al. (2011) suggest that the near-IR continuum excess can be caused by the AGNs, only 11% of their samples ($\simeq$ 70 bright SMGs from Chapman et al., 2005) show stronger AGN-contribution than stellar-contribution at near-IR wavelengths. They also suggest that nearly half of their samples has less than 10% AGN-contribution to the near-IR smissions (the median value seems to be $\sim$ 10–20%, according to Figure 6 of Hainline et al. 2011). Dunlop et al. (2017) suggests that an AGN component in faint (sub-)millimeter sources would contribute only $\simeq$ 20% to the IR luminosity and near identical values are obtained by simply fitting the star-forming component to the ALMA data points. Michałowski et al. (2014) also suggest that the contribution of the AGNs does not have any significant impact on the derived stellar masses of (sub-)millimeter sources. In the case of ASAGAO detected sources, Ueda et al. (2018) suggest that majority of X-ray detected ASAGAO sources appear to be star-formation-dominant populations. Therefore, ignoring the AGN-contribution seems not to affect our results strongly.

The results of SED fitting are shown in the Table 3.3 and the figures in Appendix C. In Table 3.3, we add a flag to distinguish whether a source has a good (flag $= 1$) or unreliable fit (flag $= 0$). Some sources with flag $= 0$ show significant discrepancies between predicted SEDs and ALMA photometries (Figure C.1 in Appendix C). Although these discrepancies seems to be caused by miss identifications, there is a possibility of being affected by gravitational lensing effect. In our analysis, we exclude sources with flag $= 0$, although we note that it does not affect our results significantly (including their redshift distribution).

Table 3.3. Results of the SED fitting

ID (ZFOURGE)	ID (ASAGAO)	$\log(M_*)$ (ZFOURGE) ($M_\odot$)	$\log(M_*)$ (MAGPHYS) ($M_\odot$)	$\log(L_{\rm IR})$ (MAGPHYS) ($L_\odot$)	$\log(L_{\rm UV})$ (MAGPHYS) ($L_\odot$)	$\log({\rm SFR_{UV+IR}})$ (ZFOURGE) ($M_\odot$ yr^{-1})	$\log({\rm SFR_{UV+IR}})$ (MAGPHYS) ($M_\odot$ yr^{-1})	$\beta_{\rm UV}$	flag
18658	1	$10.11^{+0.00}_{-0.09}$	$10.91^{+0.00}_{-0.00}$	$12.74^{+0.00}_{-0.00}$	$10.26^{+0.04}_{-0.04}$	$2.62^{+0.01}_{-0.01}$	$2.78^{+0.00}_{-0.00}$	-1.53±0.07	1
17856	2	$10.84^{+0.11}_{-0.05}$	$11.43^{+0.00}_{-0.00}$	$12.76^{+0.00}_{-0.00}$	$9.63^{+0.06}_{-0.07}$	$2.39^{+0.01}_{-0.01}$	$2.79^{+0.00}_{-0.00}$	0.14±0.27	1
13086	3	$11.09^{+0.00}_{-0.01}$	$11.71^{+0.03}_{-0.01}$	$12.83^{+0.05}_{-0.00}$	$9.97^{+0.05}_{-0.06}$	$3.11^{+0.00}_{-0.00}$	$2.87^{+0.05}_{-0.00}$	-0.43±0.16	1
18645	4	$10.78^{+0.22}_{-0.21}$	$11.59^{+0.00}_{-0.00}$	$12.43^{+0.00}_{-0.00}$	$8.94^{+0.19}_{-0.36}$	$2.47^{+0.02}_{-0.02}$	$2.46^{+0.00}_{-0.00}$	–	1
18701	5	$10.48^{+0.00}_{-0.57}$	$10.48^{+0.00}_{-0.00}$	$12.74^{+0.00}_{-0.00}$	$10.13^{+0.06}_{-0.06}$	$2.67^{+0.01}_{-0.01}$	$2.78^{+0.00}_{-0.00}$	-1.45±0.14	1
22177	6	$10.71^{+0.09}_{-0.03}$	$11.34^{+0.02}_{-0.00}$	$12.61^{+0.01}_{-0.00}$	$9.67^{+0.06}_{-0.07}$	$2.43^{+0.01}_{-0.01}$	$2.65^{+0.01}_{-0.00}$	-0.51±0.18	1
20298	7	$10.27^{+0.09}_{-0.02}$	$10.92^{+0.08}_{-0.00}$	$11.00^{+0.00}_{-0.04}$	$8.87^{+0.22}_{-0.47}$	$1.04^{+0.02}_{-0.01}$	$1.04^{+0.01}_{-0.05}$	–	1
19033	8	$11.16^{+0.07}_{-0.09}$	$11.67^{+0.00}_{-0.00}$	$12.42^{+0.00}_{-0.00}$	$10.36^{+0.05}_{-0.05}$	$2.61^{+0.01}_{-0.00}$	$2.46^{+0.00}_{-0.00}$	-0.43±0.09	1
21234	9	$9.97^{+0.08}_{-0.76}$	$10.19^{+0.00}_{-0.00}$	$11.78^{+0.00}_{-0.00}$	$9.03^{+0.13}_{-0.20}$	$1.47^{+0.09}_{-0.08}$	$1.82^{+0.00}_{-0.00}$	-0.61±0.80	1
18912	10	$10.51^{+0.12}_{-0.08}$	$11.09^{+0.04}_{-0.02}$	$11.91^{+0.01}_{-0.02}$	$8.94^{+0.17}_{-0.27}$	$2.01^{+0.03}_{-0.02}$	$1.94^{+0.01}_{-0.02}$	–	1
21730	11	$10.54^{+0.01}_{-0.08}$	$11.41^{+0.01}_{-0.00}$	$12.13^{+0.05}_{-0.02}$	$8.70^{+0.27}_{-0.85}$	$2.14^{+0.02}_{-0.01}$	$2.16^{+0.05}_{-0.02}$	–	1
16952	12	$10.41^{+0.05}_{-0.06}$	$11.12^{+0.00}_{-0.00}$	$11.90^{+0.00}_{-0.00}$	$9.42^{+0.08}_{-0.10}$	$2.08^{+0.02}_{-0.01}$	$1.94^{+0.00}_{-0.00}$	-0.59±0.37	1
17733	13	$10.79^{+0.00}_{-0.05}$	$11.73^{+0.00}_{-0.12}$	$12.09^{+0.00}_{-0.02}$	$9.05^{+0.18}_{-0.33}$	$2.02^{+0.02}_{-0.01}$	$2.13^{+0.00}_{-0.02}$	-2.03±0.02	1
18336	14	$10.44^{+0.14}_{-0.07}$	$11.10^{+0.04}_{-0.06}$	$12.12^{+0.08}_{-0.07}$	$9.27^{+0.09}_{-0.11}$	$1.22^{+0.20}_{-0.31}$	$2.16^{+0.08}_{-0.07}$	–	1
15702	15	$10.63^{+0.13}_{-0.08}$	$11.29^{+0.09}_{-0.00}$	$12.34^{+0.00}_{-0.02}$	$10.24^{+0.05}_{-0.05}$	$2.58^{+0.01}_{-0.00}$	$2.39^{+0.00}_{-0.02}$	-1.38±0.19	1
19487	16	$11.24^{+0.00}_{-0.07}$	$11.61^{+0.00}_{-0.00}$	$11.98^{+0.00}_{-0.00}$	$9.45^{+0.17}_{-0.29}$	$2.29^{+0.01}_{-0.01}$	$2.02^{+0.00}_{-0.00}$	-0.05±0.61	1
12438	18	$10.48^{+0.18}_{-0.04}$	$11.37^{+0.06}_{-0.07}$	$11.93^{+0.02}_{-0.01}$	$8.67^{+0.15}_{-0.23}$	$1.56^{+0.02}_{-0.01}$	$1.97^{+0.02}_{-0.01}$	–	1
14580	19	$10.65^{+0.02}_{-0.04}$	$10.97^{+0.00}_{-0.00}$	$11.97^{+0.00}_{-0.00}$	$9.87^{+0.04}_{-0.05}$	$2.05^{+0.03}_{-0.02}$	$2.02^{+0.00}_{-0.00}$	-0.69±0.16	1
22760	21	$10.86^{+0.00}_{-0.03}$	$11.12^{+0.00}_{-0.00}$	$12.30^{+0.00}_{-0.00}$	$9.88^{+0.13}_{-0.18}$	–	$2.34^{+0.00}_{-0.00}$	-1.77±0.27	1
18270	23	$10.71^{+0.03}_{-0.00}$	$11.36^{+0.02}_{-0.03}$	$11.90^{+0.09}_{-0.00}$	$9.38^{+0.08}_{-0.10}$	$2.09^{+0.04}_{-0.03}$	$1.94^{+0.09}_{-0.00}$	-0.64±0.60	1
14146	26	$11.49^{+0.03}_{-0.00}$	$11.20^{+0.20}_{-0.13}$	$12.47^{+0.02}_{-0.02}$	$8.14^{+0.43}_{-0.17}$	–	$2.51^{+0.02}_{-0.02}$	–	1
14419	29	$10.80^{+0.08}_{-0.27}$	$11.36^{+0.00}_{-0.00}$	$12.07^{+0.00}_{-0.00}$	$8.92^{+0.29}_{-1.51}$	$2.16^{+0.03}_{-0.03}$	$2.11^{+0.00}_{-0.00}$	-0.41±0.65	1
13714	31	$11.00^{+0.05}_{-0.12}$	$11.43^{+0.05}_{-0.00}$	$12.11^{+0.00}_{-0.04}$	$9.23^{+0.16}_{-0.25}$	$2.18^{+0.02}_{-0.02}$	$2.14^{+0.00}_{-0.04}$	-1.07±1.04	1
14122	33	$10.33^{+0.17}_{-0.08}$	$10.95^{+0.08}_{-0.09}$	$11.95^{+0.24}_{-0.41}$	$8.49^{+0.10}_{-0.13}$	$1.67^{+0.23}_{-0.51}$	$1.99^{+0.24}_{-0.41}$	–	0
14700	44	$10.79^{+0.08}_{-0.08}$	$11.79^{+0.00}_{-0.00}$	$12.15^{+0.00}_{-0.00}$	$9.04^{+0.25}_{-0.67}$	$2.54^{+0.01}_{-0.00}$	$2.19^{+0.00}_{-0.00}$	-1.94±0.76	1

Table 3.3 *(continued)*

ID (ZFOURGE)	ID (ASAGAO)	$\log(M_*)$ (ZFOURGE) ($M_\odot$)	$\log(M_*)$ (MAGPHYS) ($M_\odot$)	$\log(L_{\rm IR})$ (MAGPHYS) ($L_\odot$)	$\log(L_{\rm UV})$ (MAGPHYS) ($L_\odot$)	$\log(\mathrm{SFR_{UV+IR}})$ (ZFOURGE) ($M_\odot\ \mathrm{yr}^{-1}$)	$\log(\mathrm{SFR_{UV+IR}})$ (MAGPHYS) ($M_\odot\ \mathrm{yr}^{-1}$)	$\beta_{\rm UV}$	flag
15752	47	$6.85^{+0.00}_{-2.71}$	$7.77^{+0.14}_{-0.13}$	$7.76^{+0.37}_{-0.39}$	$7.58^{+0.06}_{-0.07}$	–	$-1.81^{+0.21}_{-0.18}$	–	0
20550	98	$8.47^{+0.06}_{-0.05}$	$8.94^{+0.10}_{-0.06}$	$9.03^{+0.44}_{-0.15}$	$8.99^{+0.02}_{-0.02}$	$-0.88^{+0.16}_{-0.02}$	$-0.46^{+0.21}_{-0.06}$	–	1
22905	102	$10.97^{+0.11}_{-0.07}$	$11.86^{+0.01}_{-0.00}$	$12.88^{+0.03}_{-0.00}$	$9.04^{+0.32}_{-1.10}$	$3.01^{+0.04}_{-0.05}$	$2.91^{+0.03}_{-0.00}$	–	1
19490	108	$9.64^{+0.04}_{-0.07}$	$10.25^{+0.04}_{-0.00}$	$10.09^{+0.03}_{-0.00}$	$8.76^{+0.11}_{-0.14}$	$0.11^{+0.17}_{-0.25}$	$0.17^{+0.04}_{-0.01}$	–	1
20394	121	$10.53^{+0.05}_{-0.11}$	$10.98^{+0.07}_{-0.03}$	$11.75^{+0.45}_{-0.01}$	$8.99^{+0.12}_{-0.16}$	$2.36^{+0.19}_{-0.34}$	$1.79^{+0.45}_{-0.01}$	–	1
19903	142	$8.72^{+0.03}_{-0.18}$	$8.98^{+0.06}_{-0.14}$	$9.87^{+0.56}_{-0.27}$	$8.93^{+0.06}_{-0.07}$	–	$0.01^{+0.49}_{-0.22}$	-2.12±0.47	1
20694	146	$10.69^{+0.06}_{-0.03}$	$11.42^{+0.00}_{-0.00}$	$11.49^{+0.00}_{-0.00}$	$9.57^{+0.07}_{-0.08}$	$1.52^{+0.02}_{-0.01}$	$1.54^{+0.00}_{-0.00}$	0.08±0.03	1
12763	167	$10.74^{+0.07}_{-0.10}$	$11.18^{+0.00}_{-0.00}$	$12.18^{+0.00}_{-0.00}$	$10.20^{+0.03}_{-0.04}$	$2.35^{+0.01}_{-0.01}$	$2.22^{+0.00}_{-0.00}$	-1.31±0.15	1
20728	178	$9.61^{+0.08}_{-0.03}$	$10.21^{+0.06}_{-0.00}$	$10.82^{+0.00}_{-0.07}$	$9.90^{+0.02}_{-0.02}$	$0.62^{+0.07}_{-0.03}$	$0.96^{+0.01}_{-0.06}$	–	1
17785	185	$9.20^{+0.03}_{-0.10}$	$9.64^{+0.08}_{-0.17}$	$11.69^{+0.25}_{-0.36}$	$9.27^{+0.06}_{-0.07}$	–	$1.73^{+0.25}_{-0.35}$	-0.45±0.52	1
21368	186	$9.75^{+0.02}_{-0.00}$	$10.22^{+0.00}_{-0.06}$	$11.43^{+0.00}_{-0.02}$	$9.86^{+0.04}_{-0.04}$	$1.52^{+0.07}_{-0.06}$	$1.49^{+0.00}_{-0.02}$	-1.59±0.11	1
21702	188	$10.53^{+0.05}_{-0.08}$	$11.14^{+0.00}_{-0.05}$	$11.74^{+0.00}_{-0.06}$	$9.54^{+0.04}_{-0.05}$	$1.99^{+0.02}_{-0.01}$	$1.79^{+0.00}_{-0.06}$	-0.69±0.23	1
15919	196	$8.49^{+0.23}_{-0.01}$	$9.04^{+0.02}_{-0.12}$	$10.43^{+0.06}_{-0.43}$	$9.25^{+0.01}_{-0.01}$	$-0.12^{+0.28}_{-0.14}$	$0.52^{+0.06}_{-0.35}$	–	1
12904	210	$9.48^{+0.01}_{-0.19}$	$11.21^{+0.15}_{-0.23}$	$12.10^{+0.31}_{-0.27}$	$7.29^{+1.93}_{-1.92}$	–	$2.14^{+0.31}_{-0.27}$	–	0
16977	236	$9.92^{+0.04}_{-0.04}$	$10.31^{+0.00}_{-0.12}$	$11.40^{+0.05}_{-0.00}$	$9.65^{+0.04}_{-0.04}$	$1.89^{+0.02}_{-0.01}$	$1.45^{+0.05}_{-0.00}$	-1.48±0.06	1
21193	243	$9.16^{+0.10}_{-0.03}$	$9.51^{+0.03}_{-0.00}$	$11.12^{+0.00}_{-0.00}$	$9.58^{+0.01}_{-0.02}$	$0.55^{+0.31}_{-0.51}$	$1.18^{+0.00}_{-0.00}$	-1.63±0.08	1
16522	260	$9.68^{+0.00}_{-0.01}$	$10.29^{+0.00}_{-0.00}$	$11.23^{+0.00}_{-0.00}$	$10.12^{+0.01}_{-0.01}$	$1.34^{+0.02}_{-0.00}$	$1.34^{+0.00}_{-0.00}$	-0.86±0.16	1
13876	264	$10.61^{+0.12}_{-0.04}$	$11.21^{+0.00}_{-0.00}$	$11.78^{+0.00}_{-0.00}$	$9.59^{+0.07}_{-0.08}$	$2.31^{+0.01}_{-0.01}$	$1.82^{+0.00}_{-0.00}$	-1.57±0.32	1
13269	276	$9.90^{+0.09}_{-0.14}$	$10.11^{+0.29}_{-0.04}$	$11.79^{+0.09}_{-0.75}$	$9.59^{+0.03}_{-0.04}$	$2.02^{+0.21}_{-0.40}$	$1.83^{+0.09}_{-0.73}$	-1.72±0.16	1
17959	282	$7.48^{+0.15}_{-0.05}$	$7.83^{+0.10}_{-0.05}$	$9.43^{+0.47}_{-0.40}$	$8.33^{+0.02}_{-0.02}$	$-0.48^{+0.58}_{-1.23}$	$-0.46^{+0.42}_{-0.32}$	–	1
16040	289	$10.21^{+0.05}_{-0.11}$	$10.76^{+0.08}_{-0.04}$	$11.47^{+0.23}_{-0.18}$	$9.59^{+0.05}_{-0.06}$	$1.66^{+0.04}_{-0.02}$	$1.52^{+0.23}_{-0.17}$	-1.08±0.32	1
14901	290	$9.92^{+0.08}_{-0.07}$	$10.52^{+0.05}_{-0.02}$	$11.57^{+0.13}_{-0.17}$	$9.11^{+0.06}_{-0.06}$	$1.36^{+0.18}_{-0.26}$	$1.61^{+0.13}_{-0.17}$	–	1
12682	328	$9.59^{+0.18}_{-0.10}$	$9.95^{+0.09}_{-0.07}$	$11.77^{+0.32}_{-0.28}$	$9.25^{+0.05}_{-0.05}$	–	$1.81^{+0.32}_{-0.28}$	-1.08±1.44	1
20008	338	$9.24^{+0.06}_{-0.03}$	$9.57^{+0.00}_{-0.00}$	$10.91^{+0.00}_{-0.00}$	$9.54^{+0.02}_{-0.02}$	$0.26^{+0.29}_{-0.21}$	$0.98^{+0.00}_{-0.00}$	-1.92±0.11	1
16562	366	$9.15^{+0.00}_{-0.01}$	$9.78^{+0.03}_{-0.05}$	$10.75^{+0.42}_{-0.08}$	$9.44^{+0.03}_{-0.03}$	$0.31^{+0.15}_{-0.06}$	$0.83^{+0.39}_{-0.07}$	–	1

Table 3.3 *(continued)*

ID (ZFOURGE)	ID (ASAGAO)	$\log(M_*)$ (ZFOURGE) ($M_\odot$)	$\log(M_*)$ (MAGPHYS) ($M_\odot$)	$\log(L_{\rm IR})$ (MAGPHYS) ($L_\odot$)	$\log(L_{\rm UV})$ (MAGPHYS) ($L_\odot$)	$\log({\rm SFR_{UV+IR}})$ (ZFOURGE) ($M_\odot$ yr^{-1})	$\log({\rm SFR_{UV+IR}})$ (MAGPHYS) ($M_\odot$ yr^{-1})	$\beta_{\rm UV}$	flag
19915	371	$10.61^{+0.12}_{-0.06}$	$11.21^{+0.01}_{-0.13}$	$10.32^{+0.23}_{-0.06}$	$9.21^{+0.18}_{-0.32}$	$0.30^{+0.10}_{-0.03}$	$0.43^{+0.22}_{-0.09}$	–	1
14407	375	$9.44^{+0.11}_{-0.18}$	$9.89^{+0.00}_{-0.00}$	$10.26^{+0.00}_{-0.00}$	$9.43^{+0.05}_{-0.06}$	–	$0.42^{+0.01}_{-0.01}$	-2.14±0.39	0
12998	380	$11.03^{+0.12}_{-0.09}$	$11.78^{+0.00}_{-0.18}$	$11.65^{+0.05}_{-0.00}$	$10.14^{+0.07}_{-0.08}$	$1.85^{+0.01}_{-0.00}$	$1.72^{+0.05}_{-0.01}$	-0.99±0.15	1
15617	382	$10.35^{+0.05}_{-0.03}$	$11.09^{+0.05}_{-0.06}$	$11.13^{+0.04}_{-0.02}$	$9.68^{+0.09}_{-0.12}$	$1.16^{+0.02}_{-0.01}$	$1.20^{+0.04}_{-0.02}$	–	1
16874	417	$7.97^{+0.06}_{-0.21}$	$8.32^{+0.02}_{-0.00}$	$8.20^{+0.12}_{-0.00}$	$8.77^{+0.02}_{-0.02}$	$-1.12^{+0.20}_{-0.03}$	$-0.80^{+0.03}_{-0.01}$	–	0
22495	418	$11.02^{+0.09}_{-0.07}$	$11.52^{+0.06}_{-0.00}$	$11.50^{+0.01}_{-0.00}$	$9.31^{+0.11}_{-0.16}$	$1.61^{+0.02}_{-0.01}$	$1.55^{+0.01}_{-0.00}$	-1.39±0.50	1
17465	424	$10.85^{+0.04}_{-0.13}$	$11.46^{+0.05}_{-0.00}$	$11.51^{+0.03}_{-0.00}$	$9.10^{+0.11}_{-0.15}$	$1.44^{+0.04}_{-0.03}$	$1.55^{+0.03}_{-0.00}$	1.95±0.54	1
15768	437	$10.47^{+0.09}_{-0.06}$	$11.17^{+0.12}_{-0.00}$	$11.74^{+0.02}_{-0.04}$	$9.76^{+0.07}_{-0.08}$	$1.91^{+0.01}_{-0.01}$	$1.79^{+0.02}_{-0.04}$	-0.22±0.12	1
18476	460	$10.10^{+0.07}_{-0.07}$	$10.87^{+0.00}_{-0.01}$	$11.44^{+0.02}_{-0.00}$	$9.57^{+0.06}_{-0.07}$	$1.46^{+0.03}_{-0.01}$	$1.49^{+0.02}_{-0.00}$	-1.25±0.26	1
20073	487	$9.44^{+0.07}_{-0.11}$	$9.83^{+0.03}_{-0.02}$	$10.40^{+0.05}_{-0.08}$	$9.65^{+0.02}_{-0.02}$	$0.13^{+0.16}_{-0.05}$	$0.58^{+0.04}_{-0.06}$	–	1
18096	497	$7.90^{+0.09}_{-0.04}$	$8.33^{+0.08}_{-0.06}$	$9.17^{+0.51}_{-0.84}$	$8.08^{+0.09}_{-0.11}$	–	$-0.72^{+0.47}_{-0.62}$	–	0
18813	502	$10.01^{+0.10}_{-0.08}$	$10.74^{+0.00}_{-0.00}$	$11.54^{+0.00}_{-0.00}$	$10.01^{+0.04}_{-0.04}$	$1.49^{+0.02}_{-0.01}$	$1.60^{+0.00}_{-0.00}$	-1.99±0.29	1
18047	505	$9.96^{+0.04}_{-0.08}$	$10.41^{+0.03}_{-0.03}$	$11.22^{+0.01}_{-0.17}$	$9.55^{+0.03}_{-0.03}$	$1.37^{+0.07}_{-0.06}$	$1.28^{+0.01}_{-0.16}$	-1.61±0.17	1
23130	517	$9.99^{+0.14}_{-0.15}$	$10.69^{+0.00}_{-0.04}$	$11.44^{+0.00}_{-0.15}$	$10.10^{+0.03}_{-0.03}$	$1.43^{+0.03}_{-0.01}$	$1.52^{+0.00}_{-0.14}$	-1.79±0.12	1
17007	524	$9.67^{+0.02}_{-0.02}$	$10.18^{+0.00}_{-0.00}$	$11.00^{+0.00}_{-0.00}$	$9.93^{+0.02}_{-0.02}$	$0.95^{+0.11}_{-0.08}$	$1.11^{+0.00}_{-0.00}$	-1.54±0.06	1
21317	531	$8.49^{+0.06}_{-0.03}$	$8.99^{+0.03}_{-0.07}$	$8.40^{+0.17}_{-0.19}$	$7.86^{+0.23}_{-0.50}$	–	$-1.35^{+0.19}_{-0.29}$	–	0

Note. — (1) ASAGAO ID. (2) Stellar mass taken from the ZFOURGE catalog (Straatman et al., 2016), which are obtained using FAST (3) Stellar mass obtained by MAGPHYS. (4) IR luminosity obtained by MAGPHYS. (5) UV luminosity obtained by rest-frame 2800 Å luminosity. (6) UV + IR SFR obtained by ZFOURGE (Straatman et al., 2016). (7) UV + IR SFR obtained by MAGPHYS. (8) UV spectral slope estimated by fitting a power law $f_\lambda \propto \lambda^\beta$ over the rest-frame wavelength range of 1500–2500 Å. (9) SED fitting flag (1: good, 0: bad). There are the reasons to classify as flag = 0: a) the number of photometry points is less than 12 (i.e., the degree of freedom of SED fit using MAGPHYS is less than one), b) the predicted millimeter photometry is inconsistent with the observed ALMA photometry and there are no photometry points at mid-IR-to-far-IR wavelengths.

3.3 Star formation properties of ASAGAO sources

3.3.1 Stellar masses & SFRs

We estimate stellar masses and SFRs of ASAGAO sources to discuss star formation properties. First, we calculate the stellar masses by using MAGPHYS. Second, we compute SFRs by summing the ultraviolet (UV) SFRs and IR SFRs based on the work of Bell et al. (2005) scaled to a Chabrier IMF:

$$\mathrm{SFR_{UV+IR}}/(\mathrm{M_\odot\ yr^{-1}}) = 1.09 \times 10^{-10}(L_{\mathrm{IR}} + 2.2L_{\mathrm{UV}})/L_\odot. \tag{3.9}$$

Here, L_{IR} is the IR luminosity obtained by using MAGPHYS[6]. The total UV luminosity, L_{UV}, is defined as $L_{\mathrm{UV}} = 1.5\nu L_{\nu 2800}$ as described in Straatman et al. (2016), where $\nu L_{\nu 2800}$ is the rest-frame 2800 Å luminosity. The derived stellar masses and SFRs are summarized in Table 3.3.

In Table 3.3, we show the stellar masses and SFRs of ASAGAO sources obtained by Straatman et al. (2016). They used the FAST code (Kriek et al., 2009), which is compatible with EAZY, to derive stellar masses. For estimating UV+IR SFRs, they used IR luminosities obtained by the IR SED template of Wuyts et al. (2008) and UV luminosities from the rest-frame 2800 Å luminosity. We compare our results with the ZFOURGE to check consistency in Figure 3.4. Although the SFRs estimated as with MAGPHYS and ZFOURGE are consistent, the stellar masses obtained by using MAGPHYS are systematically higher than that of FAST by $\gtrsim$ 0.2–0.5 dex. A similar offset is also reported by Michałowski et al. (2014) and they suggest that it can be explained by the difference of the assumed star formation histories. de Barros et al. (2014) suggest that nebular emission lines at near-IR wavelengths, which are not included in MAGPHYS, can lead to an overestimation of the stellar masses. Here, we use stellar masses obtained with FAST to compare our results with the ZFOURGE results (estimated by FAST) directly. In this paper, we compare the derived stellar masses of ASAGAO sources with stellar masses of other (sub-)millimeter

[6] Although MAGPHYS provides IR luminosities in the range of 3–1000 μm in the rest-frame, the IR luminosities by MAGPHYS can be directly compared with other estimates referring to the commonly used wavelength range 8–1000 μm in the rest-frame. This is because the contribution of dust to the emission in the range of 3–8 μm is very small, as discussed in Clemens et al. (2013).

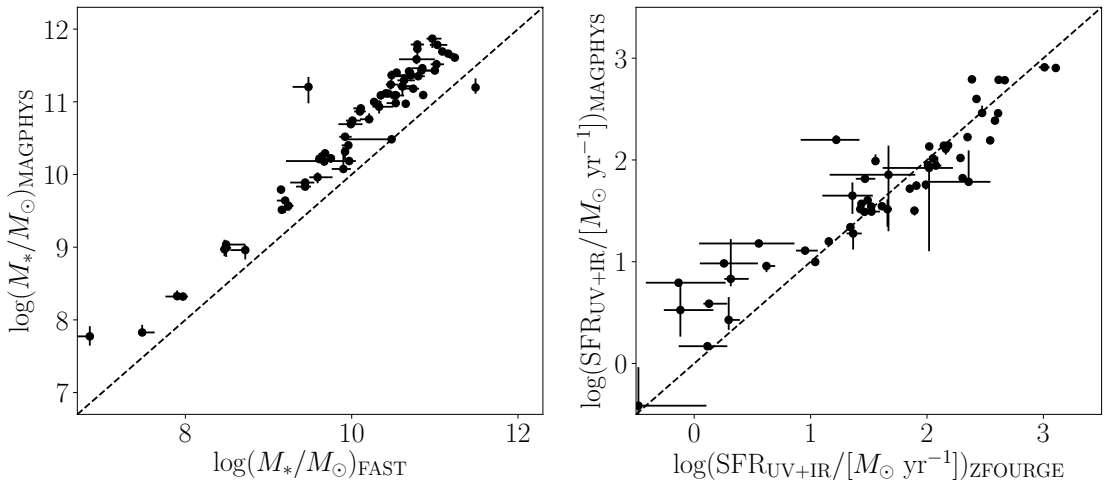

Figure 3.4 *Left)* Comparison of stellar masses obtained by MAGPHYS and FAST. The black dashed line indicates the case that $\log(M_*/M_\odot)_{\rm MAGPHYS} = \log(M_*/M_\odot)_{\rm FAST}$. *Right)* Comparison of IR + UV SFRs obtained by MAGPHYS and ZFOURGE. The black dashed line indicates the case that $\log({\rm SFR}_{\rm UV+IR})_{\rm MAGPHYS} = \log({\rm SFR}_{\rm UV+IR})_{\rm ZFOURGE}$.

selected samples obtained by previous studies. Therefore, we have to note the differences of stellar mass modeling. For example, Yamaguchi et al. (2016) also used FAST to estimate stellar masses. However, da Cunha et al. (2015) used MAGPHYS, and Dunlop et al. (2017) estimate stellar masses of ALMA sources by their SED fit using Bruzual & Charlot (2003) evolutionary synthesis models.

Figure 3.5 shows the stellar mass distribution of ASAGAO sources. We only include ASAGAO sources with SED fitting flag = 1. There are some flag = 1 sources with $p > 0.05$ (red open circle in following figures), but our results do not change significantly, even if we exclude all of these sources from our results. Here, we divide ASAGAO sources into three redshift bins (i.e., $z \leq 1.5$, $1.5 < z \leq 2.5$, and $2.5 < z \leq 5.0$). In each redshift bin, there are 26, 18, and 15 ASAGAO sources. The median stellar masses of each redshift bin are $\log(M_*/M_\odot) = 10.00 \pm 0.22$, 10.62 ± 0.11, and 10.53 ± 0.19 for $z \leq 1.5$, $1.5 < z \leq 2.5$, and $2.5 < z \leq 5.0$, respectively. The estimated stellar masses are consistent with previous studies on ALMA continuum sources at similar redshift range and with $S_{\rm obs} \simeq 1$ mJy such as Tadaki et al. (2015) or Dunlop et al. (2017). As shown in Figure 3.5, the ASAGAO sources have typically

higher stellar masses than ALMA non-detected ZFOURGE sources[7], whose median stellar masses are $\log(M_*/M_\odot) = 8.65 \pm 0.04$, 9.06 ± 0.04, and 9.3 ± 0.04 for $z \leq 1.5$, $1.5 < z \leq 2.5$, and $2.5 < z \leq 5.0$, respectively. This trend can be clearly observed when we plot the ALMA detection rate (i.e., ALMA-detected ZFOURGE sources per all ZFOURGE sources within the ASAGAO field) as a function of their stellar masses (Figure 3.5). The trend is also shown in previous ALMA survey such as Bouwens et al. (2016). Figure 3.5 shows the SFR distribution of ASAGAO sources in three redshift bins. The median SFR of each redshift bin is $\log(\mathrm{SFR}/[M_\odot\ \mathrm{yr}^{-1}]) = 1.16 \pm 0.20$, 2.07 ± 0.12, and 2.11 ± 0.18 for $z \leq 1.5$, $1.5 < z \leq 2.5$, and $2.5 < z \leq 5.0$, respectively.

3.3.2 Star formation properties

In Figure 3.5, we plot the ASAGAO sources on the M_*–SFR plane. In addition, we show the ALMA non-detected ZFOURGE sources within the ASAGAO field (Straatman et al., 2016), ALESS sources (da Cunha et al., 2015), ASPECS sources (Aravena et al., 2016b), faint SMGs in SXDF-UDS-CANDELS (Yamaguchi et al., 2016), and ALMA sources with optical/near-IR counterparts by Dunlop et al. (2017). For comparison, we also plot the position of the main sequence of star-forming galaxies at each redshift (z = 1.06, 2.01, and 2.77; median redshifts of each redshift bin) compiled by Schreiber et al. (2015).

As shown in Figure 3.5, the ASAGAO sources primarily lie on the main sequence of star-forming galaxies, although some ASAGAO sources shows starburst-like features. This is consistent with previous ALMA results (e.g., da Cunha et al., 2015; Aravena et al., 2016b; Dunlop et al., 2017). Figure 3.5 also suggests that ASAGAO sources at $z > 1.5$ mainly trace the high-mass end of the main sequence of star-forming galaxies. When we compare ASAGAO sources with ALESS sources (i.e., single-dish selected galaxies), ASAGAO sources tend to have systematically lower SFRs for a similar stellar mass range. Here we need to note that da Cunha et al. (2015) used MAGPHYS to estimate stellar masses of ALESS sources. When we consider the systematic offset of stellar masses estimated by MAGPHYS and FAST, differences between ASAGAO sources and ALESS sources on the M_*-SFR plane become even larger. This result

[7]Herein we only use the star-forming galaxies selected by the *UVJ*-technique, as presented by Whitaker et al. (2011).

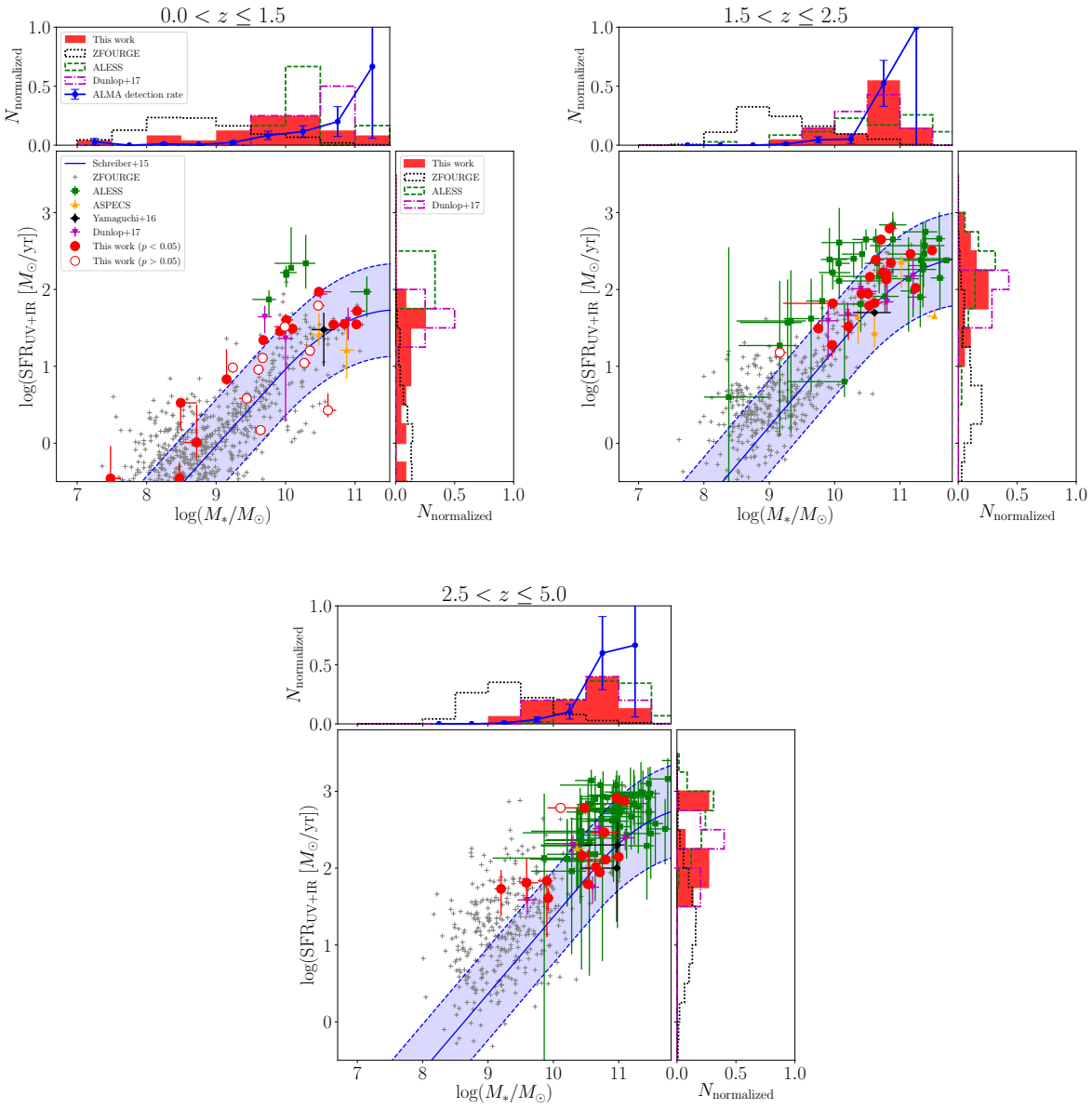

Figure 3.5 Comparison of the stellar masses and SFRs of ASAGAO sources with the "main sequence of star-forming galaxies". ASAGAO sources are plotted as red circles. The gray crosses, green squares, orange triangles, black diamonds, and magenta inverse-triangles represent the ALMA non-detected ZFOURGE sources (Straatman et al., 2016), ALESS sources (da Cunha et al., 2015), ASPEC sources (Aravena et al., 2016b), faint SMGs of Yamaguchi et al. (2016), and ALMA selected sources by Dunlop et al. (2017). The blue solid lines indicate the position of the main sequence of star-forming galaxies at $z = 1.06$, 2.02, and 2.77 as predicted by Schreiber et al. (2015). The blue dashed lines indicate a factor of 4 above or below this main sequence. In addition, we show the histograms of stellar masses and SFRs. The blue circles in the stellar-mass distributions are ALMA detection rates as a function of their stellar masses. The error bars show simple Poisson uncertainties.

implies that an ALMA continuum survey at a 1σ depth of a few tens of μJy can unveil galaxies which are more likely the normal star-forming galaxies than "classical" SMGs since they show more quiescent star-forming activities than "classical" SMGs for a similar stellar mass range. However, the ASAGAO sources at $z < 1.5$ have wide stellar masses and positions with respect to the main sequence of star-forming galaxies. This may suggest that these ASAGAO sources consist of a heterogeneous population as suggested by the recent hydrodynamical simulations of Hayward et al. (2012).

3.4 The infrared excesses (IRX) of ASAGAO sources

As shown in Figure 3.5, there are ALMA non-detected ZFOURGE sources within the ASAGAO field even though they show similar star-forming properties to ALMA detected sources on the M_*–SFR plane. In this section, we focus on IRX (i.e., $L_{\rm IR}/L_{\rm UV}$) as a key parameter to distinguish between ALMA detected sources and non-detected sources. Although many previous studies on IRX of galaxies use rest-frame 1600 Å luminosities, we note that we adopt $L_{\rm UV} = 1.5\nu L_{\nu 2800}$ to obtain $L_{\rm UV}$ (see Section 3.3.1), which are supposed to be approximately equivalent (Kennicutt, 1998; Whitaker et al., 2014).

3.4.1 The IRX–M_* and IRX–SFR relations

Several studies have shown a correlation between the IRX and stellar masses, in the sense that massive star-forming galaxies show larger IRX (e.g., Reddy et al., 2010; Whitaker et al., 2014; Bouwens et al., 2016; Dunlop et al., 2017). We plot the IRX of ASAGAO sources as a function of their stellar masses in Figure 3.6. For comparison, we also show the ALMA detected sources (da Cunha et al., 2015; Dunlop et al., 2017) and ALMA non-detected ZFOURGE sources (Straatman et al., 2016) within the ASAGAO field. We also show the consensus IRX-M_* relation compiled by Bouwens et al. (2016). They derive stellar masses using FAST and their estimated consensus relationship is consistent with the results of three separated studies (Reddy et al., 2010; Whitaker et al., 2014; Álvarez-Márquez et al., 2016).

As shown in Figure 3.6, the ALMA detected sources tend to have larger IRX compared to the ALMA non-detected sources. This trend becomes more visible for higher redshift sources; most of the ASAGAO

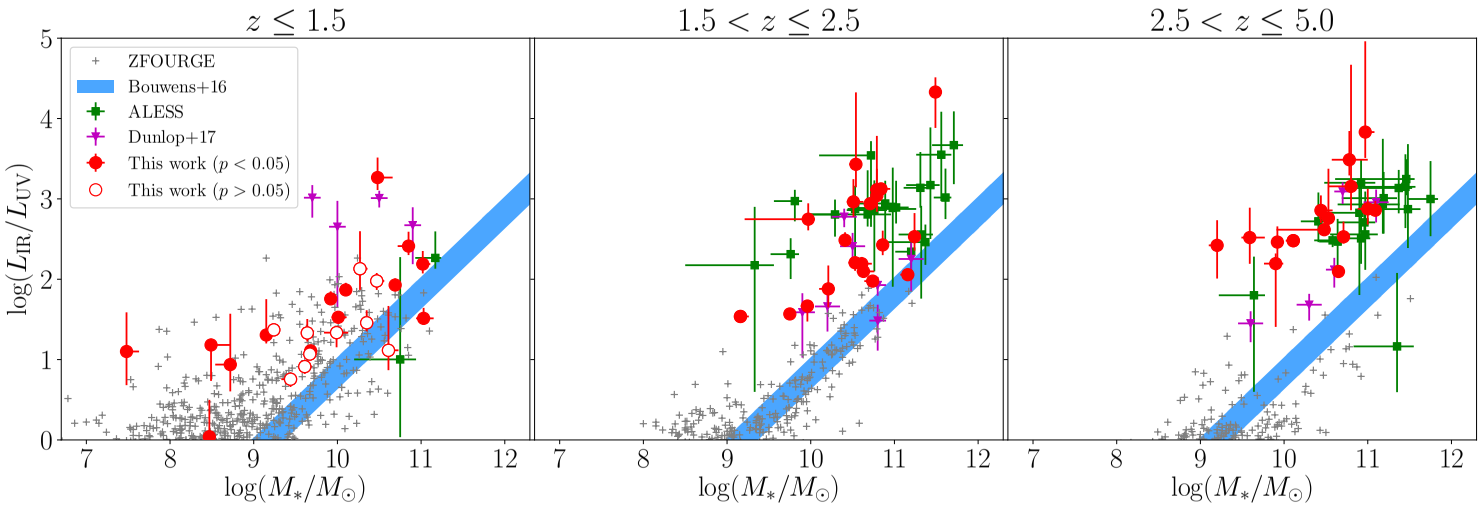

Figure 3.6 The IRX of ASAGAO sources as a function of their stellar mass (red circles). We also show the ALMA non-detected ZFOURGE sources (Straatman et al., 2016) within the ASAGAO field, ALESS sources (da Cunha et al., 2015), and ALMA selected sources by Dunlop et al. (2017). The thick shaded blue line shows the relation derived by UV-selected galaxies at $z \sim$ 2–3 (Bouwens et al., 2016).

sources at $z \leq 1.5$ are above the IRX-M_* relation of UV-selected galaxies (Bouwens et al., 2016), with a typical offset between them of 1 dex for $\log(M_*/M_\odot) \gtrsim 9$–10. A significant fraction of ALMA non-detected ZFOURGE sources also coexist with ASAGAO sources in this plot. However, the IRXs of ASAGAO sources at $z > 1.5$ are systematically larger than those from the IRX-M_* relation of UV-selected galaxies, with an offset of 1–2 dex; in contrast, no ALMA non-detected ZFOURGE sources exhibit such elevated IRX values. When we derive the IRX-M_* relation of ALMA detected sources by assuming a linear relationship[8], the offsets from the relation of Bouwens et al. (2016) are estimated to be $\sim 1.0 \pm 0.1$, 1.1 ± 0.1, and 1.2 ± 0.1 at $z \leq 1.5$, $1.5 < z \leq 2.5$, and $2.5 < z$, respectively. This can imply a weak evolution of the IRX-M_* relation of ALMA detected sources, although more samples are needed to confirm this.

When we plot the IRX-SFR relation of ASAGAO sources for three stellar mass bins (i.e., $\log(M_*/M_\odot) \leq 10$, $10 < \log(M_*/M_\odot) \leq 11$, and $11 < \log(M_*/M_\odot)$; Figure 3.7), the offset from ALMA non-detected ZFOURGE sources also become evident, particularly at $z > 1.5$. At $z \leq 1.5$, the ALMA detected sources tend to have higher IRX than those of ALMA non-detected sources for a similar SFR range even with $\log(M_*/M_\odot) > 10$, although the typical offset is smaller than that of $z > 1.5$.

3.4.2 The IRX–$\beta_{\rm UV}$ relation

An useful relation to study the properties of dust is the relation between the UV spectral slopes ($\beta_{\rm UV}$) and IRX, because this relation reflect the effect of dust attenuation. Therefore, we examine the IRX-$\beta_{\rm UV}$ relation of ALMA detected sources for further discussion on the difference between ALMA detected and non-detected sources. The IRX-$\beta_{\rm UV}$ relation has been calibrated using local star-burst galaxies (e.g., Meurer et al., 1999; Takeuchi et al., 2012).

In this study, $\beta_{\rm UV}$ is calculated by fitting a power law $f_\lambda \propto \lambda^\beta$ over the rest-frame wavelength range of 1500–2500 Å using ZFOURGE photometies. Figure 3.8 shows the IRX–$\beta_{\rm UV}$ relation of ASAGAO sources. We also plot the ALMA non-detected ZFOURGE sources within the ASAGAO field, along with

[8]We only adopt y-intercepts as free parameters and all ALMA sources in Figure 3.6 (i.e., ALESS sources and HUDF sources as well as ASAGAO sources) are included in the least-square fit.

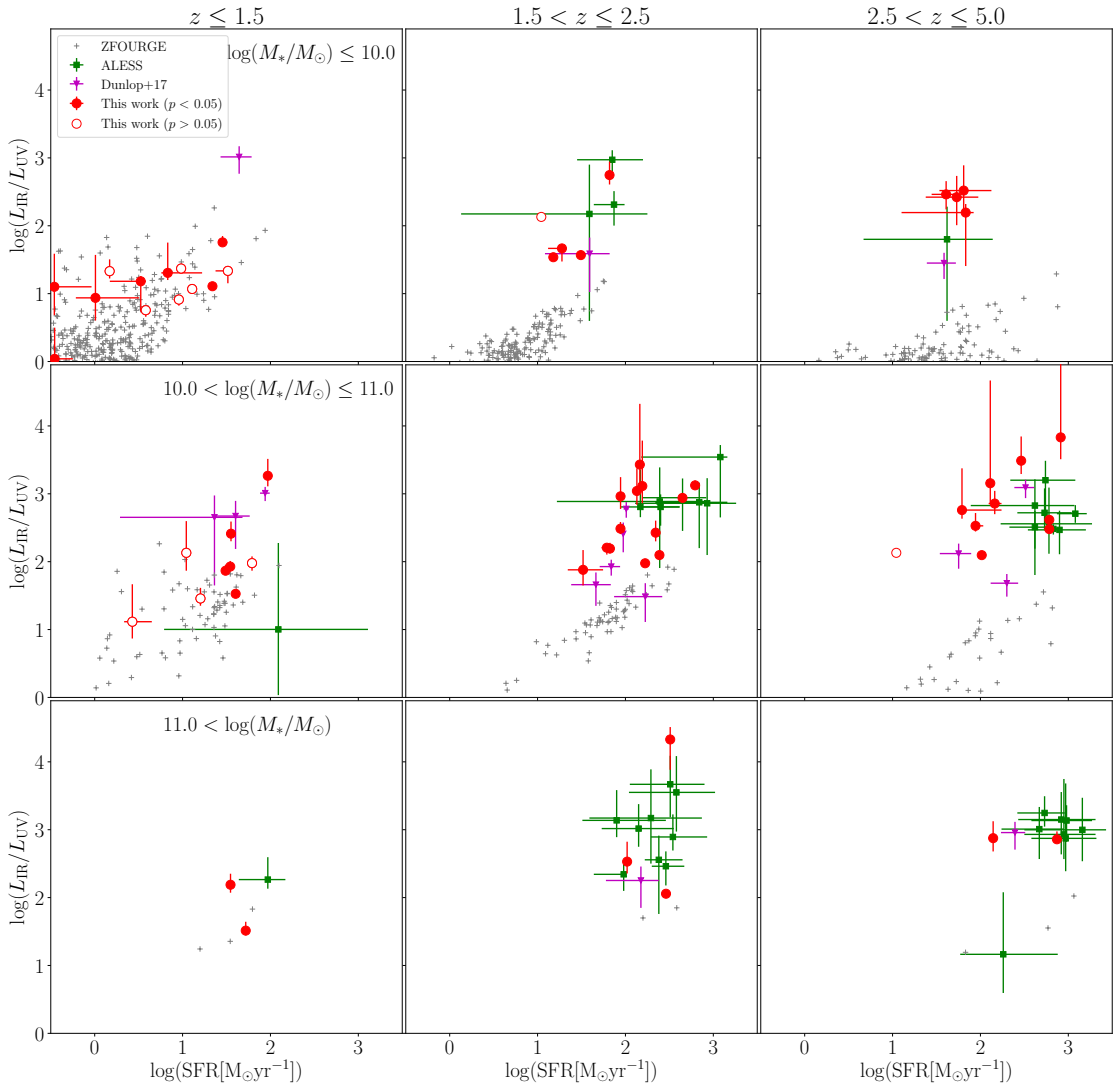

Figure 3.7 The IRX of ASAGAO sources as a function of their SFRs (red circles). We also show the ALMA non-detected ZFOURGE sources within the ASAGAO field (Straatman et al., 2016), ALESS sources (da Cunha et al., 2015), and ALMA selected sources by Dunlop et al. (2017).

the relation given in Meurer et al. (1999) and Takeuchi et al. (2012). Figure 3.8 shows that ASAGAO sources tend to have larger IRX values compared to the ALMA non-detected ZFOURGE sources, as well as the local starburst relations as provided by Meurer et al. (1999) and Takeuchi et al. (2012). This trend is consistent with the results of Casey et al. (2014), which suggest that dusty star-forming galaxies show bluer colors in the IRX-$\beta_{\rm UV}$ plane.

Then why do dusty star-forming galaxies lie above the local IRX-$\beta_{\rm UV}$ relations by Meurer et al. (1999) and Takeuchi et al. (2012)? Casey et al. (2014) suggested that the difference in a starburst timescale can be a key; specifically, dusty star-forming galaxies have short-timescale starburst (10–300 Myr). Short-lived burst events produce many young O and B-type stars that are not entirely enshrouded in thick dust cocoons yet. This can make their colors bluer. However, dust radiative transfer on a suite of hydrodynamical simulations by Safarzadeh et al. (2017) suggests that the dust composition (i.e., the difference of the chemical composition or/and the grain size distribution; see Galliano et al., 2018, for details) might be more important than the star-formation timescale. For example, when Small Magellanic Cloud-type dust is assumed, $\beta_{\rm UV}$ becomes larger (i.e., the SED is redder) than in the case of Milky Way-type dust (Safarzadeh et al., 2017). The differences of dust composition may strongly affect the way a galaxy evolves in the IRX-$\beta_{\rm UV}$ plane (Safarzadeh et al., 2017). Our result prefers their scenario, because ASAGAO sources lie primarily on the main-sequence of star-forming galaxies, which do not show short-lived starburst features as suggested by Casey et al. (2014).

Safarzadeh et al. (2017) also suggest that in simulated star-forming galaxies at $z \sim 2$–3, the different dust attenuation properties, such as dust geometries (i.e., the difference of spatial distribution between stars and dust) dominate the dispersion in $\beta_{\rm UV}$, whereas the contribution of star formation history and dust geometry variations are similar at $z \sim 0$. Similar results are also implied by a simple model by Popping et al. (2017). From the point of view of the ALMA observation, the conclusions of Chen et al. (2017) imply that the different spacial distribution between dust and stellar emission is partially responsible for the deviation from IRX–$\beta_{\rm UV}$ relation based on the high-resolution observation of an ALESS source at $z = 2.12$ (ALESS67.1). Hodge et al. (2015) and Tadaki et al. (2017) also suggest that the spatial distribution of ALMA detected dusty regions are different from the stellar emitting regions. In the ASAGAO sur-

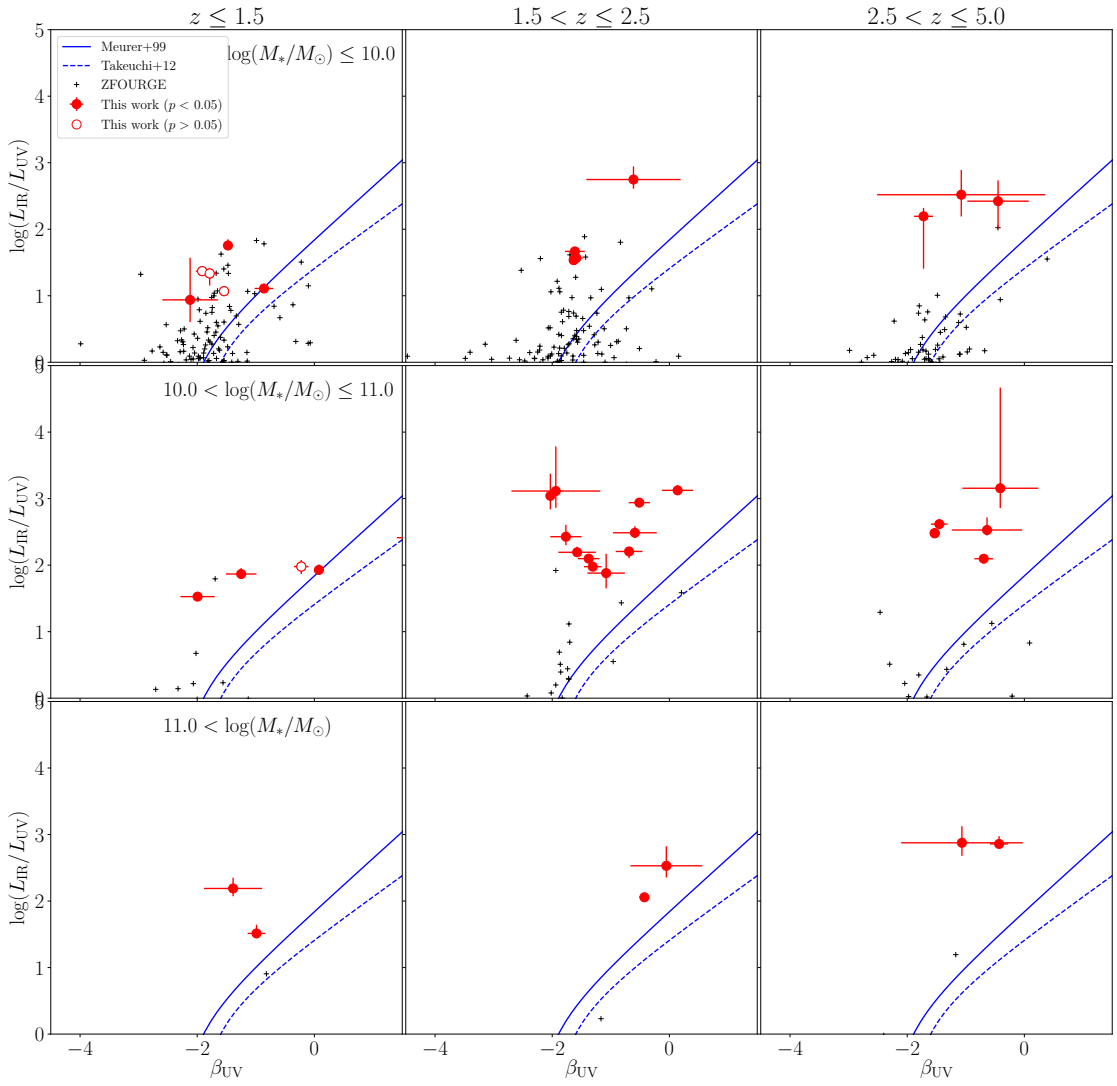

Figure 3.8 The IRX of the ASAGAO sources as a function of $\beta_{\rm UV}$ (red circles). Black crosses indicate ALMA non-detected ZFOURGE sources (Straatman et al., 2016) within the ASAGAO field. The blue solid and dashed lines are the IRX-$\beta_{\rm UV}$ relations of Meurer et al. (1999) and Takeuchi et al. (2012), respectively.

vey, Fujimoto et al. (2018) obtain an average rest-frame far-IR profile of ASAGAO sources and suggest that half-light radius at ALMA wavelength of ASAGAO sources tend to be smaller than that at optical wavelengths. This can be consistent with the hypothesis of Chen et al. (2017).

These results imply that the ALMA detected sources and non-detected sources have different dust properties, such as dust compositions or spatial distribution, even if they show similar properties on the M_*-SFR plane. Therefore, this implies the consensus stellar-mass versus IRX relation, which is known to be tight among rest-frame-UV-selected galaxies (i.e., LBGs), cannot fully predict the ALMA detectability of stellar-mass-selected galaxies. However, in this section, we only use spatially integrated ALMA continuum data. As shown in figures in Appendix A, some ASAGAO sources are more extended at near-IR wavelengths than at 1.2 mm. When we consider the spatial offsets between 1.2 mm detected regions and estimated UV luminosities of 1.2 mm detected regions like Chen et al. (2017), IRXs of these ASAGAO sources can be $\gtrsim$ 1 dex larger than we estimated in this section. Therefore, we discuss the effect of the difference in spattial distribution between dust and stars using the ASAGAO high-resolution map ($\simeq 0''.2$ resolution; see Section 2.1) in the next section.

3.5 The spatially resolved IRX–$\beta_{\rm UV}$ relation of ASAGAO sources

3.5.1 Motivation

Recent far-IR/(sub-)millimeter observations using *Herschel* or ALMA have suggested that dusty star-forming galaxies at $z \simeq$ 2–3 show the bluer IRX-$\beta_{\rm UV}$ relation than that of the local IRX-$\beta_{\rm UV}$ relation, and have large dispersion on the IRX-$\beta_{\rm UV}$ plane (e.g., Casey et al., 2014; Fudamoto et al., 2017). As shown in Figure 3.8, ASAGAO sources show similar properties on the IRX-$\beta_{\rm UV}$ plane. From a theoretical point of view, some theoretical/semi-analytical models (e.g., Safarzadeh et al., 2017; Popping et al., 2017; Narayanan et al., 2018) indicate that dust geometries (i.e., the difference of spatial distribution between stars and dust) can be responsible for the bluer IRX-$\beta_{\rm UV}$ relation as we mentioned in Section 3.4.2. Figure 3.9 is one of the results of simulations by Popping et al. (2017) and show how different physical properties

Table 3.4. ASAGAO sources with S/N > 4.5

ID (ZFOURGE) (1)	ID (ASAGAO) (2)	$S_{250k\lambda}$ (mJy) (3)	$S_{\rm untapered}$ (mJy) (4)	$r_{\rm IR}$ (5)	$r_{\rm UV}$ (6)	$\beta_{\rm UV}$ (7)
18658	1	0.985±0.036	0.877±0.032	0.886	0.013	−1.53±0.07
17856	2	1.973±0.075	1.996±0.057	1.007	0.049	0.14±0.27
13086	3	1.748±0.070	1.816±0.054	1.033	0.074	−0.43±0.16
18645	4	0.906±0.041	0.761±0.040	0.833	0.229	–
18701	5	0.735±0.039	0.634±0.035	0.851	0.039	−1.45±0.14
22177	6	0.922±0.074	0.735±0.043	0.770	0.000	−0.51±0.18
20298	7	0.778±0.086	0.593±0.065	0.715	0.003	–
19033	8	0.610±0.072	0.618±0.057	0.951	0.012	−0.43±0.09
21234	9	0.457±0.055	0.945±0.106	1.936	0.008	−0.61±0.80
18912	10	0.261±0.031	0.350±0.039	1.259	0.097	–
21730	11	0.635±0.078	0.587±0.051	0.866	0.122	–
16952	12	0.376±0.049	0.190±0.035	0.466	0.031	−0.59±0.37
17733	13	0.400±0.053	0.227±0.034	0.521	0.069	−2.03±0.02
18336	14	0.238±0.035	0.224±0.026	0.865	0.056	–
15702	15	0.416±0.064	0.166±0.032	0.362	0.018	−1.38±0.19
19487	16	0.488±0.065	0.106±0.022	0.197	0.033	−0.05±0.61
12438	18	0.975±0.172	0.353±0.094	0.324	0.000	–
14580	19	0.387±0.073	0.345±0.051	0.795	0.079	−0.69±0.16
22760	21	0.895±0.178	0.356±0.057	0.352	0.043	−1.77±0.27
18270	23	0.182±0.037	0.135±0.020	0.655	0.213	−0.64±0.60
14146	26	0.222±0.052	0.286±0.037	1.126	–	–
14419	29	0.197±0.046	0.551±0.084	2.427	0.144	−0.41±0.65
13714	31	0.733±0.158	–	–	0.032	−1.07±1.04
14122	33	0.318±0.079	0.283±0.042	0.773	0.120	–
14700	44	1.768±0.447	0.107±0.025	0.052	0.093	−1.94±0.76

Note. — (1) ZFOURGE ID. (2) ASAGAO ID. (3) Integrated flux density in the 250-kλ tapered map. (4) Integrated flux densities in the ASAGAO untapered map. (5) Flux ratios at 1.2 mm between 250-kλ tapered map and original ASAGAO map. (6) Rest-frame UV luminosity ratio between ALMA-detected dusty regions and spatially integrated lumionsities. (6) $\beta_{\rm UV}$ see also Table 3.3.

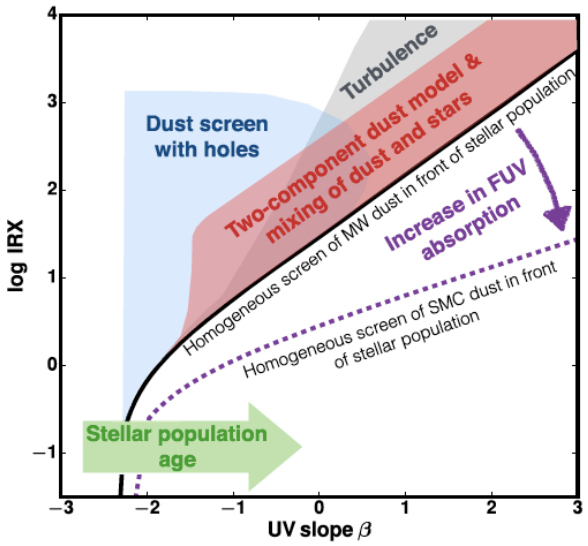

Figure 3.9 A schematic figure summarizing how different physical properties affect the IRX-$\beta_{\rm UV}$ relation (referred from Figure 11 in Popping et al., 2017).

of galaxies affect the IRX-$\beta_{\rm UV}$ relation.

In order to estimate an impact of dust geometries on the IRX-$\beta_{\rm UV}$ relation, high-angular-resolution observations by ALMA are useful. However, there are only a few studies focusing on the spatially resolved IRX-$\beta_{\rm UV}$ relation (e.g., Chen et al., 2017). Therefore, in this section, we estimate the impact of dust geometries on the IRX-$\beta_{\rm UV}$ relation (i.e., the difference between the IRX-$\beta_{\rm UV}$ relation at ALMA detected dusty region and ALMA non-detected less dusty regions) based on ASAGAO high-resolution data.

3.5.2 Methods

ASAGAO sources using this analysis

In this analysis, we use the untapered ASAGAO map with the synthesized beam size of $\simeq 0''.2$ (see Section 2.1.2) to make use of the high-resolution of ALMA. However, higher angular resolutions are realized at the expense of the surface brightness sensitivities. Therefore, we only focus on the ASAGAO

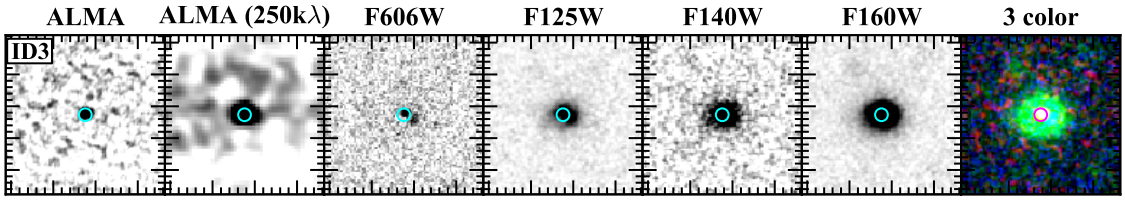

Figure 3.10 The multi-wavelength postage stamp of ASAGAO ID3. From left to right: ALMA 1.2 mm (untapered), ALMA 1.2 mm (250-kλ tapered), *HST*/*F606W*, *F125W*, *F140W*, *F160W*, and the 3 color image (R: untapered ASAGAO image, G: *HST*/*F160W*, B: *HST*/*F606W*), respectively ($5'' \times 5''$). The cyan and magenta circles indicate our $0''.4$ diameter aperture. We have to note that PSFs of *HST* images in this figure are not matched to the PSF of *F160W*.

sources with S/N $>$ 4.5 in the 250 kλ tapered image for this analysis. In Table 3.4, we show the ASAGAO sources which we use in this section. As shown in Table 3.4, some ASAGAO sources have much small flux errors in untapered ASAGAO map than 250 kλ tapered map, although this does not affect our following interpretations significantly. This can be originated our flux estimation. Here, we also include source fitting errors in addition to rms noise in the image (see, Hancock et al., 2012, 2018, for details). Details of our error estimation is explained in Hatsukade et al. (2018). Some ASAGAO sources have $r_{\rm IR} \simeq 2$ (ID9 and ID29), which can be caused by wrong source fitting in untapered ASAGAO map. Therefore, we remove these sources from our analysis.

HST photometry

We need high-resolution images at rest-frame UV wavelengths to estimate the rest-frame UV flux densities emitted from ALMA detected dusty regions. Therefore, we use *HST*/ACS/*F606W*, *F435W*, *F775W*, *F814W*, WFC3/*F125W*, *F140W*, and *F160W* images. The point spread function (PSF) of these images are matched to the WFC3/*F160W* image whose PSF has the FWHM of $\simeq 0''.16$ to account for the PSF deference between images. This resolution is comparable with that of the ASAGAO non-tapered image. We used the Image Reduction and Analysis Facility (IRAF; Tody, 1993) to measure the flux densities emitted from ALMA detected dusty regions. We performed the *HST* photometry with a $0''.4$ diameter aperture at the ALMA detected positions using the IRAF task APPHOT. Figure 3.10 shows a the

ASAGAO and the *HST* images of one of the ASAGAO sources (ID3). We defined flux densities within the cyan circle, shown in Figure 3.10, as flux densities at *HST* wavelengths emitted from ALMA detected dusty regions.

Estimation of UV and IR luminosities at ALMA detected dusty regions

In order to estimate UV luminosities at ALMA detected dusty regions, we first performed the SED fitting by EAZY using *HST* photometries to estimate flux densities at rest-frame 2800 Å at ALMA detected dusty regions. For ZFOURGE sources, Straatman et al. (2016) estimated spatially integrated flux densities at rest-frame 2800 Å by their SED fitting using EAZY. Therefore, we then calculate the ratios between rest-frame 2800 Å luminosities densities at ALMA detected dusty regions and spatially integrated ones. Finally, we multiply these luminosity ratios to spatially integrated UV luminosities calculated in Section 3.2.2 (see also Table 3.3). Here, we define these values as the UV luminosities at ALMA detected dusty regions.

In the case of IR luminosities, we calculate the ratio between ALMA 1.2 mm flux densities in the untapered ASAGAO map and that of the 250-kλ tapered ASAGAO map (see Table 3.1 and Table 3.4). As is the case with UV luminosities, we multiply these flux ratios and spatially integrated IR luminosities (Section 3.2.2 and Table 3.3) to get the IR luminosities at ALMA detected dusty regions. In case that a flux ratio is larger than unity, we treat it as unity.

3.5.3 Results & discussions

In Figure 3.11, we plot the spatially integrated IRX-$\beta_{\rm UV}$ relation of ASAGAO sources with S/N $>$ 4.5 (Left) and the spatially resolved IRX-$\beta_{\rm UV}$ relation (right). In this analysis, we use the same $\beta_{\rm UV}$ values as we obtained in Section 3.4.2 for both ALMA detected dusty regions and non-detected less dusty regions learned from Chen et al. (2017). Due to the lack of photometry points at *HST* bands, it is difficult to estimate the spatially resolved $\beta_{\rm UV}$. If we were able to estimate the spatially resolved $\beta_{\rm UV}$ values, ALMA detected regions could have larger (i.e., redder) $\beta_{\rm UV}$ values and ALMA non-detected less dusty regions could have smaller (i.e., bluer) $\beta_{\rm UV}$ values. The left panel of Figure 3.11 suggests that

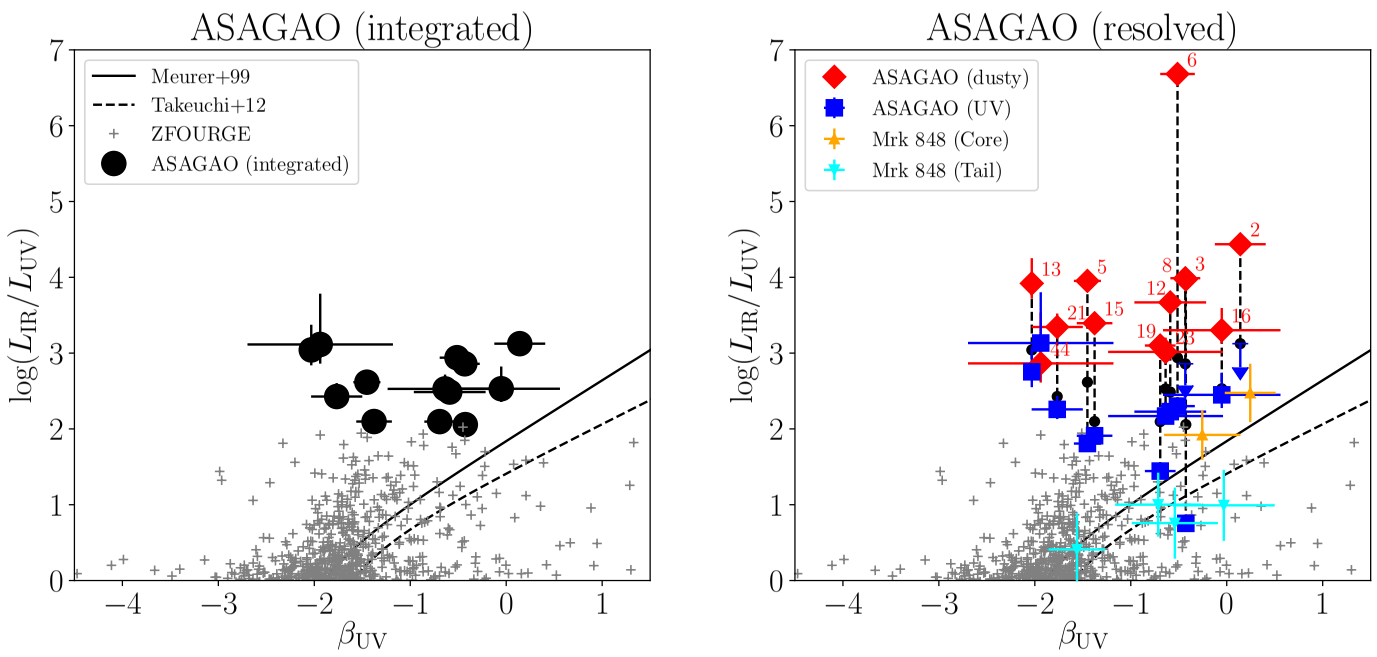

Figure 3.11 *Left)* The spatially integrated IRX-$\beta_{\rm UV}$ relation of ASAGAO sources (black circles). *Right)* The spatially resolved IRX-$\beta_{\rm UV}$ relation of ASAGAO sources. Red diamonds and blue squares indicate ALMA detected dusty regions and ALMA non-detected less dusty regions, respectively. Black circles are the spatially integrated IRX-$\beta_{\rm UV}$ relation of ASAGAO sources. Orange triangles and cyan inverse-triangles indicate merging core and tail of the local merging galaxy Mrk 848 (Yuan et al., 2018) for comparison. The black solid line and dashed line indicates the IRX-$\beta_{\rm UV}$ relation obtained by Meurer et al. (1999) and Takeuchi et al. (2012), respectively. Gray crosses are ALMA non-detected ZFOURGE sources within the ASAGAO field (Straatman et al., 2016).

the spatially integrated IRX-$\beta_{\rm UV}$ relation of ASAGAO sources are bluer than that of the local relation as mentioned in previous studies (e.g., Casey et al., 2014; Fudamoto et al., 2017)[9]. On the other hand, the right panel of Figure 3.11 implies that IRXs of ALMA detected dusty regions are $\gtrsim$ 1-dex larger than that of ALMA non-detected less dusty regions. The IRX-$\beta_{\rm UV}$ relation of ALMA non-detected less dusty region seem to be close to that of the local relation and ALMA non-detected ZFOURGE sources (the right panel of Figure 3.11). These results indicate that the different distribution between dust and stars is partly responsible for the bluer IRX-$\beta_{\rm UV}$ relation and large dispersions of high redshift dusty star-forming galaxies. Similar results are also shown by the the spatial resolved observation toward the local merging galaxy, Mrk 848 (Yuan et al., 2018) in the right panel of Figure 3.11. Yuan et al. (2018) suggest that the IR bright core regions of Mrk 848 show the bluer IRX-$\beta_{\rm UV}$ relation than that of tail regions of Mrk 848.

We have to note that differences between the IRX-$\beta_{\rm UV}$ relations of high redshift dusty star-forming galaxies and the local relation cannot be explained only by the different distribution between dust and stars. As shown in Figure 3.11, ALMA non-detected regions of some ASAGAO sources still show the bluer IRX-$\beta_{\rm UV}$ relation. In addition, the ALMA non-detected ZFOURGE sources also have large dispassion. Therefore, other dust properties also can affect the IRX-$\beta_{\rm UV}$ relation of galaxies. The bluer IRX-$\beta_{\rm UV}$ relation of these sources can be caused by their other dust properties except for dust distributions. For example, dust temperature can also affect IRX values of duty sources (e.g., Faisst et al., 2017; Narayanan et al., 2018). If we assume a maximally warm IR SED, the IR luminosity increase more than 0.6 dex (Faisst et al., 2017). In Figure 3.12, we plot dust temperatures of ASAGAO sources with S/N $>$ 4.5 as a function of their IR luminosities. As a comparison, we also show JCMT/SCUBA2 sources obtained by Zavala et al. (2018). As shown in Figure 3.12, their dust temperatures roughly follow the well-known temperature-luminosity relation found in previous studies (e.g., Chapman et al., 2005; Swinbank et al., 2014). Dust temperatures of ASAGAO sources are consistent with the results of Zavala et al. (2018) in the similar redshift and IR luminosity range. Therefore, they do not show the extremely high dust temperature as suggested by Faisst et al. (2017), and the effect of dust temperature to the IRX-$\beta_{\rm UV}$ relation seems not to be significant at least as for ASAGAO sources. However, we have to note that dust temperatures in Figure

[9]Note that they estimate the spatially integrated IRX-$\beta_{\rm UV}$ relation.

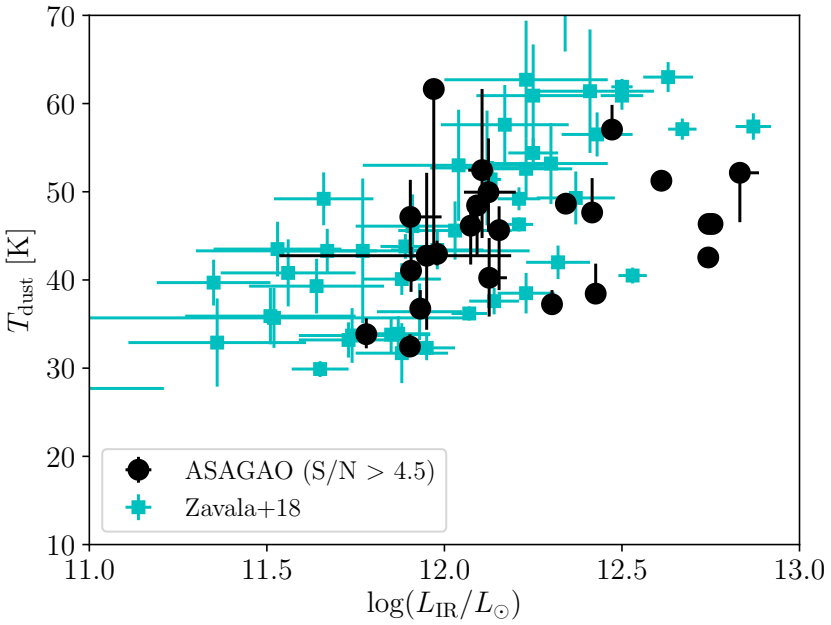

Figure 3.12 Dust temperatures versus IR luminosities. ASAGAO sources with ALMA S/N > 4.5 are plotted as black circles. Cyan squares indicate JCMT/SCUBA2-detected sources at $1 < z < 3$ (Zavala et al., 2018).

3.12 are spatially averaged values. To estimate the effect of dust temperatures to IRX-$\beta_{\rm UV}$ accurately, we have to calculate dust temperature of "ALMA detected regions" instead of spatially averaged dust temperature. After all, additional observations, such as higher-resolution or spectroscopic observations, are necessary to settle this issue.

3.6 Contributions of ASAGAO sources to the cosmic SFRD

In this section, we again focus on 66 ASAGAO sources (Table 3.1 and Table 3.3) and discuss their contribution to the cosmic SFRD. Because of the high sensitivity and high angular resolution of ALMA, we can resolve the contribution of dusty star-forming sources to the cosmic SFRD down to $\log(L_{\rm IR}/L_\odot) \sim 11$, which is $\sim$ 0.5–1 dex lower luminosity range than previous *Herschel* observations at $z \gtrsim 2$ (e.g.,

Gruppioni et al., 2013).

We estimate the contribution of the ASAGAO sources with the *K*-band counterparts to the cosmic SFRD. In Figure 3.13, we plot their contribution as a function of redshift. Here, we simply sum up the SFRs of the ASAGAO sources with the *K*-band counterparts and divide them by the co-moving volumes. Note that we can estimate their contribution to the cosmic SFRD by resolving individual sources instead of integrating luminosity functions whose faint-end slopes are fixed to the local values even in high redshift cases (e.g., Burgarella et al., 2013). This is one of the strong points using the high sensitivity and high angular resolution ALMA map by ASAGAO. Although we do not consider the completeness and false-detection rate here, our results are consistent with the results by Hatsukade et al. (2018). They estimate the cosmic SFRD by integrating the IR luminosity functions obtained by ASAGAO including completeness and false-detection rate.

As a comparison, we plot the recent parametric descriptions of the redshift evolution of the cosmic SFRD obtained by Madau & Dickinson (2014). Their results are based on the previous observations at UV-to-IR wavelengths. We also show the evolution of the cosmic SFRD at $z = 0$–3.5 derived by Burgarella et al. (2013). They use UV and IR luminosity functions estimated by VIMOS-VLT Deep Survey (VVDS; Le Fèvre et al., 2005), *Herschel*/PEP (Lutz et al., 2011; Magnelli et al., 2013), and HerMES (Oliver et al., 2012) to estimate the cosmic SFRD. At $z = 3.8$ and 4.9, we plot results of Bouwens et al. (2015). They assume UV luminosity functions estimated by *HST* data and dust correction based on the IRX-$\beta_{\rm UV}$ relation of Meurer et al. (1999). We also plot results of Rowan-Robinson et al. (2016), which are based on *Herschel*-SPIRE 500 μm sources. We also show the results of the JCMT/SCUBA2 large survey by Cowie et al. (2017), the contribution of bright ALESS sources by Swinbank et al. (2014), and the results from ALMA continuum surveys estimated by Dunlop et al. (2017).

As shown in Figure 3.13, the shape of the contribution of the cosmic SFRD from the ASAGAO sources is similar to that of the previous observations; it has a peak level at $z \sim 2$–3, and then it declines toward $z = 0$, although Rowan-Robinson et al. (2016) claimed almost constant SFRD at $z = 1$–5. Figure 3.13 shows that our results are $\sim$ 1-dex smaller than the cosmic IR SFRD obtained by Burgarella et al. (2013) at $z < 2$. The contribution of ASAGAO sources is only $\sim$ 5–30% of the cosmic IR SFRD by

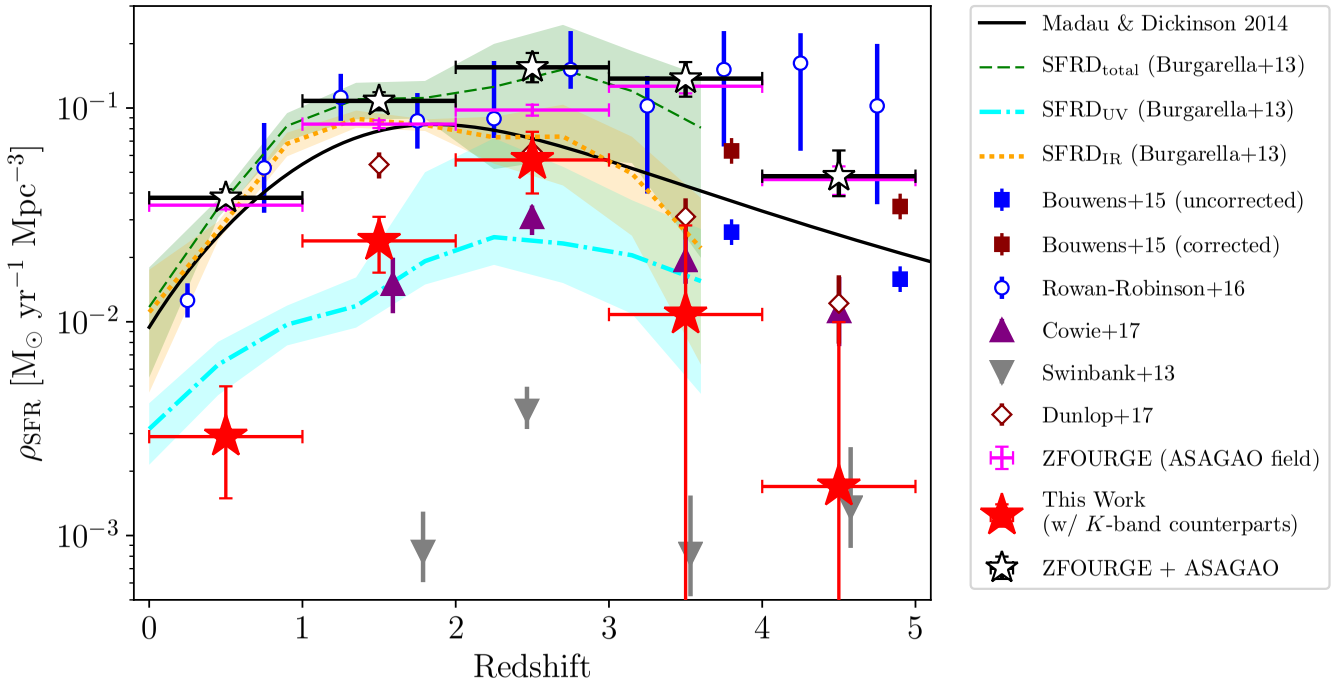

Figure 3.13 Contribution of ASAGAO sources to the cosmic SFRD as a function of redshift. Red, magenta, and black symbols are the contributions of ASAGAO sources with *K*-band counterparts, ALMA non-detected ZFOURGE sources within ASAGAO field, and their sum, respectively. We adopt simple Poisson errors and SFR-errors attributed to redshift uncertainties. The black solid line indicate the recent results of the redshift evolution of the cosmic SFRD obtained by Madau & Dickinson (2014). The green dashed line, cyan dot-dashed line, and orange dotted line show the total (i.e., UV + IR) SFRD, UV SFRD, and IR SFRD obtained by Burgarella et al. (2013). Blue and brown squares are dust-uncorrected and -corrected SFRD obtained by Bouwens et al. (2015). Blue open circles are results of Rowan-Robinson et al. (2016). Purple triangles indicate the cosmic SFRD obtained by the SCUBA2 large survey (Cowie et al., 2017). Gray inverse-triangles are the contribution of bright ALESS sources (Swinbank et al., 2014). Brown open diamonds indicate the contribution of the ALMA sources obtained by Dunlop et al. (2017). We note that these results are converted to the Chabrier IMF.

Burgarella et al. (2013) at $z \simeq 0$–2. At these redshifts, galaxies with $\log(L_{\rm IR}/L_{\odot}) \lesssim 9$–10 (i.e., fainter population than our ALMA detection limit) seems to be the main contributors to the cosmic IR SFRD. On the other hand, our results are consistent with the cosmic IR SFRD by Burgarella et al. (2013) at $z \simeq 2$–3 as shown in Figure 3.13. The contribution of ASAGAO sources reaches $\sim 60\%$ of the cosmic UV + IR SFRD and $\sim 80\%$ of the cosmic IR SFRD obtained by Burgarella et al. (2013). This implies that the ASAGAO sources are the main contributors to the cosmic IR SFRD at $z \simeq 2$–3. This can be a consequence of the evolution of the characteristic luminosities ($L^{*}_{\rm IR}$) of IR luminosity functions (i.e., at high redshift, $L^{*}_{\rm IR}$ becomes higher; Hatsukade et al. 2018). Although we have to concern about the completeness and large errors, the contributions of ASAGAO sources to the cosmic SFRD at $z \gtrsim 3$ can be consistent with, or greater than that of bright ALESS sources ($\gtrsim 10\%$ of previous studies; e.g., Madau & Dickinson 2014). We also have to note that the *K*-band completeness drops significantly at the high redshift. This seems to be one of the reasons why the contributions of ASAGAO sources to the cosmic SFRD drops significantly comparing to constraints obtained by Madau & Dickinson (2014) at $z \gtrsim 3$.

3.7 Conclusions of millimeter properties of *K*-selected galaxies

In this chapter, we report results of multi-wavelength analysis of ALMA 1.2-mm detected ZFOURGE sources using ASAGAO data to study millimeter properties of *K*-band selected galaxies. We find that 66 ZFOURGE sources have ALMA counterparts with ALMA S/N > 3.5 (ASAGAO sources). Their flux densities at 1.2 mm tend to be fainter than that of "classical" SMGs ($S_{1.2\ \rm mm} \lesssim 1$ mJy). The estimated median redshift of ASAGAO sources is $z_{\rm median} = 1.77 \pm 0.23$. This value is consistent with that of faint SMGs with $S_{\rm obs} \lesssim 1.0$ mJy, although this value us lower than that of "classical" SMGs, whose median redshift is estimated to be $z_{\rm median} \simeq 2.1$–3.1. This difference can be caused by the redshift revolution of the IR luminosity function, although we have to note that this also can be caused by selection effect (completeness of *K*-selected galaxies drop significantly at high redshift).

We estimate physical parameters of ASAGAO sources by the SED fitting from optical to millimeter wavelengths using MAGPHYS. Their stellar masses and SFRs suggest that they mainly line on the high-

mass end of the main sequence of star-forming galaxies, although $\sim$ 10% of ASAGAO sources show starburst-like features on the M_*-SFR plane. On the other hand, the IRX-M_*, IRX-SFR, and IRX-$\beta_{\rm UV}$ relations of ASAGAO sources may imply that ALMA detected sources and non-detected sources have different dust properties (i.e., dust compositions of dust distributions) even if they show similar properties on the M_*-SFR plane. Therefore, the consensus M_* versus IRX relation, which is known to be tight among UV-selected galaxies, cannot fully predict the ALMA detectability of stellar-mass-selected galaxies.

Using untapered ASAGAO map with $\simeq 0''.2$ resolution, we obtain the spatially resolved IRX-$\beta_{\rm UV}$ relation of ASAGAO sources with ALMA S/N > 4.5. Our results indicate that IRX values of ALMA detected dusty regions tend to be $\gtrsim$ 1-dex larger than that of ALMA non-detected less-dusty regions and the IRX-$\beta_{\rm UV}$ relation of ALMA non-detected less dusty regions is close to the local relation. Therefore, the different distribution between dust and stars is at least partly responsible for the bluer IRX-$\beta_{\rm UV}$ relation and large dispersions of high redshift dusty star-forming galaxies.

We resolve the contribution of dusty star-forming sources to the cosmic SFRD down to $\log(L_{\rm IR}/L_\odot)$ $\sim$ 11, because of the high sensitivity and angular resolution of ALMA. Here, we can estimate their contribution to the cosmic SFRD by resolving individual sources instead of integrating luminosity functions whose faint-end slopes are fixed to the local values even in high redshift cases. We find that the ASAGAO sources with K-band counterparts are main contributors to the cosmic SFRD at $z \simeq$ 2–3 ($\sim$ 60% of the cosmic UV + IR SFRD and $\sim$ 80% of the cosmic IR SFRD), and their contributions are $\sim$ 1 dex smaller than that of previous studies at $z < 2$ (only $\sim$ 5–30% of the cosmic IR SFRD). Although we have to concern about the completeness and large errors, the contributions of ASAGAO sources to the cosmic SFRD ($\gtrsim$ 10% of previous studies) can be consistent with, or greater than that of bright ALESS sources at $z \gtrsim 3$.

4

Near-infrared-dark millimeter sources

In this chapter, we report detections of 1.2 mm continuum sources without any counterparts in the deep *H*- and/or *K*-band image (i.e., *K*-band magnitude $\gtrsim$ 26 mag), which are detected by ASAGAO. Here, we adopt the S/N threshold of 5.0 to avoid spurious sources, because we have to treat sources which are purely selected by ALMA without using multi-wavelength information.

4.1 Identifications of near-IR-dark ASAGAO sources

We examined 25 secure ALMA sources with S/N $>$ 5 in the 26 arcmin^2 map of the ASAGAO (Section 2.1.3 and Figure 2.3, see also Hatsukade et al., 2018). As we discussed in Section 3.1, 20 of 25 ASAGAO sources candidates have been listed in *K*-band selected counterpart in the ZFOURGE catalog (Straatman et al., 2016). However, we still have 5 sources without ZFOURGE counterparts with S/N $>$ 5.0, which are

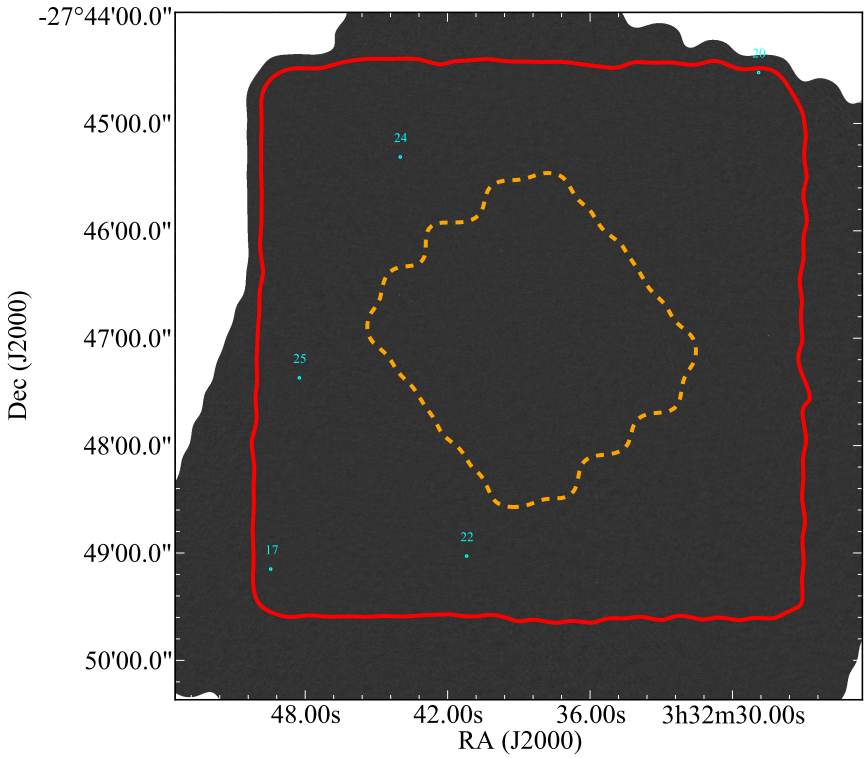

Figure 4.1 *K*-dropout ASAGAO sources positions. The cyan symbols indicate the position of 5 *K*-dropout ASAGAO sources. The red enclosed region indicate the observed area by ASAGAO. The orange enclosed region indicates observed area by Dunlop et al. (2017). See also Figure 3.1.

undetected in *K*-band. We summarize the ASAGAO sources without ZFOURGE counterparts (hereafter, *K*-dropout ASAGAO sources) in Table 4.1 and show the positions of *K*-dropout ASAGAO sources in Figure 4.1. The multi-wavelength postage stamps of these 5 *K*-dropout ASAGAO sources are presented in Figure 4.2.

We check the reliability of *K*-dropout ASAGAO sources using two independent methods. First, we apply the same source finding algorithm to the negative map in order to estimate the degree of contamination by spurious sources. The number of negative sources is 1 with S/N $>$ 5.0 to be compared with the 25 positive sources with S/N $>$ 5.0. This means that the spurious source rate, which is defined as the ratio of negative to positive source numbers, is small (0.04) in the range of S/N $>$ 5.0 (see Figure

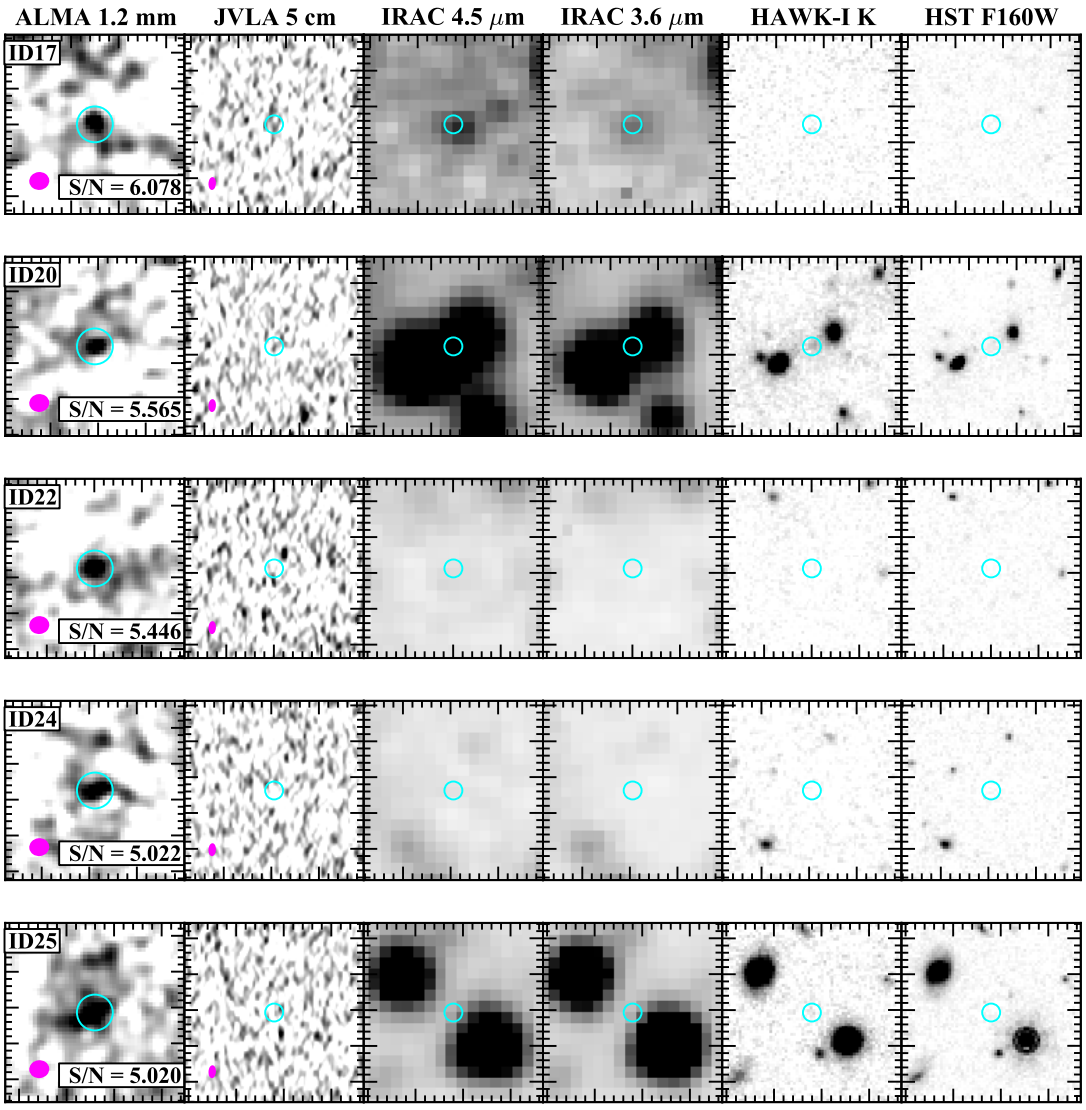

Figure 4.2 Multi-wavelength images of ASAGAO sources without *K*-band counterparts. From left to right: ALMA 1.2 mm ($5'' \times 5''$), JVLA 5 cm, *Spitzer* IRAC/4.5 μm, IRAC/3.6 μm, VLT HAWK-I/K_s, and HST WFC3/$F160W$ images ($10'' \times 10''$). Cyan circles are $1''$ apertures. The inserted S/N values are those of ALMA data. The magenta symbol is the synthesized beam of ALMA and JVLA.

Table 4.1. *K*-dropout ASAGAO sources

ID (ASAGAO) (1)	R.A. (deg.) (2)	Dec. (deg.) (3)	$S_{\rm ALMA}$ (mJy) (4)	$\rm S/N_{peak}$ (5)	$z_{\rm radio/mm}$ (6)
17	53.206042	−27.819166	0.564 ± 0.090	6.078	> 4.14
20	53.120445	−27.742093	0.614 ± 0.109	5.565	> 4.39
22	53.171662	−27.817153	0.612 ± 0.101	5.446	> 4.26
24	53.183284	−27.755207	0.446 ± 0.082	5.022	> 3.70
25	53.201002	−27.789483	0.858 ± 0.223	5.020	> 4.93

Note. — (1) ASAGAO ID. (2) Right ascension (J2000). (3) Declination (J2000). (4) Spatial integrated flux density (de-boosted). (5) Peak S/N. (6) The lower limit of photometric redshifts estimated by the flux ratios between radio and millimeter wavelengths. Here, we assume the average SED of ALESS sources with $A_{\rm V} > 3.0$ (see Section 4.3.1).

2.3). The semi-analytical model by Casey et al. (2018) also suggests that the contamination rate is small in the range of S/N $>$ 5.0. Second, we split the ASAGAO visibilities into two polarization components (i.e., XX and YY polarization images) and create two XX and YY images, which are purely independent. With these two images, we find that all 5 sources are detected with S/N $\sim$ 3–5 in both XX and YY. This is the behavior expected for $> 5\sigma$ detections. Therefore, it is likely that almost all sources with S/N $>$ 5.0 can be real detections even though they have no counterparts in the ZFOURGE catalog.

4.2 Multi-wavelength pictures of *K*-dropout ASAGAO sources

In this section, we describe multi-wavelength pictures of *K*-dropout ASAGAO sources individually:

– *ID17*: This object is detected at 3.6 and 4.5 μm bands of *Spitzer*/IRAC by the *Spitzer*-Cosmic Assembly Deep Bear infrared Extragalactic Legacy Survey (S-CANDELS; PI G.Fazio; Ashby et al., 2015, see Figure 4.2). Its apparent magnitudes at 3.6 μm and 4.5 μm are 25.38 ± 0.30 and 25.00 ± 0.27 mag (Ashby et al., 2015).

– *ID20*: This object is detected at JCMT/SCUBA2 and ALMA Band 7 (Cowie et al., 2018). The observed flux density is 1.35 ± 0.24 mJy at 870 μm (Cowie et al., 2018).

– *ID22, ID24, and ID25*: Theses objects are not detected at any wavelengths except for 1.2 mm.

All sources are not detected at the JVLA 6 GHz (5 cm).

4.3 Physical properties of *K*-dropout ASAGAO sources

4.3.1 Estimation of redshifts

The extremely red colors of *K*-dropout ASAGAO sources can be reproduced by the high-redshift sources of highly-reddened low-redshift cases. In this section, we use the shape of optical-to-radio SEDs of galaxies as important clues to estimate their redshifts. In Figure 4.3, We plot optical to radio SEDs of these *K*-dropout ASAGAO sources. As a comparison, we also show the average SED of ALESS sources with visual extinction ($A_{\rm V}$) > 3.0 (the reddest case; hereafter we call this SED as the average SED of ALESS SMGs) obtained by da Cunha et al. (2015). Even with the highly-reddened SED, upper limits at the *Spitzer*/IRAC wavelengths suggest that all *K*-dropout ASAGAO sources can lie at $z \gtrsim 3$–5 (Figure 4.3).

The fact that all *K*-dropout ASAGAO sources are not detected by the JVLA C band (5 cm) deep observation ($\sigma \simeq 0.35$ μJy beam^{-1}; Rujopakarn et al. in preparation) can help to estimate their redshift. As shown in Figure 1.2 flux densities at radio wavelengths of a galaxy decrease significantly as a function of redshift. This effect is called the positive *k*-correction against the negative *k*-correction at (sub-)millimeter wavelengths. Therefore, the flux ratio between radio and (sub-)millimeter wavelengths can be an indicator of redshift (e.g., Carilli & Yun, 1999; Dunne et al., 2000; Rengarajan & Takeuchi, 2001). Although precision accuracy of the indicator is dependent on the intrinsic variation in SED types for the given galaxy populations, indicator is useful to roughly estimate redshifts of sources without any optical/near-IR information.

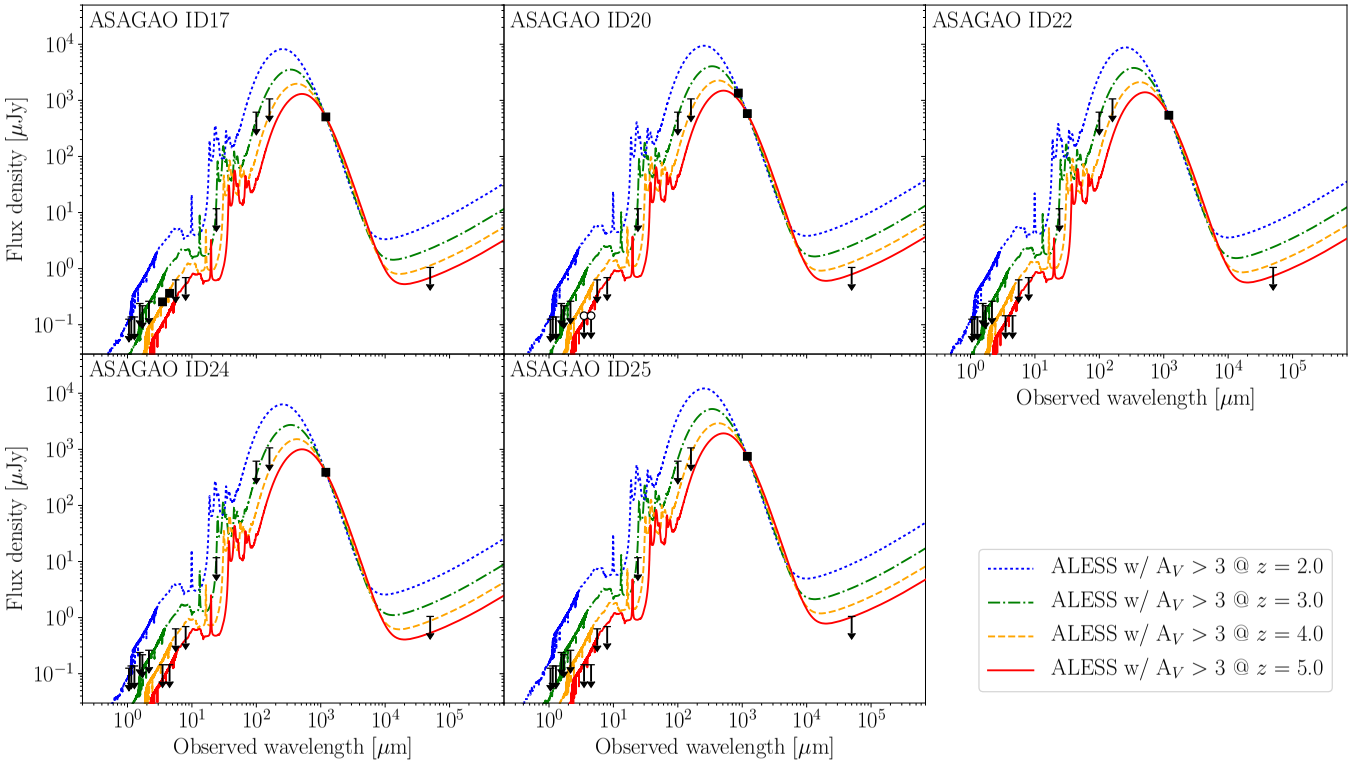

Figure 4.3 Optical-to-radio SEDs of ASAGAO sources without *K*-band counterparts. Black arrow indicate 3σ upper limits. From optical to far-IR upper limits except for IRAC 5.6 and 8.0 μm are listed in Straatman et al. (2016). The upper limits at IRAC 5.6 and 8.0 μm are presented in Dickinson et al. (2003). The radio image at 5 cm is obtained by JVLA (Rujopakarn et al. in preparation). For ID20, we also plot its ALMA Band 7 flux density. We have to note that we should not refer upper limits at *Spitzer*/IRAC bands of ID20 (white open circles with upper limits) because of the contamination from nearby sources (Figure 4.2). The blue dotted line, green dot-dashed line, orange dashed line, and red solid line indicate the average SED of ALESS sources with $A_V > 3.0$ at $z = 2$, 3, 4, and 5, respectively (da Cunha et al., 2015). Note that these SEDs are scaled to their observed flux densities at ALMA wavelength.

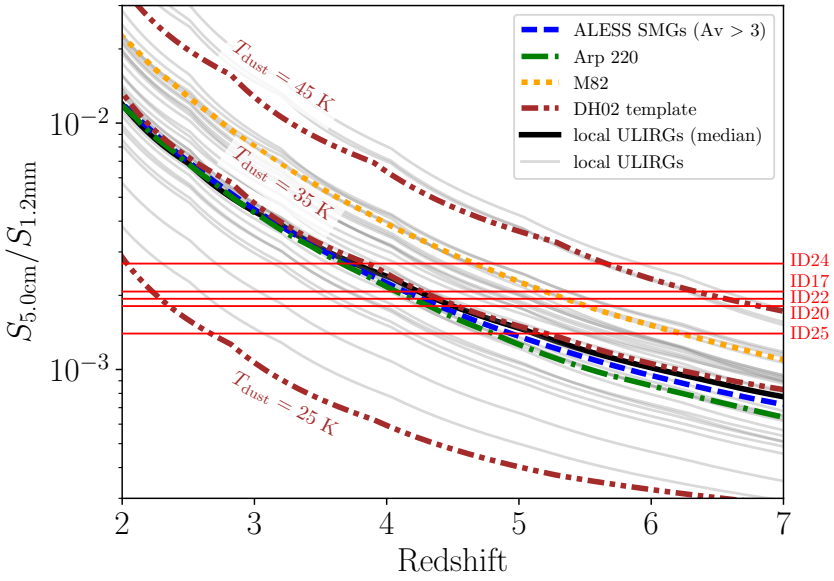

Figure 4.4 The redshift dependence of $S_{5\rm cm}/S_{1.2\rm mm}$ flux ratios. The blue dashed line, green dot-dashed line, and orange dotted line indicates the average SED of ALESS sources with $A_{\rm V} > 3.0$ (da Cunha et al., 2015), Arp 220, and M82 (Silva et al., 1998), respectively. Gray solid lines are local ULIRGs compiled by Vega et al. (2008) and the black solid line is the median of these ULIRGs. Brown chain double dashed line is SED templates of Dale & Helou (2002) with dust temperature, $T_{\rm dust}$ = 25, 35, and 45 K. Horizontal red lines are the upper limit of $S_{5\rm cm}/S_{1.2\rm mm}$ flux ratios of ASAGAO *K*-dropout sources.

In Figure 4.4, we show the redshift dependence of the flux ratio between radio and millimeter wavelengths ($S_{5\rm cm}/S_{1.2\rm mm}$). Considering the intrinsic variation in SED types, we show the redshift dependence of the flux ratio of Arp 220, M81 (Silva et al., 1998), local ULIRGs (Vega et al., 2008), and mid-IR-to-radio SED templates with dust temperature ($T_{\rm dust}$) = 25, 35, and 45 K (Dale & Helou, 2002)[1], in addition to the average SED of ALESS SMGs (da Cunha et al., 2015). When we compare the upper limits of the flux ratio of *K*-dropout ASAGAO sources with these redshift dependence in Figure 4.4, the estimated redshift of *K*-dropout ASAGAO sources are $z \gtrsim$ 3–5. In Table 4.1, we show the estimated lower limits of

[1]The SED templates are based on the observations of local star-forming galaxies by *ISO* and *IRAS* and have been used for dusty star-forming galaxies detected by such as *Herschel* (e.g., Chapman et al., 2010; Magnelli et al., 2014). Dale & Helou (2002) express the SED dispersion by $T_{\rm dust}$ as the parameter α which is defined as $dM_{\rm dust}(U) \propto U^{-\alpha}dU$. Here, $dM_{\rm dust}(U)$ is the dust mass heated by a radiation field at intensity U. The relation between α and $T_{\rm dust}$ is obtained by Magnelli et al. (2014).

photometric redshifts when we assume the average SED of ALESS SMGs. Daddi et al. (2009) and Wang et al. (2009) report that one extremely red bright SMG, GN10 (also known as GOODS850-5), lie at $z \gtrsim 4$. This can imply that K-dropout ASAGAO source are scaled-down version of GN10 if they lie at $z \sim 4$. However, as shown in Figure 4.4 a low redshift case (i.e., $z \lesssim 2$–3) is also possible if dust temperature of these galaxies are low ($T_{\rm dust} \lesssim 25$ K).

4.3.2 Estimation of stellar masses and star formation properties

We estimate stellar masses of K-dropout ASAGAO sources assuming a mass-to-light ratio obtained at the rest-frame H-band as done in previous works (e.g., Hainline et al., 2011; Wardlow et al., 2011; Simpson et al., 2014; Yamaguchi et al., 2016). There are some benefits to use rest-frame H-band luminosities instead of rest-frame K-band luminosities, which has been used in previous works (e.g., Borys et al., 2005; Michalowski et al., 2011). In addition to the fact that the cooler low-mass stars dominating the stellar mass of a galaxy emit most of their light at red optical and near-IR wavelengths, the rest-frame H-band is less sensitive to dust extinction than rest-frame optical bands and is less affected by thermally pulsating asymptotic giant branch stars than the rest-frame K-band (Hainline et al., 2011; Henriques et al., 2011). Hainline et al. (2011) estimate the mass-to-light ratio of SMGs assuming the SED template of Bruzual & Charlot (2003) with the Chabrier IMF and find that $M_*/L_H = 0.17$ and 0.13 $M_\odot\ L_\odot^{-1}$ for constant and single-burst star formation histories, respectively (L_H is the rest-frame H-band luminosity without extinction correction). Here, we adopted the average value $M_*/L_H = 0.15\ M_\odot\ L_\odot^{-1}$ of these two extreme cases. Therefore, the stellar masses of K-dropout ASAGAO sources are calculated as follows;

$$M_*/M_\odot = 10^{-0.4(M_H - 4.71)} \times 0.15, \tag{4.1}$$

where M_H is absolute AB magnitude at rest-frame H-band.

In the high-redshift case, the 3σ upper limits of stellar masses of K-dropout ASAGOA sources are estimated to be $\log(M_*/M_\odot) \lesssim 10.4$ using *Spitzer*/IRAC 8.0 μm data (3σ limiting magnitude of 24.3 mag; Dickinson et al., 2003) if they lie at $z \sim 4$. We also estimate their IR luminosities by integrating the SEDs

presented in Figure 4.3 and find that $\log(L_{\rm IR}/L_\odot) \sim 12.0$ which correspond to $\log[{\rm SFR}/({\rm M}_\odot\ {\rm yr}^{-1})] \sim 2$. These results indicate that they are on the main-sequence of star-forming galaxies at high redshift and can represent the early phase of formation of massive galaxies, which are difficult to be observed using rest-frame UV selected galaxies such as LAEs or LBGs as discussed in Wang T. et al. (2016).

In the low-redshift case, on the other hand, the estimated stellar mass of ID17 is $\log(M_*/M_\odot) \simeq 9.4$ using *Spitzer*/IRAC 4.5 μm data. According to Straatman et al. (2016), a completeness limit of the ZFOURGE survey is $\log(M_*/M_\odot) \simeq 9.0$ at $z = 2$, which implies that ID17 prefers the high-redshift case rather than the low-redshift case. For other 4 *K*-dropout ASAGAO sources, their 3σ upper limits of stellar masses are estimated to be $\log(M_*/M_\odot) \lesssim 8.8$ when we consider the 3σ limiting magnitude of S-CANDELS (26.5 mag)[2]. These upper limits are consistent with their non-detections at *K*-band. Thus, we cannot exclude the low-redshift case for these 4 *K*-dropout ASAGAO sources. If they lie at $z \sim 2$, their IR luminosities are estimated to be $\log(L_{\rm IR}/L_\odot) \sim 11.6$ when we assume the SED template of Dale & Helou (2002) with $T_{\rm dust} = 25$ K. Therefore, in this case, they seem to be extremely low-mass starburst galaxies, which have been missed in previous deep surveys at optical/near-IR wavelengths.

4.4 Contributions to the cosmic SFRD

In the case that we detect ALMA sources with $S_{1.2{\rm mm}} \simeq 0.5$–1 mJy and search for *K*-band counterparts using a deep (i.e., 5σ limiting magnitude of $K_s \simeq 26$ mag) image, the estimated surface density of *K*-band drop sources is $\simeq 0.2$ arcmin^{-2}. Although it is difficult to study these objects without multi-wavelength information, we will discuss their impact to the cosmic SFRD at high redshift in this section.

Many previous studies predict that the contribution of dust-obscured star-forming activities to the cosmic SFRD have a peak level at $z \simeq 2$–3 and decline toward $z \gtrsim 3$–4 based on, for example, IR luminosity functions obtained by *Herschel* (e.g., Burgarella et al., 2013) or dust attenuation-corrected ultraviolet (UV) observations (e.g., Bouwens et al., 2015). On the other hand, Rowan-Robinson et al. (2016) predict that the contribution seems to be constant at $z = 1$–5 based on the integrated SFR functions

[2]For ID20, it is difficult to use *Spitzer*/IRAC photometries because of heavy confusions (Figure 4.2)

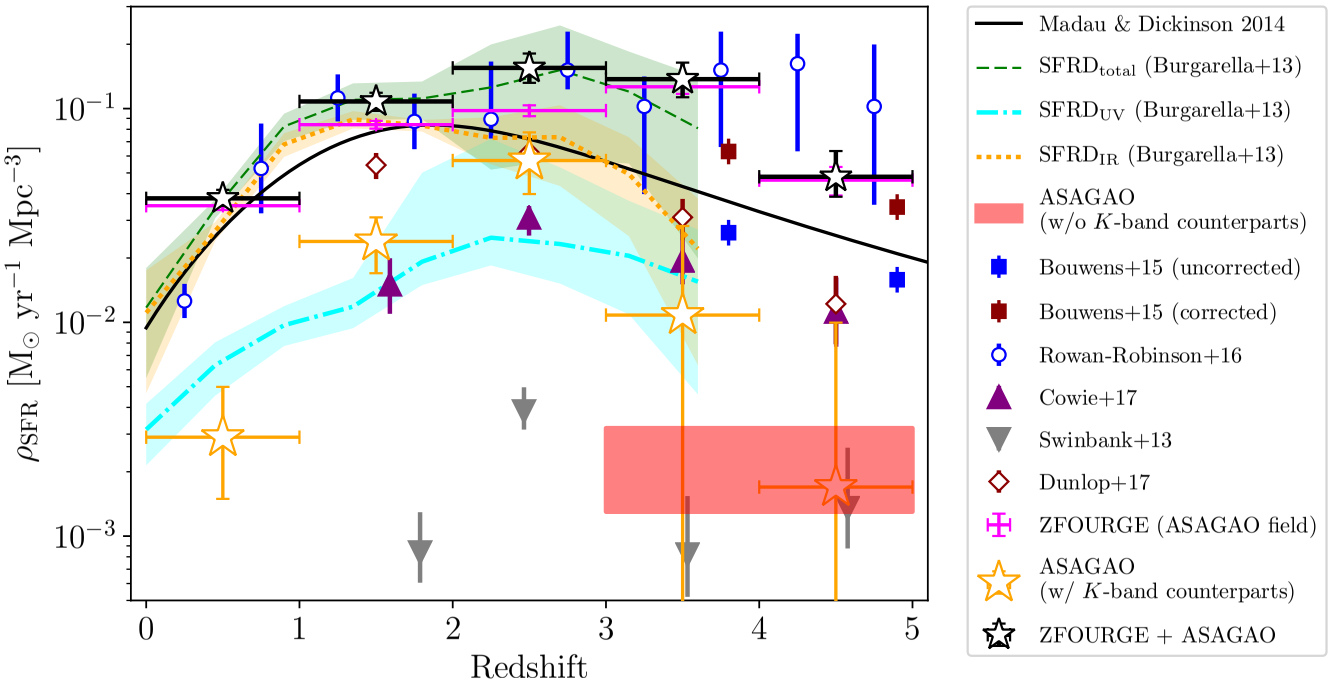

Figure 4.5 Contribution of ASAGAO sources to the cosmic SFRD as a function of redshift. The red shaded area indicates the contribution of K-drop ASAGAO sources. Orange, magenta, and black symbols are the contributions of ASAGAO sources with K-band counterparts, ALMA non-detected ZFOURGE sources within ASAGAO field, and their sum, respectively (see Section 3.6). The black solid line indicate the recent results of the redshift evolution of the cosmic SFRD obtained by Madau & Dickinson (2014). The green dashed line, cyan dot-dashed line, and orange dotted line show the total (i.e., UV + IR) SFRD, UV SFRD, and IR SFRD obtained by Burgarella et al. (2013). Blue and brown squares are dust-uncorrected and -corrected SFRD obtained by Bouwens et al. (2015). Blue open circles are results of Rowan-Robinson et al. (2016). Purple triangles indicate the cosmic SFRD obtained by the SCUBA2 large survey Cowie et al. (2017). Gray inverse-triangle are the contribution of bright ALESS sources (Swinbank et al., 2014). Brown open diamonds indicate the contribution of the ALMA sources obtained by Dunlop et al. (2017). We note that these results are converted to the Chabrier IMF.

estimated by *Hershel*/SPIRE-500 μm sources.

According to Simpson et al. (2014), their optical/near-IR-dark SMGs are located in the redshift range of $z \sim 3$–5. Thus, in this section, we assume the case that all of *K*-dropout ASAGAO sources lie somewhere in the redshift interval of $z \sim 3$–5. When we use the average SED of ALESS sources, their contribution to the cosmic IR SFRD is estimated to be $\rho_{\rm SFR} \sim 1$–$3 \times 10^{-3}\ M_\odot\ {\rm yr}^{-1}\ {\rm Mpc}^{-3}$ (corresponding to ~ 10–30% of previous studies; e.g., Madau & Dickinson 2014). Here, we simply sum up the SFRs of *K*-dropout ASAGAO sources and divide them by the co-moving volume and we also consider the reliability of *K*-dropout ASAGAO sources[3]. As shown in Figure 4.5, their contributions to the cosmic SFRD can be comparable with, or greater than that of bright ALESS SMGs ($S_{870\mu{\rm m}} > 4.2$ mJy; Swinbank et al. 2014). Therefore, the non-negligible contribution of dust-obscured star formation activities to the cosmic SFRD at high redshift could have been missed in previous surveys. This result shows the importance of ALMA deep contiguous survey to study the evolution of the cosmic SFRD. However, we cannot exclude the case that *K*-dropout ASAGAO sources lie at $z \lesssim 2$–3. Therefore, follow-up observations to get spectroscopic redshifts of these sources are needed.

4.5 Follow-up observations of near-IR-dark ALMA sources

In spite of the importance of getting the spectroscopic information of near-IR-dark ALMA sources, such kind of spectroscopic observations can be time-consuming even with ALMA. In this section, we introduce one example of the spectroscopic-scan observation by ALMA for getting spectroscopic redshift of the near-IR-dark ALMA source named SXDF-ALMA3 (see also Figure 1.5). SXDF-ALMA3 was detected by SXDF-ALMA survey (Kohno et al., 2016). Yamaguchi et al. (2016) report that it can lie at $z \sim 2$–4 based on optical/near-IR information and its IR luminosity is estimated to be $\log(L_{\rm IR}/L_\odot) \sim 12$. We carried out the spectroscopic-scan observation of SXDF-ALMA3 using ALMA Band 3 as a Cycle 3 program (Project ID: 2015.1.01222.S, PI: Y. Yamaguchi). The frequency setup covered the redshift

[3]If only two sources (i.e., ID17 and ID20) are real, $\rho_{\rm SFR} \sim 1 \times 10^{-3}\ M_\odot\ {\rm yr}^{-1}\ {\rm Mpc}^{-3}$. If all sources are real, $\rho_{\rm SFR} \sim 3 \times 10^{-3}\ M_\odot\ {\rm yr}^{-1}\ {\rm Mpc}^{-3}$

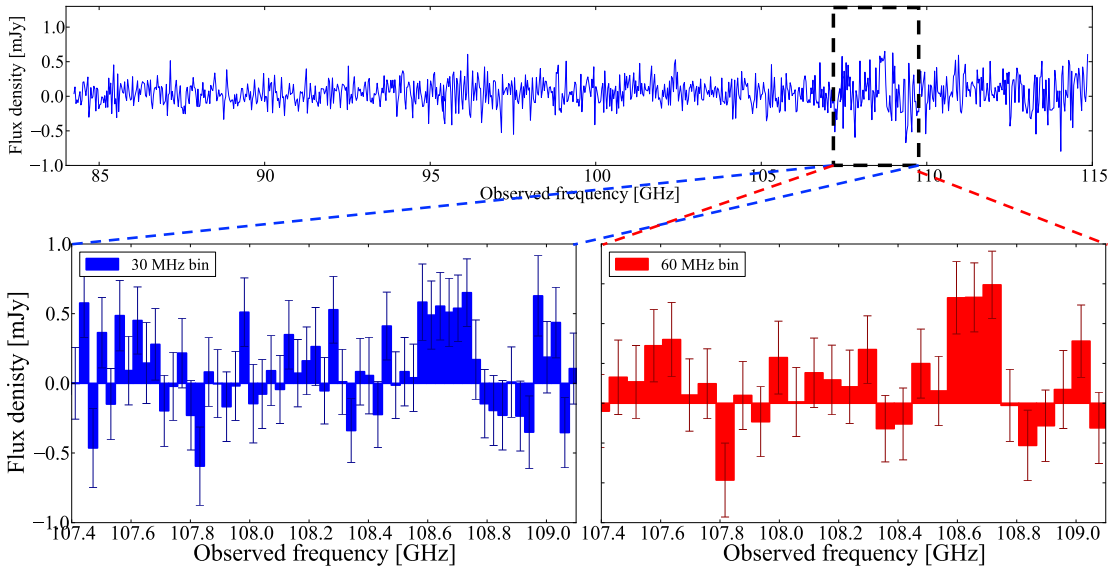

Figure 4.6 *Upper)* Results of the spectroscopic scan observation by ALMA Band 3 toward SXDF-ALMA3. *Lower-left)* The spectrum of SXDF-ALMA3 with 30-MHz frequency binning. *Lower-right)* The spectrum of SXDF-ALMA3 with 60-MHz frequency binning.

range of $z \simeq 1.00$–1.68 and 2.00–4.00 using the CO(2–1), CO(3–2), or CO(4–3) line. Even though the total observation time was $\simeq 8.5$ hours, we could only obtain a very tentative detection of a line emission with S/N $\simeq 2.5$–3.5 (Figure 4.6). Therefore, they can be good targets for the next generation telescopes.

For example, the Next Generation Very Large Array (ngVLA) is going to reach $\gtrsim 10$ times more sensitive than ALMA Band 3 at similar frequencies (Casey et al. 2015; see also Figure 4.7). Therefore, it will be much easier to detect CO rotational transition lines from near-IR-dark ALMA sources by only a few hours integration. In addition to the (sub-)millimeter emission lines, bright emissions at rest-frame mid-IR wavelengths such as the Polycyclic Aromatic Hydrocarbon features at 3.3, 6.2, 7.7, and 11.3 μm (e.g., Weingartner & Draine, 2001; Lagache et al., 2004) can also be detected by *James Webb Space Telescope* (*JWST*) or *Space Infrared Telescope for Cosmology and Astrophysics* (*SPICA*).

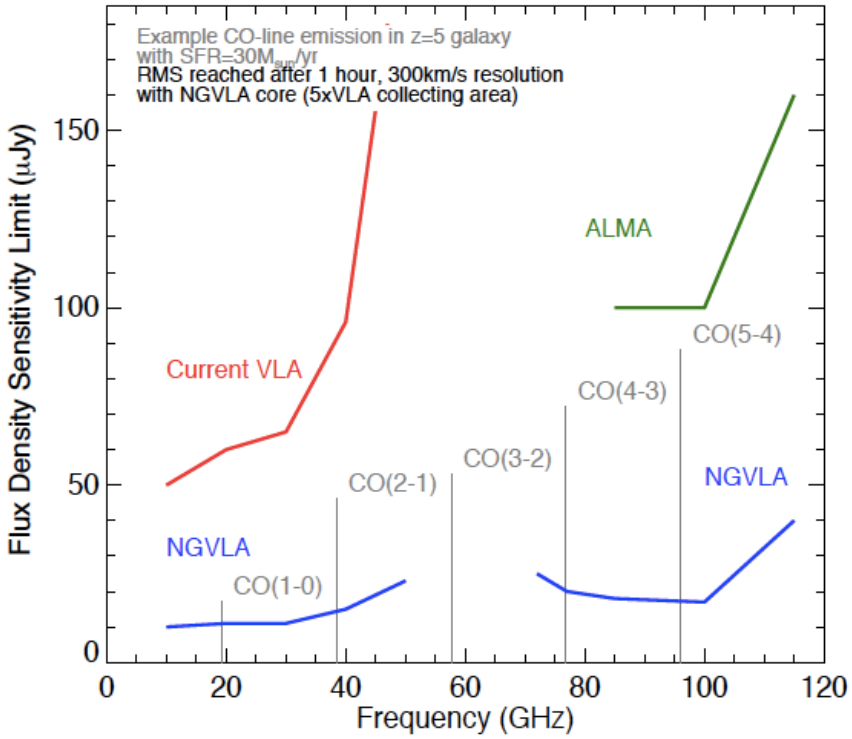

Figure 4.7 The projected sensitivity limits of the proposed ngVLA core. The blue solid lines indicate ngVLA sensitivities. Red and green solid line is the current VLA and ALMA sensitivity, respectively. This figure is referred from Figure 4 of Casey et al. (2015).

4.6 Conclusion of the near-IR-dark ASAGAO sources

In this chapter, we report detections of 5 ASAGAO sources with peak S/N $>$ 5 ($S_{1.2\mathrm{mm}}$ = 0.45–0.86 mJy) without any counterparts in the deep *H*- and *K*-band image. One of the sources has a red IRAC counterpart at 3.6 and 4.5 μm. Another one has been independently detected at 850 and 870 μm. The others have no countarpet except for ALMA 1.2 mm. Their optical to radio SEDs and the flux ratios between radio and millimeter wavelength suggest that they can lie at $z \gtrsim$ 3–5, although they can also be relatively low-redshift sources (i.e., $z \lesssim$ 2–3) with low dust temperature ($T_{\mathrm{dust}} \lesssim$ 25 K). We estimate stellar masses and SFRs of these *K*-dropout sources and find that these sources represent the early phase

of formation of massive galaxies if they lie at $z \gtrsim 3$–5. In the case that they lie at $z \lesssim 2$–3, they can be low-mass starburst galaxies with $\log(M_*/M_\odot) \lesssim 9.0$ and $\log(\mathrm{SFR}/[\mathrm{M}_\odot\ \mathrm{yr}^{-1}]) \sim 2$.

We derive the contribution of *K*-dropout ASAGAO sources to the cosmic SFRD. If they lie somewhere in the redshift range of $z \sim 3$–5, the contribution is estimated to be ~ 1–$3 \times 10^{-3}\ M_\odot\ \mathrm{yr}^{-1}\ \mathrm{Mpc}^{-3}$ (corresponding to $\sim$ 10–30% of previous studies; e.g., Madau & Dickinson 2014). This value can be consistent with, or greater than that of bright SMGs with $S_{870\mu\mathrm{m}} > 4.2$ mJy detected at $z \sim 3$–5. These results suggest that an unbiased ALMA survey can reveal the dust-obscured star formation activities, which have been missed in previous deep optical/near-IR surveys. However, follow-up observations to get spectroscopic redshifts are time-consuming even with ALMA. Therefore, these sources are good target for next generation telescopes such as ngVLA, *JWST*, and *SPICA*.

5

Blind millimeter line emitter search using ALMA toward gravitational lensing clusters

In this chapter, we present our results of a blind millimeter line emitter search using ALMA Band 6 data with a single frequency tuning toward four gravitational lensing clusters (RXJ1347.5−1145, Abell S0592, MACS J0416.1−2403, and Abell 2744). As discussed in Chapter 1, constraining the luminosity functions of (sub-)millimeter line emitters via unbiased (sub-)millimeter line emitter surveys is necessary to unveil the cosmic star formation history. This chapter is based on the published paper written by the author of this thesis (Yamaguchi et al., 2017).

In this study, we search for millimeter line emitters using ALMA Band 6 data with only a single frequency tuning (i.e., observed frequency range $\simeq$ 7.5 GHz) toward four gravitational lensing clusters; images of these gravitational lensing clusters obtained by the *HST* are displayed in Figure 5.1. From our

search, we constrain the CO luminosity functions at $z \lesssim 1$ and the [CII] luminosity function at $z \simeq 6$.

According to the predictions of semi-analytical models (e.g., Obreschkow et al., 2009a,b; Lagos et al., 2012; Popping et al., 2016), the number density of CO line emitters (i.e., CO luminosity function) evolve significantly at $z \lesssim 1$, which is in marked contrast to the weak evolution at $z = 1$–4 (Popping et al., 2016). Because of the magnification effect of gravitational lensing clusters, we can constrain the fainter end of the CO luminosity function, which is difficult to observe previous unlensed blank field observations. Constraining the faint-end of CO luminosity functions ($L'_{\rm CO} \lesssim 10^9$ K km s^{-1} pc^2) is particularly important because it is dominated by non-starburst galaxies, which are the main contributors to the cosmic SFRD. The faint-end of the CO luminosity functions are also affected by the CO spectral line energy distributions of galaxies, which reflect the density and temperature of the interstellar medium (e.g., Lagos et al., 2012; Popping et al., 2016). Furthermore, the [CII] luminosity function can be a useful tool to estimate the cosmic star formation rate density at $z \simeq 6$, where the contribution from dusty galaxies to the cosmic SFRD is still uncertain.

5.1 ALMA data toward gravitational lensing clusters

Here, we present the ALMA data. Our ALMA Band 6 continuum observations were carried out as an ALMA Cycle 2 program (Project ID: 2013.1.00724.S, PI: H. Ezawa) on April 9 and 10, 2015, toward two gravitational lensing clusters (RXJ1347.5−1145 and Abell S0592). For the ALMA observation, 35–38 antennas were employed. The minimum and maximum baselines were 15.1 and 348.5 m, respectively. For RXJ1347.5−1145 (for Abell S0592), the phase calibrator was J1337−1257 (J0608−5456), the bandpass calibrators were J1337−1257 and J1256−0547 (J1107−4449 and J1058−0133), and the flux calibrators were Titan and Ganymede (Ganymede). The observed area, observed frequency, frequency setting, achieved continuum sensitivities, and synthesized beams are summarized in Table 5.1.

We used additional Band 6 continuum observations toward another two gravitational lensing clusters (MACS J0416.1−2403 and Abell 2744) to expand our survey volume. These observations were also carried out as an ALMA Cycle 2 program (Project ID: 2013.1.00999.S, PI: F. Bauer). All data sets

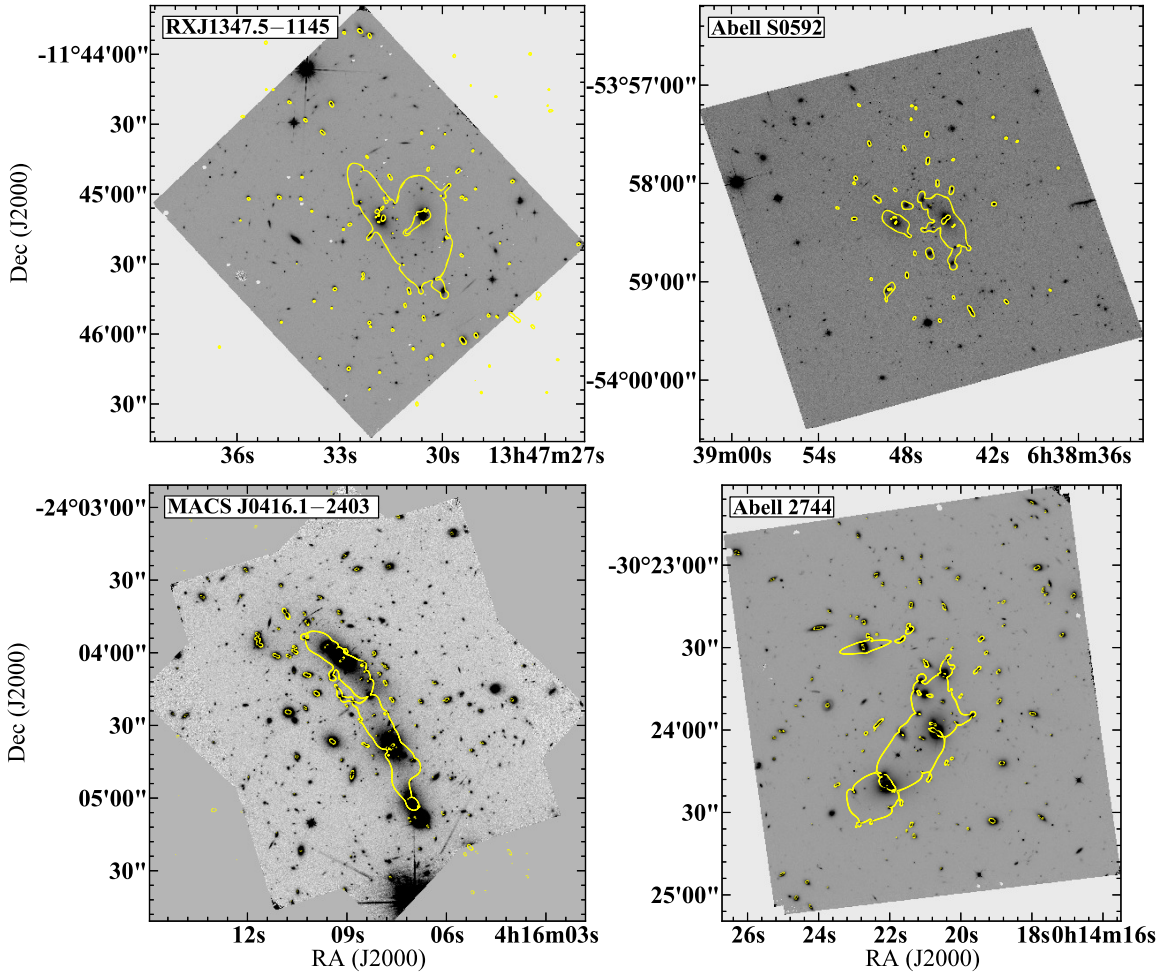

Figure 5.1 Images of 4 lensing clusters obtained by *HST*. From the upper left panel to the lower right panel, the *HST*/WFC3 *F160W* image of RXJ1347.5−1145, the *HST*/ACS *F606W* image of Abell S0592, the *HST*/WFC3 *F160W* image of MACS J0416.1−2403, and the *HST*/WFC3 *F160W* image of Abell 2744, respectively. Yellow solid lines are critical lines at $z = 1.0$ obtained by Kitayama et al. in preparation, Oguri et al. in preparation, and Kawamata et al. (2016).

are public in the ALMA science archive. In Table 5.1, we summarize the results of these continuum observations.

From the calibrated measurement sets of clusters, we create three-dimensional (3D) data cubes against each spectral window with two different frequency resolutions, i.e., 60 and 100 MHz (corresponding to

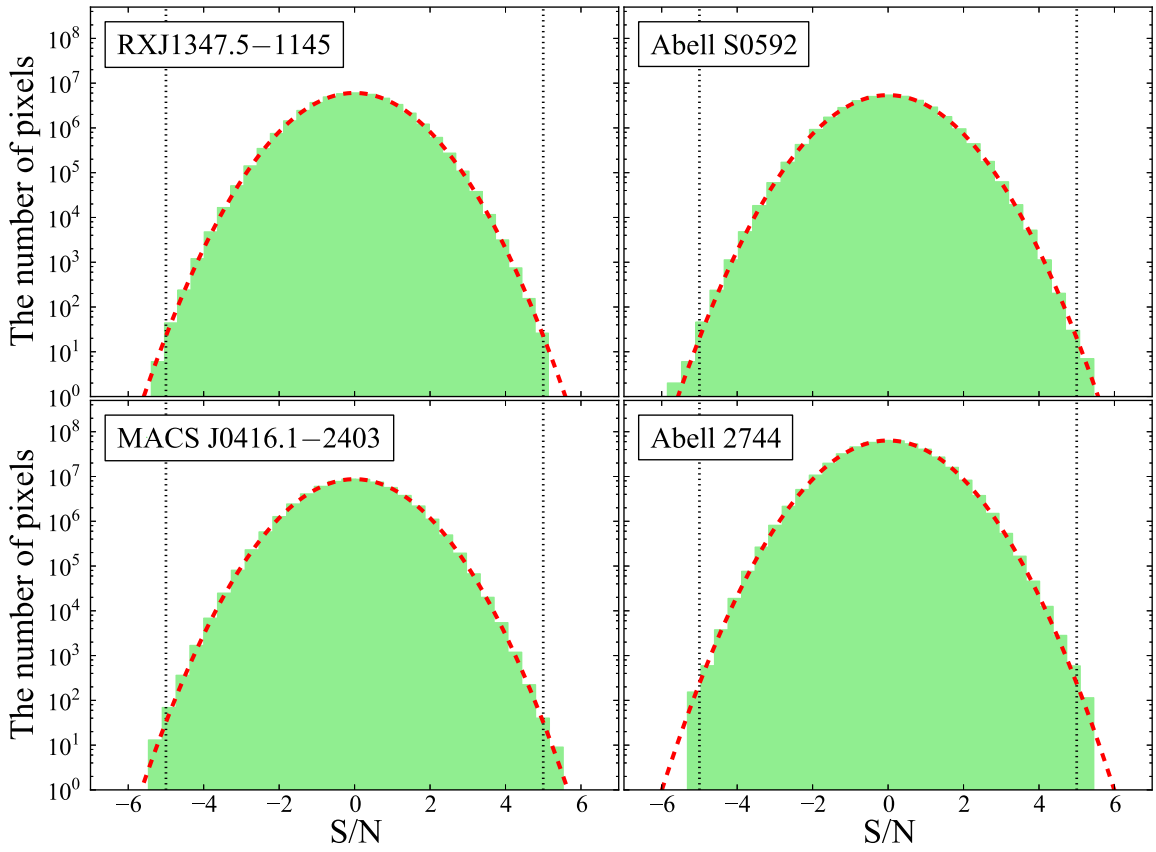

Figure 5.2 The S/N distribution of 3D data cubes with 60 MHz binning. The red dashed line shows a Gaussian function. Black dotted lines indicate S/N = ± 5.

about 66.7 km s^{-1} and 111 km s^{-1} at 270 GHz, respectively). The calibrated visibilities are Fourier transformed using the task CLEAN in the Common Astronomy Software Application (CASA; McMullin et al., 2007). In this study, we use cubes without beam deconvolution employing the CLEAN algorithm (Högbom, 1974), i.e., "dirty cubes", to search for line emitters, because no strong emission above 6σ is found in these cubes (see Figure 5.2). The achieved angular resolutions of the 3D data cubes are approximately 1″–1.″5. Note that the frequency resolutions of the original data are about 35 km s^{-1}, 35 km s^{-1}, 18 km s^{-1} and 18 km s^{-1} for RXJ1347.5−1145, Abell S0592, MACS J0416.1−2403, and Abell 2744, respectively.

Table 5.1. ALMA data toward gravitational lensing clusters

Target	$z_{\rm cluster}$	A [arcmin^2]	$\nu_{\rm obs}$ [GHz]	$\sigma_{\rm cont.}$ [μJy beam^{-1}]	Synthesized beam	$\Delta\nu$ [GHz]	$\sigma_{\rm 60\ MHz}$ [mJy beam^{-1}]	$\sigma_{\rm 100\ MHz}$ [mJy beam^{-1}]	$t_{\rm obs.}$ [hrs.]
(1)	(2)	(3)	(4)	(5)	(6)	(7)	(8)	(9)	(10)
RXJ1347.5−1145	0.451	4.75	265	155	$1.''3 \times 0.''72$ (78°)	255–259 271–275	1.4	1.2	2.26
Abell S0592	0.222	3.63	265	150	$1.''2 \times 0.''75$ (87°)	255–259 271–275	1.2	1.0	1.91
MACS J0416.1−2403	0.397	4.45	263	73	$1.''5 \times 0.''85$ (−84°)	254–257 269–272	0.73	0.56	8.50
Abell 2744	0.308	4.26	263	91	$1.''5 \times 1.''2$ (88°)	254–257 269–272	0.95	0.77	7.89

Note. — (1) Cluster name. (2) Redshifts of lensing clusters. (3) Observed area. (4) Central frequencies of observations. (5) Typical sensitivities of continuum maps. (6) Synthesized beam size of continuum map. Position angles of synthesized beams are given in parenthesis. (7) Observed frequency setting. (8) Typical sensitivities of 3D data cube with 60 MHz binning. (9) Typical sensitivities of 3D data cube with 100 MHz binning. (10) Total observation time.

5.2 Methods of our millimeter line emitter search

5.2.1 CLUMPFIND

We use CLUMPFIND software presented by Williams et al. (1994) to search for millimeter line emitters. In this section, we summarize CLUMPFIND algorithm as follows:

CLUMPFIND directly reads a 3-dimensional data cube into a 3-dimensional array. Therefore, it can search for "3-dimensional clumps" (i.e., x-axis, y-axis, and *frequency*-axis). First, it contours the data cube and finds peaks. Then, it follows them down through sequentially lower contour levels. Note that the contours are in the full 3 dimensions of the cube. In the case that pixels belonging to a clump detected at a certain contour level and they do not belong to another clump which is detected at higher contour level, the clump is recognized as a new clump. In Williams et al. (1994), they call this algorithm as "*friends-to-friends*" algorithm.

5.2.2 Methods of our millimeter line emitter search

We search for millimeter line emitters as follows:

1. We calculate the standard deviations in each channel and examine 3-dimensional signal-to-noise ratio cubes (S/N cubes) by dividing each data cube channel with its standard deviation. Note that we use the data cubes before the correction of the primary beam attenuation pattern to calculate the standard deviations. In Figure 5.2, we present the S/N distributions of the 3-dimensional data cube with 60 MHz binning.

2. We apply CLUMPFIND software, which is explaned in Section 5.2.1 to the 3-dimensional S/N cubes to search for line emitter candidates with a peak S/N > 5. We adopted the following parameters of CLUMPFIND: $\Delta S = 2\sigma$ and $S_{\rm start} = 4\sigma$, where ΔS is the contouring interval and $S_{\rm start}$ is the starting contour level as discussed in Williams et al. (1994).

3. We remove spurious detections by eye; specifically, we deem line emitter candidates that were not detected with a S/N > 3 in any channel adjacent to their peak channel as spurious and exclude them.

5.3 Results of our millimeter line emitter search

We do not detect any significant line-emission in our search. The S/N distributions are well fitted by Gaussian functions, which also support non-detections (Figure 5.2). The typical apparent 1σ noise levels of the data cubes are $\sigma \simeq 1.4$, 1.2, 0.73, and 0.95 mJy beam^{-1} with 60 MHz binning and $\sigma \simeq 1.2$, 1.0, 0.56, and 0.77 mJy beam^{-1} with 100 MHz binning for RXJ1347.5−1145, Abell S0592, MACS J0416.1−2403, and Abell 2744, respectively (Table 5.1). Thus, if we assume $\Delta V = 200$ km s^{-1}, as presumed in Decarli et al. (2016), the 3σ limiting apparent CO luminosities are estimated to be $\mu L'_{\rm CO} \simeq 5.5 \times 10^8$, 1.8×10^9, and 2.9×10^9 K km s^{-1} pc^2 for CO(3–2) at $z \simeq 0.3$, CO(4–3) at $z \simeq 0.7$, and CO(5–4) at $z \simeq 1.2$, respectively. Note that ΔV and μ are the velocity-width and the gravitational lensing magnification factor, respectively. For the [CII] 158 μm line at $z \simeq 6$, the 3σ limiting apparent [CII] luminosities are estimated to be $\mu L_{\rm [CII]} \simeq 1.0 \times 10^9$, 8.5×10^8, 4.7×10^8, 6.5×10^8 $L_\odot$. In the case of the [CII] 158 μm line, we assume $\Delta V = 300$ km s^{-1} as explained in Aravena et al. (2016a).

If we adopt a detection threshold of S/N = 4.0, there is a tentative detection of a line emitter at ($\alpha_{\rm J2000}$, $\delta_{\rm J2000}$) = ($13^{\rm h}47^{\rm m}30^{\rm s}.13$, $-11°45'26''.59$) in RXJ1347.5−1145 (see Figures in Appendix D; hereafter RXJ1347-emitter1). RXJ1347-emitter1 is detected with 4.5σ at the peak channel in the 60 MHz-binning data cube and detected with 4.3σ at next to the peak channel. RXJ1347-emitter1 is also detected with 5.8σ in the 100 MHz-binning data cube, but only detected at the peak channel. RXJ1347-emitter1 has no optical/NIR counterpart (see Figures in Appendix D). RXJ1347-emitter1 is not detected in ALMA continuum map. However, the negative tail of the noise distribution of the 60 MHz-binning data cubes also extends to S/N = −4.5 (see Figure 5.2) and is only detected at the peak channel in the 100 MHz-binning data cube. Thus, we treat RXJ1347-emitter1 as the "line emitter candidate" in this paper. Further details of RXJ1347-emitter1 will be provided in Appendix D.

González-López et al. (2017) also search for line emitters using MACS J0416.1−2403 and Abell 2744 data, and report some detections (6 in MACS J0416.1−2403, 3 in Abell 2744). This discrepancy is simply because our criterion are more conservative than their criterion.

5.4 CO and [CII] luminosity functions

We define luminosity bins to range from our 3σ limiting apparent luminosity (see Section 5.3) to a 0.5-dex higher luminosity. Because of the magnification due to gravitational lensing, we can search for lower line luminosities than the 3σ limiting apparent line luminosities. Accordingly, we adopt three intrinsic (i.e., demagnified) luminosity bins as displayed in Table 5.2. Note that for CO(3–2), we define two intrinsic luminosity bins, because the survey volume for the lowest intrinsic luminosity bin becomes very small as explained later in this section.

To constrain the CO and [CII] luminosity functions, it is necessary to estimate the co-moving survey volume. For this purpose, we used gravitational lensing models constructed with the GLAFIC software, which adopt a standard χ^2 minimization to determine the best-fit mass model (see Oguri, 2010, for details). For MACS J0416.1−2403 and Abell 2744 we use public GLAFIC mass models (version 3.0) that are available at Space Telescope Science Institute (STScI) website[1] (Kawamata et al., 2016). For the other two clusters, we use mass models obtained by Kitayama et al. in preparation (for RXJ1347.5−1145) and Oguri et al. in preparation (for Abell S0592). These models are constructed in a similar way to Kawamata et al. (2016).

In Figure 5.3 and Figure 5.4, we plot the effective (i.e. real) co-moving survey volume as a function of magnification factors and intrinsic 1σ sensitivities, respectively. For CO(3–2), the demagnified survey volume is small, especially in the high magnification area. This is because the CO(3–2) emitters at $z \sim 0.3$ are located in front of the gravitational lensing clusters at $z \lesssim 0.3$ and are thus not affected by gravitational lensing. This means that the non-null contribution at $\mu > 1$ values only comes from Abell S0592.

We use Markov Chain Monte Carlo (MCMC) methods to estimate model uncertainties as with the case of Kawamata et al. (2016). For MACS J0416.1−2403 and Abell 2744, results of MCMC methods are also available at STScI website. In MCMC methods, we change following parameters; virial mass, positions, ellipticity, position angle, concentration parameters, velocity dispersion, truncation radius, dimension less parameter η, and redshifts of lensed galaxies (see Kawamata et al., 2016, for details). The

[1] https://archive.stsci.edu/prepds/frontier/lensmodels/

Table 5.2. The constraint on densities of line emitters

Line	Redshift range	$\log L'_{\rm line}$ [K km s^{-1} pc^2]	$V_{\rm com}$ [Mpc^3]	Density [Mpc^{-3}]
(1)	(2)	(3)	(4)	(5)
CO(3–2)	0.257–0.276, 0.335–0.357[a]	8.3–8.8	$0.6778^{+0.1666}_{-0.2799}$	$< 2.7^{+1.9}_{-0.5}$
	0.286–0.271, 0.346–0.361[b]	8.8–9.3	$285.5^{+2.6}_{-0.4}$	$< (6.4^{+0.0}_{-0.1}) \times 10^{-3}$
CO(4–3)	0.677–0.701, 0.780–0.808[a]	8.3–8.8	$10.94^{+1.16}_{-1.99}$	$< (1.7^{+0.4}_{-0.2}) \times 10^{-1}$
	0.695–0.714, 0.794–0.815[b]	8.8–9.3	$316.8^{+26.5}_{-27.0}$	$< (5.8^{+0.5}_{-0.5}) \times 10^{-3}$
		9.3–9.8	$768.5^{+51.0}_{-39.9}$	$< (2.4^{+0.1}_{-0.1}) \times 10^{-3}$
CO(5–4)	1.10–1.13, 1.22–1.26[a]	8.5–9.0	$47.42^{+5.35}_{-6.88}$	$< (3.9^{+0.7}_{-0.4}) \times 10^{-2}$
	1.12–1.14, 1.24–1.27[b]	9.0–9.5	$642.5^{+50.8}_{-50.8}$	$< (2.9^{+0.2}_{-0.2}) \times 10^{-3}$
		9.5–10.0	1102^{+126}_{-96}	$< (1.7^{+0.2}_{-0.2}) \times 10^{-3}$
[CII] 158 μm	5.91–6.01, 6.34–6.45[a]	8.2–8.7[c]	$216.0^{+34.9}_{-98.5}$	$< (8.5^{+1.8}_{-1.1}) \times 10^{-3}$
	5.99–6.07, 6.40–6.48[b]	8.7–9.2[c]	1896^{+106}_{-178}	$< (9.7^{+1.0}_{-0.5}) \times 10^{-4}$
		9.2–9.7[c]	2532^{+444}_{-331}	$< (7.3^{+1.1}_{-1.1}) \times 10^{-4}$

Note. — (1) Observed line. (2) Observed redshift range. (3) Intrinsic (i.e., demagnified) line luminosities. (4) Co-moving survey volume. (5) The 1σ confidence upper limits on the densities of line emitters, which are calculated by using the Poisson statistics by Gehrels (1986).

[a]Observed redshift range of RXJ1347.5−1145 and Abell S0592.

[b]Observed redshift range of MACS J0416.1−2403 and Abell 2744.

[c]For [CII] 158 μm line, units of line luminosities are $L_\odot$.

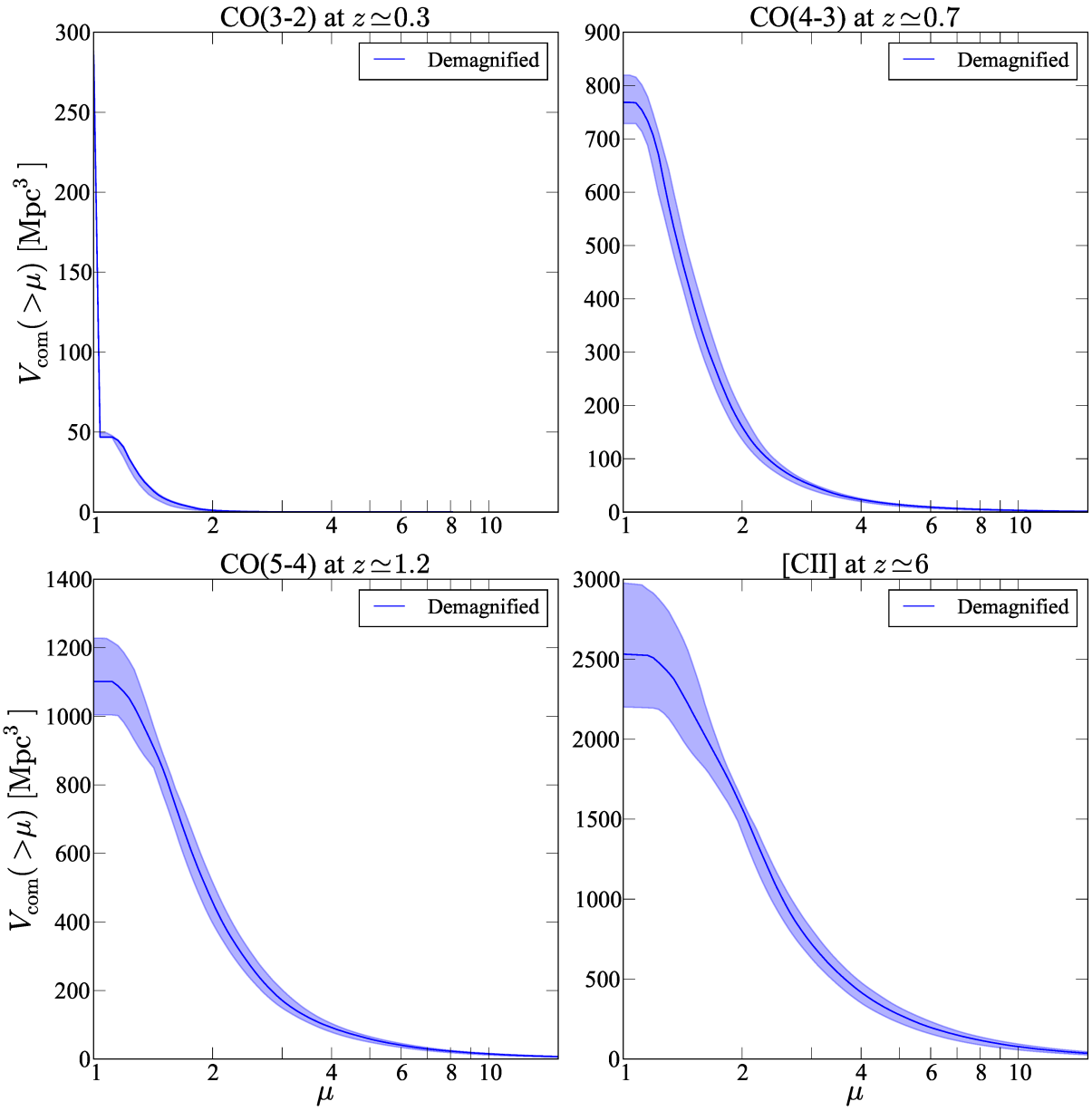

Figure 5.3 The effective (i.e. real) co-moving survey volume as a function of magnification factors (μ). Blue shaded regions indicate model uncertainties (see Section 5.4 for details).

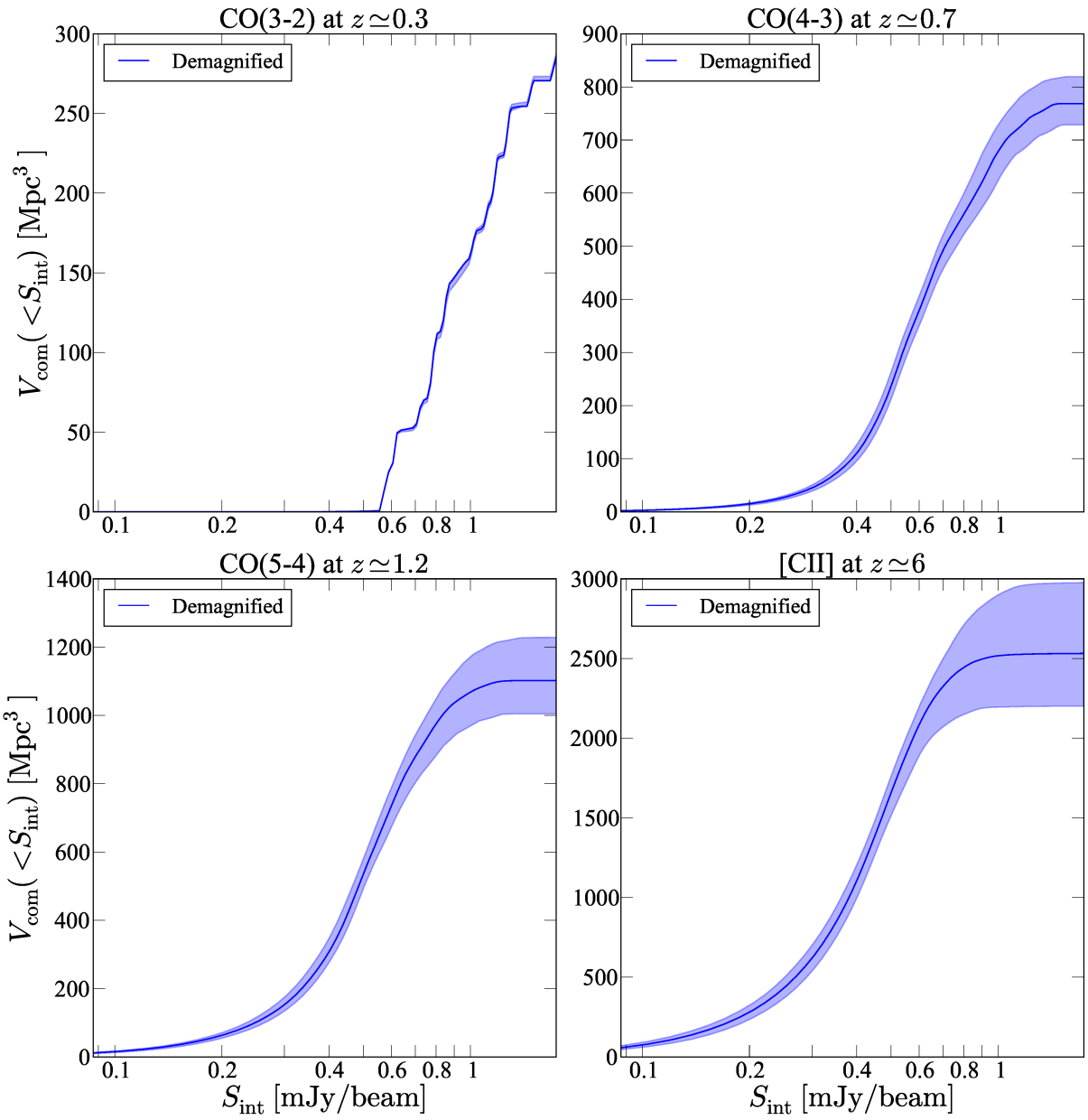

Figure 5.4 The effective (i.e. real) co-moving survey volume as a function of intrinsic 1σ sensitivities. Blue shaded regions indicate model uncertainties (see Section 5.4 for details).

resulting MCMC chain typically consists of hundreds of thousands of points. From the MCMC chain we randomly pick 100 parameter sets to estimate the error in our volume estimate from the mass model uncertainty. Specifically, we estimate the co-moving volume for each parameter set, repeat it for the 100 parameter set, and derive the model uncertainties. Here, we define the range between the maximum and minimum co-moving survey volume as the model uncertainty. Our co-moving survey volume of each luminosity bin and the 1σ confidence upper limits on the densities of line emitters, which are calculated by using the Poisson statistics by Gehrels (1986) are summarized in Table 5.2. Note that our estimated errors can be underestimated because we do not include systematic errors between different lens models. For example, the area with magnification between 5 and 10 in Abell 2744 can change by almost $\sim$ 20% between different lens models released in STScI website (Wang et al., 2015; Kawamata et al., 2016; Priewe et al., 2017).

Note that the limiting luminosities do not depend on the assumed line profiles. For instance, if we adopt the limiting luminosities following our detection criterion explained in Section 5.2.2 (i.e., it is detected with 5σ flux density in one channel, and 3σ in a neighboring channel), results do not change. For example, for CO(4–3), the apparent limiting luminosity is estimated to be $\mu L'_{\rm CO(4\text{-}3)} \simeq 10^{9.2}$ K km s^{-1} pc^2 (in 60 MHz-binning cubes), which is comparable with the limiting luminosity presented in Section 5.3. In this case, the typical magnification factor corresponding to the faintest luminosity bin in the Table 5.2 (i.e., $L'_{\rm CO(4\text{-}3)} \simeq 10^{8.5}$ K km s^{-1} pc^2) is $\mu \simeq 5$. According to Figure 5.3, the co-moving survey volume corresponding to this case (i.e., $\mu \simeq 5$) is estimated to be $V_{\rm com} \simeq 14$ Mpc^3, which is comparable with Table 5.2.

5.4.1 CO luminosity functions

In Figure 5.5, we show our constraints on the CO luminosity functions (red symbols). In order to avoid CO excitation uncertainties, we do not convert $L'_{\rm CO(3\text{-}2)}$, $L'_{\rm CO(4\text{-}3)}$, and $L'_{\rm CO(5\text{-}4)}$ into $L'_{\rm CO(1\text{-}0)}$ in this paper. In gravitational lensing clusters, the effective survey volumes with a large magnification factor is small as shown in Figure 5.3 and Figure 5.4. This is the reason why our constraints on the CO luminosity functions at the faintest intrinsic luminosity bins are not strong. We only plot the best-fitting case in

Figure 5.5, because model uncertainties on luminosity functions are small (see Table 5.2).

In the same plot (Figure 5.5), we also show the predictions based on semi-analytical cosmological models by Obreschkow et al. (2009a,b), Lagos et al. (2012), and Popping et al. (2016). As shown in Figure 5.5, our constraints are consistent with their predictions.

We also plot the latest results of the ALMA SPECtroscopic Survey in the *Hubble* Ultra-Deep Field (ASPECS Walter et al., 2016; Decarli et al., 2016, cyan shaded regions). However, they only use peak values to identify line emitters. To make a fair comparison, we reanalyze their ALMA Band 6 data (Project ID: 2013.1.00718.S, PI: M. Aravena) following our procedure, which is explained in Section 5.2.2. In our procedure, we detect two emission lines, which are detected in ASPECS as 1mm.1 and 1mm.2 (Walter et al., 2016; Decarli et al., 2016). According to Decarli et al. (2016), these two lines represent the CO emission from one line emitter at $z = 2.54$. Therefore, we can only place upper limits on the CO luminosity functions at $z \lesssim 1$ (yellow symbols in Figure 5.5) from the ASPECS data. As shown in Figure 5.5, our constraints on the CO luminosity functions are consistent with the ASPECS results at similar luminosity ranges ($L'_{\rm CO} \sim 10^9$ K km s^{-1} pc^2). Although the upper limit is about 1–2 orders of magnitude larger than the predictions of semi-analytical models, we can expand the range of luminosity to $\gtrsim 0.5$-dex lower than previous observations, although the current constraints are very coarse.

Based on our upper limits, we constrain the density evolution of the CO luminosity functions between $z = 0$ and $z \simeq 1$. As shown in Figure 5.5, the evolution of the CO luminosity functions between $z = 0$ and $z \simeq 1$ are consistent with the predictions of semi-analytical models by Obreschkow et al. (2009a,b), Lagos et al. (2012) and Popping et al. (2016), although the constraints to date are not stringent yet.

5.4.2 [CII] luminosity function

We display our constraints on the [CII] luminosity function at $z \simeq 6$ in Figure 5.6. As with the case of CO luminosity functions, we only plot the best-fitting case. In the same plot, we also show the predictions based on semi-analytical cosmological models with radiative transfer by Popping et al. (2016) and observational results of ASPECS (Aravena et al., 2016a) and Hayatsu et al. (2017). As with the case of the CO luminosity functions, we show the results of the ASPECS data reanalysis (see Section 5.4.1

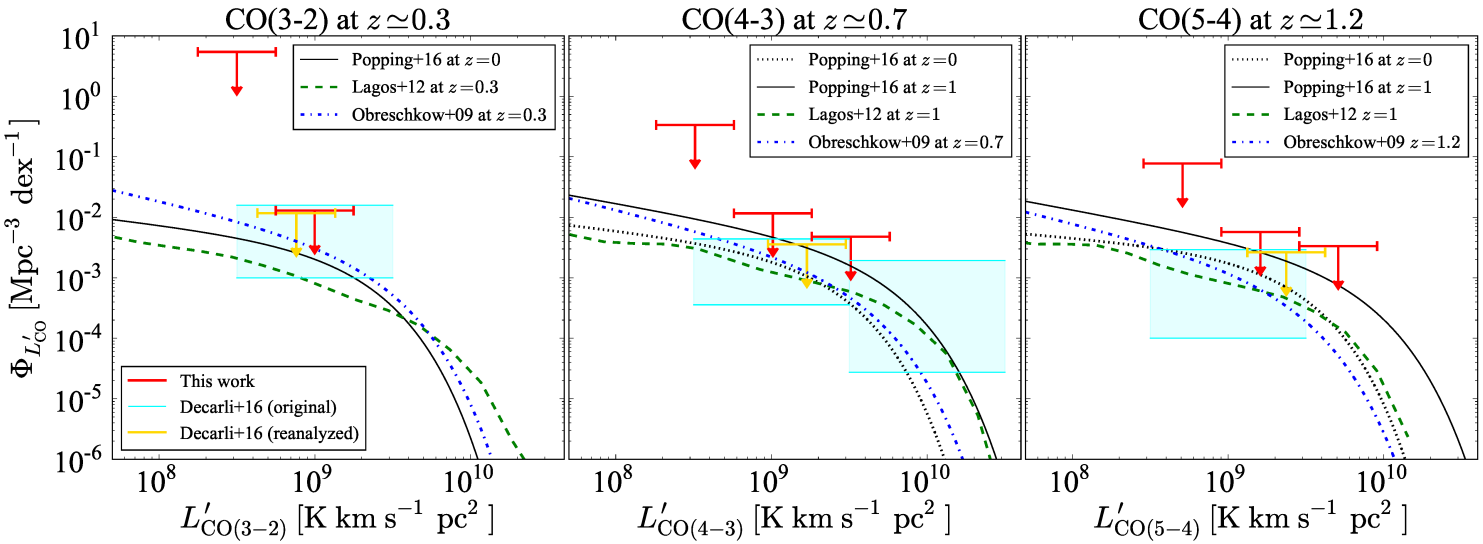

Figure 5.5 Comparison of our blind line emitter search with the empirically derived CO luminosity functions and previous observations. Our results are presented as red symbols. Black solid lines, green dashed lines, and blue dot-dashed lines are the empirically derived CO luminosity functions from Obreschkow et al. (2009a,b), Lagos et al. (2012), and Popping et al. (2016), respectively. Cyan shaded regions are the results of the ASPECS (Decarli et al., 2016). Yellow symbols are the results of our reanalysis of the ASPECS data (see Section 5.4.1).

for details). We also plot the observed [CII] luminosity function at $z = 0$ observed by the *Herschel Space Observatory* (Hemmati et al., 2017).

Although the upper limits are significantly higher than the prediction of Popping et al. (2016), our results are still consistent with previous observational results (Figure 5.6). Indeed, recent observations suggest that the semi-analytical models underestimate the number density of [CII] emitters (e.g., Swinbank et al., 2012; Aravena et al., 2016a; Miller et al., 2016; Hemmati et al., 2017; Hayatsu et al., 2017) at the luminosity range of $L_{[\mathrm{CII}]} \gtrsim 10^8\ L_\odot$. One of the reasons of this discrepancy might be explained by semi-analytical models' difficulty in the AGN feedback that affects the inflow/outflow of gas in the largest and most massive galaxies (e.g., Vallini et al., 2016; Hemmati et al., 2017; Lagache et al., 2018). Our results support previous observations at the luminosity range of $L_{[\mathrm{CII}]} \sim 10^8$–$10^{10}\ L_\odot$.

Popping et al. (2016) predict that the [CII] luminosity function at $z = 6$ returns to a level similar to that of $z = 0$, which reflect the evolution of the cosmic SFRD. This is also suggested by observational studies (e.g., Aravena et al., 2016a; Hemmati et al., 2017), regardless of [CII] luminosity function shape. As shown in Figure 5.6, our results are also consistent with the prediction.

5.5 Conclusions of our millimeter line emitter search

We carried out a blind search for millimeter line emitters using ALMA band 6 data with a single frequency tuning toward four gravitational lensing clusters. We did not detect any line emitters with a peak S/N > 5, although we did find one line emitter candidate (RXJ1347-emitter1) with a peak S/N = 4.5 in the 60 MHz-binning data cube.

We placed upper limits on the CO(3–2), CO(4–3), and CO(5–4) luminosity functions at $z \simeq 0.3$, 0.7, and 1.2, respectively. Because of the magnification effect of gravitational lensing clusters, the new data provide the first constraints on the CO luminosity functions at unprecedentedly low luminosity levels, i.e., down to $\lesssim 10^{-3}$–10^{-1} Mpc^{-3} at $L'_{\mathrm{CO}} \sim 10^8$–$10^{10}$ K km s^{-1} pc^2. These results are consistent with the predictions of semi-analytical models. Our constraint is comparable with the latest results of the ALMA spectroscopic scan observation of ASPECS at similar luminosity ranges ($L'_{\mathrm{CO}} \sim 10^9$ K km s^{-1} pc^2).

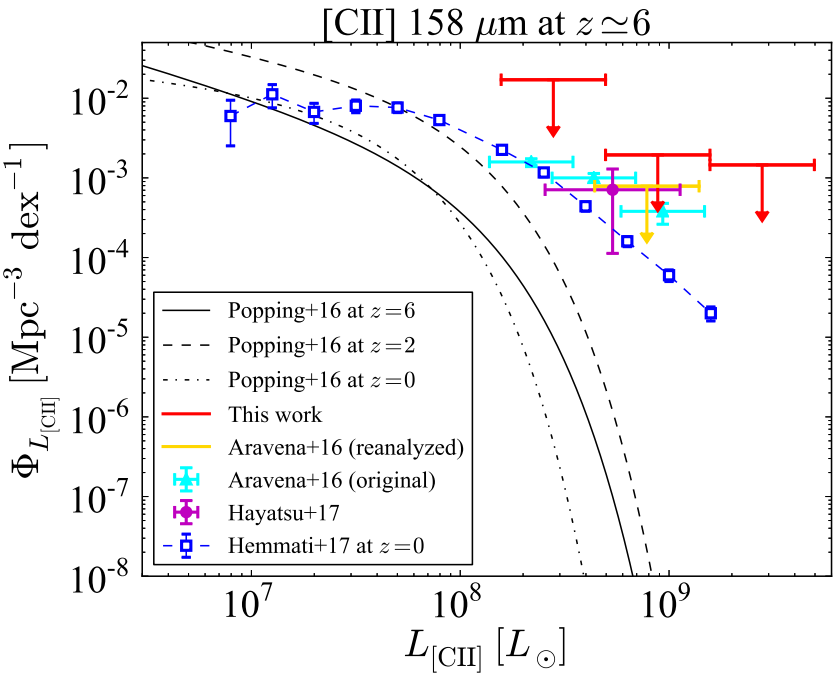

Figure 5.6 Comparison of our blind line emitter search with the empirically derived [CII] luminosity functions and previous observations. Our results are presented as red symbols. The black solid line, the dashed line and the dot-dashed line is empirically derived [CII] luminosity functions at $z = 6$, $z = 2$, and $z = 0$ from Popping et al. (2016), respectively. The cyan triangle and the magenta circle indicates the observational results of the ASPECS (Aravena et al., 2016a) and Hayatsu et al. (2017), respectively. The yellow symbol is result of our reanalysis of ASPECS data. Blue squares represent the observed [CII] luminosity function at $z = 0$ (Hemmati et al., 2017).

However, we can expand the range of luminosity to $\gtrsim$ 0.5-dex lower than previous observations. Our constraint on the evolution of CO luminosity function between $z = 0$ and $z \simeq 1$ are consistent with the predictions of semi-analytical models by Obreschkow et al. (2009a,b), Lagos et al. (2012) and Popping et al. (2016), although the constraints to date are not stringent yet.

We also placed upper limits on the [CII] luminosity function at $z \simeq 6$ ($\lesssim 10^{-3}$-10^{-2} Mpc^{-3} dex^{-1}) in the luminosity range of $L_{[CII]} \sim 10^8$–10^{10} $L_\odot$. Although the upper limits are significantly higher than the prediction of the semi-analytical model, our results are still consistent with previous observational results. Our results are consistent with the scenario that the [CII] luminosity function returns to a level

similar to that of $z = 0$ at $z \simeq 6$.

The total observation time of our data is comparable with ASPECS ($\sim$ 20 hours at Band 6). Therefore, this study demonstrates that not only the spectroscopic scan observations, but also the wide observations with a single frequency tuning toward gravitational lensing clusters are useful for constraining the CO and [CII] luminosity functions. We will also be able to apply stronger constraints by adding more ALMA Cycle 3 or 4 data toward gravitational lensing clusters, which will become public soon.

6

Summary

One of the main goals in astronomy is unveiling the cosmic star formation history. In order to understand the cosmic star formation history comprehensively from the point of view of the dusty star-forming activity itself and material of star formation, we put constraints on the evolution of the cosmic SFRD by the direct observations of dusty star-forming galaxies at $z \simeq 0$–5 (Chapter 3, Chapter 4) and CO and [CII] luminosity functions at $z \sim 1$ and 6, respectively (Chapter 5) using unbiased ALMA data. Our results and conclusions are explained in following sections.

6.1 The multi-wavelength analysis of 1.2 mm continuum sources

We extract 1.2 mm continuum sources using the deep continuum observations of a 26 arcmin^2 region in the GOODS-S obtained with ALMA Band 6, named ASAGAO. In conjunction with ALMA archival

data of the same field the final ASAGAO map reaches a typical noise level of $\sigma \sim 30$ μJy beam^{-1} at the central ~ 4 arcmin^2 and ~ 70 μm beam^{-1} at the remaining area with the synthesized beam of $0''.59 \times 0''.53$ (position angle = $-83°$). Our main results of the multi-wavelength analysis of ASAGAO sources are as follows:

- We find that 66 ASAGAO sources with the peak S/N > 3.5 have K-band counterparts in the ZFOURGE catalog. These ASAGAO sources tend to have fainter flux densities ($S_{1.2\mathrm{mm}} \lesssim 1.0$ mJy) than bright SMGs ($S_{1.2\mathrm{mm}} \gtrsim 1.0$ mJy). Their median redshift is estimated to be $z_{\mathrm{median}} = 1.77 \pm 0.23$, which is consistent with the results of faint (sub-)millimeter sources detected in recent ALMA deep continuum surveys, although this value is lower than that of bright SMGs ($z_{\mathrm{median}} \sim 2.1$–$3.1$).

- We perform the bayesian-based SED fitting from optical to millimeter wavelengths using MAGPHYS to estimate the physical properties of the ASAGAO sources. The estimated stellar masses and SFRs of ASAGAO sources suggest that they mainly lie on the high-mass end of the main sequence of star-formation galaxies on the M_*-SFR plane, although ~ 10% of ASAGAO sources show starburst-like features in the relatively small stellar mass range.

- The IRX-M_*, IRX-SFR, and IRX-β_{UV} relations of ASAGAO sources show offsets from ALMA non-detected ZFOURGE sources even if they show similar star-forming properties on the M_*-SFR plane. This implies that ALMA detected and non-detected sources have different dust properties (e.g., dust compositions or dust distribution).

- We obtain the spatially resolved IRX-β_{UV} relation of ASAGAO sources by using the ALMA image with $0''.2$ resolution and find that the different distribution between dust and stars is at least partly responsible for the bluer IRX-β_{UV} relation and large dispersion of high redshift dusty star-forming galaxies.

- We resolve the contribution of ASAGAO sources to the cosmic SFRD at $z = 0$–5. The shape of the contribution of ASAGAO sources to the cosmic SFRD is similar to the previous studies; it has a peak level at $z \sim 2$–3, and then it declines toward $z = 0$. We find that the ASAGAO sources with K-band counterparts are main contributors to the cosmic SFRD at $z \simeq 2$–3 (~ 60% of the cosmic UV + IR SFRD and ~ 80% of the cosmic IR SFRD), and their contributions are ~ 1 dex smaller than that of previous studies at $z < 2$ (only ~ 5–30% of the cosmic IR SFRD). The contributions of ASAGAO sources to the cosmic SFRD can be consistent with, or greater than that of bright ALESS sources at $z \gtrsim 3$.

– We also find 5 ASAGAO sources (S/N $>$ 5 at 1.2 mm) without any counterparts in the deep *H*- and *K*-band image. One of these *K*-dropout ASAGAO sources is also detected at *Spitzer*/IRAC 3.6- and 4.5-μm band and another one has been independently detected at 850 and 870 μm using JCMT/SCUBA2 and ALMA Band 7, respectively. The others have no counterparts.

– The optical to radio SEDs and the flux ratios between radio and millimeter wavelength of the *K*-dropout ASAGAO sources suggest that they can be at $z \gtrsim$ 3–5, although we can not exclude the case that they are relatively low-redshift (i.e., $z \lesssim$ 2–3) sources with low dust temperature ($T_{\rm dust}$ $\lesssim$ 25 K).

– The stellar masses and SFRs of *K*-dropout ASAGAO sources suggest that they can be the early phase of the formation of massive galaxies at high redshift or low-mass sturburst sources at low redshift.

– We derive the contribution of *K*-dropout ASAGAO sources to the cosmic SFRD. If they lie somewhere in the redshift range of $z \sim$ 3–5, the contribution is estimated to be $\sim$ 1–3 $\times$ 10^{-3} $M_{\odot}$ yr^{-1} Mpc^{-3} ($\gtrsim$ 10% of previous studies). This value can be consistent with, or greater than that of bright SMGs with $S_{870\mu{\rm m}} > 4.2$ mJy detected at $z \sim$ 3–5. These results suggest that an unbiased ALMA survey can reveal the dust-obscured star formation activities, which have been missed in previous deep optical/near-IR surveys.

6.2 Blind millimeter line emitter search

We carry out a blind search for millimeter line emitters using ALMA Band 6 data with a single-frequency tuning toward four gravitational lensing clusters (RXJ1347.5$-$1145, Abell S0592, MACS J0416.1$-$2403, and Abell 2744). We do not detect any line emitters with a peak S/N $>$ 5, although we do find one line emitter candidate (RXJ1347-emitter1) with a peak S/N $\simeq$ 4.5 in the 60 MHz binning data cube. Our main results are as follows:

– We place upper limits on the CO(3–2), CO(4–3), and CO(5–4) luminosity functions at $z \simeq$ 0.3, 0.7, and 1.2, respectively. Because of the magnification effect of gravitational lensing clusters, the new data provide the first constraints on the CO luminosity functions at unprecedentedly low

luminosity levels, i.e., down to $\lesssim 10^{-3}$–10^{-1} Mpc^{-3} dex^{-1} in the luminosity range of $L'_{\rm CO} \sim 10^{8}$–10^{10} K km s^{-1} pc^{2}.

– Our constraint is comparable to the latest results of the ALMA spectroscopic surveys. However, we can expand the range of luminosity to $\gtrsim 0.5$ dex lower than previous observations. Although the constraints to date are noy yet stringent, our constraint on the evolution of CO luminosity function between $z = 0$ and $z = 1$ is consistent with the predictions of semi-analytical models.

– We also put upper limits on the [CII] luminosity function at $z \simeq 6$ ($\lesssim 10^{-3}$-10^{-2} Mpc^{-3} dex^{-1}) in the luminosity range of $L_{\rm [CII]} \sim 10^{8}$–$10^{10}$ $L_{\odot}$. Although the upper limits are significantly higher than the prediction of the semi-analytical model, our results are still consistent with the evolution scenario suggested by semi-analytical models.

– The total observation time of our data is comparable with ASPECS ($\sim$ 20 hours at Band 6). Therefore, this study demonstrates that not only spectroscopic scan observations, but also observations with a single-frequency tuning toward gravitational lensing clusters are useful for constraining the CO and [CII] luminosity functions. We will also be able to obtain stronger constraints by adding more ALMA Cycle 3 or 4 data toward gravitational lensing clusters, which will become public soon.

The results in this thesis demonstrate that we have resolved the contributions of faint (sub-)millimeter sources to the cosmic SFRD in the redshift range of $z \simeq 0$–5. In addition, our constraints on millimeter line luminosity functions by our blind millimeter line emitter search are consistent with semi-analytical model which suggest that the evolution of the cosmic SFRD is caused by the lack of the molecular gas content in the universe. We also find that we have missed non-negligible contributions of near-IR-dark faint (sub-)millimeter sources to the cosmic SFRD in the high redshift universe. As a next step, obtaining the spectroscopic redshifts of these near-IR dark faint (sub-)millimeter sources via spectroscopic scan observations, which is time-consuming even with ALMA, is necessary. Therefore, these sources are good target for next generation telescopes such as ngVLA, *JWST*, and *SPICA*.

In the near future, we will get ALMA data obtained by an ALMA large program, ALMA Lensing Cluster Survey (ALCS; Project ID: 2018.1.00035.L, PI: K. Kohno). The observation will cover $\simeq 88$ arcmin^{2} apparently (33 massive galaxy clusters) and reach the apparent sensitivity of $\sigma \simeq 0.08$ mJy at

1.2 mm. The data will be able to provide a significant number of near-IR-dark faint millimeter sources as well as near-IR detected millimeter sources. The magnification effect of gravitational lensing clusters help to study multi-wavelength properties of such near-IR-dark faint millimeter sources. In addition to that, the data can also be used for a blind millimeter line emitter search as suggested in Chapter 5. The wide observation area ($\gtrsim$ 5 times wider than that of this study) and frequency range ($\simeq$ 2 times wider than that of this study) will enable us to put stronger constraints on CO and [CII] luminosity functions.

A

Multi-wavelength postage stamps

In Figure A.1, we show multi-wavelength postage stamps of ASAGAO sources with *K*-band counterparts.

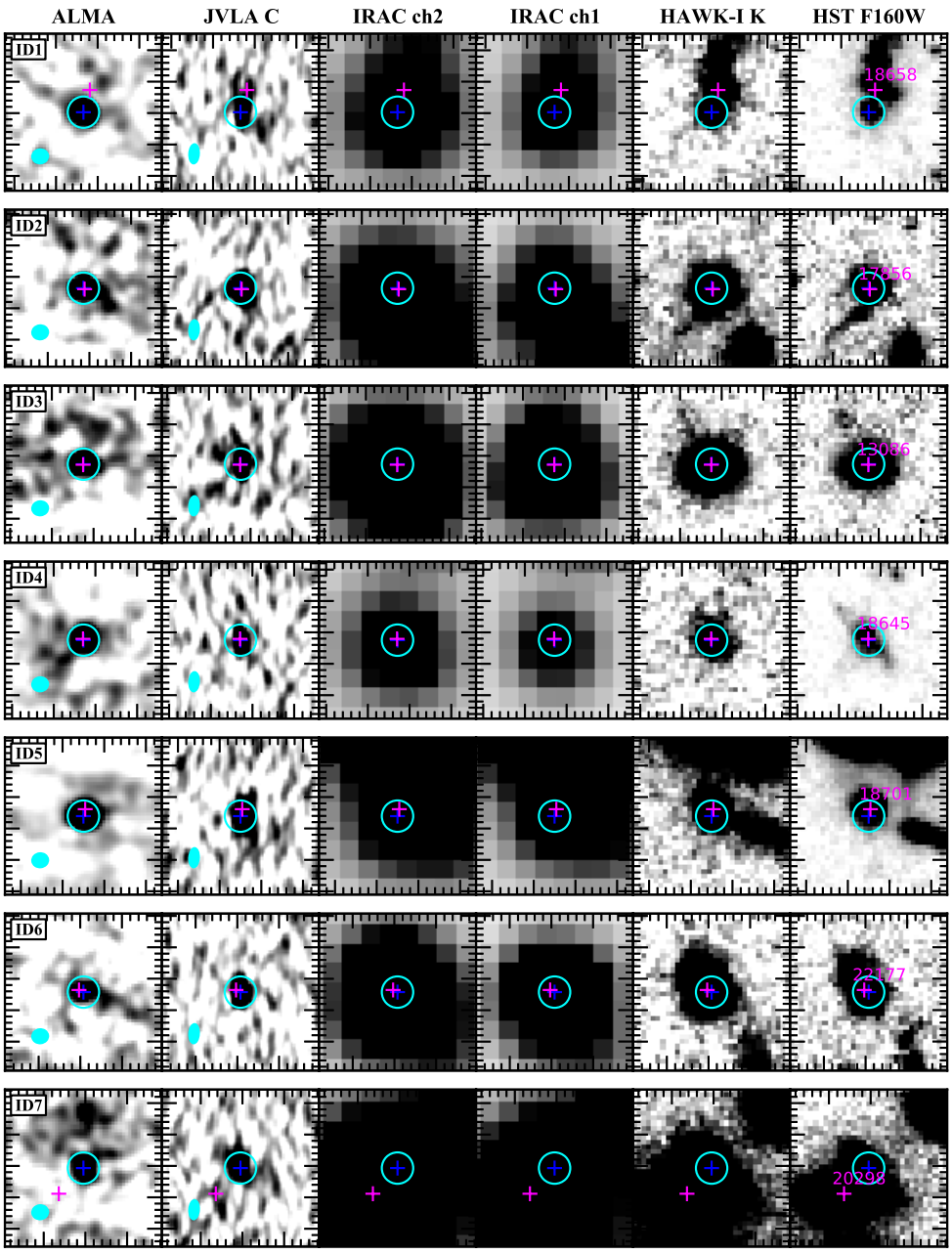

Figure A.1 Multi-wavelength images of ASAGAO sources with *K*-band counterparts. From left to right: ALMA 1.2 mm, JVLA 6 GHz, *Spitzer* IRAC/4.5 μm, IRAC/3.6 μm, VLT HAWK-I/K_s, and HST WFC3/*F*160*W* images. The field of view is 5" $\times$ 5". Blue and magenta crosses mark the ALMA positions and ZFOURGE positions, respectively. Cyan circles are 1" apertures.

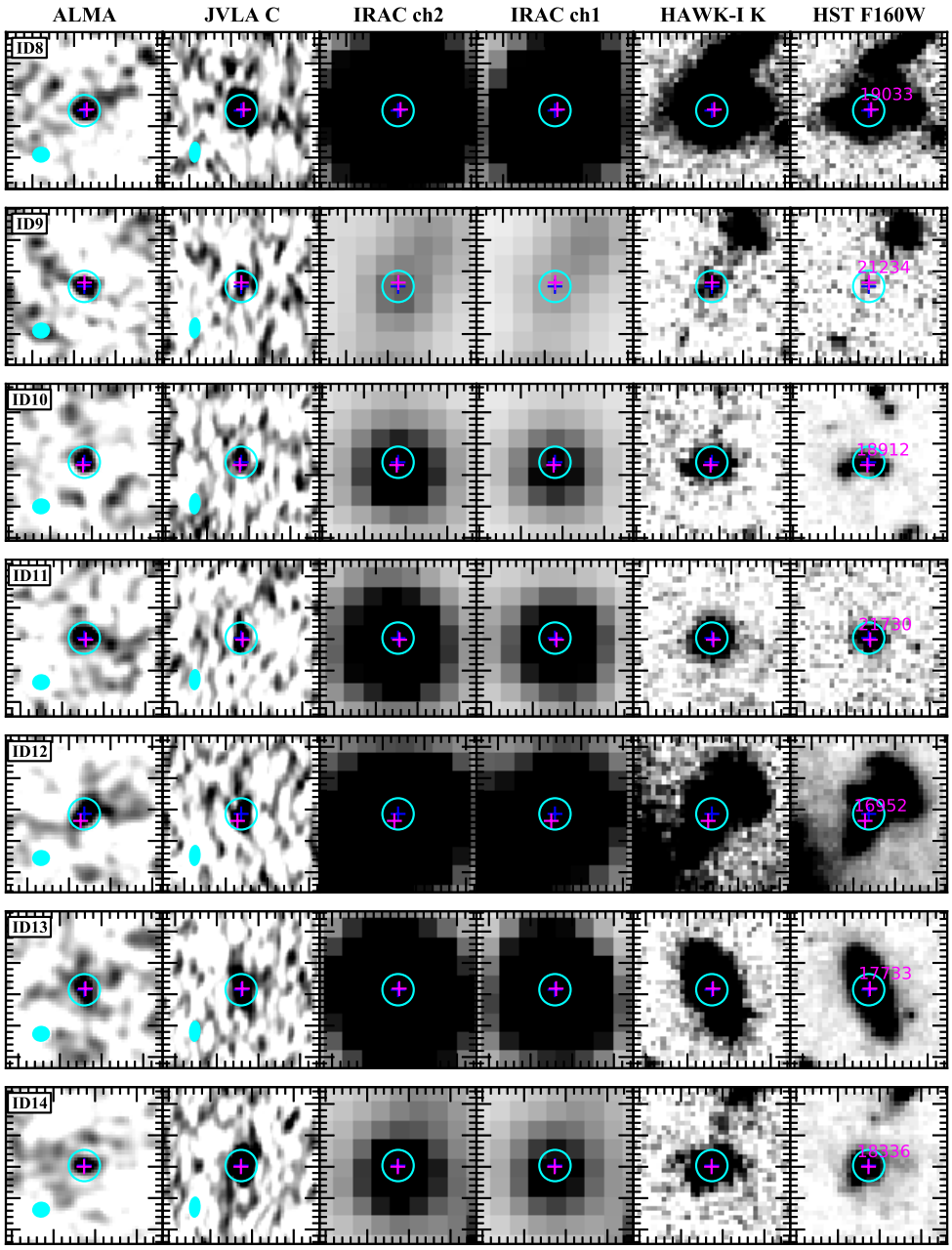

Figure A.1 (Continued.)

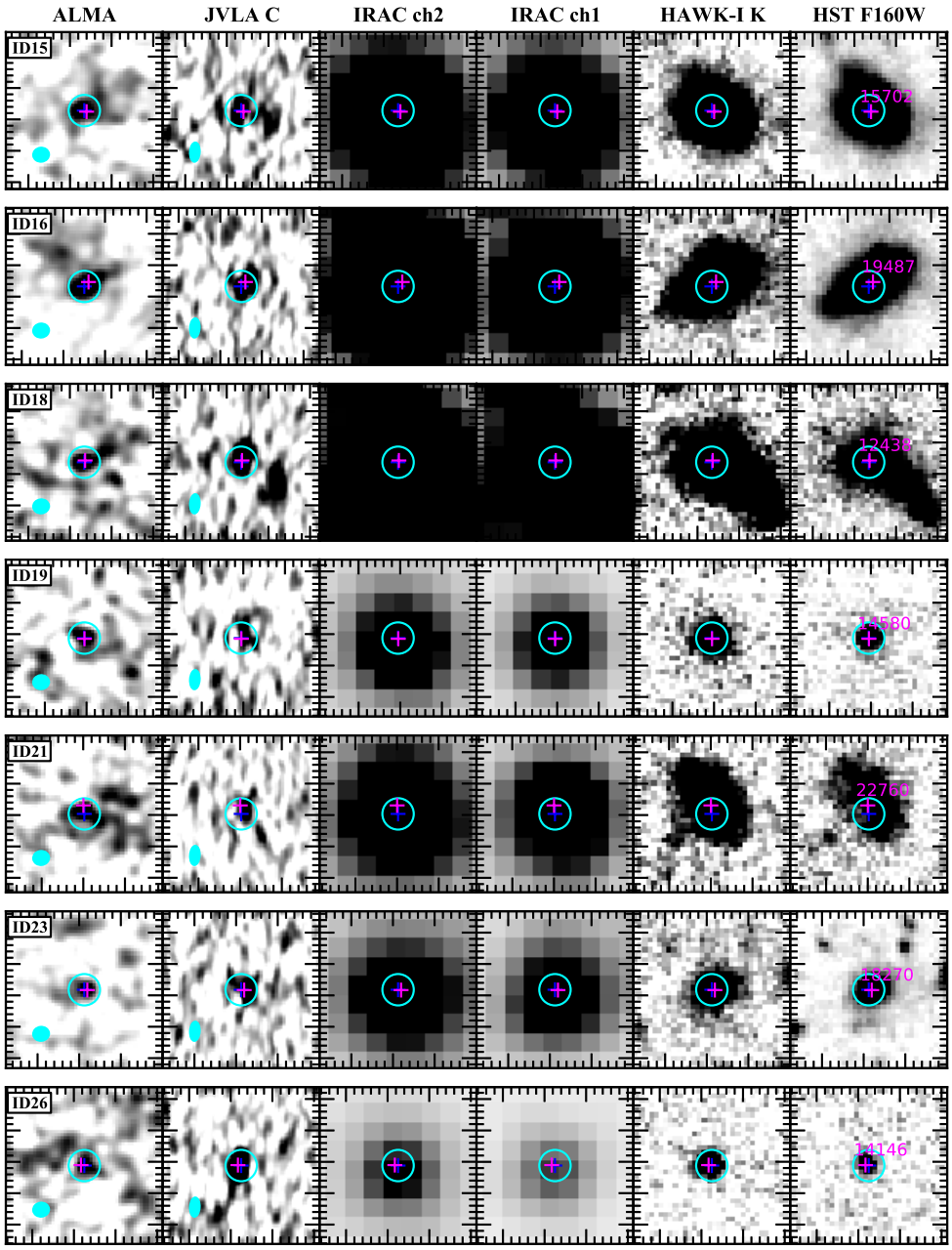

Figure A.1 (Continued.)

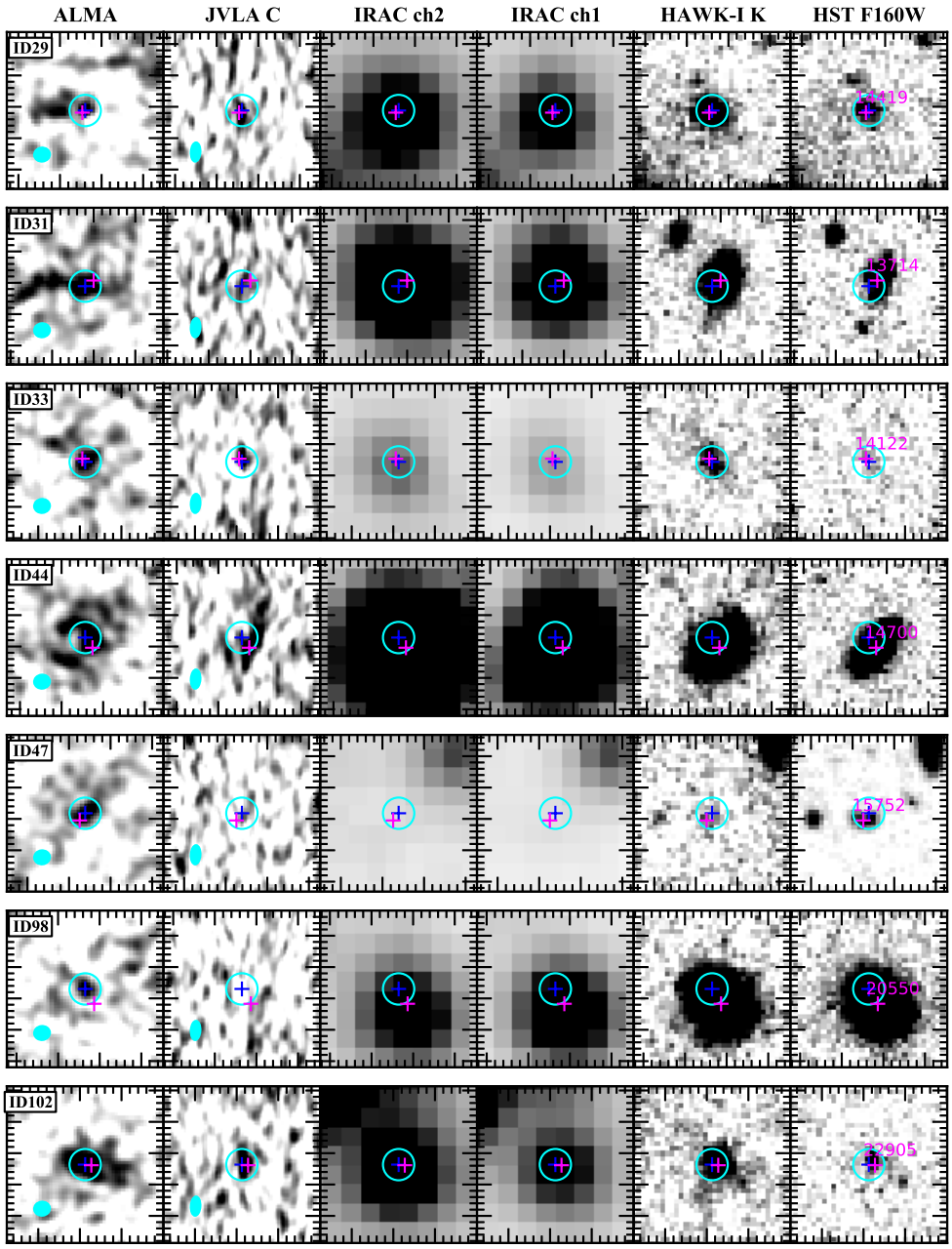

Figure A.1 (Continued.)

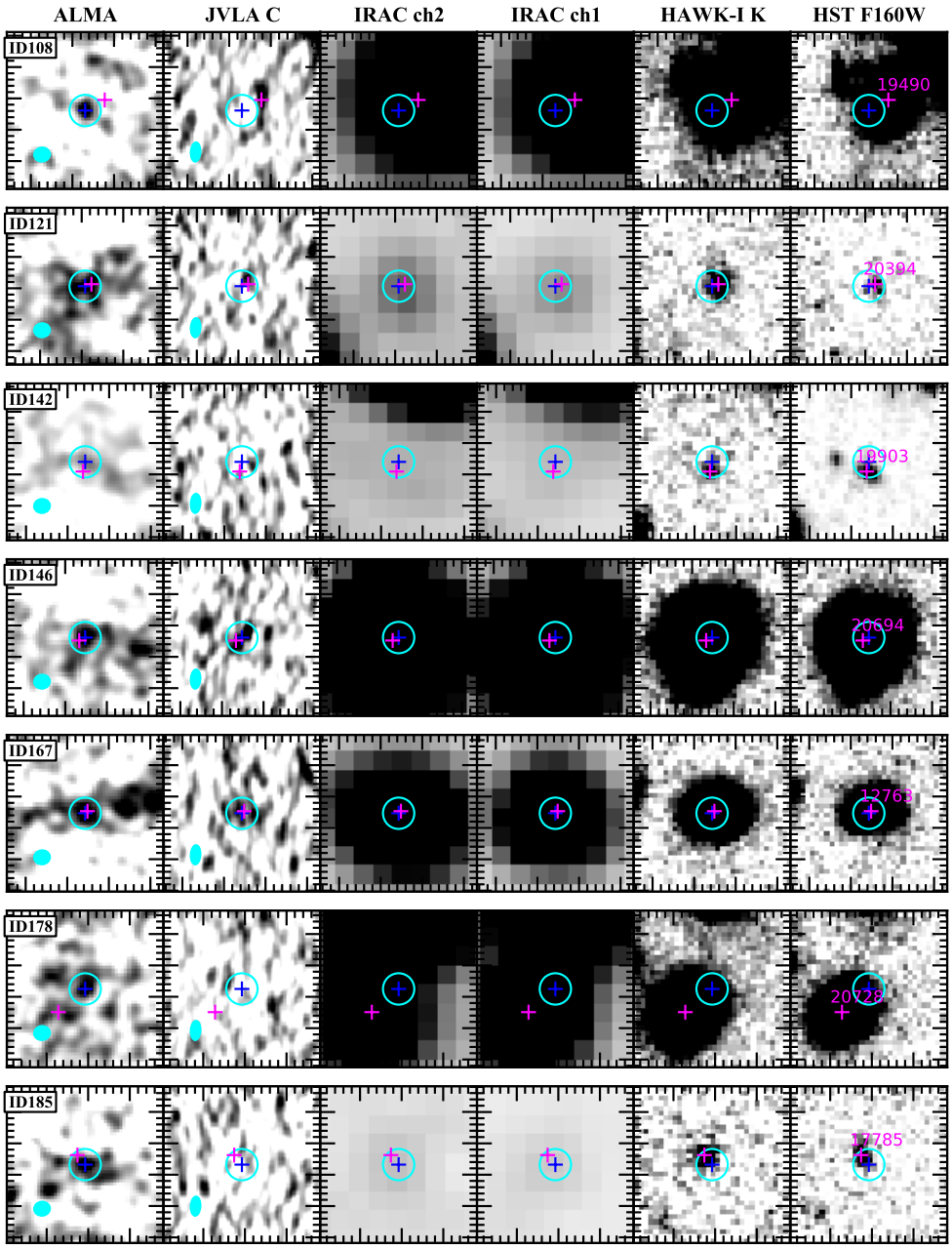

Figure A.1 (Continued.)

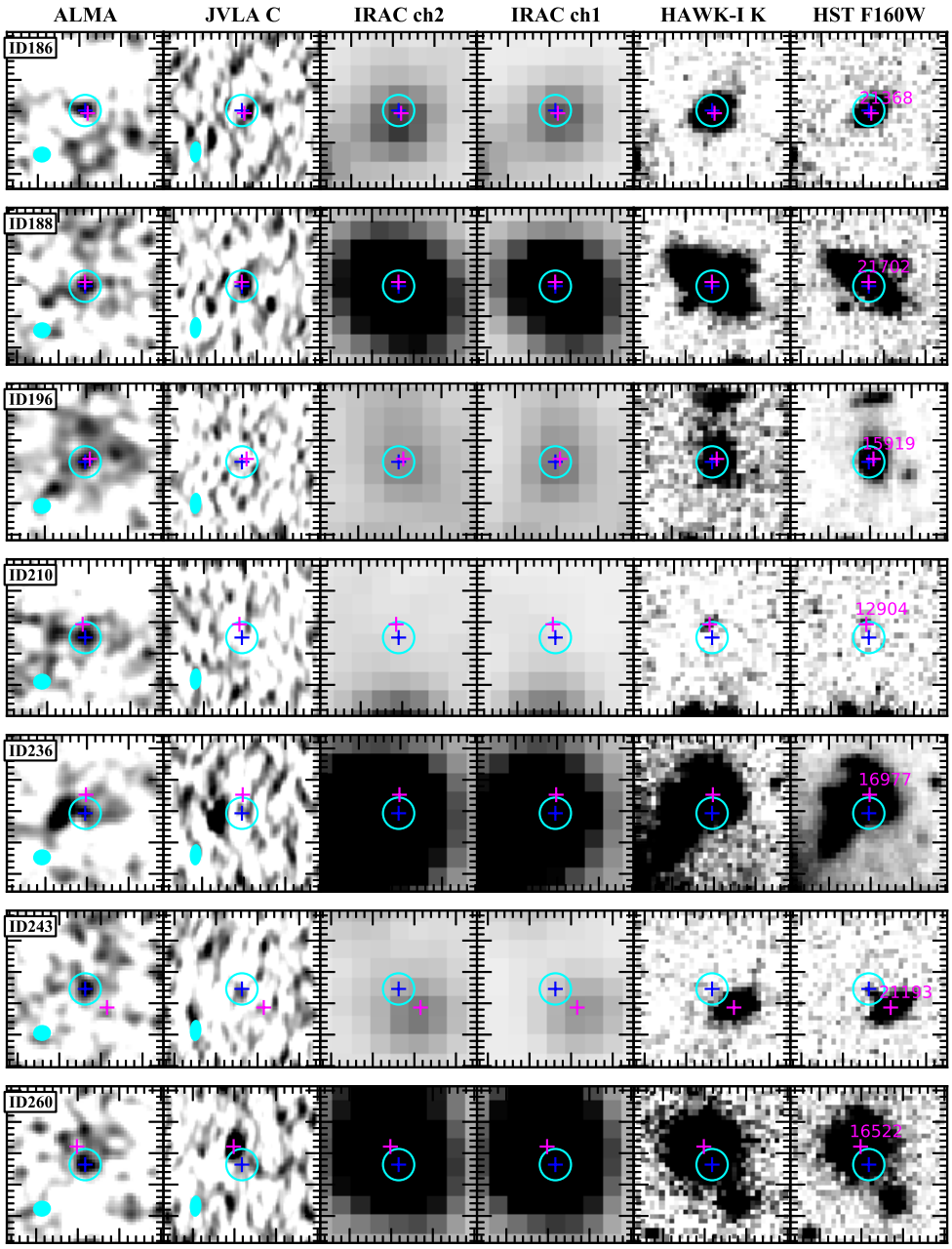

Figure A.1 (Continued.)

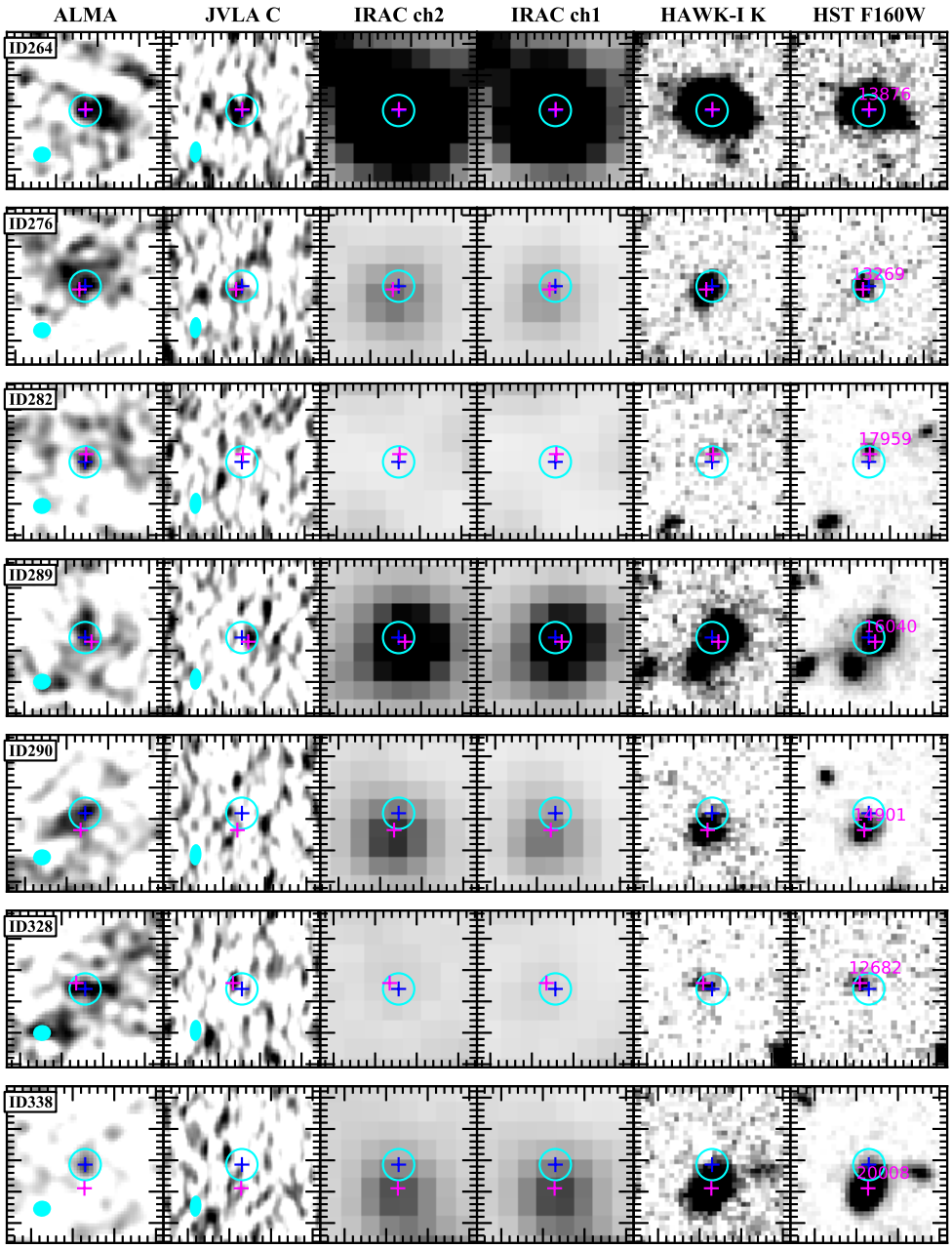

Figure A.1 (Continued.)

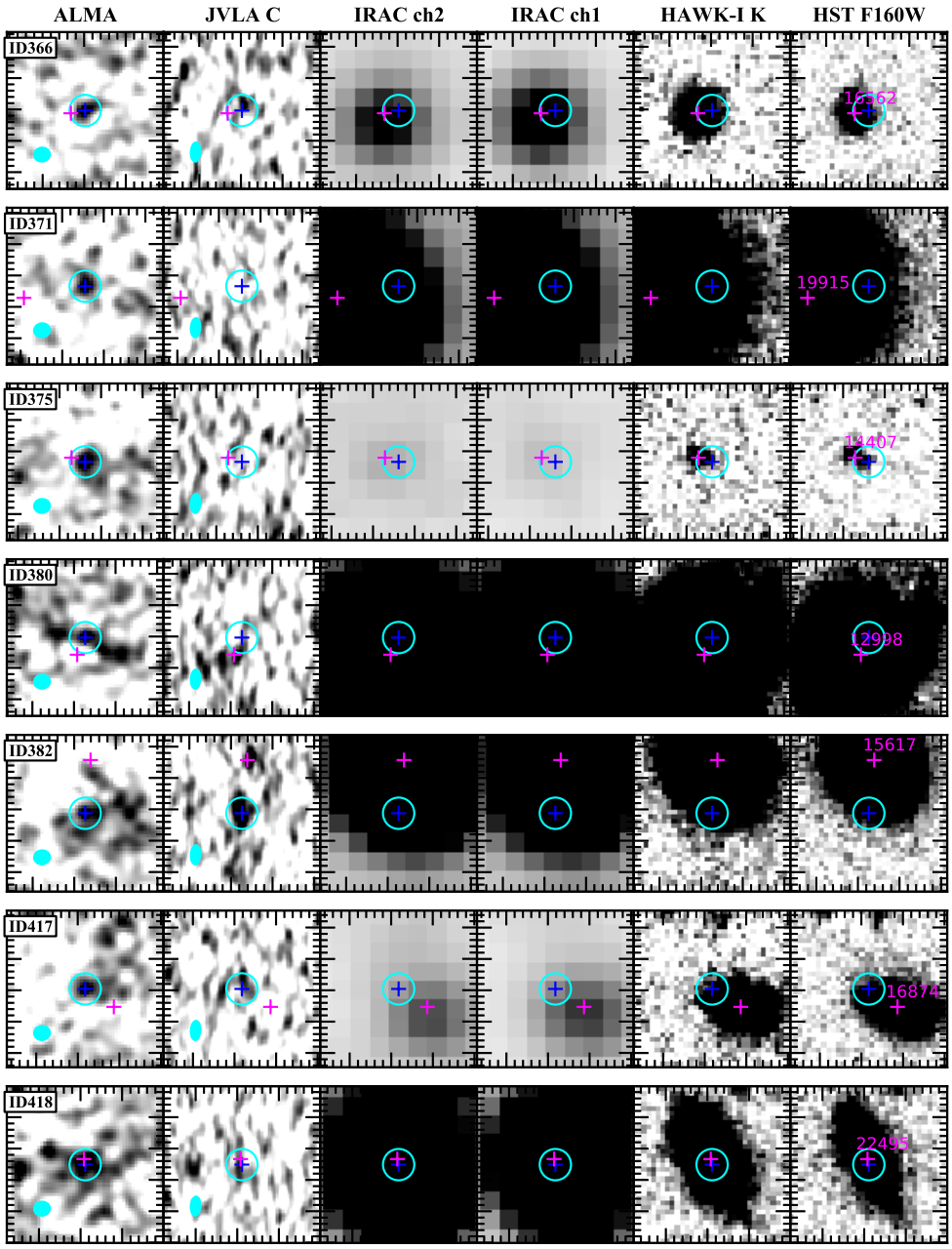

Figure A.1 (Continued.)

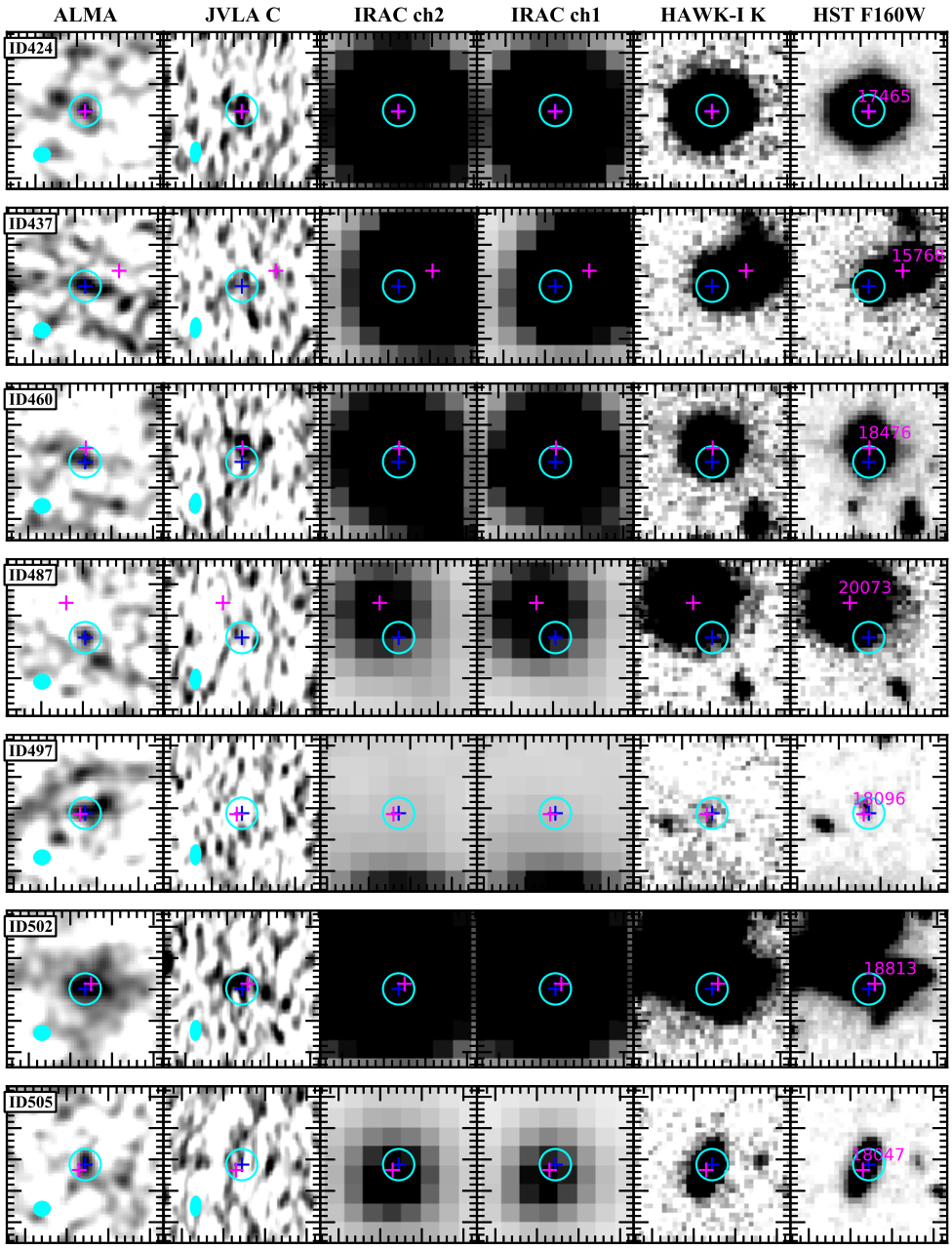

Figure A.1 (Continued.)

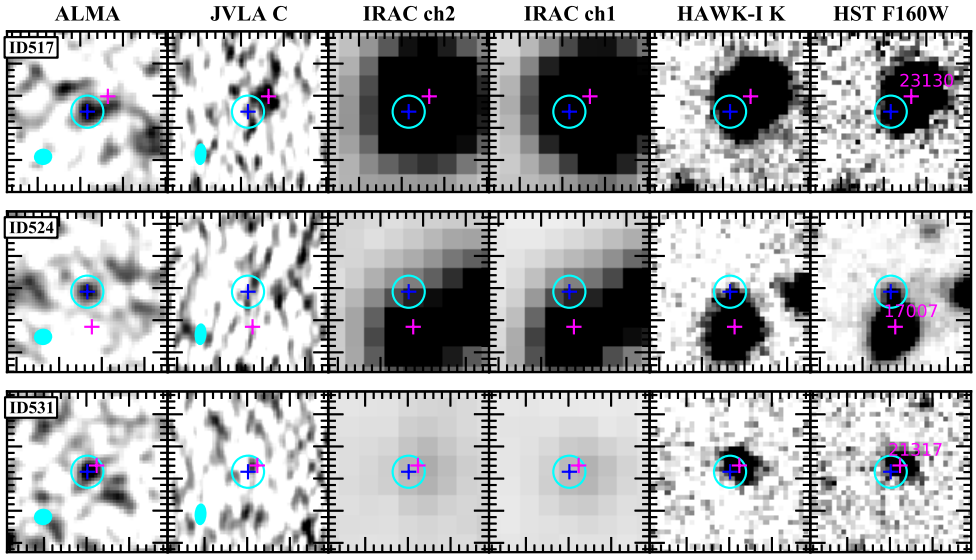

Figure A.1 (Continued.)

B

The correspondence of IDs in previous papers to ASAGAO IDs

Ueda et al. (2018) and Fujimoto et al. (2018) also report results of ASAGAO continuum sources. Aravena et al. (2016b), Dunlop et al. (2017), Franco et al. (2018), and Cowie et al. (2018) also observed the similar region of ASAGAO. In this section, we present the correspondence of their IDs to our ASAGAO IDs in Table B.1. There are no ALESS sources within the ASAGAO field.

Table B.1. The correspondence to previous ALMA surveys in GOODS-S

ASAGAO ID (1)	ID in previous studies (2)
1	UDF1, AGS6, SGS22, U3, F3
2	AGS1, SGS5, U1, F1
3	AGS3, SGS9, U2, F2
4	UDF2, AGS18, SGS25, U6, F6
5	UDF3, ASPECS/C1, AGS12, SGS48, U8, F8
6	SGS20, U4, F4
7	SGS29, U5, F6
8	AGS13, SGS40, U12, F10
9	F9
10	UDF4, F132
11	F7
12	UDF5, F322
13	UDF6, F26
14	UDF7, U7
15	UDF11, F73
16	UDF8, ASPECS/C2, F90
17	U11
19	U10, F11
23	UDF13
26	SGS54, F103
29	F148
31	F113
33	F30
44	SGS63, F66
102	SGS72
167	F52
178	F60
236	F260
380	F129
502	F180

Note. — (1) ASAGAO IDs (2) Source IDs of ASPECS (Aravena et al., 2016b), UDF (Dunlop et al., 2017), AGS (Franco et al., 2018), SGS (Cowie et al., 2018), U (Ueda et al., 2018), and F (Fujimoto et al., 2018).

C

The best fitting SEDs of ASAGAO sources

In Figure C.1, we plot our resilts of SED fittings estimated by using MAGPHYS. Procedures of our SED fit are explained in Section 3.2.2.

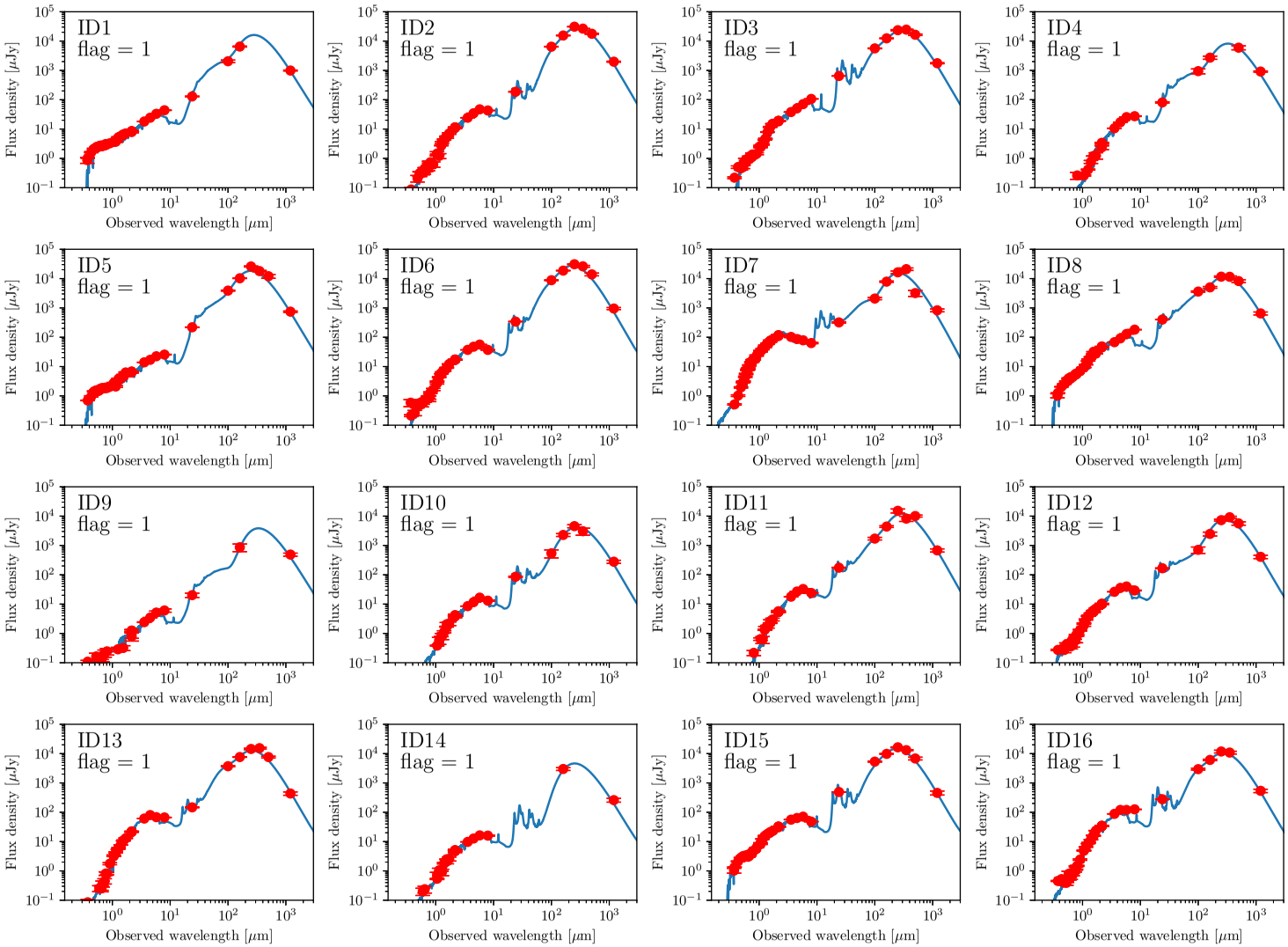

Figure C.1 Estimated SEDs of ASAGAO sources. Red symbols with errors are observed flux densities. Blue solid lines are best fit SEDs estimated by MAGPHYS (see Section 3.2.2).

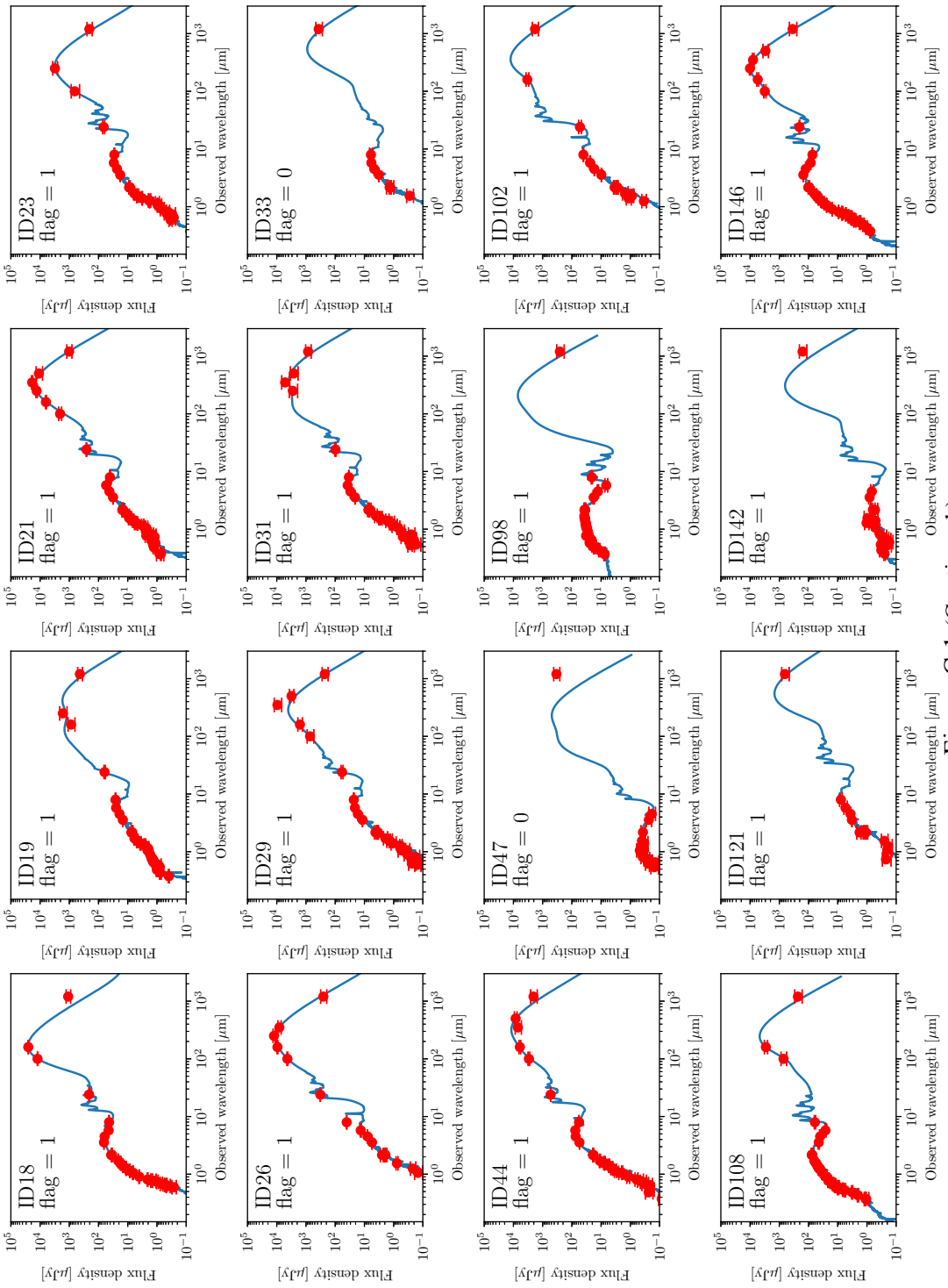

Figure C.1 (Continued.)

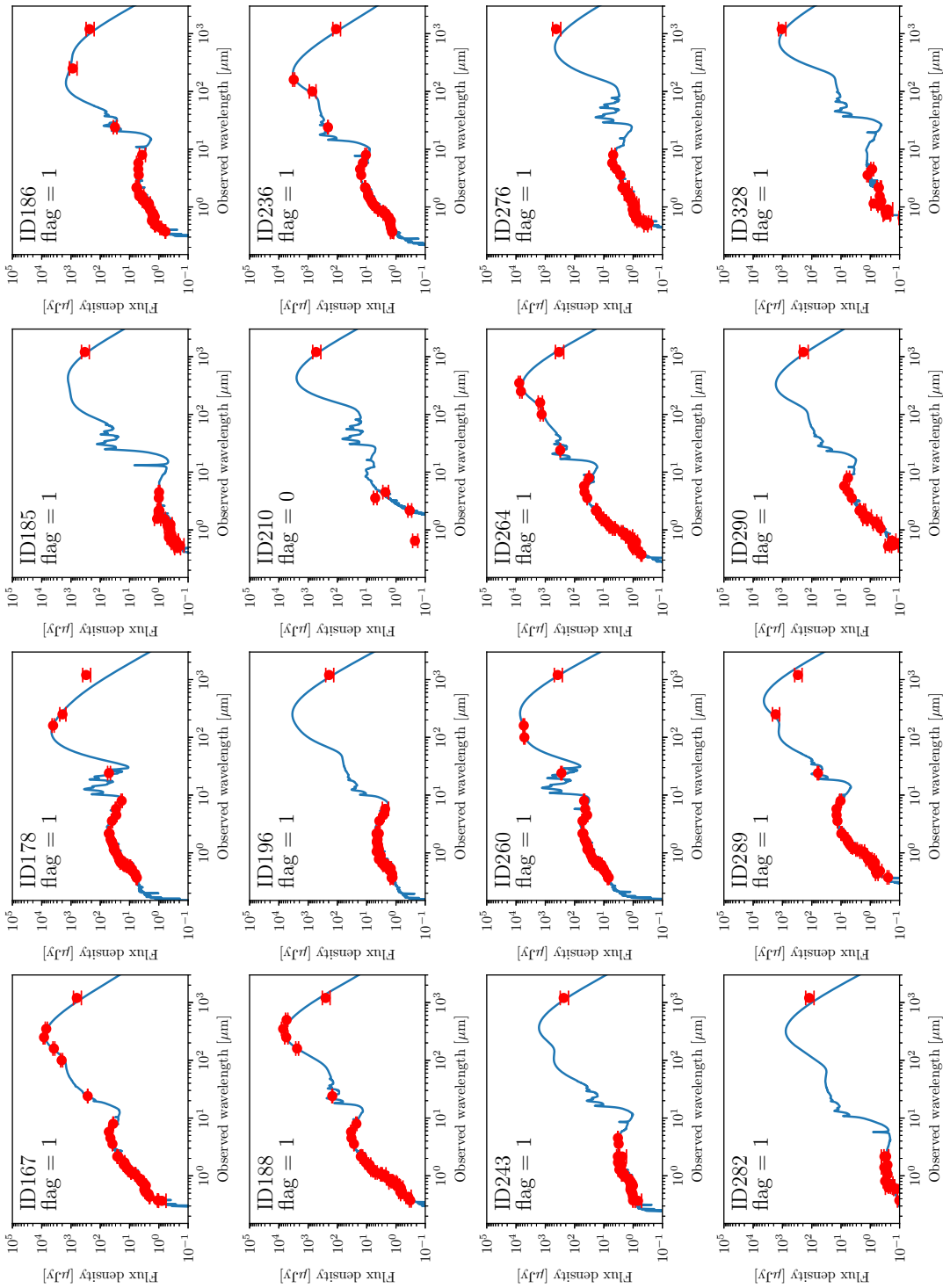

Figure C.1 (Continued.)

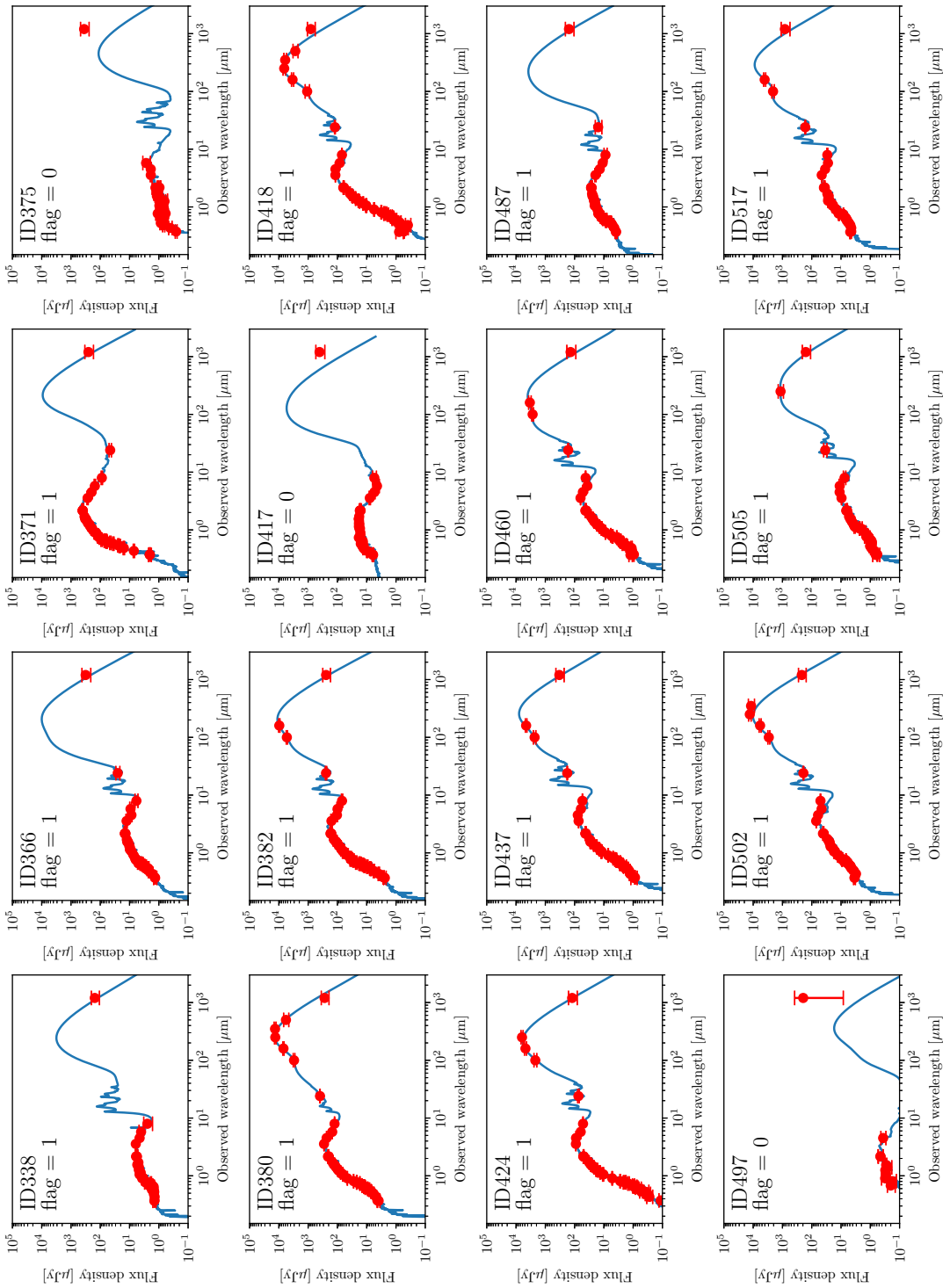

Figure C.1 (Continued.)

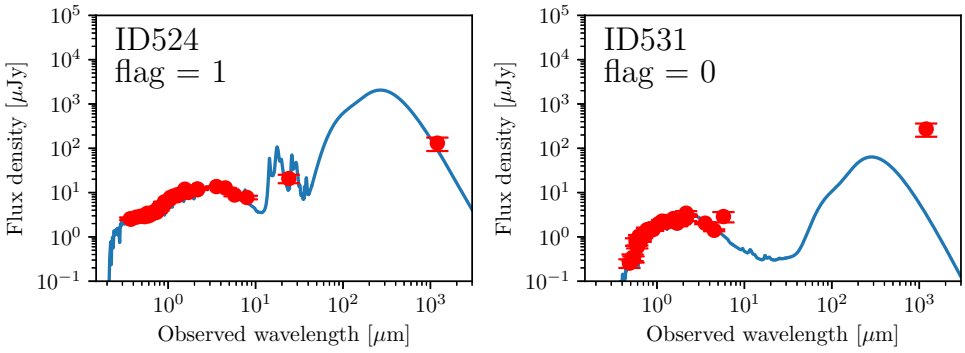

Figure C.1 (Continued.)

D

A line emitter candidate; “RXJ1347-emitter1”

We find a line emitter candidate at (R.A., Dec.) = (206.8755 deg, −11.7574 deg). In Figure D.1, we display the spectrum of RXJ1347-emitter1. RXJ1347-emitter1 is detected with S/N = 4.5 at the peak channel and with S/N = 4.3 at next to the peak channel in the 60-MHz-binning data. In the 100-MHz-binning data, it is detected with S/N = 5.8 at the peak channel. Although negative tail of the noise distribution of the 60-MHz-binning data extends to S/N = −4.5, we do not detect any pixels with S/N $<$ −5.8 in the 100-MHz-binning data. We have no atmospheric absorption lines around the peak frequency of RXJ1347-emitter1. There are no astronomical absorption features in the 3D data cubes of bandpass calibrators.

As shown in Figure D.2, RXJ1347-emitter1 has no counterpart at optical/NIR wavelengths. Thus, RXJ1347-emitter1 can be a [CII] 158 μm emitter at $z = 5.95$ rather than a CO emitter at $z \sim 1$, if it is a real line emitter. To confirm whether RXJ1347-emitter1 is a real detection or a spurious detection and determine redshift, future ALMA follow-up observation is needed.

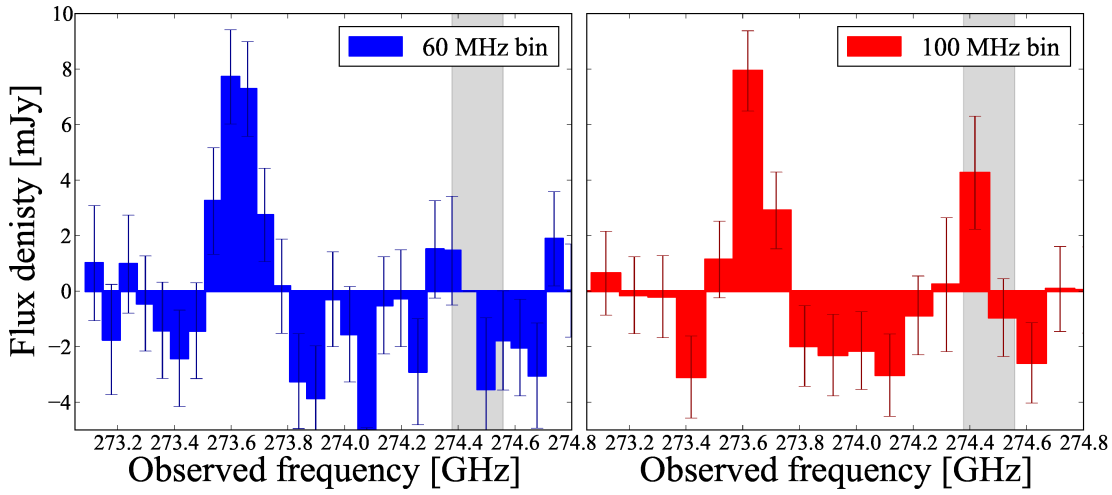

Figure D.1 From left to right, the spectrum of RXJ1347-emitter1 with 60 MHz binning and 100 MHz binning with 1σ errorbars, respectively. The gray shaded regions indicates the frequency range of an atmospheric absorption line caused by ozone.

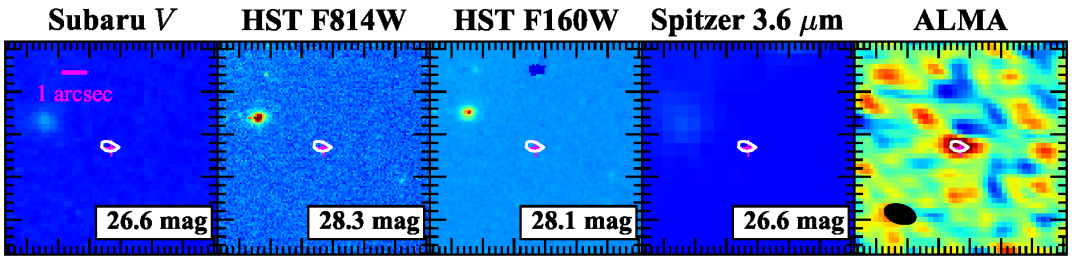

Figure D.2 From left to right: Subaru/Suprime-Cam *V* band, *HST*/ACS *F814W*, *HST*/WFC3 *F160W*, *Spitzer*/IRAC 3.6 μm, and ALMA velocity-integrated images of RXJ1347-emitter1, respectively. The magenta cross indicates the peak position of RXJ1347-emitter1. The white contour shows the 4σ level of the ALMA velocity-integrated image. The black symbol is the synthesized beam of ALMA. Insert magnitudes are apparent 3σ limiting magnitudes obtained by Postman et al. (2012), Umetsu et al. (2014), and Huang et al. (2016).

E

The publication list

Here, is the publication list of the author of this thesis.

- Yamaguchi et al. (2016), SXDF-ALMA 2 arcmin^2 deep survey: Resolving and characterizing the infrared extragalactic background light down to 0.5 mJy, PASJ, 68, 82 (based on my Master thesis)
- Yamaguchi et al. (2017), Blind Millimeter Line Emitter Search using ALMA Data Toward Gravitational Lensing Clusters, ApJ, 845, 108 (based on this thesis)
- Yamaguchi, et al. submitted, ALMA TWENTY-SIX ARCMIN^2 SURVEY OF GOODS-S AT ONE-MILLIMETER (ASAGAO): MILLIMETR PROPERTIES OF STELLAR MASS SELECTED GALAXIES (based on this thesis)
- Yamaguchi, et al. submitted, ALMA TWENTY-SIX ARCMIN^2 SURVEY OF GOODS-S AT ONE-MILLIMETER (ASAGAO): NEAR-INFRARED-DARK FAINT ALMA SOURCES (based on this thesis)

References

Alexander, D. M., Bauer, F. E., Chapman, S. C., Smail, I., Blain, A. W., Brandt, W. N., & Ivison, R. J. (2005). The X-Ray Spectral Properties of SCUBA Galaxies. *ApJ*, 632, 736–750.

Álvarez-Márquez, J., Burgarella, D., Heinis, S., Buat, V., Lo Faro, B., Béthermin, M., López-Fortín, C. E., Cooray, A., Farrah, D., Hurley, P., Ibar, E., Ilbert, O., Koekemoer, A. M., Lemaux, B. C., Pérez-Fournon, I., Rodighiero, G., Salvato, M., Scott, D., Taniguchi, Y., Vieira, J. D., & Wang, L. (2016). Dust properties of Lyman-break galaxies at z ~ 3. *A&A*, 587, A122.

Aravena, M., Decarli, R., Walter, F., Bouwens, R., Oesch, P. A., Carilli, C. L., Bauer, F. E., Da Cunha, E., Daddi, E., Gónzalez-López, J., Ivison, R. J., Riechers, D. A., Smail, I., Swinbank, A. M., Weiss, A., Anguita, T., Bacon, R., Bell, E., Bertoldi, F., Cortes, P., Cox, P., Hodge, J., Ibar, E., Inami, H., Infante, L., Karim, A., Magnelli, B., Ota, K., Popping, G., van der Werf, P., Wagg, J., & Fudamoto, Y. (2016a). The ALMA Spectroscopic Survey in the Hubble Ultra Deep Field: Search for [CII] Line and Dust Emission in 6. *ApJ*, 833, 71.

Aravena, M., Decarli, R., Walter, F., Da Cunha, E., Bauer, F. E., Carilli, C. L., Daddi, E., Elbaz, D., Ivison, R. J., Riechers, D. A., Smail, I., Swinbank, A. M., Weiss, A., Anguita, T., Assef, R. J., Bell, E., Bertoldi, F., Bacon, R., Bouwens, R., Cortes, P., Cox, P., Gónzalez-López, J., Hodge, J., Ibar, E., Inami, H., Infante, L., Karim, A., Le Le Fèvre, O., Magnelli, B., Ota, K., Popping, G., Sheth, K., van der Werf, P., & Wagg, J. (2016b). The ALMA Spectroscopic Survey in the Hubble Ultra Deep Field: Continuum Number Counts, Resolved 1.2 mm Extragalactic Background, and Properties of the Faintest Dusty Star-forming Galaxies. *ApJ*, 833, 68.

Aretxaga, I., Wilson, G. W., Aguilar, E., Alberts, S., Scott, K. S., Scoville, N., Yun, M. S., Austermann, J., Downes, T. P., Ezawa, H., Hatsukade, B., Hughes, D. H., Kawabe, R., Kohno, K., Oshima, T., Perera, T. A., Tamura, Y., & Zeballos, M. (2011). AzTEC millimetre survey of the COSMOS field - III. Source catalogue over 0.72 deg^2 and plausible boosting by large-scale structure. *MNRAS*, 415, 3831–3850.

Ashby, M. L. N., Willner, S. P., Fazio, G. G., Dunlop, J. S., Egami, E., Faber, S. M., Ferguson, H. C., Grogin, N. A., Hora, J. L., Huang, J.-S., Koekemoer, A. M., Labbé, I., & Wang, Z. (2015). S-CANDELS:

The Spitzer-Cosmic Assembly Near-Infrared Deep Extragalactic Survey. Survey Design, Photometry, and Deep IRAC Source Counts. *ApJS*, 218, 33.

Baade, D., Meisenheimer, K., Iwert, O., Alonso, J., Augusteijn, T., Beletic, J., Bellemann, H., Benesch, W., Böhm, A., Böhnhardt, H., Brewer, J., Deiries, S., Delabre, B., Donaldson, R., Dupuy, C., Franke, P., Gerdes, R., Gilliotte, A., Grimm, B., Haddad, N., Hess, G., Ihle, G., Klein, R., Lenzen, R., Lizon, J.-L., Mancini, D., Münch, N., Pizarro, A., Prado, P., Rahmer, G., Reyes, J., Richardson, F., Robledo, E., Sanchez, F., Silber, A., Sinclaire, P., Wackermann, R., & Zaggia, S. (1999). The Wide Field Imager at the 2.2-m MPG/ESO telescope: first views with a 67-million-facette eye. *The Messenger*, 95, 15–16.

Bacon, R., Accardo, M., Adjali, L., Anwand, H., Bauer, S., Biswas, I., Blaizot, J., Boudon, D., Brau-Nogue, S., Brinchmann, J., Caillier, P., Capoani, L., Carollo, C. M., Contini, T., Couderc, P., Daguisé, E., Deiries, S., Delabre, B., Dreizler, S., Dubois, J., Dupieux, M., Dupuy, C., Emsellem, E., Fechner, T., Fleischmann, A., François, M., Gallou, G., Gharsa, T., Glindemann, A., Gojak, D., Guiderdoni, B., Hansali, G., Hahn, T., Jarno, A., Kelz, A., Koehler, C., Kosmalski, J., Laurent, F., Le Floch, M., Lilly, S. J., Lizon, J.-L., Loupias, M., Manescau, A., Monstein, C., Nicklas, H., Olaya, J.-C., Pares, L., Pasquini, L., Pécontal-Rousset, A., Pelló, R., Petit, C., Popow, E., Reiss, R., Remillieux, A., Renault, E., Roth, M., Rupprecht, G., Serre, D., Schaye, J., Soucail, G., Steinmetz, M., Streicher, O., Stuik, R., Valentin, H., Vernet, J., Weilbacher, P., Wisotzki, L., & Yerle, N. (2010). The MUSE second-generation VLT instrument. In *Ground-based and Airborne Instrumentation for Astronomy III*, volume 7735 of *Proc. SPIE* (pp. 773508).

Barger, A. J., Cowie, L. L., Sanders, D. B., Fulton, E., Taniguchi, Y., Sato, Y., Kawara, K., & Okuda, H. (1998). Submillimetre-wavelength detection of dusty star-forming galaxies at high redshift. *Nature*, 394, 248–251.

Bell, E. F., Papovich, C., Wolf, C., Le Floc'h, E., Caldwell, J. A. R., Barden, M., Egami, E., McIntosh, D. H., Meisenheimer, K., Pérez-González, P. G., Rieke, G. H., Rieke, M. J., Rigby, J. R., & Rix, H.-W. (2005). Toward an Understanding of the Rapid Decline of the Cosmic Star Formation Rate. *ApJ*, 625, 23–36.

Béthermin, M., Daddi, E., Magdis, G., Lagos, C., Sargent, M., Albrecht, M., Aussel, H., Bertoldi, F., Buat, V., Galametz, M., Heinis, S., Ilbert, O., Karim, A., Koekemoer, A., Lacey, C., Le Floc'h, E., Navarrete, F., Pannella, M., Schreiber, C., Smolčić, V., Symeonidis, M., & Viero, M. (2015). Evolution of the dust emission of massive galaxies up to z = 4 and constraints on their dominant mode of star formation. *A&A*, 573, A113.

Biggs, A. D., Ivison, R. J., Ibar, E., Wardlow, J. L., Dannerbauer, H., Smail, I., Walter, F., Weiß, A., Chapman, S. C., Coppin, K. E. K., De Breuck, C., Dickinson, M., Knudsen, K. K., Mainieri, V., Menten, K., & Papovich, C. (2011). The LABOCA survey of the Extended Chandra Deep Field-South - radio and mid-infrared counterparts to submillimetre galaxies. *MNRAS*, 413, 2314–2338.

Borys, C., Smail, I., Chapman, S. C., Blain, A. W., Alexander, D. M., & Ivison, R. J. (2005). The Relationship between Stellar and Black Hole Mass in Submillimeter Galaxies. *ApJ*, 635, 853–863.

Boselli, A., Cortese, L., & Boquien, M. (2014). Cold gas properties of the Herschel Reference Survey. I. ^{12}CO(1-0) and HI data. *A&A*, 564, A65.

Bouché, N., Dekel, A., Genzel, R., Genel, S., Cresci, G., Förster Schreiber, N. M., Shapiro, K. L., Davies, R. I., & Tacconi, L. (2010). The Impact of Cold Gas Accretion Above a Mass Floor on Galaxy Scaling Relations. *ApJ*, 718, 1001–1018.

Bouwens, R. J., Aravena, M., Decarli, R., Walter, F., da Cunha, E., Labbé, I., Bauer, F. E., Bertoldi, F., Carilli, C., Chapman, S., Daddi, E., Hodge, J., Ivison, R. J., Karim, A., Le Fevre, O., Magnelli, B., Ota, K., Riechers, D., Smail, I. R., van der Werf, P., Weiss, A., Cox, P., Elbaz, D., Gonzalez-Lopez, J., Infante, L., Oesch, P., Wagg, J., & Wilkins, S. (2016). ALMA Spectroscopic Survey in the Hubble Ultra Deep Field: The Infrared Excess of UV-Selected z = 2-10 Galaxies as a Function of UV-Continuum Slope and Stellar Mass. *ApJ*, 833, 72.

Bouwens, R. J., Illingworth, G. D., Franx, M., & Ford, H. (2007). UV Luminosity Functions at z~4, 5, and 6 from the Hubble Ultra Deep Field and Other Deep Hubble Space Telescope ACS Fields: Evolution and Star Formation History. *ApJ*, 670, 928–958.

Bouwens, R. J., Illingworth, G. D., Oesch, P. A., Trenti, M., Labbé, I., Bradley, L., Carollo, M., van Dokkum, P. G., Gonzalez, V., Holwerda, B., Franx, M., Spitler, L., Smit, R., & Magee, D. (2015). UV Luminosity Functions at Redshifts z $\sim$ 4 to z $\sim$ 10: 10,000 Galaxies from HST Legacy Fields. *ApJ*, 803, 34.

Bouwens, R. J., Illingworth, G. D., Oesch, P. A., Trenti, M., Labbé, I., Franx, M., Stiavelli, M., Carollo, C. M., van Dokkum, P., & Magee, D. (2012). Lower-luminosity Galaxies Could Reionize the Universe: Very Steep Faint-end Slopes to the UV Luminosity Functions at z $\geq$ 5-8 from the HUDF09 WFC3/IR Observations. *ApJL*, 752, L5.

Brammer, G. B., van Dokkum, P. G., & Coppi, P. (2008). EAZY: A Fast, Public Photometric Redshift Code. *ApJ*, 686, 1503–1513.

Brammer, G. B., Whitaker, K. E., van Dokkum, P. G., Marchesini, D., Franx, M., Kriek, M., Labbé, I., Lee, K.-S., Muzzin, A., Quadri, R. F., Rudnick, G., & Williams, R. (2011). The Number Density and Mass Density of Star-forming and Quiescent Galaxies at $0.4 \leq z \leq 2.2$. *ApJ*, 739, 24.

Bruzual, G. & Charlot, S. (2003). Stellar population synthesis at the resolution of 2003. *MNRAS*, 344, 1000–1028.

Burgarella, D., Buat, V., Gruppioni, C., Cucciati, O., Heinis, S., Berta, S., Béthermin, M., Bock, J., Cooray, A., Dunlop, J. S., Farrah, D., Franceschini, A., Le Floc'h, E., Lutz, D., Magnelli, B., Nordon, R., Oliver, S. J., Page, M. J., Popesso, P., Pozzi, F., Riguccini, L., Vaccari, M., & Viero, M. (2013). Herschel PEP/HerMES: the redshift evolution (0 *leq* $z \leq 4$) of dust attenuation and of the total (UV+IR) star formation rate density. *A&A*, 554, A70.

Capak, P. L., Carilli, C., Jones, G., Casey, C. M., Riechers, D., Sheth, K., Carollo, C. M., Ilbert, O., Karim, A., Lefevre, O., Lilly, S., Scoville, N., Smolcic, V., & Yan, L. (2015). Galaxies at redshifts 5 to 6 with systematically low dust content and high [CII] emission. *Nature*, 522, 455–458.

Cardamone, C. N., van Dokkum, P. G., Urry, C. M., Taniguchi, Y., Gawiser, E., Brammer, G., Taylor, E., Damen, M., Treister, E., Cobb, B. E., Bond, N., Schawinski, K., Lira, P., Murayama, T., Saito, T., & Sumikawa, K. (2010). The Multiwavelength Survey by Yale-Chile (MUSYC): Deep Medium-band Optical Imaging and High-quality 32-band Photometric Redshifts in the ECDF-S. *ApJS*, 189, 270–285.

Carilli, C. L. & Walter, F. (2013). Cool Gas in High-Redshift Galaxies. *ARA&A*, 51, 105–161.

Carilli, C. L. & Yun, M. S. (1999). The Radio-to-Submillimeter Spectral Index as a Redshift Indicator. *ApJL*, 513, L13–L16.

Carniani, S., Maiolino, R., De Zotti, G., Negrello, M., Marconi, A., Bothwell, M. S., Capak, P., Carilli, C., Castellano, M., Cristiani, S., Ferrara, A., Fontana, A., Gallerani, S., Jones, G., Ohta, K., Ota, K., Pentericci, L., Santini, P., Sheth, K., Vallini, L., Vanzella, E., Wagg, J., & Williams, R. J. (2015). ALMA constraints on the faint millimetre source number counts and their contribution to the cosmic infrared background. *A&A*, 584, A78.

Casey, C. M., Chen, C.-C., Cowie, L. L., Barger, A. J., Capak, P., Ilbert, O., Koss, M., Lee, N., Le Floc'h, E., Sanders, D. B., & Williams, J. P. (2013). Characterization of SCUBA-2 450 μm and 850 μm selected galaxies in the COSMOS field. *MNRAS*, 436, 1919–1954.

Casey, C. M., Hodge, J., Zavala, J. A., Spilker, J., da Cunha, E., Staguhn, J., Finkelstein, S. L., & Drew, P. (2018). An Analysis of ALMA Deep Fields and the Perceived Dearth of High-z Galaxies. *ApJ*, 862, 78.

Casey, C. M., Hodge, J. A., Lacy, M., Hales, C. A., Barger, A., Narayanan, D., Carilli, C., Alatalo, K., da Cunha, E., Emonts, B., Ivison, R., Kimball, A., Kohno, K., Murphy, E., Riechers, D., Sargent, M., & Walter, F. (2015). Next Generation Very Large Array Memo No. 8 Science Working Group 3: Galaxy Assembly through Cosmic Time. *ArXiv e-prints*.

Casey, C. M., Scoville, N. Z., Sanders, D. B., Lee, N., Cooray, A., Finkelstein, S. L., Capak, P., Conley, A., De Zotti, G., Farrah, D., Fu, H., Le Floc'h, E., Ilbert, O., Ivison, R. J., & Takeuchi, T. T. (2014). Are Dusty Galaxies Blue? Insights on UV Attenuation from Dust-selected Galaxies. *ApJ*, 796, 95.

Chabrier, G. (2003). Galactic Stellar and Substellar Initial Mass Function. *PASP*, 115, 763–795.

Chapman, S. C., Blain, A. W., Smail, I., & Ivison, R. J. (2005). A Redshift Survey of the Submillimeter Galaxy Population. *ApJ*, 622, 772–796.

Chapman, S. C., Ivison, R. J., Roseboom, I. G., Auld, R., Bock, J., Brisbin, D., Burgarella, D., Chanial, P., Clements, D. L., Cooray, A., Eales, S., Franceschini, A., Giovannoli, E., Glenn, J., Griffin, M., Mortier, A. M. J., Oliver, S. J., Omont, A., Page, M. J., Papageorgiou, A., Pearson, C. P., Pérez-Fournon, I., Pohlen, M., Rawlings, J. I., Raymond, G., Rodighiero, G., Rowan-Robinson, M., Scott, D., Seymour, N., Smith, A. J., Symeonidis, M., Tugwell, K. E., Vaccari, M., Vieira, J. D., Vigroux, L., Wang, L., & Wright, G. (2010). Herschel-SPIRE, far-infrared properties of millimetre-bright and -faint radio galaxies. *MNRAS*, 409, L13–L18.

Charlot, S. & Fall, S. M. (2000). A Simple Model for the Absorption of Starlight by Dust in Galaxies. *ApJ*, 539, 718–731.

Chen, C.-C., Hodge, J. A., Smail, I., Swinbank, A. M., Walter, F., Simpson, J. M., Calistro Rivera, G., Bertoldi, F., Brandt, W. N., Chapman, S. C., da Cunha, E., Dannerbauer, H., De Breuck, C., Harrison, C. M., Ivison, R. J., Karim, A., Knudsen, K. K., Wardlow, J. L., Weiß, A., & van der Werf, P. P. (2017). A Spatially Resolved Study of Cold Dust, Molecular Gas, H II Regions, and Stars in the z = 2.12 Submillimeter Galaxy ALESS67.1. *ApJ*, 846, 108.

Clemens, M. S., Negrello, M., De Zotti, G., Gonzalez-Nuevo, J., Bonavera, L., Cosco, G., Guarese, G., Boaretto, L., Salucci, P., Baccigalupi, C., Clements, D. L., Danese, L., Lapi, A., Mandolesi, N., Partridge, R. B., Perrotta, F., Serjeant, S., Scott, D., & Toffolatti, L. (2013). Dust and star formation

properties of a complete sample of local galaxies drawn from the Planck Early Release Compact Source Catalogue. *MNRAS*, 433, 695–711.

Coppin, K., Chapin, E. L., Mortier, A. M. J., Scott, S. E., Borys, C., Dunlop, J. S., Halpern, M., Hughes, D. H., Pope, A., Scott, D., Serjeant, S., Wagg, J., Alexander, D. M., Almaini, O., Aretxaga, I., Babbedge, T., Best, P. N., Blain, A., Chapman, S., Clements, D. L., Crawford, M., Dunne, L., Eales, S. A., Edge, A. C., Farrah, D., Gaztañaga, E., Gear, W. K., Granato, G. L., Greve, T. R., Fox, M., Ivison, R. J., Jarvis, M. J., Jenness, T., Lacey, C., Lepage, K., Mann, R. G., Marsden, G., Martinez-Sansigre, A., Oliver, S., Page, M. J., Peacock, J. A., Pearson, C. P., Percival, W. J., Priddey, R. S., Rawlings, S., Rowan-Robinson, M., Savage, R. S., Seigar, M., Sekiguchi, K., Silva, L., Simpson, C., Smail, I., Stevens, J. A., Takagi, T., Vaccari, M., van Kampen, E., & Willott, C. J. (2006). The SCUBA Half-Degree Extragalactic Survey - II. Submillimetre maps, catalogue and number counts. *MNRAS*, 372, 1621–1652.

Coppin, K. E. K., Geach, J. E., Almaini, O., Arumugam, V., Dunlop, J. S., Hartley, W. G., Ivison, R. J., Simpson, C. J., Smith, D. J. B., Swinbank, A. M., Blain, A. W., Bourne, N., Bremer, M., Conselice, C., Harrison, C. M., Mortlock, A., Chapman, S. C., Davies, L. J. M., Farrah, D., Gibb, A., Jenness, T., Karim, A., Knudsen, K. K., Ibar, E., Michałowski, M. J., Peacock, J. A., Rigopoulou, D., Robson, E. I., Scott, D., Stevens, J., & van der Werf, P. P. (2015). The SCUBA-2 Cosmology Legacy Survey: the submillimetre properties of Lyman-break galaxies at z = 3-5. *MNRAS*, 446, 1293–1304.

Cowie, L. L., Barger, A. J., Hsu, L.-Y., Chen, C.-C., Owen, F. N., & Wang, W.-H. (2017). A Submillimeter Perspective on the GOODS Fields (SUPER GOODS). I. An Ultradeep SCUBA-2 Survey of the GOODS-N. *ApJ*, 837, 139.

Cowie, L. L., González-López, J., Barger, A. J., Bauer, F. E., Hsu, L.-Y., & Wang, W.-H. (2018). A Submillimeter Perspective on the GOODS Fields (SUPER GOODS). III. A Large Sample of ALMA Sources in the GOODS-S. *ApJ*, 865, 106.

Cowley, M. J., Spitler, L. R., Tran, K.-V. H., Rees, G. A., Labbé, I., Allen, R. J., Brammer, G. B., Glazebrook, K., Hopkins, A. M., Juneau, S., Kacprzak, G. G., Mullaney, J. R., Nanayakkara, T., Papovich, C., Quadri, R. F., Straatman, C. M. S., Tomczak, A. R., & van Dokkum, P. G. (2016). ZFOURGE catalogue of AGN candidates: an enhancement of 160-μm-derived star formation rates in active galaxies to z = 3.2. *MNRAS*, 457, 629–641.

da Cunha, E., Charlot, S., & Elbaz, D. (2008). A simple model to interpret the ultraviolet, optical and infrared emission from galaxies. *MNRAS*, 388, 1595–1617.

da Cunha, E., Walter, F., Smail, I. R., Swinbank, A. M., Simpson, J. M., Decarli, R., Hodge, J. A., Weiss, A., van der Werf, P. P., Bertoldi, F., Chapman, S. C., Cox, P., Danielson, A. L. R., Dannerbauer, H., Greve, T. R., Ivison, R. J., Karim, A., & Thomson, A. (2015). An ALMA Survey of Sub-millimeter Galaxies in the Extended Chandra Deep Field South: Physical Properties Derived from Ultraviolet-to-radio Modeling. *ApJ*, 806, 110.

Daddi, E., Dannerbauer, H., Krips, M., Walter, F., Dickinson, M., Elbaz, D., & Morrison, G. E. (2009). A CO Emission Line from the Optical and Near-IR Undetected Submillimeter Galaxy GN10. *ApJL*, 695, L176–L180.

Dale, D. A. & Helou, G. (2002). The Infrared Spectral Energy Distribution of Normal Star-forming Galaxies: Calibration at Far-Infrared and Submillimeter Wavelengths. *ApJ*, 576, 159–168.

Davé, R., Finlator, K., & Oppenheimer, B. D. (2012). An analytic model for the evolution of the stellar, gas and metal content of galaxies. *MNRAS*, 421, 98–107.

de Barros, S., Schaerer, D., & Stark, D. P. (2014). Properties of z ~ 3-6 Lyman break galaxies. II. Impact of nebular emission at high redshift. *A&A*, 563, A81.

De Looze, I., Baes, M., Bendo, G. J., Cortese, L., & Fritz, J. (2011). The reliability of [CII] as an indicator of the star formation rate. *MNRAS*, 416, 2712–2724.

De Looze, I., Cormier, D., Lebouteiller, V., Madden, S., Baes, M., Bendo, G. J., Boquien, M., Boselli, A., Clements, D. L., Cortese, L., Cooray, A., Galametz, M., Galliano, F., Graciá-Carpio, J., Isaak, K., Karczewski, O. Ł., Parkin, T. J., Pellegrini, E. W., Rémy-Ruyer, A., Spinoglio, L., Smith, M. W. L., & Sturm, E. (2014). The applicability of far-infrared fine-structure lines as star formation rate tracers over wide ranges of metallicities and galaxy types. *A&A*, 568, A62.

Decarli, R., Walter, F., Aravena, M., Carilli, C., Bouwens, R., da Cunha, E., Daddi, E., Ivison, R. J., Popping, G., Riechers, D., Smail, I. R., Swinbank, M., Weiss, A., Anguita, T., Assef, R. J., Bauer, F. E., Bell, E. F., Bertoldi, F., Chapman, S., Colina, L., Cortes, P. C., Cox, P., Dickinson, M., Elbaz, D., Gónzalez-López, J., Ibar, E., Infante, L., Hodge, J., Karim, A., Le Fevre, O., Magnelli, B., Neri, R., Oesch, P., Ota, K., Rix, H.-W., Sargent, M., Sheth, K., van der Wel, A., van der Werf, P., & Wagg, J. (2016). ALMA Spectroscopic Survey in the Hubble Ultra Deep Field: CO Luminosity Functions and the Evolution of the Cosmic Density of Molecular Gas. *ApJ*, 833, 69.

Decarli, R., Walter, F., Carilli, C., Riechers, D., Cox, P., Neri, R., Aravena, M., Bell, E., Bertoldi, F., Colombo, D., Da Cunha, E., Daddi, E., Dickinson, M., Downes, D., Ellis, R., Lentati, L., Maiolino, R.,

Menten, K. M., Rix, H.-W., Sargent, M., Stark, D., Weiner, B., & Weiss, A. (2014). A Molecular Line Scan in the Hubble Deep Field North. *ApJ*, 782, 78.

Dickinson, M. & FIDEL Team (2007). The Far-Infrared Deep Extragalactic Legacy Survey. In *American Astronomical Society Meeting Abstracts*, volume 39 of *Bulletin of the American Astronomical Society* (pp. 822).

Dickinson, M., Giavalisco, M., & GOODS Team (2003). The Great Observatories Origins Deep Survey. In R. Bender & A. Renzini (Eds.), *The Mass of Galaxies at Low and High Redshift* (pp. 324).

Downes, A. J. B., Peacock, J. A., Savage, A., & Carrie, D. R. (1986). The Parkes selected regions - Powerful radio galaxies and quasars at high redshifts. *MNRAS*, 218, 31–62.

Dunlop, J. S., McLure, R. J., Biggs, A. D., Geach, J. E., Michałowski, M. J., Ivison, R. J., Rujopakarn, W., van Kampen, E., Kirkpatrick, A., Pope, A., Scott, D., Swinbank, A. M., Targett, T. A., Aretxaga, I., Austermann, J. E., Best, P. N., Bruce, V. A., Chapin, E. L., Charlot, S., Cirasuolo, M., Coppin, K., Ellis, R. S., Finkelstein, S. L., Hayward, C. C., Hughes, D. H., Ibar, E., Jagannathan, P., Khochfar, S., Koprowski, M. P., Narayanan, D., Nyland, K., Papovich, C., Peacock, J. A., Rieke, G. H., Robertson, B., Vernstrom, T., Werf, P. P. v. d., Wilson, G. W., & Yun, M. (2017). A deep ALMA image of the Hubble Ultra Deep Field. *MNRAS*, 466, 861–883.

Dunne, L., Clements, D. L., & Eales, S. A. (2000). Constraining the radio-submillimetre redshift indicator using data from the SCUBA Local Universe Galaxy Survey. *MNRAS*, 319, 813–820.

Eales, S., Lilly, S., Gear, W., Dunne, L., Bond, J. R., Hammer, F., Le Fèvre, O., & Crampton, D. (1999). The Canada-UK Deep Submillimeter Survey: First Submillimeter Images, the Source Counts, and Resolution of the Background. *ApJ*, 515, 518–524.

Elbaz, D., Dickinson, M., Hwang, H. S., Díaz-Santos, T., Magdis, G., Magnelli, B., Le Borgne, D., Galliano, F., Pannella, M., Chanial, P., Armus, L., Charmandaris, V., Daddi, E., Aussel, H., Popesso, P., Kartaltepe, J., Altieri, B., Valtchanov, I., Coia, D., Dannerbauer, H., Dasyra, K., Leiton, R., Mazzarella, J., Alexander, D. M., Buat, V., Burgarella, D., Chary, R.-R., Gilli, R., Ivison, R. J., Juneau, S., Le Floc'h, E., Lutz, D., Morrison, G. E., Mullaney, J. R., Murphy, E., Pope, A., Scott, D., Brodwin, M., Calzetti, D., Cesarsky, C., Charlot, S., Dole, H., Eisenhardt, P., Ferguson, H. C., Förster Schreiber, N., Frayer, D., Giavalisco, M., Huynh, M., Koekemoer, A. M., Papovich, C., Reddy, N., Surace, C., Teplitz, H., Yun, M. S., & Wilson, G. (2011). GOODS-Herschel: an infrared main sequence for star-forming galaxies. *A&A*, 533, A119.

Erben, T., Schirmer, M., Dietrich, J. P., Cordes, O., Haberzettl, L., Hetterscheidt, M., Hildebrandt, H., Schmithuesen, O., Schneider, P., Simon, P., Deul, E., Hook, R. N., Kaiser, N., Radovich, M., Benoist, C., Nonino, M., Olsen, L. F., Prandoni, I., Wichmann, R., Zaggia, S., Bomans, D., Dettmar, R. J., & Miralles, J. M. (2005). GaBoDS: The Garching-Bonn Deep Survey. IV. Methods for the image reduction of multi-chip cameras demonstrated on data from the ESO Wide-Field Imager. *Astronomische Nachrichten*, 326, 432–464.

Faisst, A. L., Capak, P. L., Yan, L., Pavesi, R., Riechers, D. A., Barišić, I., Cooke, K. C., Kartaltepe, J. S., & Masters, D. C. (2017). Are High-redshift Galaxies Hot? Temperature of z $>$ 5 Galaxies and Implications for Their Dust Properties. *ApJ*, 847, 21.

Fazio, G. G., Hora, J. L., Allen, L. E., Ashby, M. L. N., Barmby, P., Deutsch, L. K., Huang, J.-S., Marengo, M., Megeath, S. T., Pahre, M. A., Patten, B. M., Wang, Z., Willner, S. P., Hoffmann, W. F., Moseley, S. H., Arendt, R. G., Mentzell, J. E., Trout-Marx, C., Eisenhardt, E., Stern, D., Gorjian, V., Bhattacharya, B., Carey, S., Glaccum, W. J., Lacy, M., Lowrance, P. J., Laine, S., Nelson, B. O., Reach, W. T., Stauffer, J. R., Surace, J. A., Wilson, G., Pipher, J. L., Forrest, W. J., McMurty, C. W., McCreight, C. R., McKelvey, M. E., & McMurray, R. E. (2004). In-Flight Performance of the Infrared Array Camera (IRAC) for the Spitzer Space Telescope. In *American Astronomical Society Meeting Abstracts #204*, volume 36 of *Bulletin of the American Astronomical Society* (pp. 699).

Fontana, A., Dunlop, J. S., Paris, D., Targett, T. A., Boutsia, K., Castellano, M., Galametz, A., Grazian, A., McLure, R., Merlin, E., Pentericci, L., Wuyts, S., Almaini, O., Caputi, K., Chary, R.-R., Cirasuolo, M., Conselice, C. J., Cooray, A., Daddi, E., Dickinson, M., Faber, S. M., Fazio, G., Ferguson, H. C., Giallongo, E., Giavalisco, M., Grogin, N. A., Hathi, N., Koekemoer, A. M., Koo, D. C., Lucas, R. A., Nonino, M., Rix, H. W., Renzini, A., Rosario, D., Santini, P., Scarlata, C., Sommariva, V., Stark, D. P., van der Wel, A., Vanzella, E., Wild, V., Yan, H., & Zibetti, S. (2014). The Hawk-I UDS and GOODS Survey (HUGS): Survey design and deep K-band number counts. *A&A*, 570, A11.

Ford, H. C., Bartko, F., Bely, P. Y., Broadhurst, T., Burrows, C. J., Cheng, E. S., Clampin, M., Crocker, J. H., Feldman, P. D., Golimowski, D. A., Hartig, G. F., Illingworth, G., Kimble, R. A., Lesser, M. P., Miley, G., Neff, S. G., Postman, M., Sparks, W. B., Tsvetanov, Z., White, R. L., Sullivan, P., Krebs, C. A., Leviton, D. B., La Jeunesse, T., Burmester, W., Fike, S., Johnson, R., Slusher, R. B., Volmer, P., & Woodruff, R. A. (1998). Advanced camera for the Hubble Space Telescope. In P. Y. Bely & J. B. Breckinridge (Eds.), *Space Telescopes and Instruments V*, volume 3356 of *Proc. SPIE* (pp. 234–248).

Franco, M., Elbaz, D., Béthermin, M., Magnelli, B., Schreiber, C., Ciesla, L., Dickinson, M., Nagar, N., Silverman, J., Daddi, E., Alexander, D. M., Wang, T., Pannella, M., Le Floc'h, E., Pope, A., Giavalisco,

M., Maury, A. J., Bournaud, F., Chary, R., Demarco, R., Ferguson, H., Finkelstein, S. L., Inami, H., Iono, D., Juneau, S., Lagache, G., Leiton, R., Lin, L., Magdis, G., Messias, H., Motohara, K., Mullaney, J., Okumura, K., Papovich, C., Pforr, J., Rujopakarn, W., Sargent, M., Shu, X., & Zhou, L. (2018). GOODS-ALMA: 1.1 mm galaxy survey. I. Source catalog and optically dark galaxies. *A&A*, 620, A152.

Fudamoto, Y., Oesch, P. A., Schinnerer, E., Groves, B., Karim, A., Magnelli, B., Sargent, M. T., Cassata, P., Lang, P., Liu, D., Le Fèvre, O., Leslie, S., Smolčić, V., & Tasca, L. (2017). The dust attenuation of star-forming galaxies at z $\sim$ 3 and beyond: New insights from ALMA observations. *MNRAS*, 472, 483–490.

Fujimoto, S., Ouchi, M., Kohno, K., Yamaguchi, Y., Hatsukade, B., Ueda, Y., Shibuya, T., Inoue, S., Oogi, T., Toft, S., Gómez-Guijarro, C., Wang, T., Espada, D., Nagao, T., Tanaka, I., Ao, Y., Umehata, H., Taniguchi, Y., Nakanishi, K., Rujopakarn, W., Ivison, R. J., Wang, W.-h., Lee, M. M., Tadaki, K.-i., Tamura, Y., & Dunlop, J. S. (2018). ALMA 26 Arcmin^2 Survey of GOODS-S at One Millimeter (ASAGAO): Average Morphology of High-z Dusty Star-forming Galaxies in an Exponential Disk ($n \simeq$ 1). *ApJ*, 861, 7.

Fujimoto, S., Ouchi, M., Ono, Y., Shibuya, T., Ishigaki, M., Nagai, H., & Momose, R. (2016). ALMA Census of Faint 1.2 mm Sources Down to $\sim$ 0.02 mJy: Extragalactic Background Light and Dust-poor, High-z Galaxies. *ApJS*, 222, 1.

Gaia Collaboration, Brown, A. G. A., Vallenari, A., Prusti, T., de Bruijne, J. H. J., Mignard, F., Drimmel, R., Babusiaux, C., Bailer-Jones, C. A. L., Bastian, U., & et al. (2016). Gaia Data Release 1. Summary of the astrometric, photometric, and survey properties. *A&A*, 595, A2.

Galliano, F., Galametz, M., & Jones, A. P. (2018). The Interstellar Dust Properties of Nearby Galaxies. *ARA&A*, 56, 673–713.

Geach, J. E., Chapin, E. L., Coppin, K. E. K., Dunlop, J. S., Halpern, M., Smail, I., van der Werf, P., Serjeant, S., Farrah, D., Roseboom, I., Targett, T., Arumugam, V., Asboth, V., Blain, A., Chrysostomou, A., Clarke, C., Ivison, R. J., Jones, S. L., Karim, A., Mackenzie, T., Meijerink, R., Michałowski, M. J., Scott, D., Simpson, J. M., Swinbank, A. M., Alexander, D. M., Almaini, O., Aretxaga, I., Best, P., Chapman, S., Clements, D. L., Conselice, C., Danielson, A. L. R., Eales, S., Edge, A. C., Gibb, A. G., Hughes, D., Jenness, T., Knudsen, K. K., Lacey, C. G., Marsden, G., McMahon, R., Oliver, S. J., Page, M. J., Peacock, J. A., Rigopoulou, D., Robson, E. I., Spaans, M., Stevens, J., Webb, T. M. A., Willott, C., Wilson, C. D., & Zemcov, M. (2013). The SCUBA-2 Cosmology Legacy Survey: blank-field number

counts of 450-μm-selected galaxies and their contribution to the cosmic infrared background. *MNRAS*, 432, 53–61.

Gehrels, N. (1986). Confidence limits for small numbers of events in astrophysical data. *ApJ*, 303, 336–346.

Giavalisco, M., Ferguson, H. C., Koekemoer, A. M., Dickinson, M., Alexander, D. M., Bauer, F. E., Bergeron, J., Biagetti, C., Brandt, W. N., Casertano, S., Cesarsky, C., Chatzichristou, E., Conselice, C., Cristiani, S., Da Costa, L., Dahlen, T., de Mello, D., Eisenhardt, P., Erben, T., Fall, S. M., Fassnacht, C., Fosbury, R., Fruchter, A., Gardner, J. P., Grogin, N., Hook, R. N., Hornschemeier, A. E., Idzi, R., Jogee, S., Kretchmer, C., Laidler, V., Lee, K. S., Livio, M., Lucas, R., Madau, P., Mobasher, B., Moustakas, L. A., Nonino, M., Padovani, P., Papovich, C., Park, Y., Ravindranath, S., Renzini, A., Richardson, M., Riess, A., Rosati, P., Schirmer, M., Schreier, E., Somerville, R. S., Spinrad, H., Stern, D., Stiavelli, M., Strolger, L., Urry, C. M., Vandame, B., Williams, R., & Wolf, C. (2004). The Great Observatories Origins Deep Survey: Initial Results from Optical and Near-Infrared Imaging. *ApJL*, 600, L93–L98.

Glenn, J., Bock, J. J., Chattopadhyay, G., Edgington, S. F., Lange, A. E., Zmuidzinas, J., Mauskopf, P. D., Rownd, B., Yuen, L., & Ade, P. A. (1998). Bolocam: a millimeter-wave bolometric camera. In T. G. Phillips (Ed.), *Advanced Technology MMW, Radio, and Terahertz Telescopes*, volume 3357 of *Proc. SPIE* (pp. 326–334).

González-López, J., Bauer, F. E., Aravena, M., Laporte, N., Bradley, L., Carrasco, M., Carvajal, R., Demarco, R., Infante, L., Kneissl, R., Koekemoer, A. M., Muñoz Arancibia, A. M., Troncoso, P., Villard, E., & Zitrin, A. (2017). The ALMA Frontier Fields Survey. III. 1.1 mm emission line identifications in Abell 2744, MACSJ 0416.1-2403, MACSJ 1149.5+2223, Abell 370, and Abell S1063. *A&A*, 608, A138.

Goto, T., Arnouts, S., Malkan, M., Takagi, T., Inami, H., Pearson, C., Wada, T., Matsuhara, H., Yamauchi, C., Takeuchi, T. T., Nakagawa, T., Oyabu, S., Ishihara, D., Sanders, D. B., Le Floc'h, E., Lee, H. M., Jeong, W.-S., Serjeant, S., & Sedgwick, C. (2011). Infrared luminosity functions of AKARI Sloan Digital Sky Survey galaxies. *MNRAS*, 414, 1903–1913.

Greve, T. R., Ivison, R. J., Bertoldi, F., Stevens, J. A., Dunlop, J. S., Lutz, D., & Carilli, C. L. (2004). A 1200-μm MAMBO survey of ELAISN2 and the Lockman Hole - I. Maps, sources and number counts. *MNRAS*, 354, 779–797.

Griffin, M. J., Abergel, A., Abreu, A., Ade, P. A. R., André, P., Augueres, J.-L., Babbedge, T., Bae, Y., Baillie, T., Baluteau, J.-P., Barlow, M. J., Bendo, G., Benielli, D., Bock, J. J., Bonhomme, P., Brisbin,

D., Brockley-Blatt, C., Caldwell, M., Cara, C., Castro-Rodriguez, N., Cerulli, R., Chanial, P., Chen, S., Clark, E., Clements, D. L., Clerc, L., Coker, J., Communal, D., Conversi, L., Cox, P., Crumb, D., Cunningham, C., Daly, F., Davis, G. R., de Antoni, P., Delderfield, J., Devin, N., di Giorgio, A., Didschuns, I., Dohlen, K., Donati, M., Dowell, A., Dowell, C. D., Duband, L., Dumaye, L., Emery, R. J., Ferlet, M., Ferrand, D., Fontignie, J., Fox, M., Franceschini, A., Frerking, M., Fulton, T., Garcia, J., Gastaud, R., Gear, W. K., Glenn, J., Goizel, A., Griffin, D. K., Grundy, T., Guest, S., Guillemet, L., Hargrave, P. C., Harwit, M., Hastings, P., Hatziminaoglou, E., Herman, M., Hinde, B., Hristov, V., Huang, M., Imhof, P., Isaak, K. J., Israelsson, U., Ivison, R. J., Jennings, D., Kiernan, B., King, K. J., Lange, A. E., Latter, W., Laurent, G., Laurent, P., Leeks, S. J., Lellouch, E., Levenson, L., Li, B., Li, J., Lilienthal, J., Lim, T., Liu, S. J., Lu, N., Madden, S., Mainetti, G., Marliani, P., McKay, D., Mercier, K., Molinari, S., Morris, H., Moseley, H., Mulder, J., Mur, M., Naylor, D. A., Nguyen, H., O'Halloran, B., Oliver, S., Olofsson, G., Olofsson, H.-G., Orfei, R., Page, M. J., Pain, I., Panuzzo, P., Papageorgiou, A., Parks, G., Parr-Burman, P., Pearce, A., Pearson, C., Pérez-Fournon, I., Pinsard, F., Pisano, G., Podosek, J., Pohlen, M., Polehampton, E. T., Pouliquen, D., Rigopoulou, D., Rizzo, D., Roseboom, I. G., Roussel, H., Rowan-Robinson, M., Rownd, B., Saraceno, P., Sauvage, M., Savage, R., Savini, G., Sawyer, E., Scharmberg, C., Schmitt, D., Schneider, N., Schulz, B., Schwartz, A., Shafer, R., Shupe, D. L., Sibthorpe, B., Sidher, S., Smith, A., Smith, A. J., Smith, D., Spencer, L., Stobie, B., Sudiwala, R., Sukhatme, K., Surace, C., Stevens, J. A., Swinyard, B. M., Trichas, M., Tourette, T., Triou, H., Tseng, S., Tucker, C., Turner, A., Vaccari, M., Valtchanov, I., Vigroux, L., Virique, E., Voellmer, G., Walker, H., Ward, R., Waskett, T., Weilert, M., Wesson, R., White, G. J., Whitehouse, N., Wilson, C. D., Winter, B., Woodcraft, A. L., Wright, G. S., Xu, C. K., Zavagno, A., Zemcov, M., Zhang, L., & Zonca, E. (2010). The Herschel-SPIRE instrument and its in-flight performance. *A&A*, 518, L3.

Grogin, N. A., Kocevski, D. D., Faber, S. M., Ferguson, H. C., Koekemoer, A. M., Riess, A. G., Acquaviva, V., Alexander, D. M., Almaini, O., Ashby, M. L. N., Barden, M., Bell, E. F., Bournaud, F., Brown, T. M., Caputi, K. I., Casertano, S., Cassata, P., Castellano, M., Challis, P., Chary, R.-R., Cheung, E., Cirasuolo, M., Conselice, C. J., Roshan Cooray, A., Croton, D. J., Daddi, E., Dahlen, T., Davé, R., de Mello, D. F., Dekel, A., Dickinson, M., Dolch, T., Donley, J. L., Dunlop, J. S., Dutton, A. A., Elbaz, D., Fazio, G. G., Filippenko, A. V., Finkelstein, S. L., Fontana, A., Gardner, J. P., Garnavich, P. M., Gawiser, E., Giavalisco, M., Grazian, A., Guo, Y., Hathi, N. P., Häussler, B., Hopkins, P. F., Huang, J.-S., Huang, K.-H., Jha, S. W., Kartaltepe, J. S., Kirshner, R. P., Koo, D. C., Lai, K., Lee, K.-S., Li, W., Lotz, J. M., Lucas, R. A., Madau, P., McCarthy, P. J., McGrath, E. J., McIntosh, D. H., McLure, R. J., Mobasher, B., Moustakas, L. A., Mozena, M., Nandra, K., Newman, J. A., Niemi, S.-M., Noeske, K. G., Papovich, C. J., Pentericci, L., Pope, A., Primack, J. R., Rajan, A., Ravindranath, S., Reddy,

N. A., Renzini, A., Rix, H.-W., Robaina, A. R., Rodney, S. A., Rosario, D. J., Rosati, P., Salimbeni, S., Scarlata, C., Siana, B., Simard, L., Smidt, J., Somerville, R. S., Spinrad, H., Straughn, A. N., Strolger, L.-G., Telford, O., Teplitz, H. I., Trump, J. R., van der Wel, A., Villforth, C., Wechsler, R. H., Weiner, B. J., Wiklind, T., Wild, V., Wilson, G., Wuyts, S., Yan, H.-J., & Yun, M. S. (2011). CANDELS: The Cosmic Assembly Near-infrared Deep Extragalactic Legacy Survey. *ApJS*, 197, 35.

Gruppioni, C., Pozzi, F., Rodighiero, G., Delvecchio, I., Berta, S., Pozzetti, L., Zamorani, G., Andreani, P., Cimatti, A., Ilbert, O., Le Floc'h, E., Lutz, D., Magnelli, B., Marchetti, L., Monaco, P., Nordon, R., Oliver, S., Popesso, P., Riguccini, L., Roseboom, I., Rosario, D. J., Sargent, M., Vaccari, M., Altieri, B., Aussel, H., Bongiovanni, A., Cepa, J., Daddi, E., Domínguez-Sánchez, H., Elbaz, D., Förster Schreiber, N., Genzel, R., Iribarrem, A., Magliocchetti, M., Maiolino, R., Poglitsch, A., Pérez García, A., Sanchez-Portal, M., Sturm, E., Tacconi, L., Valtchanov, I., Amblard, A., Arumugam, V., Bethermin, M., Bock, J., Boselli, A., Buat, V., Burgarella, D., Castro-Rodríguez, N., Cava, A., Chanial, P., Clements, D. L., Conley, A., Cooray, A., Dowell, C. D., Dwek, E., Eales, S., Franceschini, A., Glenn, J., Griffin, M., Hatziminaoglou, E., Ibar, E., Isaak, K., Ivison, R. J., Lagache, G., Levenson, L., Lu, N., Madden, S., Maffei, B., Mainetti, G., Nguyen, H. T., O'Halloran, B., Page, M. J., Panuzzo, P., Papageorgiou, A., Pearson, C. P., Pérez-Fournon, I., Pohlen, M., Rigopoulou, D., Rowan-Robinson, M., Schulz, B., Scott, D., Seymour, N., Shupe, D. L., Smith, A. J., Stevens, J. A., Symeonidis, M., Trichas, M., Tugwell, K. E., Vigroux, L., Wang, L., Wright, G., Xu, C. K., Zemcov, M., Bardelli, S., Carollo, M., Contini, T., Le Févre, O., Lilly, S., Mainieri, V., Renzini, A., Scodeggio, M., & Zucca, E. (2013). The Herschel PEP/HerMES luminosity function - I. Probing the evolution of PACS selected Galaxies to z $\simeq$ 4. *MNRAS*, 432, 23–52.

Guilloteau, S., Delannoy, J., Downes, D., Greve, A., Guelin, M., Lucas, R., Morris, D., Radford, S. J. E., Wink, J., Cernicharo, J., Forveille, T., Garcia-Burillo, S., Neri, R., Blondel, J., Perrigourad, A., Plathner, D., & Torres, M. (1992). The IRAM interferometer on Plateau de Bure. *A&A*, 262, 624–633.

Hainline, L. J., Blain, A. W., Smail, I., Alexander, D. M., Armus, L., Chapman, S. C., & Ivison, R. J. (2011). The Stellar Mass Content of Submillimeter-selected Galaxies. *ApJ*, 740, 96.

Hancock, P. J., Murphy, T., Gaensler, B. M., Hopkins, A., & Curran, J. R. (2012). Compact continuum source finding for next generation radio surveys. *MNRAS*, 422, 1812–1824.

Hancock, P. J., Trott, C. M., & Hurley-Walker, N. (2018). Source Finding in the Era of the SKA (Precursors): Aegean 2.0. *PASA*, 35, e011.

Hatsukade, B., Kohno, K., Aretxaga, I., Austermann, J. E., Ezawa, H., Hughes, D. H., Ikarashi, S., Iono, D., Kawabe, R., Khan, S., Matsuo, H., Matsuura, S., Nakanishi, K., Oshima, T., Perera, T., Scott, K. S., Shirahata, M., Takeuchi, T. T., Tamura, Y., Tanaka, K., Tosaki, T., Wilson, G. W., & Yun, M. S. (2011). AzTEC/ASTE 1.1-mm survey of the AKARI Deep Field South: source catalogue and number counts. *MNRAS*, 411, 102–116.

Hatsukade, B., Kohno, K., Umehata, H., Aretxaga, I., Caputi, K. I., Dunlop, J. S., Ikarashi, S., Iono, D., Ivison, R. J., Lee, M., Makiya, R., Matsuda, Y., Motohara, K., Nakanishi, K., Ohta, K., Tadaki, K.-i., Tamura, Y., Wang, W.-H., Wilson, G. W., Yamaguchi, Y., & Yun, M. S. (2016). SXDF-ALMA 2-arcmin^2 deep survey: 1.1-mm number counts. *PASJ*, 68, 36.

Hatsukade, B., Kohno, K., Yamaguchi, Y., Umehata, H., Ao, Y., Aretxaga, I., Caputi, K. I., Dunlop, J. S., Egami, E., Espada, D., Fujimoto, S., Hayatsu, N. H., Hughes, D. H., Ikarashi, S., Iono, D., Ivison, R. J., Kawabe, R., Kodama, T., Lee, M., Matsuda, Y., Nakanishi, K., Ohta, K., Ouchi, M., Rujopakarn, W., Suzuki, T., Tamura, Y., Ueda, Y., Wang, T., Wang, W.-H., Wilson, G. W., Yoshimura, Y., & Yun, M. S. (2018). ALMA twenty-six arcmin^2 survey of GOODS-S at one millimeter (ASAGAO): Source catalog and number counts. *PASJ*, 70, 105.

Hatsukade, B., Ohta, K., Seko, A., Yabe, K., & Akiyama, M. (2013). Faint End of 1.3 mm Number Counts Revealed by ALMA. *ApJL*, 769, L27.

Hatsukade, B., Ohta, K., Yabe, K., Seko, A., Makiya, R., & Akiyama, M. (2015). Optical-Infrared Properties of Faint 1.3 mm Sources Detected with ALMA. *ApJ*, 810, 91.

Hayatsu, N. H., Matsuda, Y., Umehata, H., Yoshida, N., Smail, I., Swinbank, A. M., Ivison, R., Kohno, K., Tamura, Y., Kubo, M., Iono, D., Hatsukade, B., Nakanishi, K., Kawabe, R., Nagao, T., Inoue, A. K., Takeuchi, T. T., Lee, M., Ao, Y., Fujimoto, S., Izumi, T., Yamaguchi, Y., Ikarashi, S., & Yamada, T. (2017). ALMA deep field in SSA22: Blindly detected CO emitters and [CII] emitter candidates. *PASJ*, 69, 45.

Hayward, C. C., Jonsson, P., Kereš, D., Magnelli, B., Hernquist, L., & Cox, T. J. (2012). How to distinguish starbursts and quiescently star-forming galaxies: the 'bimodal' submillimetre galaxy population as a case study. *MNRAS*, 424, 951–970.

Hemmati, S., Yan, L., Diaz-Santos, T., Armus, L., Capak, P., Faisst, A., & Masters, D. (2017). The Local [CII] 158 μm Emission Line Luminosity Function. *ApJ*, 834, 36.

Henriques, B., Maraston, C., Monaco, P., Fontanot, F., Menci, N., De Lucia, G., & Tonini, C. (2011). The effect of thermally pulsating asymptotic giant branch stars on the evolution of the rest-frame near-infrared galaxy luminosity function. *MNRAS*, 415, 3571–3579.

Hildebrandt, H., Erben, T., Dietrich, J. P., Cordes, O., Haberzettl, L., Hetterscheidt, M., Schirmer, M., Schmithuesen, O., Schneider, P., Simon, P., & Trachternach, C. (2006). GaBoDS: The Garching-Bonn Deep Survey. V. Data release of the ESO Deep-Public-Survey. *A&A*, 452, 1121–1128.

Hodge, J. A., Karim, A., Smail, I., Swinbank, A. M., Walter, F., Biggs, A. D., Ivison, R. J., Weiss, A., Alexander, D. M., Bertoldi, F., Brandt, W. N., Chapman, S. C., Coppin, K. E. K., Cox, P., Danielson, A. L. R., Dannerbauer, H., De Breuck, C., Decarli, R., Edge, A. C., Greve, T. R., Knudsen, K. K., Menten, K. M., Rix, H.-W., Schinnerer, E., Simpson, J. M., Wardlow, J. L., & van der Werf, P. (2013). An ALMA Survey of Submillimeter Galaxies in the Extended Chandra Deep Field South: Source Catalog and Multiplicity. *ApJ*, 768, 91.

Hodge, J. A., Riechers, D., Decarli, R., Walter, F., Carilli, C. L., Daddi, E., & Dannerbauer, H. (2015). The Kiloparsec-scale Star Formation Law at Redshift 4: Widespread, Highly Efficient Star Formation in the Dust-obscured Starburst Galaxy GN20. *ApJL*, 798, L18.

Högbom, J. A. (1974). Aperture Synthesis with a Non-Regular Distribution of Interferometer Baselines. *A&AS*, 15, 417.

Holland, W. S., Bintley, D., Chapin, E. L., Chrysostomou, A., Davis, G. R., Dempsey, J. T., Duncan, W. D., Fich, M., Friberg, P., Halpern, M., Irwin, K. D., Jenness, T., Kelly, B. D., MacIntosh, M. J., Robson, E. I., Scott, D., Ade, P. A. R., Atad-Ettedgui, E., Berry, D. S., Craig, S. C., Gao, X., Gibb, A. G., Hilton, G. C., Hollister, M. I., Kycia, J. B., Lunney, D. W., McGregor, H., Montgomery, D., Parkes, W., Tilanus, R. P. J., Ullom, J. N., Walther, C. A., Walton, A. J., Woodcraft, A. L., Amiri, M., Atkinson, D., Burger, B., Chuter, T., Coulson, I. M., Doriese, W. B., Dunare, C., Economou, F., Niemack, M. D., Parsons, H. A. L., Reintsema, C. D., Sibthorpe, B., Smail, I., Sudiwala, R., & Thomas, H. S. (2013). SCUBA-2: the 10 000 pixel bolometer camera on the James Clerk Maxwell Telescope. *MNRAS*, 430, 2513–2533.

Holland, W. S., Robson, E. I., Gear, W. K., Cunningham, C. R., Lightfoot, J. F., Jenness, T., Ivison, R. J., Stevens, J. A., Ade, P. A. R., Griffin, M. J., Duncan, W. D., Murphy, J. A., & Naylor, D. A. (1999). SCUBA: a common-user submillimetre camera operating on the James Clerk Maxwell Telescope. *MNRAS*, 303, 659–672.

Hsieh, B.-C., Wang, W.-H., Hsieh, C.-C., Lin, L., Yan, H., Lim, J., & Ho, P. T. P. (2012). The Taiwan ECDFS Near-Infrared Survey: Ultra-deep J and K_S Imaging in the Extended Chandra Deep Field-South. *ApJS*, 203, 23.

Hsu, L.-Y., Stockton, A., & Shih, H.-Y. (2014). Compact Quiescent Galaxies at Intermediate Redshifts. *ApJ*, 796, 92.

Huang, K.-H., Bradač, M., Lemaux, B. C., Ryan, Jr., R. E., Hoag, A., Castellano, M., Amorín, R., Fontana, A., Brammer, G. B., Cain, B., Lubin, L. M., Merlin, E., Schmidt, K. B., Schrabback, T., Treu, T., Gonzalez, A. H., von der Linden, A., & Knight, R. I. (2016). Spitzer UltRa Faint SUrvey Program (SURFS UP). II. IRAC-detected Lyman-Break Galaxies at $6 \lesssim z \lesssim 10$ behind Strong-lensing Clusters. *ApJ*, 817, 11.

Hughes, D. H., Serjeant, S., Dunlop, J., Rowan-Robinson, M., Blain, A., Mann, R. G., Ivison, R., Peacock, J., Efstathiou, A., Gear, W., Oliver, S., Lawrence, A., Longair, M., Goldschmidt, P., & Jenness, T. (1998). High-redshift star formation in the Hubble Deep Field revealed by a submillimetre-wavelength survey. *Nature*, 394, 241–247.

Ikarashi, S. (2014). *Study of Dust-Obscured Massive Galaxies beyond Redshift 5 based on Submillimeter Photometric and Spectroscopic Surveys*. PhD thesis, The University of Tokyo.

Inami, H., Bacon, R., Brinchmann, J., Richard, J., Contini, T., Conseil, S., Hamer, S., Akhlaghi, M., Bouché, N., Clément, B., Desprez, G., Drake, A. B., Hashimoto, T., Leclercq, F., Maseda, M., Michel-Dansac, L., Paalvast, M., Tresse, L., Ventou, E., Kollatschny, W., Boogaard, L. A., Finley, H., Marino, R. A., Schaye, J., & Wisotzki, L. (2017). The MUSE Hubble Ultra Deep Field Survey. II. Spectroscopic redshifts and comparisons to color selections of high-redshift galaxies. *A&A*, 608, A2.

Ivison, R. J., Greve, T. R., Dunlop, J. S., Peacock, J. A., Egami, E., Smail, I., Ibar, E., van Kampen, E., Aretxaga, I., Babbedge, T., Biggs, A. D., Blain, A. W., Chapman, S. C., Clements, D. L., Coppin, K., Farrah, D., Halpern, M., Hughes, D. H., Jarvis, M. J., Jenness, T., Jones, J. R., Mortier, A. M. J., Oliver, S., Papovich, C., Pérez-González, P. G., Pope, A., Rawlings, S., Rieke, G. H., Rowan-Robinson, M., Savage, R. S., Scott, D., Seigar, M., Serjeant, S., Simpson, C., Stevens, J. A., Vaccari, M., Wagg, J., & Willott, C. J. (2007). The SCUBA HAlf Degree Extragalactic Survey - III. Identification of radio and mid-infrared counterparts to submillimetre galaxies. *MNRAS*, 380, 199–228.

Ivison, R. J., Smail, I., Barger, A. J., Kneib, J.-P., Blain, A. W., Owen, F. N., Kerr, T. H., & Cowie, L. L. (2000). The diversity of SCUBA-selected galaxies. *MNRAS*, 315, 209–222.

Kashikawa, N., Takata, T., Ohyama, Y., Yoshida, M., Maihara, T., Iwamuro, F., Motohara, K., Totani, T., Nagashima, M., Shimasaku, K., Furusawa, H., Ouchi, M., Yagi, M., Okamura, S., Iye, M., Sasaki, T., Kosugi, G., Aoki, K., & Nakata, F. (2003). Subaru Deep Survey. III. Evolution of Rest-Frame Luminosity Functions Based on the Photometric Redshifts for a K'-Band-Selected Galaxy Sample. *AJ*, 125, 53–65.

Kawamata, R., Oguri, M., Ishigaki, M., Shimasaku, K., & Ouchi, M. (2016). Precise Strong Lensing Mass Modeling of Four Hubble Frontier Field Clusters and a Sample of Magnified High-redshift Galaxies. *ApJ*, 819, 114.

Keating, G. K., Marrone, D. P., Bower, G. C., Leitch, E., Carlstrom, J. E., & DeBoer, D. R. (2016). COPSS II: The Molecular Gas Content of Ten Million Cubic Megaparsecs at Redshift z $\sim$ 3. *ApJ*, 830, 34.

Kennicutt, Jr., R. C. (1998). The Global Schmidt Law in Star-forming Galaxies. *ApJ*, 498, 541–552.

Keres, D., Yun, M. S., & Young, J. S. (2003). CO Luminosity Functions for Far-Infrared- and B-Band-selected Galaxies and the First Estimate for Ω_{HI}+H_2. *ApJ*, 582, 659–667.

Kimble, R. A., MacKenty, J. W., O'Connell, R. W., & Townsend, J. A. (2008). Wide Field Camera 3: a powerful new imager for the Hubble Space Telescope. In *Space Telescopes and Instrumentation 2008: Optical, Infrared, and Millimeter*, volume 7010 of *Proc. SPIE* (pp. 70101E).

Kissler-Patig, M., Pirard, J.-F., Casali, M., Moorwood, A., Ageorges, N., Alves de Oliveira, C., Baksai, P., Bedin, L. R., Bendek, E., Biereichel, P., Delabre, B., Dorn, R., Esteves, R., Finger, G., Gojak, D., Huster, G., Jung, Y., Kiekebush, M., Klein, B., Koch, F., Lizon, J.-L., Mehrgan, L., Petr-Gotzens, M., Pritchard, J., Selman, F., & Stegmeier, J. (2008). HAWK-I: the high-acuity wide-field K-band imager for the ESO Very Large Telescope. *A&A*, 491, 941–950.

Knudsen, K. K., van der Werf, P. P., & Kneib, J.-P. (2008). Probing the submillimetre number counts at $f_{850\mu m} < 2$mJy. *MNRAS*, 384, 1611–1626.

Koekemoer, A. M., Faber, S. M., Ferguson, H. C., Grogin, N. A., Kocevski, D. D., Koo, D. C., Lai, K., Lotz, J. M., Lucas, R. A., McGrath, E. J., Ogaz, S., Rajan, A., Riess, A. G., Rodney, S. A., Strolger, L., Casertano, S., Castellano, M., Dahlen, T., Dickinson, M., Dolch, T., Fontana, A., Giavalisco, M., Grazian, A., Guo, Y., Hathi, N. P., Huang, K.-H., van der Wel, A., Yan, H.-J., Acquaviva, V., Alexander, D. M., Almaini, O., Ashby, M. L. N., Barden, M., Bell, E. F., Bournaud, F., Brown, T. M., Caputi, K. I., Cassata, P., Challis, P. J., Chary, R.-R., Cheung, E., Cirasuolo, M., Conselice, C. J., Roshan Cooray, A.,

Croton, D. J., Daddi, E., Davé, R., de Mello, D. F., de Ravel, L., Dekel, A., Donley, J. L., Dunlop, J. S., Dutton, A. A., Elbaz, D., Fazio, G. G., Filippenko, A. V., Finkelstein, S. L., Frazer, C., Gardner, J. P., Garnavich, P. M., Gawiser, E., Gruetzbauch, R., Hartley, W. G., Häussler, B., Herrington, J., Hopkins, P. F., Huang, J.-S., Jha, S. W., Johnson, A., Kartaltepe, J. S., Khostovan, A. A., Kirshner, R. P., Lani, C., Lee, K.-S., Li, W., Madau, P., McCarthy, P. J., McIntosh, D. H., McLure, R. J., McPartland, C., Mobasher, B., Moreira, H., Mortlock, A., Moustakas, L. A., Mozena, M., Nandra, K., Newman, J. A., Nielsen, J. L., Niemi, S., Noeske, K. G., Papovich, C. J., Pentericci, L., Pope, A., Primack, J. R., Ravindranath, S., Reddy, N. A., Renzini, A., Rix, H.-W., Robaina, A. R., Rosario, D. J., Rosati, P., Salimbeni, S., Scarlata, C., Siana, B., Simard, L., Smidt, J., Snyder, D., Somerville, R. S., Spinrad, H., Straughn, A. N., Telford, O., Teplitz, H. I., Trump, J. R., Vargas, C., Villforth, C., Wagner, C. R., Wandro, P., Wechsler, R. H., Weiner, B. J., Wiklind, T., Wild, V., Wilson, G., Wuyts, S., & Yun, M. S. (2011). CANDELS: The Cosmic Assembly Near-infrared Deep Extragalactic Legacy Survey–The Hubble Space Telescope Observations, Imaging Data Products, and Mosaics. *ApJS*, 197, 36.

Kohno, K., Yamaguchi, Y., Tamura, Y., Tadaki, K., Hatsukade, B., Ikarashi, S., Caputi, K. I., Rujopakarn, W., Ivison, R. J., Dunlop, J. S., Motohara, K., Umehata, H., Yabe, K., Wang, W. H., Kodama, T., Koyama, Y., Hayashi, M., Matsuda, Y., Hughes, D., Aretxaga, I., Wilson, G. W., Yun, M. S., Ohta, K., Akiyama, M., Kawabe, R., Iono, D., Nakanishi, K., Lee, M., & Makiya, R. (2016). SXDF-UDS-CANDELS-ALMA 1.5 arcmin^2 deep survey. In S. Kaviraj (Ed.), *Galaxies at High Redshift and Their Evolution Over Cosmic Time*, volume 319 of *IAU Symposium* (pp. 92–95).

Koprowski, M. P., Coppin, K. E. K., Geach, J. E., McLure, R. J., Almaini, O., Blain, A. W., Bremer, M., Bourne, N., Chapman, S. C., Conselice, C. J., Dunlop, J. S., Farrah, D., Hartley, W., Karim, A., Knudsen, K. K., Michałowski, M. J., Scott, D., Simpson, C., Smith, D. J. B., & van der Werf, P. P. (2018). A direct calibration of thtae IRX-β relation in Lyman-break Galaxies at z = 3-5. *MNRAS*, 479, 4355–4366.

Koprowski, M. P., Dunlop, J. S., Michałowski, M. J., Coppin, K. E. K., Geach, J. E., McLure, R. J., Scott, D., & van der Werf, P. P. (2017). The evolving far-IR galaxy luminosity function and dust-obscured star formation rate density out to z$\sim$5. *MNRAS*, 471, 4155–4169.

Kreysa, E., Gemuend, H.-P., Gromke, J., Haslam, C. G., Reichertz, L., Haller, E. E., Beeman, J. W., Hansen, V., Sievers, A., & Zylka, R. (1998). Bolometer array development at the Max-Planck-Institut fuer Radioastronomie. In T. G. Phillips (Ed.), *Advanced Technology MMW, Radio, and Terahertz Telescopes*, volume 3357 of *Proc. SPIE* (pp. 319–325).

Kriek, M., van Dokkum, P. G., Franx, M., Illingworth, G. D., & Magee, D. K. (2009). The Hubble Sequence Beyond z = 2 for Massive Galaxies: Contrasting Large Star-forming and Compact Quiescent Galaxies. *ApJL*, 705, L71–L75.

Labbé, I., Oesch, P. A., Illingworth, G. D., van Dokkum, P. G., Bouwens, R. J., Franx, M., Carollo, C. M., Trenti, M., Holden, B., Smit, R., González, V., Magee, D., Stiavelli, M., & Stefanon, M. (2015). Ultradeep IRAC Imaging Over the HUDF and GOODS-South: Survey Design and Imaging Data Release. *ApJS*, 221, 23.

Lagache, G., Cousin, M., & Chatzikos, M. (2018). The [CII] 158 μm line emission in high-redshift galaxies. *A&A*, 609, A130.

Lagache, G., Dole, H., Puget, J.-L., Pérez-González, P. G., Le Floc'h, E., Rieke, G. H., Papovich, C., Egami, E., Alonso-Herrero, A., Engelbracht, C. W., Gordon, K. D., Misselt, K. A., & Morrison, J. E. (2004). Polycyclic Aromatic Hydrocarbon Contribution to the Infrared Output Energy of the Universe at z ~= 2. *ApJS*, 154, 112–117.

Lagos, C. d. P., Bayet, E., Baugh, C. M., Lacey, C. G., Bell, T. A., Fanidakis, N., & Geach, J. E. (2012). Predictions for the CO emission of galaxies from a coupled simulation of galaxy formation and photon-dominated regions. *MNRAS*, 426, 2142–2165.

Laird, E. S., Nandra, K., Pope, A., & Scott, D. (2010). On the X-ray properties of sub-mm-selected galaxies. *MNRAS*, 401, 2763–2772.

Laurent, G. T., Aguirre, J. E., Glenn, J., Ade, P. A. R., Bock, J. J., Edgington, S. F., Goldin, A., Golwala, S. R., Haig, D., Lange, A. E., Maloney, P. R., Mauskopf, P. D., Nguyen, H., Rossinot, P., Sayers, J., & Stover, P. (2005). The Bolocam Lockman Hole Millimeter-Wave Galaxy Survey: Galaxy Candidates and Number Counts. *ApJ*, 623, 742–762.

Le Fèvre, O., Saisse, M., Mancini, D., Brau-Nogue, S., Caputi, O., Castinel, L., D'Odorico, S., Garilli, B., Kissler-Patig, M., Lucuix, C., Mancini, G., Pauget, A., Sciarretta, G., Scodeggio, M., Tresse, L., & Vettolani, G. (2003). Commissioning and performances of the VLT-VIMOS instrument. In M. Iye & A. F. M. Moorwood (Eds.), *Instrument Design and Performance for Optical/Infrared Ground-based Telescopes*, volume 4841 of *Proc. SPIE* (pp. 1670–1681).

Le Fèvre, O., Vettolani, G., Garilli, B., Tresse, L., Bottini, D., Le Brun, V., Maccagni, D., Picat, J. P., Scaramella, R., Scodeggio, M., Zanichelli, A., Adami, C., Arnaboldi, M., Arnouts, S., Bardelli, S., Bolzonella, M., Cappi, A., Charlot, S., Ciliegi, P., Contini, T., Foucaud, S., Franzetti, P., Gavignaud,

I., Guzzo, L., Ilbert, O., Iovino, A., McCracken, H. J., Marano, B., Marinoni, C., Mathez, G., Mazure, A., Meneux, B., Merighi, R., Paltani, S., Pellò, R., Pollo, A., Pozzetti, L., Radovich, M., Zamorani, G., Zucca, E., Bondi, M., Bongiorno, A., Busarello, G., Lamareille, F., Mellier, Y., Merluzzi, P., Ripepi, V., & Rizzo, D. (2005). The VIMOS VLT deep survey. First epoch VVDS-deep survey: 11 564 spectra with $17.5 \leq \mathrm{IAB} \leq 24$, and the redshift distribution over $0 \leq z \leq 5$. *A&A*, 439, 845–862.

Liu, D., Daddi, E., Dickinson, M., Owen, F., Pannella, M., Sargent, M., Béthermin, M., Magdis, G., Gao, Y., Shu, X., Wang, T., Jin, S., & Inami, H. (2018). "Super-deblended" Dust Emission in Galaxies. I. The GOODS-North Catalog and the Cosmic Star Formation Rate Density out to Redshift 6. *ApJ*, 853, 172.

Luo, B., Brandt, W. N., Xue, Y. Q., Lehmer, B., Alexander, D. M., Bauer, F. E., Vito, F., Yang, G., Basu-Zych, A. R., Comastri, A., Gilli, R., Gu, Q.-S., Hornschemeier, A. E., Koekemoer, A., Liu, T., Mainieri, V., Paolillo, M., Ranalli, P., Rosati, P., Schneider, D. P., Shemmer, O., Smail, I., Sun, M., Tozzi, P., Vignali, C., & Wang, J.-X. (2017). The Chandra Deep Field-South Survey: 7 Ms Source Catalogs. *ApJS*, 228, 2.

Lutz, D., Poglitsch, A., Altieri, B., Andreani, P., Aussel, H., Berta, S., Bongiovanni, A., Brisbin, D., Cava, A., Cepa, J., Cimatti, A., Daddi, E., Dominguez-Sanchez, H., Elbaz, D., Förster Schreiber, N. M., Genzel, R., Grazian, A., Gruppioni, C., Harwit, M., Le Floc'h, E., Magdis, G., Magnelli, B., Maiolino, R., Nordon, R., Pérez García, A. M., Popesso, P., Pozzi, F., Riguccini, L., Rodighiero, G., Saintonge, A., Sanchez Portal, M., Santini, P., Shao, L., Sturm, E., Tacconi, L. J., Valtchanov, I., Wetzstein, M., & Wieprecht, E. (2011). PACS Evolutionary Probe (PEP) - A Herschel key program. *A&A*, 532, A90.

Madau, P. & Dickinson, M. (2014). Cosmic Star-Formation History. *ARA&A*, 52, 415–486.

Madau, P., Ferguson, H. C., Dickinson, M. E., Giavalisco, M., Steidel, C. C., & Fruchter, A. (1996). High-redshift galaxies in the Hubble Deep Field: colour selection and star formation history to z~4. *MNRAS*, 283, 1388–1404.

Magnelli, B., Lutz, D., Saintonge, A., Berta, S., Santini, P., Symeonidis, M., Altieri, B., Andreani, P., Aussel, H., Béthermin, M., Bock, J., Bongiovanni, A., Cepa, J., Cimatti, A., Conley, A., Daddi, E., Elbaz, D., Förster Schreiber, N. M., Genzel, R., Ivison, R. J., Le Floc'h, E., Magdis, G., Maiolino, R., Nordon, R., Oliver, S. J., Page, M., Pérez García, A., Poglitsch, A., Popesso, P., Pozzi, F., Riguccini, L., Rodighiero, G., Rosario, D., Roseboom, I., Sanchez-Portal, M., Scott, D., Sturm, E., Tacconi, L. J., Valtchanov, I., Wang, L., & Wuyts, S. (2014). The evolution of the dust temperatures of galaxies in the SFR-M plane up to $z \sim 2$. *A&A*, 561, A86.

Magnelli, B., Popesso, P., Berta, S., Pozzi, F., Elbaz, D., Lutz, D., Dickinson, M., Altieri, B., Andreani, P., Aussel, H., Béthermin, M., Bongiovanni, A., Cepa, J., Charmandaris, V., Chary, R.-R., Cimatti, A., Daddi, E., Förster Schreiber, N. M., Genzel, R., Gruppioni, C., Harwit, M., Hwang, H. S., Ivison, R. J., Magdis, G., Maiolino, R., Murphy, E., Nordon, R., Pannella, M., Pérez García, A., Poglitsch, A., Rosario, D., Sanchez-Portal, M., Santini, P., Scott, D., Sturm, E., Tacconi, L. J., & Valtchanov, I. (2013). The deepest Herschel-PACS far-infrared survey: number counts and infrared luminosity functions from combined PEP/GOODS-H observations. *A&A*, 553, A132.

Matsuda, Y., Nagao, T., Iono, D., Hatsukade, B., Kohno, K., Tamura, Y., Yamaguchi, Y., & Shimizu, I. (2015). The ALMA Patchy Deep Survey: a blind search for [CII] emitters at z $\sim$ 4.5. *MNRAS*, 451, 1141–1145.

McMullin, J. P., Waters, B., Schiebel, D., Young, W., & Golap, K. (2007). CASA Architecture and Applications. In R. A. Shaw, F. Hill, & D. J. Bell (Eds.), *Astronomical Data Analysis Software and Systems XVI*, volume 376 of *Astronomical Society of the Pacific Conference Series* (pp. 127).

Meurer, G. R., Heckman, T. M., & Calzetti, D. (1999). Dust Absorption and the Ultraviolet Luminosity Density at z $\sim$ 3 as Calibrated by Local Starburst Galaxies. *ApJ*, 521, 64–80.

Michałowski, M. J., Hayward, C. C., Dunlop, J. S., Bruce, V. A., Cirasuolo, M., Cullen, F., & Hernquist, L. (2014). Determining the stellar masses of submillimetre galaxies: the critical importance of star formation histories. *A&A*, 571, A75.

Michalowski, M. J., Murphy, E. J., Hjorth, J., Watson, D., Gall, C., & Dunlop, J. S. (2011). Dust Grain Growth in the Interstellar Medium of Galaxies at Redshifts $4 < z < 6.5$. In W. Wang, J. Lu, Z. Luo, Z. Yang, H. Hua, & Z. Chen (Eds.), *Galaxy Evolution: Infrared to Millimeter Wavelength Perspective*, volume 446 of *Astronomical Society of the Pacific Conference Series* (pp. 387).

Miller, T. B., Chapman, S. C., Hayward, C. C., Behroozi, P. S., Bradford, C. M., Willott, C. J., & Wagg, J. (2016). Investigating overdensities around z>6 galaxies through ALMA observations of [CII]. *ArXiv e-prints*.

Miyazaki, S., Komiyama, Y., Sekiguchi, M., Okamura, S., Doi, M., Furusawa, H., Hamabe, M., Imi, K., Kimura, M., Nakata, F., Okada, N., Ouchi, M., Shimasaku, K., Yagi, M., & Yasuda, N. (2002). Subaru Prime Focus Camera – Suprime-Cam. *PASJ*, 54, 833–853.

Moorwood, A., Cuby, J.-G., Ballester, P., Biereichel, P., Brynnel, J., Conzelmann, R., Delabre, B., Devillard, N., van Dijsseldonk, A., Finger, G., Gemperlein, H., Lidman, C., Herlin, T., Huster, G., Knud-

strup, J., Lizon, J.-L., Mehrgan, H., Meyer, M., Nicolini, G., Silber, A., Spyromilio, J., & Stegmeier, J. (1999). ISAAC at the VLT. *The Messenger*, 95, 1–5.

Muchovej, S., Mroczkowski, T., Carlstrom, J. E., Cartwright, J., Greer, C., Hennessy, R., Loh, M., Pryke, C., Reddall, B., Runyan, M., Sharp, M., Hawkins, D., Lamb, J. W., Woody, D., Joy, M., Leitch, E. M., & Miller, A. D. (2007). Observations of High-Redshift X-Ray Selected Clusters with the Sunyaev-Zel'dovich Array. *ApJ*, 663, 708–716.

Narayanan, D., Davé, R., Johnson, B. D., Thompson, R., Conroy, C., & Geach, J. (2018). The IRX-β dust attenuation relation in cosmological galaxy formation simulations. *MNRAS*, 474, 1718–1736.

Nonino, M., Dickinson, M., Rosati, P., Grazian, A., Reddy, N., Cristiani, S., Giavalisco, M., Kuntschner, H., Vanzella, E., Daddi, E., Fosbury, R. A. E., & Cesarsky, C. (2009). Deep U Band and R Imaging of Goods-South: Observations, Data Reduction and First Results. *ApJS*, 183, 244–260.

Obreschkow, D., Croton, D., De Lucia, G., Khochfar, S., & Rawlings, S. (2009a). Simulation of the Cosmic Evolution of Atomic and Molecular Hydrogen in Galaxies. *ApJ*, 698, 1467–1484.

Obreschkow, D., Heywood, I., Klöckner, H.-R., & Rawlings, S. (2009b). A Heuristic Prediction of the Cosmic Evolution of the Co-luminosity Functions. *ApJ*, 702, 1321–1335.

Oguri, M. (2010). The Mass Distribution of SDSS J1004+4112 Revisited. *PASJ*, 62, 1017–1024.

Oliver, S. J., Bock, J., Altieri, B., Amblard, A., Arumugam, V., Aussel, H., Babbedge, T., Beelen, A., Béthermin, M., Blain, A., Boselli, A., Bridge, C., Brisbin, D., Buat, V., Burgarella, D., Castro-Rodríguez, N., Cava, A., Chanial, P., Cirasuolo, M., Clements, D. L., Conley, A., Conversi, L., Cooray, A., Dowell, C. D., Dubois, E. N., Dwek, E., Dye, S., Eales, S., Elbaz, D., Farrah, D., Feltre, A., Ferrero, P., Fiolet, N., Fox, M., Franceschini, A., Gear, W., Giovannoli, E., Glenn, J., Gong, Y., González Solares, E. A., Griffin, M., Halpern, M., Harwit, M., Hatziminaoglou, E., Heinis, S., Hurley, P., Hwang, H. S., Hyde, A., Ibar, E., Ilbert, O., Isaak, K., Ivison, R. J., Lagache, G., Le Floc'h, E., Levenson, L., Faro, B. L., Lu, N., Madden, S., Maffei, B., Magdis, G., Mainetti, G., Marchetti, L., Marsden, G., Marshall, J., Mortier, A. M. J., Nguyen, H. T., O'Halloran, B., Omont, A., Page, M. J., Panuzzo, P., Papageorgiou, A., Patel, H., Pearson, C. P., Pérez-Fournon, I., Pohlen, M., Rawlings, J. I., Raymond, G., Rigopoulou, D., Riguccini, L., Rizzo, D., Rodighiero, G., Roseboom, I. G., Rowan-Robinson, M., Sánchez Portal, M., Schulz, B., Scott, D., Seymour, N., Shupe, D. L., Smith, A. J., Stevens, J. A., Symeonidis, M., Trichas, M., Tugwell, K. E., Vaccari, M., Valtchanov, I., Vieira, J. D., Viero, M., Vigroux, L., Wang, L., Ward, R., Wardlow, J., Wright, G., Xu, C. K., & Zemcov, M. (2012). The Herschel Multi-tiered Extragalactic Survey: HerMES. *MNRAS*, 424, 1614–1635.

Ono, Y., Ouchi, M., Kurono, Y., & Momose, R. (2014). Faint Submillimeter Galaxies Revealed by Multifield Deep ALMA Observations: Number Counts, Spatial Clustering, and a Dark Submillimeter Line Emitter. *ApJ*, 795, 5.

Oteo, I., Zwaan, M. A., Ivison, R. J., Smail, I., & Biggs, A. D. (2016). ALMACAL I: First Dual-band Number Counts from a Deep and Wide ALMA Submillimeter Survey, Free from Cosmic Variance. *ApJ*, 822, 36.

Ouchi, M., Mobasher, B., Shimasaku, K., Ferguson, H. C., Fall, S. M., Ono, Y., Kashikawa, N., Morokuma, T., Nakajima, K., Okamura, S., Dickinson, M., Giavalisco, M., & Ohta, K. (2009). Large Area Survey for z = 7 Galaxies in SDF and GOODS-N: Implications for Galaxy Formation and Cosmic Reionization. *ApJ*, 706, 1136–1151.

Persson, S. E., Murphy, D. C., Smee, S., Birk, C., Monson, A. J., Uomoto, A., Koch, E., Shectman, S., Barkhouser, R., Orndorff, J., Hammond, R., Harding, A., Scharfstein, G., Kelson, D., Marshall, J., & McCarthy, P. J. (2013). FourStar: The Near-Infrared Imager for the 6.5 m Baade Telescope at Las Campanas Observatory. *PASP*, 125, 654.

Poglitsch, A., Waelkens, C., Geis, N., Feuchtgruber, H., Vandenbussche, B., Rodriguez, L., Krause, O., Renotte, E., van Hoof, C., Saraceno, P., Cepa, J., Kerschbaum, F., Agnèse, P., Ali, B., Altieri, B., Andreani, P., Augueres, J.-L., Balog, Z., Barl, L., Bauer, O. H., Belbachir, N., Benedettini, M., Billot, N., Boulade, O., Bischof, H., Blommaert, J., Callut, E., Cara, C., Cerulli, R., Cesarsky, D., Contursi, A., Creten, Y., De Meester, W., Doublier, V., Doumayrou, E., Duband, L., Exter, K., Genzel, R., Gillis, J.-M., Grözinger, U., Henning, T., Herreros, J., Huygen, R., Inguscio, M., Jakob, G., Jamar, C., Jean, C., de Jong, J., Katterloher, R., Kiss, C., Klaas, U., Lemke, D., Lutz, D., Madden, S., Marquet, B., Martignac, J., Mazy, A., Merken, P., Montfort, F., Morbidelli, L., Müller, T., Nielbock, M., Okumura, K., Orfei, R., Ottensamer, R., Pezzuto, S., Popesso, P., Putzeys, J., Regibo, S., Reveret, V., Royer, P., Sauvage, M., Schreiber, J., Stegmaier, J., Schmitt, D., Schubert, J., Sturm, E., Thiel, M., Tofani, G., Vavrek, R., Wetzstein, M., Wieprecht, E., & Wiezorrek, E. (2010). The Photodetector Array Camera and Spectrometer (PACS) on the Herschel Space Observatory. *A&A*, 518, L2.

Popping, G., Puglisi, A., & Norman, C. A. (2017). Dissecting the IRX-β dust attenuation relation: exploring the physical origin of observed variations in galaxies. *MNRAS*, 472, 2315–2333.

Popping, G., van Kampen, E., Decarli, R., Spaans, M., Somerville, R. S., & Trager, S. C. (2016). Sub-mm emission line deep fields: CO and [CII] luminosity functions out to z = 6. *MNRAS*, 461, 93–110.

Postman, M., Coe, D., Benítez, N., Bradley, L., Broadhurst, T., Donahue, M., Ford, H., Graur, O., Graves, G., Jouvel, S., Koekemoer, A., Lemze, D., Medezinski, E., Molino, A., Moustakas, L., Ogaz, S., Riess, A., Rodney, S., Rosati, P., Umetsu, K., Zheng, W., Zitrin, A., Bartelmann, M., Bouwens, R., Czakon, N., Golwala, S., Host, O., Infante, L., Jha, S., Jimenez-Teja, Y., Kelson, D., Lahav, O., Lazkoz, R., Maoz, D., McCully, C., Melchior, P., Meneghetti, M., Merten, J., Moustakas, J., Nonino, M., Patel, B., Regös, E., Sayers, J., Seitz, S., & Van der Wel, A. (2012). The Cluster Lensing and Supernova Survey with Hubble: An Overview. *ApJS*, 199, 25.

Priewe, J., Williams, L. L. R., Liesenborgs, J., Coe, D., & Rodney, S. A. (2017). Lens models under the microscope: comparison of Hubble Frontier Field cluster magnification maps. *MNRAS*, 465, 1030–1045.

Puget, P., Stadler, E., Doyon, R., Gigan, P., Thibault, S., Luppino, G., Barrick, G., Benedict, T., Forveille, T., Rambold, W., Thomas, J., Vermeulen, T., Ward, J., Beuzit, J.-L., Feautrier, P., Magnard, Y., Mella, G., Preis, O., Vallee, P., Wang, S.-y., Lin, C.-J., Hall, D. N., & Hodapp, K. W. (2004). WIRCam: the infrared wide-field camera for the Canada-France-Hawaii Telescope. In A. F. M. Moorwood & M. Iye (Eds.), *Ground-based Instrumentation for Astronomy*, volume 5492 of *Proc. SPIE* (pp. 978–987).

Reddy, N. A., Erb, D. K., Pettini, M., Steidel, C. C., & Shapley, A. E. (2010). Dust Obscuration and Metallicity at High Redshift: New Inferences from UV, Hα, and 8 μm Observations of $z \sim 2$ Star-forming Galaxies. *ApJ*, 712, 1070–1091.

Rengarajan, T. N. & Takeuchi, T. T. (2001). The Radio-to-Submillimeter Flux Density Ratio of Galaxies as a Measure of Redshift. *PASJ*, 53, 433–437.

Retzlaff, J., Rosati, P., Dickinson, M., Vandame, B., Rité, C., Nonino, M., Cesarsky, C., & GOODS Team (2010). The Great Observatories Origins Deep Survey. VLT/ISAAC near-infrared imaging of the GOODS-South field. *A&A*, 511, A50.

Rieke, G. H., Young, E. T., Engelbracht, C. W., Kelly, D. M., Low, F. J., Haller, E. E., Beeman, J. W., Gordon, K. D., Stansberry, J. A., Misselt, K. A., Cadien, J., Morrison, J. E., Rivlis, G., Latter, W. B., Noriega-Crespo, A., Padgett, D. L., Stapelfeldt, K. R., Hines, D. C., Egami, E., Muzerolle, J., Alonso-Herrero, A., Blaylock, M., Dole, H., Hinz, J. L., Le Floc'h, E., Papovich, C., Pérez-González, P. G., Smith, P. S., Su, K. Y. L., Bennett, L., Frayer, D. T., Henderson, D., Lu, N., Masci, F., Pesenson, M., Rebull, L., Rho, J., Keene, J., Stolovy, S., Wachter, S., Wheaton, W., Werner, M. W., & Richards, P. L. (2004). The Multiband Imaging Photometer for Spitzer (MIPS). *ApJS*, 154, 25–29.

Robertson, B. E., Ellis, R. S., Dunlop, J. S., McLure, R. J., Stark, D. P., & McLeod, D. (2014). Accounting for Cosmic Variance in Studies of Gravitationally Lensed High-redshift Galaxies in the Hubble Frontier Field Clusters. *ApJL*, 796, L27.

Rowan-Robinson, M., Oliver, S., Wang, L., Farrah, D., Clements, D. L., Gruppioni, C., Marchetti, L., Rigopoulou, D., & Vaccari, M. (2016). The star formation rate density from z = 1 to 6. *MNRAS*, 461, 1100–1111.

Rujopakarn, W., Dunlop, J. S., Rieke, G. H., Ivison, R. J., Cibinel, A., Nyland, K., Jagannathan, P., Silverman, J. D., Alexander, D. M., Biggs, A. D., Bhatnagar, S., Ballantyne, D. R., Dickinson, M., Elbaz, D., Geach, J. E., Hayward, C. C., Kirkpatrick, A., McLure, R. J., Michałowski, M. J., Miller, N. A., Narayanan, D., Owen, F. N., Pannella, M., Papovich, C., Pope, A., Rau, U., Robertson, B. E., Scott, D., Swinbank, A. M., van der Werf, P., van Kampen, E., Weiner, B. J., & Windhorst, R. A. (2016). VLA and ALMA Imaging of Intense Galaxy-wide Star Formation in z $\sim$ 2 Galaxies. *ApJ*, 833, 12.

Safarzadeh, M., Hayward, C. C., & Ferguson, H. C. (2017). The IRX-β Relation: Insights from Simulations. *ApJ*, 840, 15.

Sargent, M. T., Daddi, E., Béthermin, M., Aussel, H., Magdis, G., Hwang, H. S., Juneau, S., Elbaz, D., & da Cunha, E. (2014). Regularity Underlying Complexity: A Redshift-independent Description of the Continuous Variation of Galaxy-scale Molecular Gas Properties in the Mass-star Formation Rate Plane. *ApJ*, 793, 19.

Sargsyan, L., Lebouteiller, V., Weedman, D., Spoon, H., Bernard-Salas, J., Engels, D., Stacey, G., Houck, J., Barry, D., Miles, J., & Samsonyan, A. (2012). [CII] 158 μm Luminosities and Star Formation Rate in Dusty Starbursts and Active Galactic Nuclei. *ApJ*, 755, 171.

Sargsyan, L., Samsonyan, A., Lebouteiller, V., Weedman, D., Barry, D., Bernard-Salas, J., Houck, J., & Spoon, H. (2014). Star Formation Rates from [CII] 158 μm and Mid-infrared Emission Lines for Starbursts and Active Galactic Nuclei. *ApJ*, 790, 15.

Schreiber, C., Pannella, M., Elbaz, D., Béthermin, M., Inami, H., Dickinson, M., Magnelli, B., Wang, T., Aussel, H., Daddi, E., Juneau, S., Shu, X., Sargent, M. T., Buat, V., Faber, S. M., Ferguson, H. C., Giavalisco, M., Koekemoer, A. M., Magdis, G., Morrison, G. E., Papovich, C., Santini, P., & Scott, D. (2015). The Herschel view of the dominant mode of galaxy growth from z = 4 to the present day. *A&A*, 575, A74.

Scott, K. S., Austermann, J. E., Perera, T. A., Wilson, G. W., Aretxaga, I., Bock, J. J., Hughes, D. H., Kang, Y., Kim, S., Mauskopf, P. D., Sanders, D. B., Scoville, N., & Yun, M. S. (2008). AzTEC millimetre survey of the COSMOS field - I. Data reduction and source catalogue. *MNRAS*, 385, 2225–2238.

Scott, K. S., Wilson, G. W., Aretxaga, I., Austermann, J. E., Chapin, E. L., Dunlop, J. S., Ezawa, H., Halpern, M., Hatsukade, B., Hughes, D. H., Kawabe, R., Kim, S., Kohno, K., Lowenthal, J. D., Montaña, A., Nakanishi, K., Oshima, T., Sanders, D., Scott, D., Scoville, N., Tamura, Y., Welch, D., Yun, M. S., & Zeballos, M. (2012). The source counts of submillimetre galaxies detected at λ= 1.1 mm. *MNRAS*, 423, 575–589.

Scott, K. S., Yun, M. S., Wilson, G. W., Austermann, J. E., Aguilar, E., Aretxaga, I., Ezawa, H., Ferrusca, D., Hatsukade, B., Hughes, D. H., Iono, D., Giavalisco, M., Kawabe, R., Kohno, K., Mauskopf, P. D., Oshima, T., Perera, T. A., Rand, J., Tamura, Y., Tosaki, T., Velazquez, M., Williams, C. C., & Zeballos, M. (2010). Deep 1.1mm-wavelength imaging of the GOODS-S field by AzTEC/ASTE - I. Source catalogue and number counts. *MNRAS*, 405, 2260–2278.

Serra, P., Doré, O., & Lagache, G. (2016). Dissecting the High-z Interstellar Medium through Intensity Mapping Cross-correlations. *ApJ*, 833, 153.

Silva, L., Granato, G. L., Bressan, A., & Danese, L. (1998). Modeling the Effects of Dust on Galactic Spectral Energy Distributions from the Ultraviolet to the Millimeter Band. *ApJ*, 509, 103–117.

Simpson, J. M., Smail, I., Swinbank, A. M., Chapman, S. C., Geach, J. E., Ivison, R. J., Thomson, A. P., Aretxaga, I., Blain, A. W., Cowley, W. I., Chen, C.-C., Coppin, K. E. K., Dunlop, J. S., Edge, A. C., Farrah, D., Ibar, E., Karim, A., Knudsen, K. K., Meijerink, R., Michałowski, M. J., Scott, D., Spaans, M., & van der Werf, P. P. (2015). The SCUBA-2 Cosmology Legacy Survey: ALMA Resolves the Bright-end of the Sub-millimeter Number Counts. *ApJ*, 807, 128.

Simpson, J. M., Smail, I., Swinbank, A. M., Ivison, R. J., Dunlop, J. S., Geach, J. E., Almaini, O., Arumugam, V., Bremer, M. N., Chen, C.-C., Conselice, C., Coppin, K. E. K., Farrah, D., Ibar, E., Hartley, W. G., Ma, C. J., Michałowski, M. J., Scott, D., Spaans, M., Thomson, A. P., & van der Werf, P. P. (2017). The SCUBA-2 Cosmology Legacy Survey: Multi-wavelength Properties of ALMA-identified Submillimeter Galaxies in UKIDSS UDS. *ApJ*, 839, 58.

Simpson, J. M., Swinbank, A. M., Smail, I., Alexander, D. M., Brandt, W. N., Bertoldi, F., de Breuck, C., Chapman, S. C., Coppin, K. E. K., da Cunha, E., Danielson, A. L. R., Dannerbauer, H., Greve, T. R., Hodge, J. A., Ivison, R. J., Karim, A., Knudsen, K. K., Poggianti, B. M., Schinnerer, E., Thomson, A. P.,

Walter, F., Wardlow, J. L., Weiß, A., & van der Werf, P. P. (2014). An ALMA Survey of Submillimeter Galaxies in the Extended Chandra Deep Field South: The Redshift Distribution and Evolution of Submillimeter Galaxies. *ApJ*, 788, 125.

Siringo, G., Kreysa, E., De Breuck, C., Kovacs, A., Lundgren, A., Schuller, F., Stanke, T., Weiss, A., Guesten, R., Jethava, N., May, T., Menten, K. M., Meyer, H.-G., Starkloff, M., & Zakosarenko, V. (2010). A New Facility Receiver on APEX: The Submillimetre APEX Bolometer Camera, SABOCA. *The Messenger*, 139, 20–23.

Skelton, R. E., Whitaker, K. E., Momcheva, I. G., Brammer, G. B., van Dokkum, P. G., Labbé, I., Franx, M., van der Wel, A., Bezanson, R., Da Cunha, E., Fumagalli, M., Förster Schreiber, N., Kriek, M., Leja, J., Lundgren, B. F., Magee, D., Marchesini, D., Maseda, M. V., Nelson, E. J., Oesch, P., Pacifici, C., Patel, S. G., Price, S., Rix, H.-W., Tal, T., Wake, D. A., & Wuyts, S. (2014). 3D-HST WFC3-selected Photometric Catalogs in the Five CANDELS/3D-HST Fields: Photometry, Photometric Redshifts, and Stellar Masses. *ApJS*, 214, 24.

Smail, I., Ivison, R. J., & Blain, A. W. (1997). A Deep Sub-millimeter Survey of Lensing Clusters: A New Window on Galaxy Formation and Evolution. *ApJL*, 490, L5–L8.

Smail, I., Swinbank, A. M., Ivison, R. J., & Ibar, E. (2011). The potential influence of far-infrared emission lines on the selection of high-redshift galaxies. *MNRAS*, 414, L95–L99.

Solomon, P. M., Rivolo, A. R., Barrett, J., & Yahil, A. (1987). Mass, luminosity, and line width relations of Galactic molecular clouds. *ApJ*, 319, 730–741.

Steidel, C. C., Adelberger, K. L., Giavalisco, M., Dickinson, M., & Pettini, M. (1999). Lyman-Break Galaxies at z$\geq$4 and the Evolution of the Ultraviolet Luminosity Density at High Redshift. *ApJ*, 519, 1–17.

Straatman, C. M. S., Spitler, L. R., Quadri, R. F., Labbé, I., Glazebrook, K., Persson, S. E., Papovich, C., Tran, K.-V. H., Brammer, G. B., Cowley, M., Tomczak, A., Nanayakkara, T., Alcorn, L., Allen, R., Broussard, A., van Dokkum, P., Forrest, B., van Houdt, J., Kacprzak, G. G., Kawinwanichakij, L., Kelson, D. D., Lee, J., McCarthy, P. J., Mehrtens, N., Monson, A., Murphy, D., Rees, G., Tilvi, V., & Whitaker, K. E. (2016). The FourStar Galaxy Evolution Survey (ZFOURGE): Ultraviolet to Far-infrared Catalogs, Medium-bandwidth Photometric Redshifts with Improved Accuracy, Stellar Masses, and Confirmation of Quiescet Galaxies to z $\sim$ 3.5. *ApJ*, 830, 51.

Strandet, M. L., Weiss, A., Vieira, J. D., de Breuck, C., Aguirre, J. E., Aravena, M., Ashby, M. L. N., Béthermin, M., Bradford, C. M., Carlstrom, J. E., Chapman, S. C., Crawford, T. M., Everett, W., Fassnacht, C. D., Furstenau, R. M., Gonzalez, A. H., Greve, T. R., Gullberg, B., Hezaveh, Y., Kamenetzky, J. R., Litke, K., Ma, J., Malkan, M., Marrone, D. P., Menten, K. M., Murphy, E. J., Nadolski, A., Rotermund, K. M., Spilker, J. S., Stark, A. A., & Welikala, N. (2016). The Redshift Distribution of Dusty Star-forming Galaxies from the SPT Survey. *ApJ*, 822, 80.

Swinbank, A. M., Karim, A., Smail, I., Hodge, J., Walter, F., Bertoldi, F., Biggs, A. D., de Breuck, C., Chapman, S. C., Coppin, K. E. K., Cox, P., Danielson, A. L. R., Dannerbauer, H., Ivison, R. J., Greve, T. R., Knudsen, K. K., Menten, K. M., Simpson, J. M., Schinnerer, E., Wardlow, J. L., Weiß, A., & van der Werf, P. (2012). An ALMA survey of submillimetre galaxies in the Extended Chandra Deep Field-South: detection of [CII] at z = 4.4. *MNRAS*, 427, 1066–1074.

Swinbank, A. M., Simpson, J. M., Smail, I., Harrison, C. M., Hodge, J. A., Karim, A., Walter, F., Alexander, D. M., Brandt, W. N., de Breuck, C., da Cunha, E., Chapman, S. C., Coppin, K. E. K., Danielson, A. L. R., Dannerbauer, H., Decarli, R., Greve, T. R., Ivison, R. J., Knudsen, K. K., Lagos, C. D. P., Schinnerer, E., Thomson, A. P., Wardlow, J. L., Weiß, A., & van der Werf, P. (2014). An ALMA survey of sub-millimetre Galaxies in the Extended Chandra Deep Field South: the far-infrared properties of SMGs. *MNRAS*, 438, 1267–1287.

Tacconi, L. J., Genzel, R., Saintonge, A., Combes, F., García-Burillo, S., Neri, R., Bolatto, A., Contini, T., Förster Schreiber, N. M., Lilly, S., Lutz, D., Wuyts, S., Accurso, G., Boissier, J., Boone, F., Bouché, N., Bournaud, F., Burkert, A., Carollo, M., Cooper, M., Cox, P., Feruglio, C., Freundlich, J., Herrera-Camus, R., Juneau, S., Lippa, M., Naab, T., Renzini, A., Salome, P., Sternberg, A., Tadaki, K., Übler, H., Walter, F., Weiner, B., & Weiss, A. (2018). PHIBSS: Unified Scaling Relations of Gas Depletion Time and Molecular Gas Fractions. *ApJ*, 853, 179.

Tacconi, L. J., Neri, R., Genzel, R., Combes, F., Bolatto, A., Cooper, M. C., Wuyts, S., Bournaud, F., Burkert, A., Comerford, J., Cox, P., Davis, M., Förster Schreiber, N. M., García-Burillo, S., Gracia-Carpio, J., Lutz, D., Naab, T., Newman, S., Omont, A., Saintonge, A., Shapiro Griffin, K., Shapley, A., Sternberg, A., & Weiner, B. (2013). Phibss: Molecular Gas Content and Scaling Relations in z ~ 1-3 Massive, Main-sequence Star-forming Galaxies. *ApJ*, 768, 74.

Tadaki, K.-i., Kodama, T., Nelson, E. J., Belli, S., Förster Schreiber, N. M., Genzel, R., Hayashi, M., Herrera-Camus, R., Koyama, Y., Lang, P., Lutz, D., Shimakawa, R., Tacconi, L. J., Übler, H., Wisnioski, E., Wuyts, S., Hatsukade, B., Lippa, M., Nakanishi, K., Ikarashi, S., Kohno, K., Suzuki, T. L., Tamura, Y., & Tanaka, I. (2017). Rotating Starburst Cores in Massive Galaxies at z = 2.5. *ApJL*, 841, L25.

Tadaki, K.-i., Kohno, K., Kodama, T., Ikarashi, S., Aretxaga, I., Berta, S., Caputi, K. I., Dunlop, J. S., Hatsukade, B., Hayashi, M., Hughes, D. H., Ivison, R., Izumi, T., Koyama, Y., Lutz, D., Makiya, R., Matsuda, Y., Nakanishi, K., Rujopakarn, W., Tamura, Y., Umehata, H., Wang, W.-H., Wilson, G. W., Wuyts, S., Yamaguchi, Y., & Yun, M. S. (2015). SXDF-ALMA 1.5 arcmin^2 Deep Survey: A Compact Dusty Star-forming Galaxy at z = 2.5. *ApJL*, 811, L3.

Takeuchi, T. T., Buat, V., & Burgarella, D. (2005). The evolution of the ultraviolet and infrared luminosity densities in the universe at $0 < z < 1$. *A&A*, 440, L17–L20.

Takeuchi, T. T., Yuan, F.-T., Ikeyama, A., Murata, K. L., & Inoue, A. K. (2012). Reexamination of the Infrared Excess-Ultraviolet Slope Relation of Local Galaxies. *ApJ*, 755, 144.

Tamura, Y., Iono, D., Wilner, D. J., Kajisawa, M., Uchimoto, Y. K., Alexander, D. M., Chung, A., Ezawa, H., Hatsukade, B., Hayashino, T., Hughes, D. H., Ichikawa, T., Ikarashi, S., Kawabe, R., Kohno, K., Lehmer, B. D., Matsuda, Y., Nakanishi, K., Takata, T., Wilson, G. W., Yamada, T., & Yun, M. S. (2010). Submillimeter Array Identification of the Millimeter-selected Galaxy SSA22-AzTEC1: A Protoquasar in a Protocluster? *ApJ*, 724, 1270–1282.

Tamura, Y., Kohno, K., Nakanishi, K., Hatsukade, B., Iono, D., Wilson, G. W., Yun, M. S., Takata, T., Matsuda, Y., Tosaki, T., Ezawa, H., Perera, T. A., Scott, K. S., Austermann, J. E., Hughes, D. H., Aretxaga, I., Chung, A., Oshima, T., Yamaguchi, N., Tanaka, K., & Kawabe, R. (2009). Spatial correlation between submillimetre and Lyman-α galaxies in the SSA22 protocluster. *Nature*, 459, 61–63.

Tamura, Y., Saito, T., Tsuru, T. G., Uchida, H., Iono, D., Yun, M. S., Espada, D., & Kawabe, R. (2014). Serendipitous ALMA Detection of a Distant CO-emitting X-Ray Bright Galaxy. *ApJL*, 781, L39.

Thompson, A. R., Moran, J. M., & Swenson Jr., G. W. (2017). *Interferometry and Synthesis in Radio Astronomy third edition*. Springer International Publishing.

Tody, D. (1993). IRAF in the Nineties. In R. J. Hanisch, R. J. V. Brissenden, & J. Barnes (Eds.), *Astronomical Data Analysis Software and Systems II*, volume 52 of *Astronomical Society of the Pacific Conference Series* (pp. 173).

Ueda, Y., Hatsukade, B., Kohno, K., Yamaguchi, Y., Tamura, Y., Umehata, H., Akiyama, M., Ao, Y., Aretxaga, I., Caputi, K., Dunlop, J. S., Espada, D., Fujimoto, S., Hayatsu, N. H., Imanishi, M., Inoue, A. K., Ivison, R. J., Kodama, T., Lee, M. M., Matsuoka, K., Miyaji, T., Morokuma-Matsui, K., Nagao, T., Nakanishi, K., Nyland, K., Ohta, K., Ouchi, M., Rujopakarn, W., Saito, T., Tadaki, K., Tanaka, I., Taniguchi, Y., Wang, T., Wang, W.-H., Yoshimura, Y., & Yun, M. S. (2018). ALMA 26 arcmin^2 Survey

of GOODS-S at One-millimeter (ASAGAO): X-Ray AGN Properties of Millimeter-selected Galaxies. *ApJ*, 853, 24.

Umehata, H., Hatsukade, B., Smail, I., Alexander, D. M., Ivison, R. J., Matsuda, Y., Tamura, Y., Kohno, K., Kato, Y., Hayatsu, N. H., Kubo, M., & Ikarashi, S. (2018). ALMA deep field in SSA22: Survey design and source catalog of a 20 arcmin^2 survey at 1.1 mm. *PASJ*, 70, 65.

Umehata, H., Tamura, Y., Kohno, K., Hatsukade, B., Scott, K. S., Kubo, M., Yamada, T., Ivison, R. J., Cybulski, R., Aretxaga, I., Austermann, J., Hughes, D. H., Ezawa, H., Hayashino, T., Ikarashi, S., Iono, D., Kawabe, R., Matsuda, Y., Matsuo, H., Nakanishi, K., Oshima, T., Perera, T., Takata, T., Wilson, G. W., & Yun, M. S. (2014). AzTEC/ASTE 1.1-mm survey of SSA22: Counterpart identification and photometric redshift survey of submillimetre galaxies. *MNRAS*, 440, 3462–3478.

Umehata, H., Tamura, Y., Kohno, K., Ivison, R. J., Smail, I., Hatsukade, B., Nakanishi, K., Kato, Y., Ikarashi, S., Matsuda, Y., Fujimoto, S., Iono, D., Lee, M., Steidel, C. C., Saito, T., Alexander, D. M., Yun, M. S., & Kubo, M. (2017). ALMA Deep Field in SSA22: Source Catalog and Number Counts. *ApJ*, 835, 98.

Umetsu, K., Medezinski, E., Nonino, M., Merten, J., Postman, M., Meneghetti, M., Donahue, M., Czakon, N., Molino, A., Seitz, S., Gruen, D., Lemze, D., Balestra, I., Benítez, N., Biviano, A., Broadhurst, T., Ford, H., Grillo, C., Koekemoer, A., Melchior, P., Mercurio, A., Moustakas, J., Rosati, P., & Zitrin, A. (2014). CLASH: Weak-lensing Shear-and-magnification Analysis of 20 Galaxy Clusters. *ApJ*, 795, 163.

Vallini, L., Gruppioni, C., Pozzi, F., Vignali, C., & Zamorani, G. (2016). CO luminosity function from Herschel-selected galaxies and the contribution of AGN. *MNRAS*, 456, L40–L44.

Vega, O., Clemens, M. S., Bressan, A., Granato, G. L., Silva, L., & Panuzzo, P. (2008). Modelling the spectral energy distribution of ULIRGs. II. The energetic environment and the dense interstellar medium. *A&A*, 484, 631–653.

Walter, F., Decarli, R., Aravena, M., Carilli, C., Bouwens, R., da Cunha, E., Daddi, E., Ivison, R. J., Riechers, D., Smail, I., Swinbank, M., Weiss, A., Anguita, T., Assef, R., Bacon, R., Bauer, F., Bell, E. F., Bertoldi, F., Chapman, S., Colina, L., Cortes, P. C., Cox, P., Dickinson, M., Elbaz, D., Gónzalez-López, J., Ibar, E., Inami, H., Infante, L., Hodge, J., Karim, A., Le Fevre, O., Magnelli, B., Neri, R., Oesch, P., Ota, K., Popping, G., Rix, H.-W., Sargent, M., Sheth, K., van der Wel, A., van der Werf, P., & Wagg, J. (2016). ALMA Spectroscopic Survey in the Hubble Ultra Deep Field: Survey Description. *ApJ*, 833, 67.

Walter, F., Decarli, R., Carilli, C., Bertoldi, F., Cox, P., da Cunha, E., Daddi, E., Dickinson, M., Downes, D., Elbaz, D., Ellis, R., Hodge, J., Neri, R., Riechers, D. A., Weiss, A., Bell, E., Dannerbauer, H., Krips, M., Krumholz, M., Lentati, L., Maiolino, R., Menten, K., Rix, H.-W., Robertson, B., Spinrad, H., Stark, D. P., & Stern, D. (2012). The intense starburst HDF 850.1 in a galaxy overdensity at z $\simeq$ 5.2 in the Hubble Deep Field. *Nature*, 486, 233–236.

Walter, F., Decarli, R., Sargent, M., Carilli, C., Dickinson, M., Riechers, D., Ellis, R., Stark, D., Weiner, B., Aravena, M., Bell, E., Bertoldi, F., Cox, P., Da Cunha, E., Daddi, E., Downes, D., Lentati, L., Maiolino, R., Menten, K. M., Neri, R., Rix, H.-W., & Weiss, A. (2014). A Molecular Line Scan in the Hubble Deep Field North: Constraints on the CO Luminosity Function and the Cosmic H_2 Density. *ApJ*, 782, 79.

Wang, W.-H., Barger, A. J., & Cowie, L. L. (2009). Ultradeep Near-Infrared Observations of Goods 850-5. *ApJ*, 690, 319–329.

Wang, X., Hoag, A., Huang, K.-H., Treu, T., Bradač, M., Schmidt, K. B., Brammer, G. B., Vulcani, B., Jones, T. A., Ryan, Jr., R. E., Amorín, R., Castellano, M., Fontana, A., Merlin, E., & Trenti, M. (2015). The Grism Lens-amplified Survey from Space (GLASS). IV. Mass Reconstruction of the Lensing Cluster Abell 2744 from Frontier Field Imaging and GLASS Spectroscopy. *ApJ*, 811, 29.

Wang T., Elbaz, D., Daddi, E., Finoguenov, A., Liu, D., Schreiber, C., Martín, S., Strazzullo, V., Valentino, F., van der Burg, R., Zanella, A., Ciesla, L., Gobat, R., Le Brun, A., Pannella, M., Sargent, M., Shu, X., Tan, Q., Cappelluti, N., & Li, Y. (2016). Discovery of a Galaxy Cluster with a Violently Starbursting Core at z = 2.506. *ApJ*, 828, 56.

Wang W.-H., Kohno, K., Hatsukade, B., Umehata, H., Aretxaga, I., Hughes, D., Caputi, K. I., Dunlop, J. S., Ikarashi, S., Iono, D., Ivison, R. J., Lee, M., Makiya, R., Matsuda, Y., Motohara, K., Nakanish, K., Ohta, K., Tadaki, K.-i., Tamura, Y., Kodama, T., Rujopakarn, W., Wilson, G. W., Yamaguchi, Y., Yun, M. S., Coupon, J., Hsieh, B.-C., & Foucaud, S. (2016). The SXDF-ALMA 2-arcmin^2 Deep Survey: Stacking Rest-frame Near-infrared Selected Objects. *ApJ*, 833, 195.

Wardlow, J. L., Smail, I., Coppin, K. E. K., Alexander, D. M., Brandt, W. N., Danielson, A. L. R., Luo, B., Swinbank, A. M., Walter, F., Weiß, A., Xue, Y. Q., Zibetti, S., Bertoldi, F., Biggs, A. D., Chapman, S. C., Dannerbauer, H., Dunlop, J. S., Gawiser, E., Ivison, R. J., Knudsen, K. K., Kovács, A., Lacey, C. G., Menten, K. M., Padilla, N., Rix, H.-W., & van der Werf, P. P. (2011). The LABOCA survey of the Extended Chandra Deep Field-South: a photometric redshift survey of submillimetre galaxies. *MNRAS*, 415, 1479–1508.

Weingartner, J. C. & Draine, B. T. (2001). Electron-Ion Recombination on Grains and Polycyclic Aromatic Hydrocarbons. *ApJ*, 563, 842–852.

Weiß, A., Kovács, A., Coppin, K., Greve, T. R., Walter, F., Smail, I., Dunlop, J. S., Knudsen, K. K., Alexander, D. M., Bertoldi, F., Brandt, W. N., Chapman, S. C., Cox, P., Dannerbauer, H., De Breuck, C., Gawiser, E., Ivison, R. J., Lutz, D., Menten, K. M., Koekemoer, A. M., Kreysa, E., Kurczynski, P., Rix, H.-W., Schinnerer, E., & van der Werf, P. P. (2009). The Large Apex Bolometer Camera Survey of the Extended Chandra Deep Field South. *ApJ*, 707, 1201–1216.

Weisskopf, M. C., Tananbaum, H. D., Van Speybroeck, L. P., & O'Dell, S. L. (2000). Chandra X-ray Observatory (CXO): overview. In J. E. Truemper & B. Aschenbach (Eds.), *X-Ray Optics, Instruments, and Missions III*, volume 4012 of *Proc. SPIE* (pp. 2–16).

Whitaker, K. E., Franx, M., Leja, J., van Dokkum, P. G., Henry, A., Skelton, R. E., Fumagalli, M., Momcheva, I. G., Brammer, G. B., Labbé, I., Nelson, E. J., & Rigby, J. R. (2014). Constraining the Low-mass Slope of the Star Formation Sequence at $0.5 < z < 2.5$. *ApJ*, 795, 104.

Whitaker, K. E., Labbé, I., van Dokkum, P. G., Brammer, G., Kriek, M., Marchesini, D., Quadri, R. F., Franx, M., Muzzin, A., Williams, R. J., Bezanson, R., Illingworth, G. D., Lee, K.-S., Lundgren, B., Nelson, E. J., Rudnick, G., Tal, T., & Wake, D. A. (2011). The NEWFIRM Medium-band Survey: Photometric Catalogs, Redshifts, and the Bimodal Color Distribution of Galaxies out to $z \sim 3$. *ApJ*, 735, 86.

Williams, J. P., de Geus, E. J., & Blitz, L. (1994). Determining structure in molecular clouds. *ApJ*, 428, 693–712.

Wilson, G. W., Austermann, J. E., Perera, T. A., Scott, K. S., Ade, P. A. R., Bock, J. J., Glenn, J., Golwala, S. R., Kim, S., Kang, Y., Lydon, D., Mauskopf, P. D., Predmore, C. R., Roberts, C. M., Souccar, K., & Yun, M. S. (2008). The AzTEC mm-wavelength camera. *MNRAS*, 386, 807–818.

Windhorst, R. A., Cohen, S. H., Hathi, N. P., McCarthy, P. J., Ryan, Jr., R. E., Yan, H., Baldry, I. K., Driver, S. P., Frogel, J. A., Hill, D. T., Kelvin, L. S., Koekemoer, A. M., Mechtley, M., O'Connell, R. W., Robotham, A. S. G., Rutkowski, M. J., Seibert, M., Straughn, A. N., Tuffs, R. J., Balick, B., Bond, H. E., Bushouse, H., Calzetti, D., Crockett, M., Disney, M. J., Dopita, M. A., Hall, D. N. B., Holtzman, J. A., Kaviraj, S., Kimble, R. A., MacKenty, J. W., Mutchler, M., Paresce, F., Saha, A., Silk, J. I., Trauger, J. T., Walker, A. R., Whitmore, B. C., & Young, E. T. (2011). The Hubble Space Telescope Wide Field Camera 3 Early Release Science Data: Panchromatic Faint Object Counts for 0.2-2 μm Wavelength. *ApJS*, 193, 27.

Wisnioski, E., Förster Schreiber, N. M., Wuyts, S., Wuyts, E., Bandara, K., Wilman, D., Genzel, R., Bender, R., Davies, R., Fossati, M., Lang, P., Mendel, J. T., Beifiori, A., Brammer, G., Chan, J., Fabricius, M., Fudamoto, Y., Kulkarni, S., Kurk, J., Lutz, D., Nelson, E. J., Momcheva, I., Rosario, D., Saglia, R., Seitz, S., Tacconi, L. J., & van Dokkum, P. G. (2015). The KMOS^{3D} Survey: Design, First Results, and the Evolution of Galaxy Kinematics from 0.7 <= z <= 2.7. *ApJ*, 799, 209.

Wuyts, S., Labbé, I., Förster Schreiber, N. M., Franx, M., Rudnick, G., Brammer, G. B., & van Dokkum, P. G. (2008). FIREWORKS U_{38}-to-24 μm Photometry of the GOODS Chandra Deep Field-South: Multiwavelength Catalog and Total Infrared Properties of Distant K_s-selected Galaxies. *ApJ*, 682, 985–1003.

Yamaguchi, Y., Kohno, K., Tamura, Y., Oguri, M., Ezawa, H., Hayatsu, N. H., Kitayama, T., Matsuda, Y., Matsuo, H., Oshima, T., Ota, N., Izumi, T., & Umehata, H. (2017). Blind Millimeter Line Emitter Search using ALMA Data Toward Gravitational Lensing Clusters. *ApJ*, 845, 108.

Yamaguchi, Y., Tamura, Y., Kohno, K., Aretxaga, I., Dunlop, J. S., Hatsukade, B., Hughes, D., Ikarashi, S., Ishii, S., Ivison, R. J., Izumi, T., Kawabe, R., Kodama, T., Lee, M., Makiya, R., Matsuda, Y., Nakanishi, K., Ohta, K., Rujopakarn, W., Tadaki, K.-i., Umehata, H., Wang, W.-H., Wilson, G. W., Yabe, K., & Yun, M. S. (2016). SXDF-ALMA 2 arcmin^2 deep survey: Resolving and characterizing the infrared extragalactic background light down to 0.5 mJy. *PASJ*, 68, 82.

Yuan, F.-T., Argudo-Fernández, M., Shen, S., Hao, L., Jiang, C., Yin, J., Boquien, M., & Lin, L. (2018). Spatially resolved star formation and dust attenuation in Mrk 848: Comparison of the integral field spectra and the UV-to-IR SED. *A&A*, 613, A13.

Yun, M. S., Aretxaga, I., Ashby, M. L. N., Austermann, J., Fazio, G. G., Giavalisco, M., Huang, J.-S., Hughes, D. H., Kim, S., Lowenthal, J. D., Perera, T., Scott, K., Wilson, G., & Younger, J. D. (2008). Spitzer IRAC infrared colours of submillimetre-bright galaxies. *MNRAS*, 389, 333–340.

Yun, M. S., Scott, K. S., Guo, Y., Aretxaga, I., Giavalisco, M., Austermann, J. E., Capak, P., Chen, Y., Ezawa, H., Hatsukade, B., Hughes, D. H., Iono, D., Johnson, S., Kawabe, R., Kohno, K., Lowenthal, J., Miller, N., Morrison, G., Oshima, T., Perera, T. A., Salvato, M., Silverman, J., Tamura, Y., Williams, C. C., & Wilson, G. W. (2012). Deep 1.1 mm-wavelength imaging of the GOODS-S field by AzTEC/ASTE - II. Redshift distribution and nature of the submillimetre galaxy population. *MNRAS*, 420, 957–985.

Zavala, J. A., Aretxaga, I., Dunlop, J. S., Michałowski, M. J., Hughes, D. H., Bourne, N., Chapin, E., Cowley, W., Farrah, D., Lacey, C., Targett, T., & van der Werf, P. (2018). The SCUBA-2 Cosmology

Legacy Survey: The EGS deep field - II. Morphological transformation and multiwavelength properties of faint submillimetre galaxies. *MNRAS*, 475, 5585–5602.